THE UNIVERSITY *of* EDINBURGH

THE UNIVERSITY *of* EDINBURGH
School of GeoSciences

Nutrient cycling and the biological pump in the Southern Ocean across the last deglaciation

by

Matthew Dumont

A thesis submitted in partial fulfillment for the degree of
PhD

School of Geosciences
UNIVERSITY OF EDINBURGH

February 2019

Declaration of Authorship

I, Matthew Dumont, declare that this thesis titled, 'Nutrient cycling and the biological pump in the Southern Ocean across the last deglaciation' and the work presented in it are my own. I confirm that:

- This work was done wholly or mainly while in candidature for a research degree at this University.
- Where any part of this thesis has previously been submitted for a degree or any other qualification at this University or any other institution, this has been clearly stated.
- Where I have consulted the published work of others, this is always clearly attributed.
- Where I have quoted from the work of others, the source is always given. With the exception of such quotations, this thesis is entirely my own work.
- I have acknowledged all main sources of help.
- Where the thesis is based on work done by myself jointly with others, I have made clear exactly what was done by others and what I have contributed myself.

Signed: 

Date: 21/03/2019

UNIVERSITY OF EDINBURGH

Lay Summary

School of Geosciences

PhD

by Matthew Dumont

Carbon dioxide (CO_2) is a greenhouse gas, the concentration of which in the atmosphere has a strong influence on the temperature of the Earth's surface. Throughout Earth's history CO_2 has had an important impact on the global climate, driving or amplifying global temperature changes. However, the causes of atmospheric CO_2 variability through time are not fully understood. By looking into the past during periods when CO_2 changed, we can attempt to better understand the processes that drive such variability.

This study focuses on the transition out of the last ice age, known as the deglaciation that occurred 10,000 – 18,000 years before present. Across the deglaciation atmospheric CO_2 rose by approximately 80 ppm, the largest increase in CO_2 for over 100,000 years (aside from the present day CO_2 rise). Here we provide evidence that the CO_2 rise across the deglaciation was caused by a change in the circulation of water within the oceans. Before the deglaciation, the flow and mixing of water from the surface ocean to the bottom of the ocean slowed, effectively isolating a portion of the deep ocean from the rest. CO_2 accumulated within this deep isolated reservoir until the circulation of water abruptly changed. During the deglaciation, this isolated reservoir was carried up to the surface within the ocean that surrounds Antarctica, the Southern Ocean. Part of the reason why this change of water circulation occurred appears to have been the removal of sea ice around Antarctica.

In addition, it was demonstrated that the amount and distribution of silicon and nitrogen within the oceans changed across the deglaciation. Chemicals containing these elements are important for the growth of many algae in the oceans, which play an essential role in drawing down atmospheric CO_2. Therefore, changes in the amount of silicon and nitrogen available to the algae can influence atmospheric CO_2 concentrations and hence the climate. Ultimately it was found that an important factor controlling the amount and distribution of silicon and nitrogen across the world's oceans was the flow and mixing of water within the deepest parts of the ocean. This demonstrates that changes in deep water flow and mixing can have a profound influence on ocean chemistry and the global climate.

UNIVERSITY OF EDINBURGH

Abstract

School of Geosciences

PhD

by Matthew Dumont

Three high resolution multi-proxy records from the Indian sector of the Southern Ocean are presented that reconstruct nutrient cycling and the biological pump across the last deglaciation. Three new diatom silicon isotope records were constructed that demonstrate a major redistribution of the silicic acid and silicon isotopes in the world's oceans between the last glacial maximum and the present driven by changes in iron availability and oceanic circulation. Such changes have important implications for the power of diatoms to efficiently export carbon to the deep ocean.

New records of diatom-bound nitrogen isotopes ($\delta^{15}N_{DB}$), paleo-productivity proxies and planktic foraminiferal radiocarbon together demonstrate the role of Antarctic stratification in restricting deep ocean ventilation and promoting the drawdown of atmospheric CO_2 across glacial-interglacial cycles. The presence of 14C-depleted surface waters in the Antarctic during the deglaciation invokes a strong link between the upwelling of aged deep waters in the Southern Ocean and the rise in atmospheric CO_2.

Anomalously heavy $\delta^{15}N_{DB}$ observations during the deglacial upwelling intervals were interpreted as evidence for enhanced denitrification outside of the known oxygen minimum zones, driven by the deoxygenation of the deep ocean during glacial periods. The development of new denitrification regions has important implications for the marine nitrogen cycle and may have modulated the atmospheric CO_2 rise across the last deglaciation by weakening the biological pump.

Because Southern Ocean surface waters impart chemical properties on Southern Ocean intermediate waters, the new proxy records predict that intermediate waters became deoxygenated, ^{14}C-depleted and silica-rich during the deglaciation. This hypothesis helps explain numerous lower latitude proxy records from regions fed by intermediate waters, including the enhancement of denitrification in oxygen minimum zones, anomalously ^{14}C-depleted intermediate waters in the Arabian Sea, and the enhancement of diatom productivity in low latitude upwelling regions. Consequently, this work highlights the role of Southern Ocean hydrographical and biogeochemical processes in regulating nutrient cycling and the biological pump at low latitudes.

Acknowledgements

I would like to express my very great appreciation to Laetitia Pichevin and Raja Ganeshram for their supervision and guidance throughout this doctorate degree.

I would also like to offer a very special thanks to Steve Mowbray, Colin Chilcott and Walter Geibert for their time and and tireless work helping to produce the data presented here.

My special thanks goes to Elisabeth Michel for her advice, supply of sample material and unpublished carbonate isotope records.

My special thanks goes to Xavier Crosta for providing diatom assemblage data.

A thanks goes to Steve Moreton for assisting with the radiocarbon analysis at the NRCF, East Kilbride.

Advice given by Robyn Tuerena has been a great help in support of the nitrogen isotope analyses.

I am particularly grateful to NERC for finacially supporting me through this degree.

A thanks goes to Nisha Gurusamy for that foram picking.

An immense thank you goes to my family and friends for the unconditional support.

Finally, thank you Rebecca Chan.

Contents

1

Introduction

In 1896 Svante Arrhenius established a relationship between global average surface temperatures and atmospheric CO_2 concentrations, stating that "In order to get the temperature of the ice age ... the carbonic acid in the air should sink to 0.62 – 0.55 of its present value..." (Arrhenius, 1896). It was not until the advent of ice core research almost a century later that the remarkable accuracy of this prediction was realised. By measuring the partial pressure of CO_2 in air bubbles trapped within the ice cores it was shown that the atmosphere at peak ice ages had a CO_2 concentration of ≈180 ppmv (Figure 1.1), equivalent to $\sim 64\%$ of the pre-industrial atmosphere (Petit et al., 1999; Monnin et al., 2001; Lüthi et al., 2008; Parrenin et al., 2013; Bereiter et al., 2015). Given the context of anthropogenic climate change, renewed efforts have been made to uncover the mechanism for how CO_2 varies across these climatic states and how different natural systems respond during the abrupt transitions.

Oceanic cycling of carbon has been implicated as the source of the glacial-interglacial oscillation of the atmospheric carbon budget (Archer et al., 2000; Broecker, 2000; Sigman

and Boyle, 2000; Sigman et al., 2010), given the capacity of the ocean to store carbon and release it over the multi-millennial timescales required. Three processes have been described to explain how the carbon content of the oceans may have varied through time, which together have become known as the oceanic pumps (Volk and Hoffert, 1985). The solubility pump refers to the change in the equilibration of CO_2 between the ocean and atmosphere under changing water temperature and salinity. The biological (soft-tissue) pump is the drawdown of atmospheric CO_2 by photosynthesising organisms and their export into the deep ocean. Finally, the carbonate pump is the change in carbon uptake by the oceans with changing saturation state of carbon in the surface waters forced by the production and/or removal of carbonate in the ocean. Although all three pumps could have operated to reduce atmospheric CO_2 during glacial periods, the biological pump is regarded as the most powerful of the three over glacial-interglacial cycles (Sigman and Boyle, 2000).

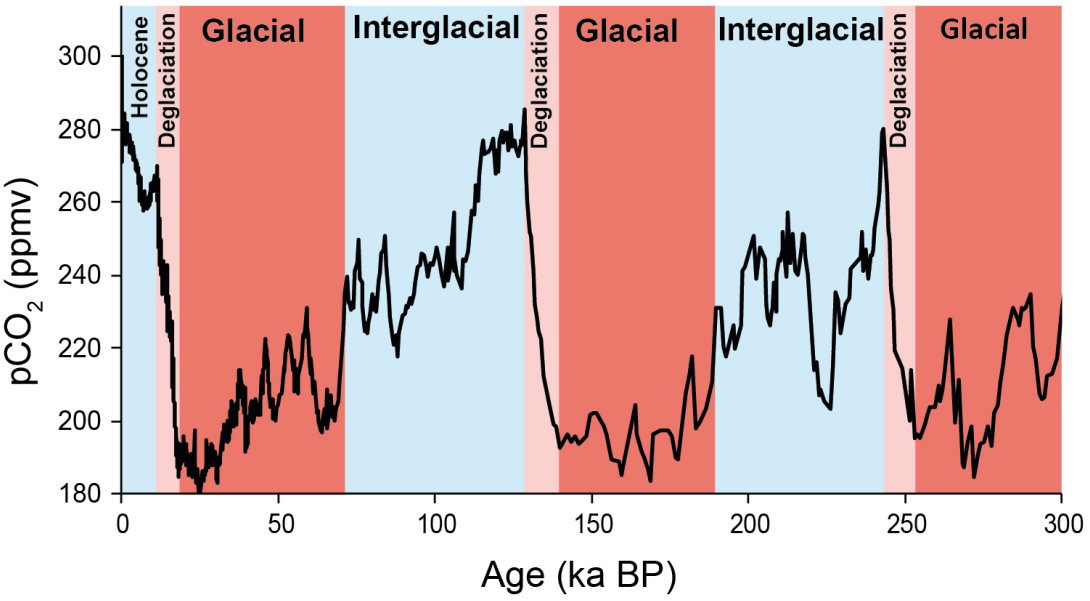

FIGURE 1.1: Atmospheric CO_2 concentrations across the last 300, 000 years (to 300 ka BP) from a composite of Antarctic ice core records (Bereiter et al., 2015 and references therein).

The biological pump operates to produce a gradient in dissolved inorganic carbon (DIC) and nutrients between the surface ocean/atmosphere and the deep ocean. This gradient is produced through the uptake of DIC by marine organisms in the surface ocean and its export as organic carbon upon their death or excretion to the deep ocean (collectively known as export production) where it remineralises back to DIC.

The concept of the biological pump could be aided by an analogy. In their 1983 book 'Tracers in the Sea', Broecker and Peng (1983) provided a surreal yet accurate analogy for the oceanic cycling of nutrients. They describe ocean circulation as a funhouse, however the scarcity of these amusements in modern fairgrounds warrants an update to the analogy which has been attempted here:

Sukura's sushi restaurant has two levels, the kitchen below and the dining room above. Sukura and her colleagues supply plated sushi to customers on the upper floor via innumerable conveyor belts that run all around the dining room above but eventually join as one before returning down to the kitchen. The customers pick up the sushi, eat wherever they like, and then drop the empty plates down holes at the table where they sat that lead down to the kitchen. The sushi is not made to order, so Sukura plates up sushi whenever plates are available. Should sushi go through the dining room uneaten, it returns to the kitchen and is thrown away, which represents a loss for Sukura. At any given moment, the distribution of sushi plates within the restaurant is controlled by the speed of the conveyor belts and the appetite of the customers. Fortunately, there are no overheads for Sukura, so her profit only depends on how much sushi is eaten by the customers versus how much is supplied.

In this analogy the sushi plates are the nutrients, the customers are biological export, the conveyor belts the ocean circulation and Sukura's profit is the efficiency of the biological pump. Should the speed of the conveyor belts (ocean circulation) increase then it is possible that more sushi will go uneaten (nutrients unutilized) and Sukura's profits will decline (inefficient biological pump, rise in atmospheric CO_2). If there are more customers or their appetite increases (increased biological export) then less sushi will be wasted, and Sukura's profit will rise (strengthened biological pump, decline in atmospheric CO_2) and vice versa.

In other words, increasing the amount of organic carbon exported to the deep ocean, either by increasing the primary production or the efficiency by which the organic carbon is transferred to the deep, would strengthen the vertical DIC gradient and lower atmospheric CO_2. On the other hand, the ocean's vertical mixing acts to remove vertical physical and chemical gradients, therefore more sluggish vertical mixing would also lead to a lowering of atmospheric CO_2 (Eppley and Peterson, 1979; Broecker, 1982).

Based on this framework, global oceanic circulation plays an important role in driving changes in atmospheric CO_2. The modern global overturning circulation can be described in terms of the two deep water formation regions and the oceanic basins their water masses

fill, which is schematically displayed in Figure 1.2. Antarctic Bottom Water (AABW) forms in the Southern Ocean and is the primary contributor of water mass fluxes through the Indian and Pacific basins, eventually transforming into Indian and Pacific Deep Waters (IDW and PDW, respectively). North Atlantic Deep Water forms in the North Atlantic and is both saltier and warmer than AABW. The deep waters of the three oceanic basins (NADW, PDW and IDW) meet in the Southern Ocean, mixing together to form the circumpolar deep waters (CDW) that upwell to the surface. The higher salinity of NADW causes it to contribute its entire flux to the lower component of CDW (LCDW), which has a negative buoyancy flux upon upwelling to the Southern Ocean and is therefore circulated poleward to eventually form part of the sinking AABW (Talley, 2013). This effectively produces a figure-eight meridional overturning loop of density-driven ocean circulation (depicted in Figure 1.2), which promotes homogenisation tracers between the Pacific, Indian and Atlantic basins (Marshall and Speer, 2012; Sikes et al., 2017).

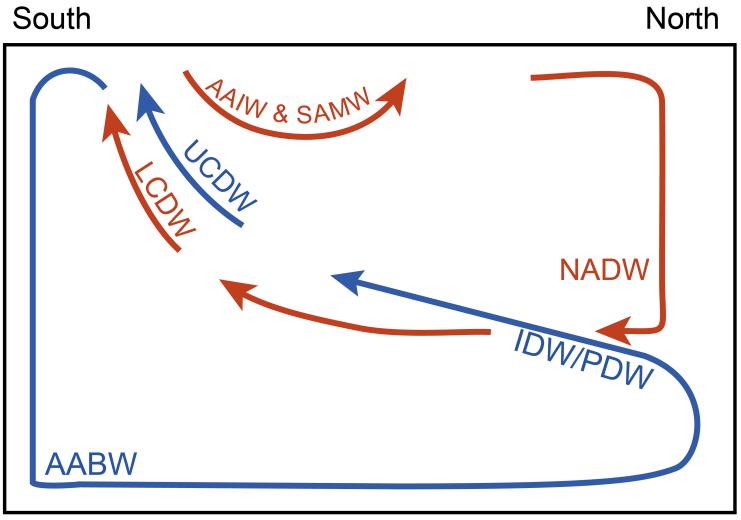

FIGURE 1.2: Schematic conceptualisation of the modern global overturning circulation. Note that upon approaching the Southern Ocean, the NADW/LCDW limb outcrops south of the IDW/PDW/UCDW limb before transforming into AABW. This creates a figure-eight global circulation loop.

During glacial periods, this meridional overturning circulation was fundamentally different. Benthic $\delta^{13}C$ records have been used to reconstruct the global deep ocean water mass structure through the last glacial maximum (e.g. Curry and Oppo, 2005). These data (Figure 1.3) suggest the boundary between northern-source waters (NADW) and southern-source waters (AABW) shoaled at the LGM and the vertical chemical gradient between the two strengthened. The mechanisms for these changes remain hotly debated. Nevertheless, a

strong common feature in many hypotheses is the role of sea ice (e.g. Adkins, 2013; Ferrari et al., 2014). For example, greater sea ice production in the Southern Ocean in the colder climate would act to create more saline bottom waters due to the increased production of dense brines. Consequently, the salinity gradient between northern- and southern- source waters in the deep ocean may have been reversed, resulting in poorer mixing between the two circulatory cells (Adkins, 2013).

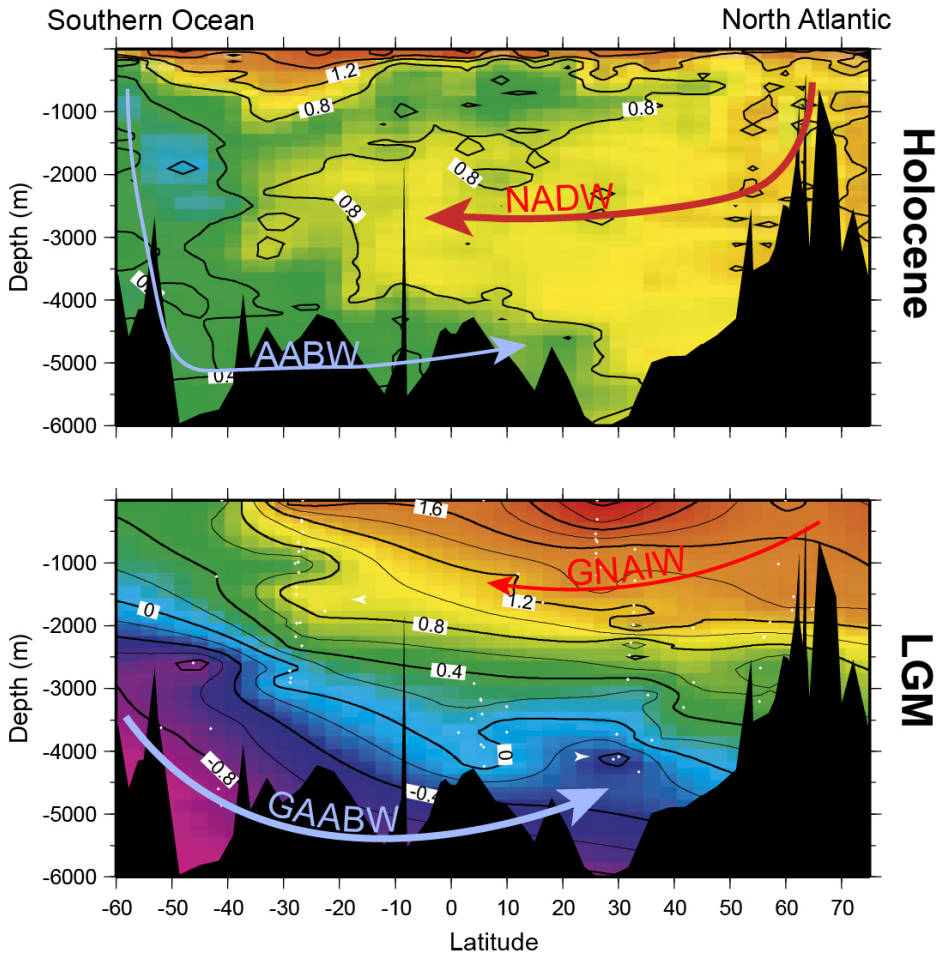

FIGURE 1.3: Reconstructions of the Atlantic water d13C from modern water samples (**top**) and benthic foraminifera sampled from last glacial maximum sediments (**bottom**) (from Curry and Oppo, 2005). A comparison of these profiles reveals a strengthening of the vertical chemical gradient between the southern-sourced bottom waters and the northern-sourced deep/intermediate waters during the last glacial maximum relative to the present as well as a shoaling of the boundary between the two water masses.

It has been hypothesised that the shoaling of the NADW limb of the global overturning (becoming glacial North Atlantic Intermediate Water, GNAIW) would have forced GNAIW into the northward limb of water mass transport as it outcrops in the glacial Southern Ocean

(Ferrari et al., 2014). Consequently, the modern figure-eight circulatory pattern would have been broken into a two more distinctly isolated circulatory loops, with the southern-source waters filling a greater volume of the three oceanic basins than today. This hypothesised glacial configuration of the water mass circulation is schematically depicted in Figure 1.4. With a greater volume of ocean filled by southern-source waters and inhibited vertical mixing throughout the oceans, biological pump of the Southern Ocean would have had a much greater role in dictating the vertical DIC gradient across much of the world's oceans and hence the atmospheric CO_2 draw down by the oceans during glacial periods.

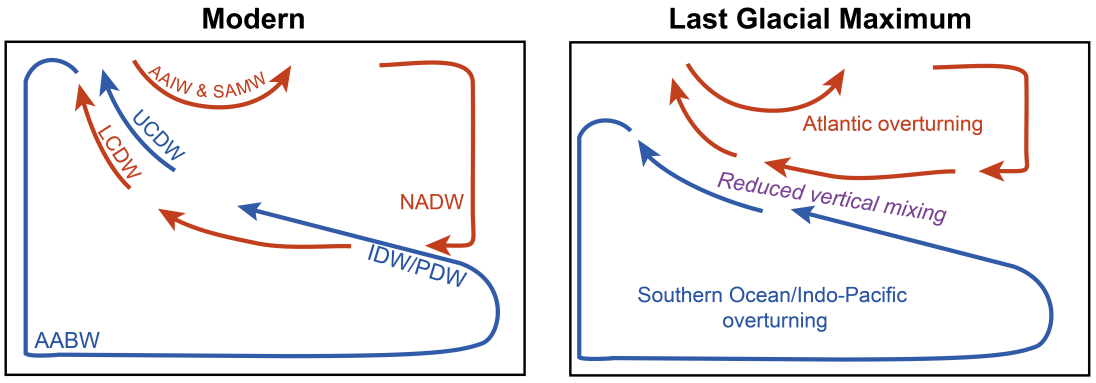

FIGURE 1.4: Schematic conceptualisations of the modern global overturning circulation (**left**) and the hypothesised overturning circulation during the last glacial maximum (**right**). Note that during the LGM, the Atlantic limb of the circulation loop approaches the Southern Ocean north of the Indo-Pacific loop, creating two more distinct overturning loops that may encourage greater heterogeneity of tracer distributions in the deep ocean.

A prevailing scientific question over the past few decades has been how the biological pump in the Southern Ocean may have changed between the last glacial period and today in order to drive the observed changes in atmospheric CO_2 (e.g. Knox and McElroy, 1984; Sarmiento and Toggweiler, 1984; Archer et al., 2000; Sigman and Boyle, 2000; Sigman et al., 2010; Hain et al., 2014). Proposed mechanisms include reduced vertical overturning in the Southern Ocean (Francois et al., 1997, Toggweiler, 1999), inhibited air-sea gas exchange due to the expanded sea ice cover (Stephens and Keeling, 2000), more efficient biological uptake of nutrients due to iron fertilisation in the Southern Ocean itself (Martin, 1990), and the redistribution of nutrients from the Southern Ocean to the remainder of the ocean to fertilise higher carbon export elsewhere (Brzezinski et al., 2002; Matsumoto et al., 2002). The importance of each of these mechanisms remains poorly constrained. Moreover, the scarcity of high-resolution records has limited our understanding of how each of these processes may have developed across rapid climate transitions such as the last deglaciation.

The aim of this work is to further elucidate the processes that controlled the evolution of the biological pump in the Southern Ocean, from its apparent strengthened state during the last glacial maximum to the weakened state during the Holocene. In doing so this thesis will address the question, what drives the variability of atmospheric CO_2 through time. Further, this project will explore new ideas for how biogeochemical and physical processes in the Southern Ocean may have controlled the global cycling of nutrients between the last glacial maximum and the Holocene, mediating the strength of global carbon export and providing further pathways to explain the glacial-interglacial variability in atmospheric CO_2.

These aims will be addressed by developing multi-proxy records reconstructing primary productivity and nutrient cycling from three sediment cores in the Indian sector of the Southern Ocean. The utilisation of three sediment cores enables the reconstruction of meridional gradients that are an important feature governing the biogeochemistry in the modern Southern Ocean. Further details on the hydrography of the Southern Ocean and the location of the core sites is given in Chapter 2. In Chapter 3 the methodology behind the construction of the age models within each sediment record is presented. In addition, the radiocarbon history of the Antarctic surface ocean is described in Chapter 3, providing a reconstruction of Southern Ocean overturning across the last deglaciation. In Chapter 4 the changes in productivity in the Southern Ocean across the last deglaciation are described by interpreting biogenic material export proxies from the three sediment records. In doing so the variable controls on carbon export from the Southern Ocean will be explored with reference to the strength of the biological pump. Chapter 5 will focus on the reconstruction of nitrogen cycling in the Southern Ocean. From this work the glacial-interglacial variability in nutrient supply to the Southern Ocean will be described. In addition, a novel hypothesis regarding the influence of deep ocean ventilation changes on global denitrification rates will be proposed, with implications for the N-cycle modulation of the global biological pump across the deglaciation. Chapter 6 will explore the global cycling of silicic acid across the deglaciation. In this work, a novel hypothesis regarding the influences of iron availability and deep ocean circulation changes on silicic acid availability across the global ocean will be proposed, with implications for the role of diatoms in controlling the strength of the biological pump. Finally, the Synthesis chapter will provide a summary of the material presented in this thesis.

References

Archer , D., Winguth , A., Lea , D., and Mahowald , N. M. What caused the glacial/interglacial atmospheric pCO2 cycles? *Reviews of Geophysics*, 38:159–189, 2000.

Arrhenius , S. On the influence of carbonic acid in the air upon the temperature of the ground. *Philosophical Magazine and Journal of Science, Series 5*, 41:237–276, 1896. doi: 10.1080/14786449608620846.

Bereiter , B., Eggins , S., Schmitt , J., Nehrbass-Ahles , C., Stocker , T., Fischer , H., Kipfstuhl , S., and Chappellaz , J. Antarcti Ice Cores Revised 800KYr CO2 data. *Geophysical Research Letters*, 2015.

Broecker , W. Abrupt climate change: causal constraints provided by the paleoclimate record. *Earth-Science Reviews*, 51(1-4):137–154, aug 2000. doi: 10.1016/S0012-8252(00)00019-2.

Broecker , W. S. and Peng , T. *Tracers in the sea*. Lamont-Doherty Geological Observatory, 1983. ISBN 0029-8182. doi: 10.1016/0016-7037(83)90075-3.

Broecker , W. Glacial to interglacial changes in ocean chemistry. *Progress in Oceanography*, 11:151–197, 1982.

Brzezinski , M., Pride , C., Franck , V. M., Sigman , D. M., Sarmiento , J. L., Matsumoto , K., Gruber , N., Rau , G. H., and Coale , K. H. A switch from Si (OH) 4 to NO3 depletion in the glacial Southern Ocean. *Geophysical Research Letters*, 29(12):3–6, 2002.

Curry , W. B. and Oppo , D. W. Glacial water mass geometry and the distribution of d13C of \$$CO2 in the western Atlantic Ocean. *Paleoceanography*, 20(1):1–12, 2005. doi: 10.1029/2004PA001021.

Eppley , R. W. and Peterson , B. Particulate organic matter flux and planktonic new production in the deep ocean. *Nature*, 282:677–680, 1979.

Francois , R., Altabet , M. A., Yu , E.-f., Sigman , D. M., Bacon , M. P., Frank , M., Bohrmann , G., Bareille , G., and Labeyrie , L. D. Contribution of Southern Ocean surface-water stratification to low atmospheric CO 2 concentrations during the last glacial period. *Nature*, 389:929–935, 1997.

Hain , M. P., Sigman , D. M., and Haug , G. H. The Biological Pump in the Past. In *Treatise on Geochemistry*, volume 8, chapter Volume 8:, pages 373–397. Elsevier, 2 edition, 2014. ISBN 9780080983004. doi: 10.1016/B978-0-08-095975-7.00614-8.

Knox , F. and McElroy , M. B. Changes in Atmospheric Influence of the Marine Biota at High Latitude. *Journal of Geophysical Research*, 89(D3):4629–4637, 1984.

Marshall , J. and Speer , K. Closure of the meridional overturning circulation through Southern Ocean upwelling. *Nature Geoscience*, 5(3):171–180, 2012. doi: 10.1038/ngeo1391.

Martin , J. H. Glacial-interglacial CO2 change: The iron hypothesis. *Paleoceanography*, 5(1):1–13, 1990.

Matsumoto , K., Sarmiento , J. L., and Brzezinski , M. A. Silicic acid leakage from the Southern Ocean: A possible explanation for glacial atmospheric pCO2. *Global Biogeochemical Cycles*, 16(3), 2002.

Monnin , E., Indermühle , a., Dällenbach , a., Flückiger , J., Stauffer , B., Stocker , T. F., Raynaud , D., and Barnola , J. M. Atmospheric CO2 concentrations over the last glacial termination. *Science (New York, N.Y.)*, 291(5501):112–4, jan 2001. doi: 10.1126/science.291.5501.112.

Petit , J., Jouzel , J., Raynaud , D., Barkov , N., Barnola , J. M., Basile , I., Chappellaz , J., Davis , M., Delaygue , G., Delmotte , M., Kotlyakov , V. M., Legrand , M., Lipenkov , V. Y., Lorius , C., Pepin , L., Ritz , C., Saltzman , E., and Stievenard , M. Climate and atmospheric history of the past 420,000 years from the Vostok ice core, Antarctica. *Nature*, 399:429–436, 1999.

Sarmiento , J. and Toggweiler , J. A new model for the role of the oceans in determining atmospheric pCO 2. *Nature*, 308:621–624, 1984.

Sigman , D. M. and Boyle , E. A. Glacial/interglacial variation in atmospheric carbon dioxide. *Nature*, 407: 859–869, 2000.

Sikes , E. L., Allen , K. A., and Lund , D. C. Enhanced δ13C and δ18O Differences Between the South Atlantic and South Pacific During the Last Glaciation: The Deep Gateway Hypothesis. *Paleoceanography*, 32(10):1000–1017, 2017. doi: $10.1002/2017\mathrm{PA}003118$.

Stephens , B. and Keeling , R. The influence of Antarctic sea ice on glacial-interglacial CO2 variations. *Nature*, 404(6774):171–4, mar 2000. doi: $10.1038/35004556$.

Talley , L. D. Closure of the global overturning circulation through the Indian, Pacific and Southern Oceans: schematics and transports. *Oceanography*, 26(1):80–97, 2013.

Toggweiler , J. Variation of atmospheric CO2 by ventilation of the ocean's deepest water. *Paleoceanography*, 14(5), 1999.

Volk , T. and Hoffert , M. Ocean carbon pumps: Analysis of relative strengths and efficiencies in ocean-driven atmospheric CO2 changes. *The Carbon Cycle and Atmospheric CO: Natrual Variations Archean to Present*, 32:99–110, 1985.

2

Environmental Setting

This chapter will provide some background to the region of study and outline some important processes occurring within the region that may be important when interpreting the data presented in further chapters.

The Southern Ocean is the body of water surrounding Antarctica and connecting the three major oceanic basins at their southern limits. A defining feature of the Southern Ocean is the confluence and formation water masses that fill much of the world's ocean volume. Spatially the Southern Ocean can be partitioned into numerous geographical zones defined by fronts, currents, water masses and sea ice (Whitworth, 1980; Orsi et al., 1995).

2.1 The Antarctic Circumpolar Current

The broad circulatory regime in the Southern Ocean is dominated by the westerly wind-driven Antarctic Circumpolar Current (ACC). The ACC is bound to the north by the subtropical

front (STF), beyond which lies the subtropical gyres of the three major oceanic basins, and to the south by what is known as the Southern Boundary, defined as the southern-most extent of upper circumpolar deep water (UCDW) (Orsi et al., 1995). Poleward of the Southern Boundary lies the Antarctic counter current, Ross Sea and Weddell Sea gyres, and the Antarctic continent.

The strength of the ACC (130 – 140 Sv, Nowling and Klinck, 1986) and the requirement for geostrophic balance forces isopycnals to slope upwards to the south. This exposes several water masses to the surface ocean separated by hydrographical boundaries known as fronts (Orsi et al., 1995; Pollard et al., 2002). This natural separation permits the division of the surface ocean into regions of different water mass exposure, which consequently display contrasting ecological and biogeochemical characteristics (Nowlin and Klinck, 1986; Pollard et al., 2002). Not only does the exposure of subsurface waters at the surface influence surface ocean biogeochemical processes, but also these process help define the chemistry of the waters that will eventually subduct back to the deep ocean. Therefore, changes in biogeochemical processes in the Southern Ocean should be considered with respect to the location of the fronts and the organisation of the subsurface water masses.

2.2 Hydrography and Zonation of the Southern Ocean

In the following text the geographical zonation and water masses of the Southern Ocean will be discussed in detail. Figure 2.1 provides a simplified view of the water mass circulation and hydrographical zonation around the Southern Ocean. Circumpolar deep water (CDW) occupies much of the Southern Ocean subsurface and is composed of an upper (UCDW) and lower component (LCDW). LCDW is formed mostly from North Atlantic Deep Water (NADW), which provides it with a distinctly higher oxygen content than UCDW, which is formed from the more aged Indian and Pacific Deep Waters (IDW and PDW) (Talley, 2013). Both UCDW and LCDW upwell south of the polar front (PF) in the Southern Ocean, which is known as the Antarctic Zone (AZ). Ekman transport forces a divergence of the ACC from the Antarctic continent, generating bifurcation of UCDW. Hence, waters travelling equatorward to the Subantarctic are derived from UCDW (Deacon, 1982; Pollard et al., 2002; Sokolov and Rintoul, 2002). The poleward limb of UCDW mixes with LCDW and eventually becomes denser due to brine rejection as sea ice forms, leading to the formation of Antarctic Bottom Water (AABW) (Orsi et al., 1999; Ohshimi et al., 2013). Being the

world's coolest and densest water mass, AABW occupies the abyssal depths of the major oceanic basins.

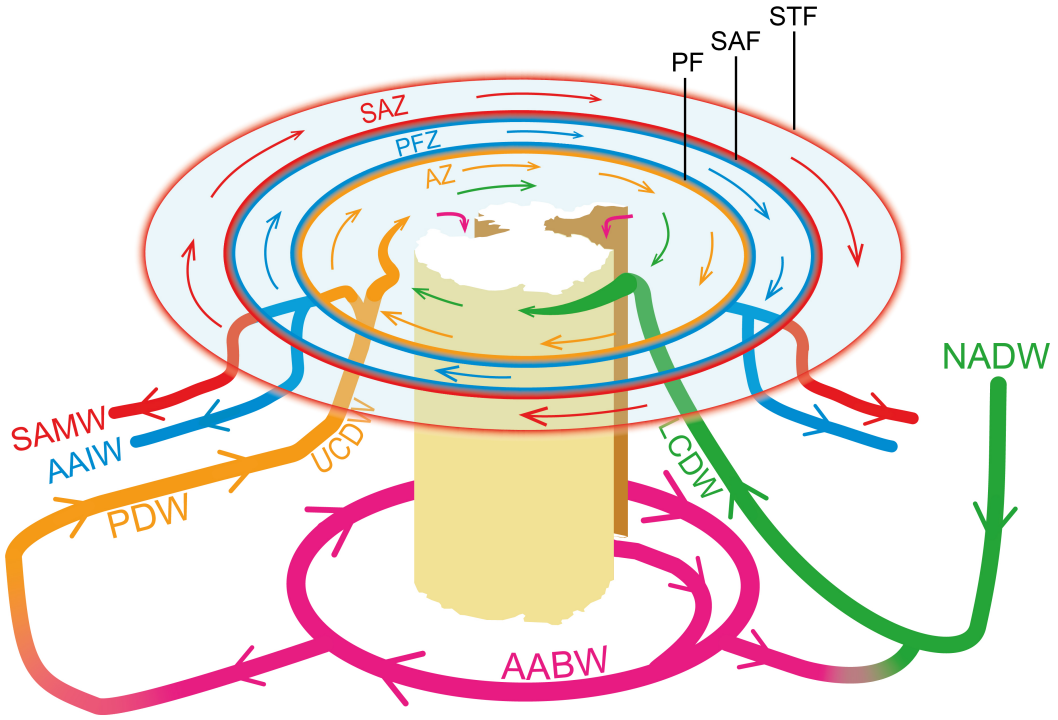

FIGURE 2.1: Schematic diagram of modern water mass circulation to and from the Southern Ocean based on Talley (2013). Note that NADW primarily contributes to LCDW, which outcrops poleward of UCDW due to its higher density. LCDW and a portion of UCDW sink to form AABW that recirculates back to the three major oceanic basins. This effectively creates a figure-eight global circulation loop.

North of the PF lies the Subantarctic. An important contrasting feature between the AZ and Subantarctic is that lateral advection and recycling of nutrients and other chemical constituents become increasingly more important in the Subantarctic further from the deep upwelling in the AZ (Sigman et al., 1999). The Subantarctic is divided into two zones, the Polar Front Zone (PFZ) to the south and the Subantarctic Zone (SAZ) to the north, separated by the Subantarctic Front (SAF). Surface waters crossing the PF are precursor to Antarctic Intermediate Water (AAIW), which is formed in the southeast Pacific and southwest Atlantic sectors (Piola and Georgi, 1982; Sloyan and Rintoul, 2001). Likewise, SAZ surface waters that subduct form the Subantarctic Mode Water (SAMW). Both AAIW and SAMW propagate northward, feeding the thermocline waters of low latitude regions. Hence, biogeochemical processes that occur within the surface waters that feed these water masses can regulate the supply of chemical constituents to distant locations, providing teleconnections between surface biogeochemical processes in the Southern Ocean

and biological productivity elsewhere (Sloyan and Rintoul, 2001; Sarmiento et al., 2004; Talley, 2013). At the northern limit of the SAZ is the subtropical front (STF), beyond which lie the subtropical gyres. At these lower latitudes the influence of the ACC and the deep upwelling within the AZ are diminished.

2.3 Defining fronts

Oceanic fronts are hydrographical boundaries separating water masses. By definition, fronts exhibit strong gradients in temperature and/or salinity and can be identified as such (Orsi et al., 1995; Belkin and Gordon, 1996). For example, the PF in the Southern Ocean is commonly identified as the 2°C isotherm at 200 m depth (Orsi et al., 1995). An alternative identification technique explored by Sokolov and Rintoul (2007a) is the identification of fronts based maxima in sea surface height. This is possible because strong density gradients are naturally associated with geostrophic currents, producing strong jets that flow along the boundary (Thompson, 2008; Graham et al., 2012; Chapman, 2014). Through this definition fronts can be effectively identified using remote sensing satellite data, which is more accessible than subsurface temperature and salinity data.

The distinction between these two definitions of fronts is important. As discussed by Graham (2014), the conceptual view of fronts defined as water mass boundaries implies that they are inherently longitudinally continuous in the Southern Ocean, and in the paleo record they can be theoretically identified using temperature-based reconstructions (e.g. Sikes et al., 2009). On the other hand, the fronts-as-currents definition does not require longitudinal continuity. This is because it is possible to have little or no gradient in density (and therefore sea surface height) between water masses in a scenario whereby temperature and salinity gradients are offsetting. In addition, the influence of sea floor topography is very important for the fronts-as-currents framework, for example there are differences in cross-front tracer transport between areas of high mean zonal advective transport, such as the open ocean, versus areas of high eddy kinetic energy, such as on the lee side of islands or submerged bathymetric features (Thompson and Sallee, 2012). Also, sea floor topography can force frontal jets to split into branches or several fronts to merge into 'superfronts' (Sokolov and Rintoul, 2007a), which may influence biogeochemical processes but not fully represented or detected in sea surface temperature records.

From the perspective of this study the fronts-as-currents definition is important as it may provide a more accurate understanding of tracer transport and the biophysical effects of fronts on primary productivity. However, at present there is no way to reconstruct past geostrophic flow on the scale that is relevant for front identification. Although there appears to often be a strong correspondence of the water mass boundary and jet definitions of the Southern Ocean fronts (Sokolov and Rintoul, 2007a; Graham and de Boer, 2013), it is important to highlight that paleo-front reconstructions based on temperature proxies (e.g. Gersonde et al., 2005) imply a continuous and uniform circumpolar front system, however in reality the cross-front or vertical mixing associated with fronts will likely vary between different regions and through time. Consequently, a full description of the modern frontal regime around the core sites will be provided below.

2.4 Core Locations

Three piston sediment cores were collected from the Indian Sector of the Southern Ocean. The cores were collected between 1984 and 1988 and have since been archived in cold storage at Gif-Sur-Yvette, Paris.

- MD88-772: -50.0225°N, 100.1°E, 3310 m water depth
- MD88-773: -52.9005°N, 109.869667°E, 2460 m water depth
- MD84-551: -55.01°N, 73.17°E, 2230 m water depth

The above three cores were chosen from the Indian sector of the Southern Ocean to provide a meridional transect from the Antarctic Zone (AZ) south of the Polar Front, to the Polar Front Zone (PFZ) north of the Polar Front. The cores were chosen based on location but also on estimations of sedimentation rate, which are required to be high enough to sufficiently resolve the last deglaciation.

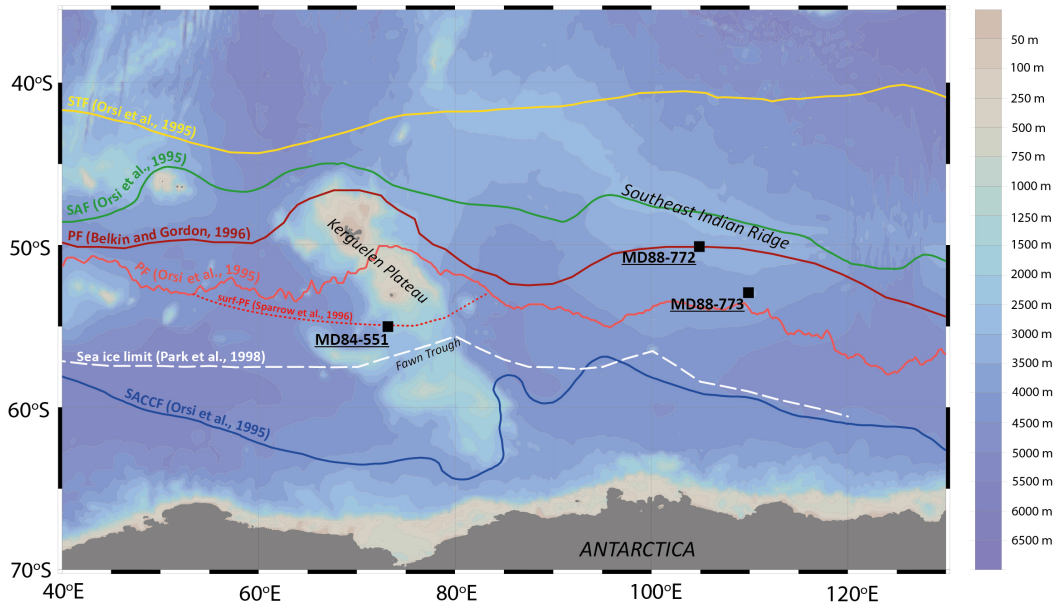

FIGURE 2.2: Map of the core locations used in this study. Also included are the approximate average locations of the major fronts in the Southern Ocean as well as an estimate of the northern extent of pack-ice defined by low surface salinity (< 33.8 psu) (Park et al., 1998). The PF has multiple branches here due to the varying definitions of the front (see text for details). Bathymetry is from the GEBCO Digital Atlas published by the British Oceanographic Data Centre on behalf of IOC and IHO, 2003. Produced using ODV software (Schlitzer, 2002).

2.5 Local hydrography

MD84-551 is the southern-most core, located south of Heard Island on the western slope of the Kerguelen Plateau. In this region of the Southern Ocean the Kerguelen Plateau presents a barrier to the flow of the ACC and forces it to bifurcate. 60% of the ACC transport within this region is directed across the northern edge of the plateau (Park et al., 2014), forcing the PF to one of its most northerly positions in the Southern Ocean. A portion of the ACC that does not flow across the northern edge is channelled through a gap in the plateau known as the Fawn Trough (Roquet et al., 2009). The result is a splitting of the PF with a main branch to the north and a secondary branch to the south. The main branch appears to express the characteristics of a deep water mass boundary, with subsurface salinity and temperature gradients separating the Subantarctic waters to the north from the cool AZ waters to the south. Some studies have estimated the main branch of the polar front to be positioned north of Kerguelen Island (Belkin and Gordon, 1996; Kostianoy et al., 2003), whilst others have identified it meandering just south of Kerguelen Island before abruptly

deflecting northwards (Orsi et al., 1995; Park et al., 2014) (see Figure 2.2). The southern branch is a surface expression of the polar front current, identified by surface temperature gradients and has an associated jet with a velocity of about half of that of the main branch (Sparrow et al., 1996). Argo float data from the region suggest that deep water flow follows the southern branch trajectory, before being focused into the Fawn Trough (Roquet et al., 2009). MD84-551 lies close to the gateway to the Fawn Trough, south of the main flow of the ACC but within close proximity to the southern branch of the PF. Hence, biogenic constituents accumulating within MD84-551 at present likely reflect surface ocean conditions within AZ waters (south of the main/northern PF branch) west of the Kerguelen Plateau.

Due to the topographic influences of the Crozet and Kerguelen plateaus, the polar front branches throughout much of the region have very weak baroclinic shear (Park et al., 1991; Park et al., 1993). This manifests as muted cross-frontal gradients of chemical and physical properties. As a result, the position of the PF branches across the last deglaciation will be elusive but reconstructions of meridional tracer transport will be less influenced by changes in the polar front position.

MD88-773 and MD88-772 were collected from the eastern Indian sector on the Southeast Indian Ridge. Fewer studies on the frontal structure have been performed in the region between the Kerguelen Plateau and Australia, so the hydrography is less well known. However, broad estimations of the frontal positions indicate that both the PF and SAF are deflected to the southeast following the axis of the Southeast Indian Ridge (Belkin and Gordon, 1996; Kostianoy et al., 2004). At 140°E, east of the core sites, the frontal structure has been well-described by Sokolov and Rintoul (2002). Here the authors note that the PF remains as two branches as in the Kerguelen region, with the northern branch representing the water mass boundary and the southern branch being a secondary jet with a sea surface temperature gradient. Based on the identifying properties provided by Sokolov and Rintoul (2002), temperature surveys of the region around MD88-773 suggest that this record is situated close to, but just south of the northern PF branch (Figure 2.3). Hence, the core will be described hereon as an AZ record, but lies within the transitionary zone between the AZ and PFZ. The location of MD88-772 is less ambiguous and the record is situated within the centre of the PFZ, between the PF and SAF.

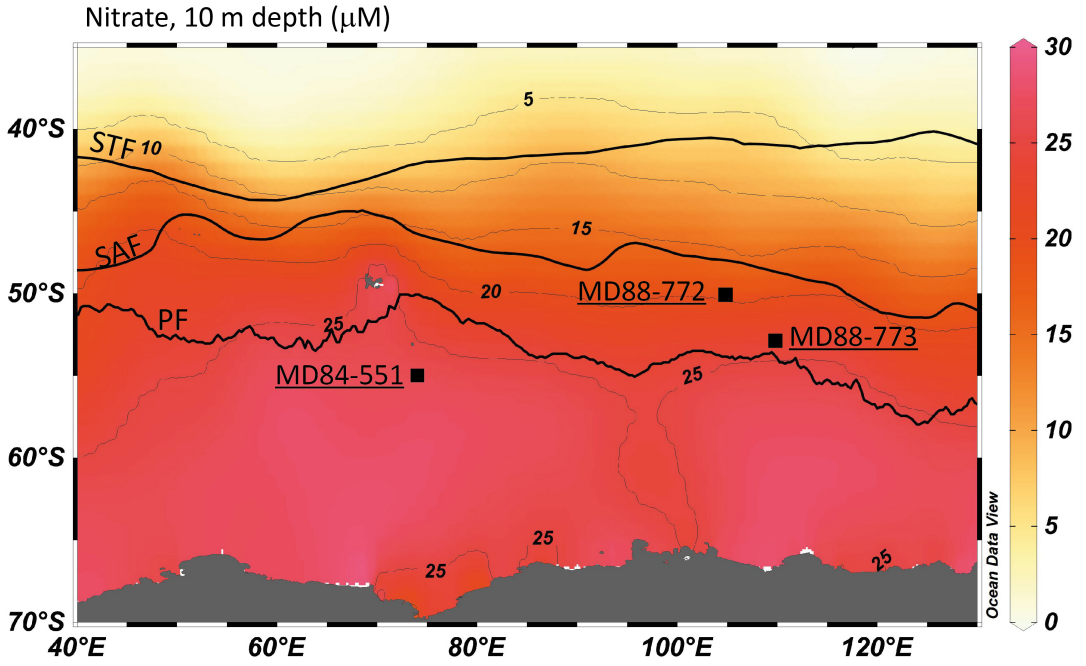

FIGURE 2.3: Gridded surface water nitrate concentrations across the study area. Nitrate data from WOA13 (Garcia et al., 2013). Front locations based on Orsi et al (1995). Produced using ODV software (Schlitzer, 2002).

During the deglaciation the fronts may have shifted position due to a number of factors such as a shift in the westerly winds (Kohfeld et al., 2013), although, as demonstrated above their position is also dictated by topography. The interest of this study is to reconstruct nutrient uptake and supply dynamics across the deglaciation. Because mixing between fronts and along isopycnals is typically greater than across fronts each of the oceanic zones (AZ, PFZ, SAZ) display characteristic surface nutrient inventories. The importance of using the meridional transect of cores in this study is it allows us to discern whether downcore signals are merely local effects of switching between zones or broader changes in nutrient dynamics and productivity.

2.6 Sea ice

Sea ice presence and formation play important roles in both the biogeochemical and physical oceanographic processes that occur in the Southern Ocean. From a physical oceanographic perspective, sea ice presence modulates the wind-stress field, which determines the strength of wind-driven overturning (Liu et al., 2015; Sime et al., 2016). In addition, sea ice formation and melting alter the salinity of surface waters, creating strong haloclines and dense brines.

In the modern Southern Ocean, the warm CDW melts the sea ice causing it to freshen and cool before brine formation in the Ross Sea and Weddell Sea transform it into sinking AABW.

From a biogeochemical perspective, the presence of sea ice not only directly reduces light availability for phytoplankton, but also often produces a halocline in summer during sea ice melt (Wilson et al., 1986). This halocline stabilises the surface water column, inhibiting vertical mixing. The reduced vertical mixing prevents phytoplankton growing in the surface layer from being mixed down below the euphotic layer, encouraging growth. Further, the resupply of nutrients from below becomes inhibited causing nutrient stocks to become depleted more easily. Under these conditions phytoplankton, such as diatoms will bloom, rapidly consuming the available nutrients in the surface layer during summer before collapsing in autumn.

At present, the winter sea ice limit lies south of the three records (Figure 2.2), therefore there is no associated light limitation on phytoplankton growth at these latitudes. Past sea ice extent can be reconstructed using taxonomic indicators (Crosta et al., 1998). These reconstructions suggest the winter sea ice in the Indian sector extended to the modern polar front position (Crosta et al., 1998; Gersonde et al., 2003). Consequently, diatom-based reconstructions of sea ice presence will be used to evaluate the influence of sea ice presence at MD88-773 and MD84-551 across the last deglaciation. Diatom assemblage data for these two records has been provided by Crosta, X.

2.7 Nutrients

Nutrient supply to the Southern Ocean is dominated by the upwelling of CDW in the AZ (Pollard et al., 2002). Euphotic zone nutrient concentrations decrease northwards from the AZ towards the STF, as is expected from biological utilisation of the nutrients along the path of Ekman transport and the influence of deep upwelling decreases. However, annual mean surface nitrate and phosphate concentrations ([NO_3] and [PO4], respectively) remain relatively high throughout the Southern Ocean (Garcia et al., 2013) and mean chlorophyll concentrations remain relatively low (Moore and Abbott, 2000). This is a result of productivity being stifled by a lack of bioavailable iron in the surface ocean (Martin et al.,

1990; de Baar et al., 1990; de Baar et al., 1995; Moore et al., 2001). Hence the Southern Ocean has been termed the largest high-nutrient, low-chlorophyll zone in the world.

Summer phytoplankton growth in the AZ is supported by nutrients derived from vertical mixing between the surface ocean and upwelled CDW during the previous winter. During winter, CDW supplies nutrient-rich waters ($[NO_3^-] = 30 - 34$ µM, $[Si(OH)_4] = 70 - 120$ µM) to the surface ocean via wind-driven upwelling and buoyancy-driven mixing. The strong winter mixing produces a deep, cool mixed layer known as winter water (WW) (Park et al., 1998). During summer, freshening and warming of the surface ocean produces a surface layer that caps the WW and constitutes the layer from which nutrients are utilised by phytoplankton.

Upwelled nitrate is relatively under-utilised across the AZ, with surface $[NO_3^-]$ maintained above 20 µM throughout the year (Figure 2.3, Sigman et al., 1999; Pollard et al., 2006). Conversely, silicic acid depletion is more exhaustive (Figure 2.4, Fripiat et al., 2011).

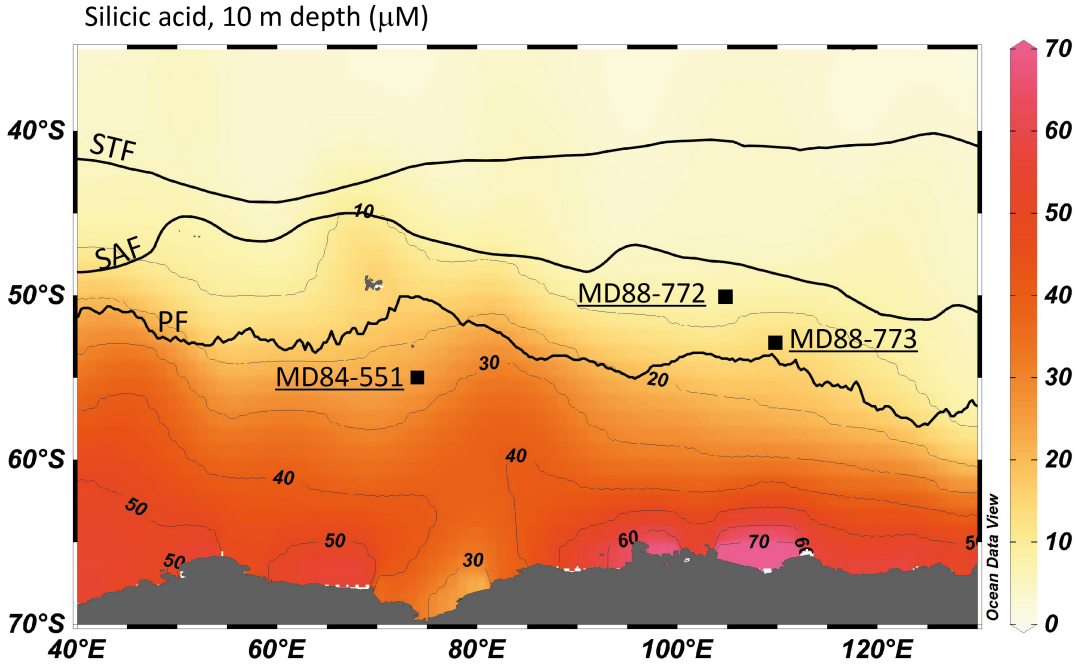

FIGURE 2.4: Gridded surface water silicic acid concentrations across the study area. Silicic acid data from WOA13 (Garcia et al., 2013). Front locations based on Orsi et al (1995). Produced using ODV software (Schlitzer, 2002).

There is only a weak northward gradient of $[NO_3^-]$ in the surface waters between MD84-551 and MD88-772 (Figure 2.3), demonstrating the low uptake and efficient recycling of nitrogen in these waters. The surface nitrate gradient steepens at the SAF, which is situated at

approximately 48°S at 105°E (Orsi et al., 1995). Silicic acid, on the other hand, is almost exhausted in the summer mixed layer around MD88-772 ([Si(OH)4] $<$ 5 µM) with little noticeable gradient northwards of the core position (Figure 2.4), demonstrating that silicic acid use throughout much of Subantarctic is dependent on silica recycling in the surface ocean (Fripiat et al., 2011).

2.8 Iron biogeochemistry in the Southern Ocean

Iron is used as an electron transporter and for the synthesis of several enzymes essential in metabolic processes, including nitrate reductase in the reduction of nitrate to ammonium via nitrite (Timmermans et al., 1994) and coproporhyrinogen oxidase used in the synthesis of chlorophyll (Spiller et al., 1982; Chereskin and Castelfranco, 1982). As such, iron-deficiency within phytoplankton cells can lead to insufficient utilisation of nitrate and chlorosis, hampering growth and leaving ambient nutrients unutilised.

The basin-scale distribution of bioavailable dissolved iron is decoupled from that of the macronutrients. This is largely a result of particle scavenging of iron throughout the water column which itself is modulated by the concentration of iron-complexing ligands (Boyd and Ellwood, 2010; Tagliabeau et al., 2017). The result is that iron is stoichiometrically depleted relative to the macronutrients in upwelled CDW due to scavenging within the ocean interior (Johnson et al., 1997; Moore and Braucher, 2008).

Much of the productivity in the Southern Ocean is supported by biologically-mediated recycling in the euphotic zone during summer (Boyd and Ellwood, 2010) and deep entrainment of remineralised iron into the mixed layer during winter mixing (Tagliabue et al., 2014). However, the winter regeneration of iron stocks in the surface layer is less efficient than other nutrients because the particle scavenging and slow remineralisation rates of iron-bearing particles deepen the ferricline below that of the mixed layer depth and nitricline. As a result, winter mixing supplies lower DFe:NO_3 ratios than what required for phytoplankton uptake (Bowie et al., 2009).

The iron limitation in the Southern Ocean means that primary productivity in the region is rather sensitive to exogenous iron inputs (Boyd et al., 2012). These inputs tend to be episodic, and phytoplankton appear to have adapted to this by exhibiting plastic stoichiometric iron requirements, assimilating luxury quantities or iron when availability is high (Twining

and Baines, 2013). This further decouples the biogeochemical cycling of iron from the macronutrients (Bowie et al., 2009).

Supplementary sources of new iron to the Southern Ocean include aeolian deposition (Johnson et al., 1997; Mahowald et al., 2005), erosion or resuspension of sediments from bathymetric features and continental shelves (Johnson et al., 1999; Blain et all., 2007; Moore and Braucher., 2008), hydrothermal vents (Tagliabue et al., 2010), and the melting of ice-bergs (Smith et al., 2007; Raiswell, 2011) and sea ice (Geibert et al., 2010; Wang et al., 2014).

Supply of iron through resuspension of sediments appears to be the biggest contributor of exogenous iron to the modern Southern Ocean water column (Tagliabue et al., 2010). However, it is unclear whether it is the most important with respect to supporting primary production as the rapid scavenging and luxurious biological uptake of this iron mean that productivity is only enhanced close to islands and continents (Boyd et al., 2012; Wadley et al., 2014. Graham et al., 2015).

Observations of phytoplankton blooms near the fronts in the Southern Ocean have led to the interpretation that the fronts provide a mechanism for increasing productivity (Laubscher et al., 1993). However, further investigations have revealed that as a whole the PF is only slightly more productive than more poleward regions and less productive (annually) than the Subantarctic (Moore and Abbott, 2000). Likewise, organic carbon and biogenic silica export does not appear to be enhanced by the presence of fronts universally in the Southern Ocean (Nelson et al., 2002). In the open ocean, productivity enhancements by fronts are limited and have been attributed to increased subsurface nutrient supply through meander-induced upwelling and increased eddy activity (Moore et al., 1999; Moore and Abbott, 2000).

Large phytoplankton blooms are associated with fronts that interact with topography (Moore et al., 2002; Sokolov and Rintoul, 2007b, Graham et al., 2015). At very shallow bathymetric features and islands, frontal-bathymetric interactions can supply iron to surface waters (Blain et al., 2008; Bowie et al., 2015; Queroue et al., 2015; Van Der Merwe et al., 2015) creating massive local blooms (Mongin et al., 2008; Trull et al., 2015). New iron from sediments can then be supplied to the open ocean via the fronts and support enhanced productivity over wide areas. However, productivity enhancements associated with iron supply from fronts have been found to be limited to fronts that pass close to continental shelves (Graham et al., 2015).

Aeolian iron inputs are lower overall than sedimentary sources (Rea, 1994; Kohfeld and Harrison, 2001), but they are more dispersed and supplied directly to the surface ocean and so it has been argued that productivity in the Southern Ocean is most sensitive to dust supply (Boyd et al., 2012; Wadley et al., 2014). South American and Australian sources account for the bulk of aeolian dust supply to the Southern Ocean (Jickells, 2005; Mahowald et al., 2005; Li et al., 2008). The westerlies dominate the transport vector for atmospheric dust and so dust deposition is greatest to the east of dust sources. Hence, the western Atlantic and Pacific sectors receive the most dust in the Southern Ocean (from South America and Australia, respectively), whilst the eastern regions of the Indian and Pacific sectors receive the least (Li et al., 2008).

The iron limitation on productivity in the Southern Ocean means that appreciable depletion in surface $[NO_3]$ and $[PO_4]$ inventory does not occur until northward of the PF, with much of the depletion occurring in the SAZ. In general, N/P depletion ratios across the Southern Ocean are similar to the Redfield ratio (Lourey and Trull, 2001). However, some regions dominated by a single phytoplankton group (namely either diatoms or *Phaeocystis antarctica*) display N/P depletion ratios that deviated from Redfield (Arrigo et al., 1999; Wang et al., 2003). Nevertheless, neither N nor P availability limits phytoplankton growth southward of the SAF and oligotrophic conditions are only met northward of the STF (Sedwick et al., 2002).

2.9 Past iron supply

Spurred on by the 'Iron Hypothesis' (Martin, 1990) that glacial-interglacial CO_2 may be in part controlled by the availability of iron in iron-deficient regions such as the Southern Ocean, many have sought to reconstruct iron fluxes to the surface of the Southern Ocean.

Dust deposition to the Southern Ocean has been hypothesised to have been greater during the LGM than today primarily based on evidence from dust accumulation in Antarctic ice cores (Petit et al., 1981; Delmonte et al., 2002; Wolff et al., 2006; Lambert et al., 2012), with an increase in dust deposition by a factor of approximately 20 during the LGM relative to the Holocene. The glacial increase in dust flux observed in records from Antarctica have been attributed to an encumbered hydrological cycle (Mahowald et al., 1999 and references

therein), reduction in vegetation cover (Petit et al., 1981; Marticorena and Bergametti, 1996) and an increase in wind strength or gustiness (McGee et al., 2007; 2010).

The accumulation of lithogenic material in Southern Ocean sediments often correlates well to these ice core records. Some studies have used this correlation to infer a common source, Patagonia (Basile et al., 1997; Sugden et al., 2009) and thus interpreting changes in lithogenic flux to indicate changes in iron fertilization (Kumar et al., 1995; Anderson et al., 2014). Whilst others have used the variability in lithogenic flux to tune age models of marine records to ice cores (Pugh et al., 2009; Anderson et al., 2014), assuming the lithogenic material is either derived from the same source as the ice core dust or that non-aeolian material is controlled by the same process that distributes dust material.

The accumulation rates of lithogenic material in Southern Ocean marine sediments are commonly >20 times greater than that expected during the LGM if derived from aeolian dust (Bareille et al., 1994; Diekmann, 2007; Pugh et al., 2009). Hence, dust reconstructions from marine sediment cores must distinguish between aeolian material from the lithogenic material supplied by other means. Much of the lithogenic material accumulating in Southern Ocean sediments has originated from erosion of bathymetry and may have not contributed to the iron supply to the surface ocean. Another common source of lithogenic material, particularly in Antarctic sediments is glacial scouring and ice-rafted debris (Diekmann, 2007).

2.10 Silica biogeochemistry of the Southern Ocean

A secondary effect of the iron limitation in the modern Southern Ocean is the alteration of the silicic acid uptake efficiency of diatom communities. It has been found that iron-stressed diatoms cannot utilise silicic acid efficiently, forcing the uptake ratio of silicic acid to nitrate to rise by up to four-fold (Hutchins and Bruland, 1998; Takeda, 1998). This alteration in the stoichiometry of nutrient uptake is caused by a reduction in the organic matter content within diatoms and a hindrance to their cell division capabilities (Marchetti and Varela, 2010). Since diatoms are a major contributor to autotrophic production across the Southern Ocean (Nelson et al., 1995); excessive silicic acid utilisation has led to the observed steep meridional [$Si(OH)_4$] gradient and resulted in silicic acid – iron co-limitation in the Subantarctic (Sedwick et al., 2002). The extent of excessive Si utilisation can be

illustrated with a map of Si* ($[Si(OH)_4] - [NO_3]$) (Figure 2.5), which shows that much of the modern Subantarctic is silica-deficient.

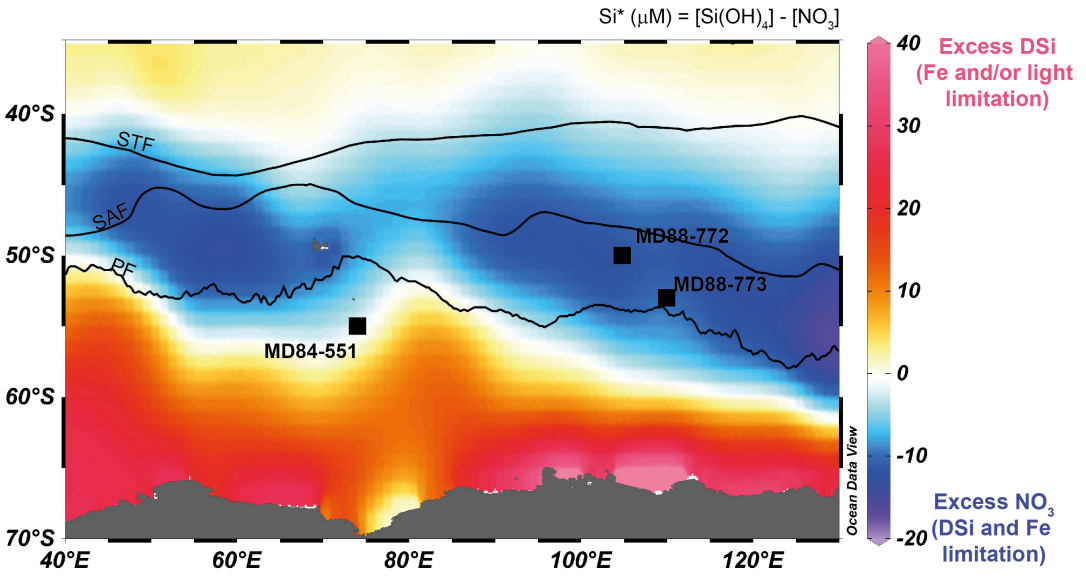

FIGURE 2.5: Gridded surface water Si* across the study area. Silicic acid and nitrate data from WOA13 (Garcia et al., 2013). Front locations based on Orsi et al (1995). Produced using ODV software (Schlitzer, 2002).

The exhaustive silicic acid uptake means that the Southern Ocean is estimated to be responsible for 57 % - 70 % of the global opal export (compared to having only 26% of the total ocean surface area) (Sarmiento et al., 2007; Holzer et al., 2014). Much of this export is confined to a band of diatom productivity close to the PF, bounded by light-limitation to the south and silicon limitation to the north. This has produced a ring of opal-rich sediments circumventing the AZ, known as the opal belt (Burckle and Cirilli, 1987; Geibert et al., 2005). Chapter 4 will explore how this opal belt may have changed between the last glacial maximum and today and what the driving forces were behind those changes.

The abiotic temperature-dependent process that controls opal dissolution is generally slower than the biologically-mediated processes that control nitrate and phosphate remineralisation (Erez et al., 1982; Gnanadesikan, 1999). As a result, silicic acid regeneration is decoupled from that of other nutrients and occurs deeper in the water column. Because the transport pathway of deeper water in the Southern Ocean is generally towards the surface, silicic acid is trapped in a loop, whereas other nutrients escape the Southern Ocean (e.g. via AAIW and SAMW). This trapping is so efficient that it has been estimated that any given silicic acid molecule last utilized in the Southern Ocean has only around 5 % chance of next being

utilized elsewhere, compared to phosphate which has a $\sim$ 44 % chance (Holzer et al., 2014). Chapter 6 will explore the trapping of silicic acid further by reconstructing the supply and utilization of silicic acid in the Southern Ocean across the last deglaciation.

References

Anderson , R., Barker , S., Fleisher , M. Q., Gesonde , R., Goldstein , S. L., Kuhn , G., Pahnke , K., and Sachs , J. P. Biological response to millennial variability of dust and nutrient supply in the Subantarctic South Atlantic Ocean. *Philosophical Transactions of the Royal Society A: Mathematical, Physical and Engineering Sciences*, 372, 2014.

Arrigo , K. R., Robinson , D. H., Worthen , D. L., Dunbar , R. B., DiTullio , G., VanWoert , M. L., and Lizotte , M. P. Phytoplankton Community Structure and the Drawdown of Nutrients and CO2 in the Southern Ocean. *Science*, 283(5400):365–367, jan 1999. doi: 10.1126/science.283.5400.365.

Bareille , G., Grousset , F. E., Labracherie , M., Labeyrie , L. D., and Petit , J. Origin of detrital fluxes in the southeast Indian Ocean during the last climatic cycles. *Paleoceanography*, 9(6):799–819, 1994.

Basile , I., Grousset , F. E., Revel , M., Petit , J. R., Biscaye , P. E., and Barkov , N. I. Patagonian origin of glacial dust deposited in East Antarctica (Vostok and Dome C) during glacial stages 2, 4 and 6. *Earth and Planetary Science Letters*, 146(3-4):573–589, 1997. doi: 10.1016/S0012-821X(96)00255-5.

Belkin , I. M. and Gordon , A. L. Southern Ocean fronts from the Greenwich meridian to Tasmania. *Journal of Geophysical Research*, 101(C2):3675, 1996. doi: 10.1029/95JC02750.

Blain , S., Quéguiner , B., Armand , L., Belviso , S., Bombled , B., Bopp , L., Bowie , A., Brunet , C., Brussaard , C., Carlotti , F., Christaki , U., Corbière , A., Durand , I., Ebersbach , F., Fuda , J. L., Garcia , N., Gerringa , L., Griffiths , B., Guigue , C., Guillerm , C., Jacquet , S., Jeandel , C., Laan , P., Lefèvre , D., Lo Monaco , C., Malits , A., Mosseri , J., Obernosterer , I., Park , Y. H., Picheral , M., Pondaven , P., Remenyi , T., Sandroni , V., Sarthou , G., Savoye , N., Scouarnec , L., Souhaut , M., Thuiller , D., Timmermans , K., Trull , T., Uitz , J., Van Beek , P., Veldhuis , M., Vincent , D., Viollier , E., Vong , L., and Wagener , T. Effect of natural iron fertilization on carbon sequestration in the Southern Ocean. *Nature*, 446(7139):1070–1074, 2007. doi: 10.1038/nature05700.

Bowie , A. R., Van Der Merwe , P., Quéroué , F., Trull , T., Fourquez , M., Planchon , F., Sarthou , G., Chever , F., Townsend , A. T., Obernosterer , I., Sallée , J. B., and Blain , S. Iron budgets for three distinct biogeochemical sites around the Kerguelen Archipelago (Southern Ocean) during the natural fertilisation study, KEOPS-2. *Biogeosciences*, 12(14):4421–4445, 2015. doi: 10.5194/bg-12-4421-2015.

Bowie , A. R., Lannuzel , D., Remenyi , T. A., Wagener , T., Lam , P. J., Boyd , P. W., Guieu , C., Townsend , A. T., and Trull , T. W. Biogeochemical iron budgets of the Southern Ocean south of Australia: Decoupling of iron and nutrient cycles in the subantarctic zone by the summertime supply. *Global Biogeochemical Cycles*, 23(4):1–14, 2009. doi: 10.1029/2009GB003500.

Boyd , P. W., Arrigo , K. R., Strzepek , R., and van Dijken , G. L. Mapping phytoplankton iron utilization: Insights into Southern Ocean supply mechanisms. *Journal of Geophysical Research*, 117(C6):C06009, jun 2012. doi: 10.1029/2011JC007726.

Boyd , P. W. and Ellwood , M. J. The biogeochemical cycle of iron in the ocean. *Nature Geoscience*, 3(10): 675–682, sep 2010. doi: 10.1038/ngeo964.

Burckle , L. H. and Cirilli , J. Origin of diatom ooze belt in the Southern Ocean : for late Quaternary Implications paleoceanography. *Micropaleontology*, 33(1):82–86, 1987.

Chapman , C. Southern Ocean jets and how to find them: Improving and comparing common jet detection methods. *Journal of Geophysical Research: Oceans*, pages 4318–4339, 2014. doi: 10.1002/2014JC009810. Received.

Chereskin , B. M. and Castelfranco , P. A. Effects of Iron and Oxygen on Chlorophyll Biosynthesis 2: Observations on the biosynthetic pathway in isolated etiochloroplasts. *Plant physiology*, 68:112–116, 1982.

Crosta , X., Pichon , J., and Burckle , L. H. Application of modern analog technique to marine Antarctic diatoms: Reconstruction of maximum sea-ice extent at the Last Glacial Maximum. *Paleoceanography*, 13 (3):284–297, 1998.

de Baar , H. J., Buma , A. G. J., Nolting , R. F., Cadee , G. C., Jacques , G., and Treguer , P. On iron limitation of the Southern Ocean: experimental observations in the Weddell and Scotia Seas. *Marine Ecology Progress Series*, 65:105–122, 1990.

de Baar , H. J., de Jong , J. T., Bakker , D. C. E., Loscher , B. M., Veth , C., Bathmann , U., and Smetacek , V. Importance of iron for plankton blooms and carbon dioxide drawdown in the Southern Ocean. *Nature*, 373, 1995.

Deacon , G. Physical and biological zonation in the Southern Ocean. *Deep Sea Research Part A. Oceanographic Research Papers*, 29(1978):1–15, 1982.

Delmonte , B., Petit , J., and Maggi , V. Glacial to Holocene implications of the new 27000-year dust record from the EPICA Dome C (East Antarctica) ice core. *Climate Dynamics*, 18(8):647–660, 2002. doi: 10.1007/s00382-001-0193-9.

Diekmann , B. Sedimentary patterns in the late Quaternary Southern Ocean. *Deep-Sea Research Part II: Topical Studies in Oceanography*, 54(21-22):2350–2366, 2007. doi: 10.1016/j.dsr2.2007.07.025.

Erez , J., Takahashi , K., and Honjo , S. In-situ dissolution experiments of Radiolaria in the central North Pacific. *Earth Planetary Science Letters*, 59:245–254, 1982.

Fripiat , F., Cavagna , a. J., Dehairs , F., Speich , S., Andr?? , L., and Cardinal , D. Silicon pool dynamics and biogenic silica export in the Southern Ocean inferred from Si-isotopes. *Ocean Science*, 7(5):533–547, 2011. doi: 10.5194/osd-8-639-2011.

Garcia , H. E., Locarnini , R. A., Boyer , T. P., Antonov , J. I., Baranova , O. K., Zweng , M., Reagan , J. R., and Johnson , D. R. World Ocean Atlas 2013, Volume 4: Dissolved Inorganic Nutrients (phosphate, nitrate, silicate). In Levitus , S. and Mishonov , A. V., editors, *NOAA Atlas NESDIS 76*. 2013.

Geibert , W., Assmy , P., Bakker , D. C. E., Hanfland , C., Hoppema , M., Pichevin , L. E., Schröder , M., Schwarz , J. N., Stimac , I., Usbeck , R., and Webb , a. High productivity in an ice melting hot spot at the eastern boundary of the Weddell Gyre. *Global Biogeochemical Cycles*, 24(3):n/a–n/a, sep 2010. doi: 10.1029/2009GB003657.

Geibert , W., Rutgers van der Loeff , M. M., Usbeck , R., Gersonde , R., Kuhn , G., and Seeberg-Elverfeldt , J. Quantifying the opal belt in the Atlantic and southeast Pacific sector of the Southern Ocean by means of 230 Th normalization. *Global Biogeochemical Cycles*, 19(4):n/a–n/a, dec 2005. doi:

10.1029/2005GB002465.

Gersonde , R., Abelmann , A., Brathauer , U., Becquey , S., Bianchi , C., Cortese , G., Grobe , H., Kuhn , G., Niebler , H. S., Segl , M., Sieger , R., Zielinski , U., and Futterer , D. K. Last glacial sea surface temperatures and sea-ice extent in the Southern Ocean (Atlantic-Indian sector): A multiproxy approach. *Paleoceanography*, 18(3):1061, 2003. doi: 10.1029/2002PA000809.

Gersonde , R., Crosta , X., Abelmann , A., and Armand , L. Sea-surface temperature and sea ice distribution of the Southern Ocean at the EPILOG Last Glacial Maximum—a circum-Antarctic view based on siliceous microfossil records. *Quaternary Science Reviews*, 24(7-9):869–896, apr 2005. doi: 10.1016/j.quascirev.2004.07.015.

Gnanadesikan , A. A global model of silicon cycling : Sensitivity to eddy parameterization and dissolution. *Global Biogeochemical Cycles*, 13(1):199–220, 1999.

Graham , R. *The role of Southern Ocean fronts in the global climate system*. PhD thesis, Stockholms Universitet, 2014.

Graham , R. M. and De Boer , A. M. The Dynamical Subtropical Front. *Journal of Geophysical Research: Oceans*, 118(10):5676–5685, oct 2013. doi: 10.1002/jgrc.20408.

Graham , R. M., de Boer , A. M., Heywood , K. J., Chapman , M. R., and Stevens , D. P. Southern Ocean fronts: Controlled by wind or topography? *Journal of Geophysical Research*, 117(C8):C08018, aug 2012. doi: 10.1029/2012JC007887.

Graham , R. M., Boer , A. M. D., Sebille , E. V., Kohfeld , K. E., and Schlosser , C. Inferring source regions and supply mechanisms of iron in the Southern Ocean from satellite chlorophyll data. *Deep-Sea Research Part I*, 104:9–25, 2015. doi: 10.1016/j.dsr.2015.05.007.

Holzer , M., Primeau , F. W., DeVries , T., and Matear , R. The Southern Ocean silicon trap: Data-constrained estimates of regenerated silicic acid, trapping efficiencies, and global transport paths. *Journal of Geophysical Research: Oceans*, 119(1):313–331, jan 2014. doi: 10.1002/2013JC009356.

Hutchins , D. and Bruland , K. Iron-limited diatom growth and Si: N uptake ratios in a coastal upwelling regime. *Nature*, 393(June):65–68, 1998.

Jickells , T. D. Global Iron Connections Between Desert Dust, Ocean Biogeochemistry, and Climate. *Science*, 308(5718):67–71, 2005. doi: 10.1126/science.1105959.

Johnson , K. S., Gordon , R. M., and Coale , K. H. What controls dissolved iron concentrations in the world ocean? *Marine Chemistry*, 57(3-4):137–161, jul 1997. doi: 10.1016/S0304-4203(97)00043-1.

Johnson , K., Chavez , F., and Friederich , G. Continental-shelf sediment as a primary source of iron for coastal phytoplankton. *Nature*, 398:697–700, 1999.

Kohfeld , K., Graham , R., a.M. de Boer , Sime , L., Wolff , E., Le Quéré , C., and Bopp , L. Southern Hemisphere westerly wind changes during the Last Glacial Maximum: paleo-data synthesis. *Quaternary Science Reviews*, 68:76–95, may 2013. doi: 10.1016/j.quascirev.2013.01.017.

Kohfeld , K. E. and Harrison , S. P. DIRTMAP: The geological record of dust. *Earth-Science Reviews*, 54 (1-3):81–114, 2001. doi: 10.1016/S0012-8252(01)00042-3.

Kostianoy , A. G., Ginzburg , A. I., Lebedev , S. A., Frankignoulle , M., and Delille , B. Fronts and Mesoscale Variability in the Southern Indian Ocean as Inferred from the TOPEX / POSEIDON and ERS-2 Altimetry Data. *Oceanology*, 43(5):671–682, 2003. doi: 10.4067/10.4067/S0717-65382004000300003.

Kostianoy , A. G., Ginzburg , A. I., Frankignoulle , M., and Delille , B. Fronts in the Southern Indian Ocean

as inferred from satellite sea surface temperature data. *Journal of Marine Systems*, 45(1-2):55–73, mar 2004. doi: 10.1016/j.jmarsys.2003.09.004.

Kumar , N., Anderson , R., Mortlock , R., Froelich , P., Kubik , P., Dittrich-Hannen , B., and Suter , M. Increased biological productivity and export production in the glacial Southern Ocean. *Nature*, 378: 678–680, 1995.

Laubscher , R., Perissinotto , R., and McQuaid , C. Phytoplankton production and biomass at frontal zones in the Atlantic sector of the Southern Ocean. *Polar Biology*, 13(7):471–481, sep 1993. doi: 10.1007/BF00233138.

Li , F., Ginoux , P., and Ramaswamy , V. Distribution, transport, and deposition of mineral dust in the Southern Ocean and Antarctica: Contribution of major sources. *Journal of Geophysical Research: Atmospheres*, 113(10):1–15, 2008. doi: 10.1029/2007JD009190.

Lourey , M. J. and Trull , T. W. Seasonal nutrient depletion and carbon export in the Subantarctic and Polar Front Zones of the Southern Ocean south of Australia. *Journal of Geophysical Research*, 106(2000), 2001.

Mahowald , N., Kohfeld , K., Hansson , M., Balkanski , Y., Harrison , S. P., Prentice , I. C., Schulz , M., and Rodhe , H. Dust sources and deposition during the last glacial maximum and current climate: A comparison of model results with paleodata from ice cores and marine. *Journal of Geophysical Research*, 104(D13):15,895–15,916, 1999.

Mahowald , N. M., Baker , A. R., Bergametti , G., Brooks , N., Duce , R. a., Jickells , T. D., Kubilay , N., Prospero , J. M., and Tegen , I. Atmospheric global dust cycle and iron inputs to the ocean. *Global Biogeochemical Cycles*, 19(4), dec 2005. doi: 10.1029/2004GB002402.

Marchetti , A. and Varela , D. Iron and silicic acid effects on phytoplankton productivity, diversity, and chemical composition in the central equatorial Pacific Ocean. *Limnology and Oceanography*, 55(1):11–29, 2010.

Marshall , J. and Speer , K. Closure of the meridional overturning circulation through Southern Ocean upwelling. *Nature Geoscience*, 5(3):171–180, 2012. doi: 10.1038/ngeo1391.

Marticorena , B. and Bergametti , G. Modeling the atmospheric dust cycle: 1. Design of a soil-derived dust emission scheme. *Journal of Geophysical Research*, 100(D8):16415, 1995. doi: 10.1029/95JD00690.

Martin , J. Glacial-interglacial CO2 change: The iron hypothesis. *Paleoceanography*, 5(1):1–13, 1990.

Martin , J. H., Fitzwater , S. E., and Gordon , R. M. Iron deficiency limits phytoplankton growth in Antarctic waters. *Global Biogeochemical Cycles*, 4(1):5–12, 1990.

McGee , D., Marcantonio , F., and Lynch-Stieglitz , J. Deglacial changes in dust flux in the eastern equatorial Pacific. *Earth and Planetary Science Letters*, 257(1-2):215–230, may 2007. doi: 10.1016/j.epsl.2007.02.033.

McGee , D., Broecker , W. S., and Winckler , G. Gustiness: The driver of glacial dustiness? *Quaternary Science Reviews*, 29(17-18):2340–2350, aug 2010. doi: 10.1016/j.quascirev.2010.06.009.

Mongin , M., Molina , E., and Trull , T. W. Seasonality and scale of the Kerguelen plateau phytoplankton bloom: A remote sensing and modeling analysis of the influence of natural iron fertilization in the Southern Ocean. *Deep Sea Research Part II: Topical Studies in Oceanography*, 55(5-7):880–892, mar 2008. doi: 10.1016/j.dsr2.2007.12.039.

Moore , J. K. and Abbott , M. R. Phytoplankton chlorophyll distributions and primary production in the Southern Ocean. *Journal of Geophysical Research*, 105(C12):28709, 2000. doi: 10.1029/1999JC000043.

Moore , J. and Braucher , O. Sedimentary and mineral dust sources of dissolved iron to the world ocean. *Biogeosciences*, 5:631–656, 2008.

Moore , J., Doney , S., Glover , D., and Fung , I. Iron cycling and nutrient-limitation patterns in surface waters of the World Ocean. *Deep Sea Research Part II: Topical Studies in Oceanography*, 49:463–507, 2001.

Moore , K. J., Abbott , R., Richman , G., Smith , O., Cowles , J., Coale , H., Gardner , D., and Barber , T. SeaWiFS satellite ocean color data from the Southern Ocean. *Geophysical Research Letters*, 26(1): 1465–1468, 1999.

Nelson , D. M., Anderson , R. F., Barber , R. T., Brzezinski , M. A., Buesseler , K. O., Chase , Z., Collier , R. W., Dickson , M. L., François , R., Hiscock , M. R., Honjo , S., Marra , J., Martin , W. R., Sambrotto , R. N., Sayles , F. L., and Sigmon , D. E. Vertical budgets for organic carbon and biogenic silica in the Pacific sector of the Southern Ocean, 1996-1998. *Deep-Sea Research Part II: Topical Studies in Oceanography*, 49(9-10):1645–1674, 2002. doi: 10.1016/S0967-0645(02)00005-X.

Nelson , D. M., Trrguer , P., Brzezinski , M. A., Leynaert , A., and Queginer , B. Production and dissolution of biogenic silica in the ocean : Revised global estimates , comparison with regional data and relationship to biogenic sedimentation. *Global Biogeochem. Cycles*, 9(3):359–372, 1995.

Nowlin , W. D. and Klinck , J. M. The physics of the Antarctic Circumpolar Current. *Reviews of Geophysics*, 24(3):469, 1986. doi: 10.1029/RG024i003p00469.

Ohshima , K. I., Fukamachi , Y., Williams , G. D., Nihashi , S., Roquet , F., Kitade , Y., Tamura , T., Hirano , D., Herraiz-Borreguero , L., Field , I., Hindell , M., Aoki , S., and Wakatsuchi , M. Antarctic Bottom Water production by intense sea-ice formation in the Cape Darnley polynya. *Nature Geoscience*, 6(3):235–240, feb 2013. doi: 10.1038/ngeo1738.

Orsi , A. H., Johnson , G. C., and Bullister , J. L. Circulation, mixing, and production of Antarctic Bottom Water. *Progress in Oceanography*, 43:55–109, 1999.

Orsi , A., Whitworth , T., and Nowlin , W. On the meridional extent and fronts of the Antarctic Circumpolar Current. *Deep Sea Research Part I: Oceanographic Research Papers*, 42(5):641–673, 1995.

Park , Y. H., Charriaud , E., and Fieux , M. Thermohaline structure of the Antarctic surface water/Winter Water in the Indian sector of the Southern Ocean. *Journal of Marine Systems*, 17(1-4):5–23, 1998. doi: 10.1016/S0924-7963(98)00026-8.

Park , Y. H., Durand , I., Kestenare , E., Rougier , G., Zhou , M., D'Ovidio , F., Cotté , C., and Lee , J. H. Polar Front around the Kerguelen Islands: An up-to-date determination and associated circulation of surface/subsurface waters. *Journal of Geophysical Research: Oceans*, 119(10):6575–6592, 2014. doi: 10.1002/2014JC010061.

Park , Y. H., Gambéroni , L., and Charriaud , E. Frontal structure and transport of the Antarctic Circumpolar Current in the south Indian Ocean sector, 40–80°E. *Marine Chemistry*, 35(1-4):45–62, 1991. doi: 10.1016/S0304-4203(09)90007-X.

Park , Y.-H., Gamberoni , L., and Charriaud , E. Frontal structure, water masses, and circulation in the Crozet Basin. *Journal of Geophysical Research*, 98:12361, 1993. doi: 10.1029/93JC00938.

Petit , J., Briat , M., and Royer , A. Ice age aerosol content from East Antarctic ice core samples and past wind strength. *Nature*, 293:391–394, 1981.

Piola , A. and Georgi , D. Circumpolar properties of Antarctic intermediate water and Subantarctic Mode Water. *Dee Sea Research Part A. Oceanographic Papers*, 29(6):687–711, 1982.

Pollard , R., Tréguer , P., and Read , J. Quantifying nutrient supply to the Southern Ocean. *Journal of Geophysical Research: Oceans*, 111(5):1–9, 2006. doi: 10.1029/2005JC003076.

Pollard , R., Lucas , M., and Read , J. Physical controls on biogeochemical zonation in the Southern Ocean. *Deep Sea Research Part II: Topical Studies in Oceanography*, 49(2002):3289–3305, 2002.

Pugh , R. S., McCave , I. N., Hillenbrand , C. D., and Kuhn , G. Circum-Antarctic age modelling of Quaternary marine cores under the Antarctic Circumpolar Current: Ice-core dust-magnetic correlation. *Earth and Planetary Science Letters*, 284(1-2):113–123, 2009. doi: 10.1016/j.epsl.2009.04.016.

Quéroué , F., Sarthou , G., Planquette , H. F., Bucciarelli , E., Chever , F., Van Der Merwe , P., Lannuzel , D., Townsend , A. T., Cheize , M., Blain , S., D'Ovidio , F., and Bowie , A. R. High variability in dissolved iron concentrations in the vicinity of the Kerguelen Islands (Southern Ocean). *Biogeosciences*, 12(12):3869–3883, 2015. doi: 10.5194/bg-12-3869-2015.

Raiswell , R. Deep-Sea Research II Iceberg-hosted nanoparticulate Fe in the Southern Ocean : Mineralogy , origin , dissolution kinetics and source of bioavailable Fe. *Deep-Sea Research Part II*, 58(11-12):1364–1375, 2011. doi: 10.1016/j.dsr2.2010.11.011.

Rea , D. K. The paleoclimatic record provided by eolian deposition in the deep sea: The geologic history of wind. *Reviews of Geophysics*, 32(2):159–195, 1994. doi: 10.1029/93RG03257.

Roquet , F., Park , Y. H., Guinet , C., Bailleul , F., and Charrassin , J. B. Observations of the Fawn Trough Current over the Kerguelen Plateau from instrumented elephant seals. *Journal of Marine Systems*, 78(3): 377–393, 2009. doi: 10.1016/j.jmarsys.2008.11.017.

Sarmiento , J. L., Gruber , N., Brzezinski , M. A., and Dunne , J. P. High-latitude controls of thermocline nutrients and low latitude biological productivity. *Nature*, 427:56–60, 2004. doi: 10.1038/nature02204.1.

Sarmiento , J. L., Simeon , J., Gnanadesikan , A., Gruber , N., Key , R. M., and Schlitzer , R. Deep ocean biogeochemistry of silicic acid and nitrate. *Global Biogeochemical Cycles*, 21(1):1–16, 2007. doi: 10.1029/2006GB002720.

Sedwick , P. N., Blain , S., Quéguiner , B., Griffiths , F. B., Fiala , M., Bucciarelli , E., and Denis , M. Resource limitation of phytoplankton growth in the Crozet Basin, Subantarctic Southern Ocean. *Deep-Sea Research Part II: Topical Studies in Oceanography*, 49(16):3327–3349, 2002. doi: 10.1016/S0967-0645(02)00086-3.

Sigman , D. M., Altabet , M. A., Mccorkle , D. C., Francois , R., and Fischer , G. The d15N of nitrate in the Southern Ocean : Consumption of nitrate in surface waters. *Global Biogeochemical Cycles*, 13(4): 1149–1166, 1999.

Sikes , E. L., Howard , W. R., Samson , C. R., Mahan , T. S., Robertson , L. G., and Volkman , J. K. Southern ocean seasonal temperature and subtropical front movement on the south tasman rise in the late quaternary. *Paleoceanography*, 24(2):1–13, 2009. doi: 10.1029/2008PA001659.

Sloyan , B. M. and Rintoul , S. R. Circulation, Renewal, and Modification of Antarctic Mode and Intermediate Water*. *Journal of Physical Oceanography*, 31(4):1005–1030, apr 2001. doi: 10.1175/1520-0485(2001)031⟨1005:CRAMOA⟩2.0.CO;2.

Smith , K. L., Robison , B. H., Helly , J. J., Kaufmann , R. S., Ruhl , H. A., Shaw , T. J., Twining , B. S., and Vernet , M. Enrichment in the Weddell Sea Free-Drifting Icebergs: Hot Spots of Chemical and Biological Free-Drifting Icebergs: Hot Spots of Chemical and Biological Enrichment in the Weddell Sea.

478(July):478–483, 2007. doi: 10.1126/science.1142834.

Sokolov , S. and Rintoul , S. R. Structure of Southern Ocean fronts at 140°E. *Journal of Marine Systems*, 37(1-3):151–184, nov 2002. doi: 10.1016/S0924-7963(02)00200-2.

Sokolov , S. and Rintoul , S. R. Multiple Jets of the Antarctic Circumpolar Current South of Australia*. *Journal of Physical Oceanography*, 37(5):1394–1412, 2007. doi: 10.1175/JPO3111.1.

Sparrow , M. D., Heywood , K. J., and Brown , J. Current structure of the south Indian Ocean. *Journal of Geophysical Research*, 101:6377–6391, 1996.

Spiller , S. C., Castelfranco , A. M., and Castelfranco , P. A. Effects of Iron and Oxygen on Chlorophyll Biosynthesis 1: In vivo observations on iron and oxygen-deficient plants. *Plant physiology*, 69:107–111, 1982.

Sugden , D. E., McCulloch , R. D., Bory , A. J.-M., and Hein , A. S. Influence of Patagonian glaciers on Antarctic dust deposition during the last glacial period. *Nature Geoscience*, 2(4):281–285, 2009. doi: 10.1038/ngeo474.

Tagliabue , A., Bopp , L., and Aumont , O. Evaluating the importance of atmospheric and sedimentary iron sources to Southern Ocean biogeochemistry. *Geophysical Research Letters*, 36:1–5, 2009. doi: 10.1029/2009GL038914.

Tagliabue , A., Bowie , A. R., Boyd , P. W., Buck , K. N., Johnson , K. S., and Saito , M. A. The integral role of iron in ocean biogeochemistry. *Nature*, 543(7643):51–59, 2017. doi: 10.1038/nature21058.

Tagliabue , A., Sallée , J.-B., Bowie , A. R., Lévy , M., Swart , S., and Boyd , P. W. Surface-water iron supplies in the Southern Ocean sustained by deep winter mixing. *Nature Geoscience*, 7(4):314–320, mar 2014. doi: 10.1038/ngeo2101.

Takeda , S. Influence of iron availability on nutrient consumption ratio of diatoms in oceanic waters. *Nature*, 393(JUNE):774–777, 1998.

Talley , L. D. Closure of the global overturning circulation through the Indian, Pacific and Southern Oceans: schematics and transports. *Oceanography*, 26(1):80–97, 2013.

Thompson , A. F. The atmospheric ocean: eddies and jets in the Antarctic Circumpolar Current. *Philosophical transactions. Series A, Mathematical, physical, and engineering sciences*, 366(1885):4529–41, dec 2008. doi: 10.1098/rsta.2008.0196.

Thompson , A. F. and Sallée , J.-B. Jets and Topography: Jet Transitions and the Impact on Transport in the Antarctic Circumpolar Current. *Journal of Physical Oceanography*, 42(6):956–972, 2012. doi: 10.1175/JPO-D-11-0135.1.

Timmermans , K., Stolte , W., and Baar , H. D. Iron-mediated effects on nitrate reductase in marine phytoplankton. *Marine Biology*, (April):389–396, 1994.

Trull , T. W., Davies , D. M., Dehairs , F., Cavagna , A. J., Lasbleiz , M., Laurenceau-Cornec , E. C., D'Ovidio , F., Planchon , F., Leblanc , K., Quéguiner , B., and Blain , S. Chemometric perspectives on plankton community responses to natural iron fertilisation over and downstream of the Kerguelen Plateau in the Southern Ocean. *Biogeosciences*, 12(4):1029–1056, 2015. doi: 10.5194/bg-12-1029-2015.

Twining , B. S. and Baines , S. B. The Trace Metal Composition of Marine Phytoplankton. *Annual review of marine science*, 5:191–215, 2013. doi: 10.1146/annurev-marine-121211-172322.

Van Der Merwe , P., Bowie , A. R., Quéroué , F., Armand , L., Blain , S., Chever , F., Davies , D., Dehairs , F., Planchon , F., Sarthou , G., Townsend , A. T., and Trull , T. W. Sourcing the iron in the naturally

fertilised bloom around the Kerguelen Plateau: Particulate trace metal dynamics. *Biogeosciences*, 12(3): 739–755, 2015. doi: 10.5194/bg-12-739-2015.

Wadley , M. R., Jickells , T. D., and Heywood , K. J. The role of iron sources and transport for Southern Ocean productivity. *Deep Sea Research Part I: Oceanographic Research Papers*, 87:82–94, may 2014. doi: 10.1016/j.dsr.2014.02.003.

Wang , S., Bailey , D., Lindsay , K., Moore , J. K., and Holland , M. Impact of sea ice on the marine iron cycle and phytoplankton productivity. *Biogeosciences*, 11(17):4713–4731, sep 2014. doi: 10.5194/bg-11-4713-2014.

Wang , X., Matear , R. J., and Trull , T. W. Nutrient utilization ratios in the Polar Frontal Zone in the Australian sector of the Southern Ocean: A model. *Global Biogeochemical Cycles*, 17(1):1009, doi:10.1029/2002GB001938, 2003. doi: 10.1029/2002GB001938.

Whitworth , T. Zonation and geostrophic flow of the Antarctic circumpolar current at Drake Passage. *Deep Sea Research Part A, Oceanographic Research Papers*, 27(7):497–507, 1980. doi: 10.1016/0198-0149(80)90036-9.

Wolff , E. W., Fischer , H., Fundel , F., Ruth , U., Twarloh , B., Littot , G. C., Mulvaney , R., Röthlisberger , R., de Angelis , M., Boutron , C. F., Hansson , M., Jonsell , U., Hutterli , M. a., Lambert , F., Kaufmann , P., Stauffer , B., Stocker , T. F., Steffensen , J. P., Bigler , M., Siggaard-Andersen , M. L., Udisti , R., Becagli , S., Castellano , E., Severi , M., Wagenbach , D., Barbante , C., Gabrielli , P., and Gaspari , V. Southern Ocean sea-ice extent, productivity and iron flux over the past eight glacial cycles. *Nature*, 440 (7083):491–6, mar 2006. doi: 10.1038/nature04614.

3

Age models & radiocarbon records

3.1 Age model construction

The construction of age models for Southern Ocean sediment cores is notoriously difficult. The use of traditional carbonate dating methods such as radiocarbon dating and $\delta^{18}O$ stratigraphy are often limited due to the poor carbonate preservation. Even where carbonates are preserved there are further limitations. ^{14}C dating requires knowledge of the reservoir age from which the carbonate formed. In most parts of the world ocean planktic foraminifera display a relatively constant reservoir age (Bard, 1988). However, in the Southern Ocean, reservoir ages have been shown to significantly vary by many hundreds of years through time (Sikes et al., 2000). $\delta^{18}O$ stratigraphy is useful at low resolution (glacial-interglacial time scales), but large local variability significantly limits its effectiveness through the deglaciation.

Other, methods include the use of diatom stratigraphy, e.g. peak *Eucampia antarctica* abundance as a marker for the LGM (Burckle and Cook, 1983; Crosta and Shemesh, 2002; Anderson et al., 2009). Also, detritus-based stratigraphy that involves correlating proxies of

lithogenic flux (such as ^{232}Th and magnetic susceptibility) with Antarctic dust flux records from ice cores (Pugh et al., 2009; Anderson et al., 2014). %Opal has been used to align multiple cores to the same age model (e.g. Robinson et al., 2014), however, it is unclear whether diatom productivity changes were synchronous throughout the Southern Ocean across the deglaciation, a topic that will be addressed in Chapter 4.

The age models for the three cores (MD84-551, MD88-773 and MD88-772) presented here were constructed utilising a suite of the above dating methods. In the following text each of the methods used will be described followed by a synthesis of the stratigraphic data and the methodology of the age model construction.

Radiocarbon dating

Neogloboquadrina pachyderma were hand-picked from sieved (75 µM) and Milli-Q water washed bulk sediments. Accelerator Mass Spectrometry (AMS) ^{14}C dates were produced from the planktonic foraminifera samples at the NERC Radiocarbon Facility (NRCF), East Kilbride.

For MD84-551, 16 ^{14}C dates were already available (Labracherie et al., 1989; Pichon et al., 1992; E. Michel pers comms) at 35 – 182 cm. An additional 19 ^{14}C dates were added as part of this study within the same depth bracket to provide an improved resolution.

Cores MD88-773 and MD88-772 from the southeast Indian ridge had little or no foraminifera preservation below 375 cm and 65 cm, respectively. Consequently, only 8 ^{14}C dates were acquired for MD88-773 at 120 – 335 cm, and 6 ^{14}C dates for MD88-772 at 18 – 56 cm. The uncalibrated ^{14}C dates are presented in Tables 3.1 - 3.3 and Figures 3.1-3.3 versus core depth.

^{14}C dates reflect the radiocarbon content of the material at the point at which its production ceases (i.e. the death of the foraminifera). Due to the variable rate of radiocarbon production in the upper atmosphere through time, a correction must be applied to convert the measured radiocarbon dates into calendar dates. This is done using the Calib 7.04 program (Stuiver and Reimer, 1993), which utilises the Marine13 calibration curve constructed from a variety of independently dated (U/Th dating, for instance) materials. In addition, the construction of biominerals (i.e. foraminiferal calcium carbonate) within media that is not the atmosphere (i.e. the surface ocean) will impart a reservoir effect on the radiocarbon content of that

Depth (cm)	$^{14}C_{age} \pm 1\sigma$ (years)	Depth (cm)	$^{14}C_{age} \pm 1\sigma$ (years)
35*	7900 ± 70	133	11567 ± 40
47*	9440 ± 60	136	12116 ± 39
58*	9400 ± 60	137	7871 ± 38
73.5*	9120 ± 80	141*	12720 ± 200
75	9698 ± 37	143.5	13090 ± 43
82*	9950 ± 170	144	12498 ± 40
86	11239 ± 39	148	11703 ± 40
89	9798 ± 38	150	12853 ± 41
92*	10530 ± 70	152*	14400 ± 100
102*	11140 ± 60	153	15286 ± 47
106	11363 ± 40	155	16589 ± 51
112*	9560 ± 80	157	16828 ± 52
115	7983 ± 37	158	15870 ± 48
121*	11330 ± 170	161*	17510 ± 160
122	11387 ± 40	172*	19630 ± 150
125*	10450 ± 90	175	14997 ± 49
128	12005 ± 48	182*	14860 ± 100
132*	12140 ± 70		

TABLE 3.1: Uncalibrated radiocarbon dates for MD84-551. Marked samples (*) were analysed previously (Labracherie et al., 1989; Pichon et al., 1992; E. Michel pers comms) at CNRS-CEA, Gif-sur-Yvette. The remaining were prepared as part of this study with AMS ^{14}C analysis performed at the NRCF, East Kilbride.

Depth (cm)	$^{14}C_{age} \pm 1\sigma$ (years)	Depth (cm)	$^{14}C_{age} \pm 1\sigma$ (years)
120	4392 ± 36	274	9466 ± 38
170	6126 ± 38	295	9762 ± 38
215	6666 ± 37	315	10580 ± 39
255	8841 ± 39	335	12103 ± 41

TABLE 3.2: Uncalibrated radiocarbon dates for MD88-773

Depth (cm)	$^{14}C_{age} \pm 1\sigma$ (years)	Depth (cm)	$^{14}C_{age} \pm 1\sigma$ (years)
18	7075 ± 37	44	11411 ± 39
26	8437 ± 36	48	12062 ± 42
37	10088 ± 38	56	11985 ± 40

TABLE 3.3: Uncalibrated radiocarbon dates for MD88-772

mineral. The apparent age of waters residing in the much of world's surface oceans (after correcting for nuclear bomb radiocarbon) is approximately 400 years ($\Delta^{14}C \approx$ -50 ‰). As a result, foraminifera growing in the surface ocean will appear to be 400 years older than the contemporaneous atmosphere (Bard, 1988). However, upon approaching the Southern Ocean this reservoir age increases due to the influence of radiocarbon depleted deep waters upwelling to the surface ocean. As a result, the modern reservoir ages of waters surrounding MD84-551, MD88-773 and MD88-772 estimated from the gridded GLODAP database (Key

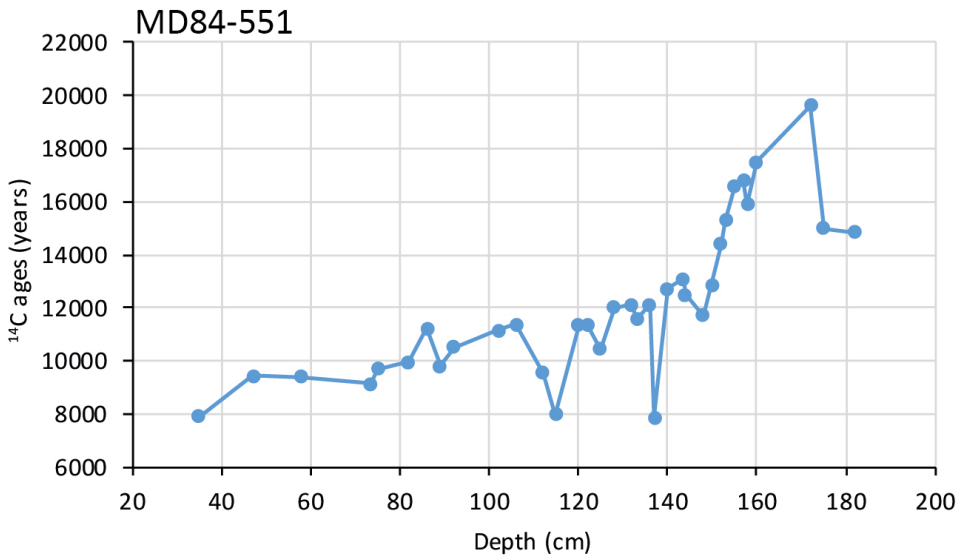

FIGURE 3.1: Uncalibrated 14C ages in MD84-551

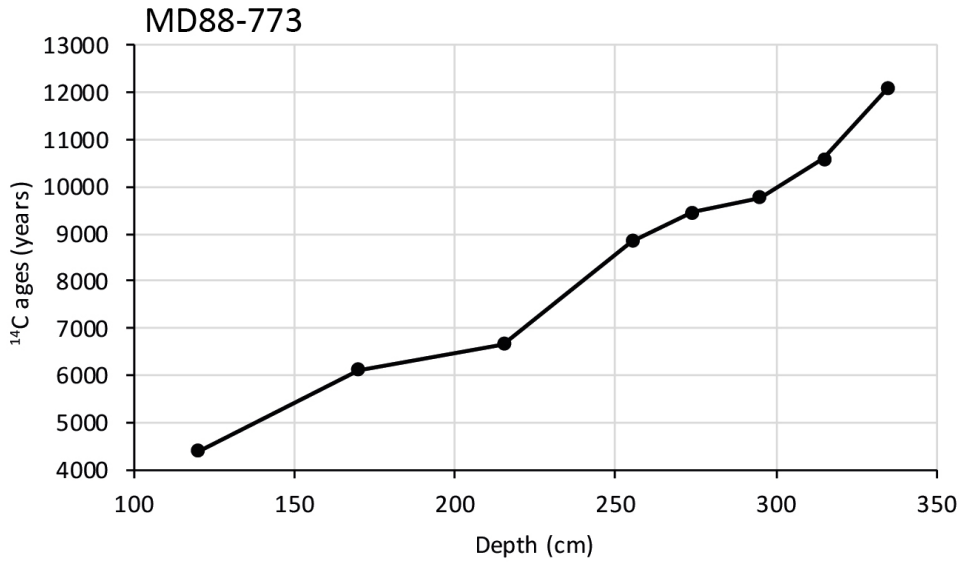

FIGURE 3.2: Uncalibrated 14C ages in MD88-773

et al., 2004) are 1100 years ($\Delta^{14}C$ = -128 ‰), 990 years ($\Delta^{14}C$ = -116 ‰) and 840 years ($\Delta^{14}C$ = -100 ‰), respectively.

Importantly, it has been suggested that the reservoir age of the Southern Ocean surface waters varied significantly across the last deglaciation (Sikes et al., 2016). Radiocarbon analyses on benthic foraminifera (Skinner et al., 2010) and deep sea corals (Burke and Robinson, 2012) suggest the ventilation age of the deep Southern Ocean was at least 4000 years older than the contemporaneous atmosphere and these waters were upwelled to the Southern Ocean surface during the deglaciation. As a result, it is possible that radiocarbon

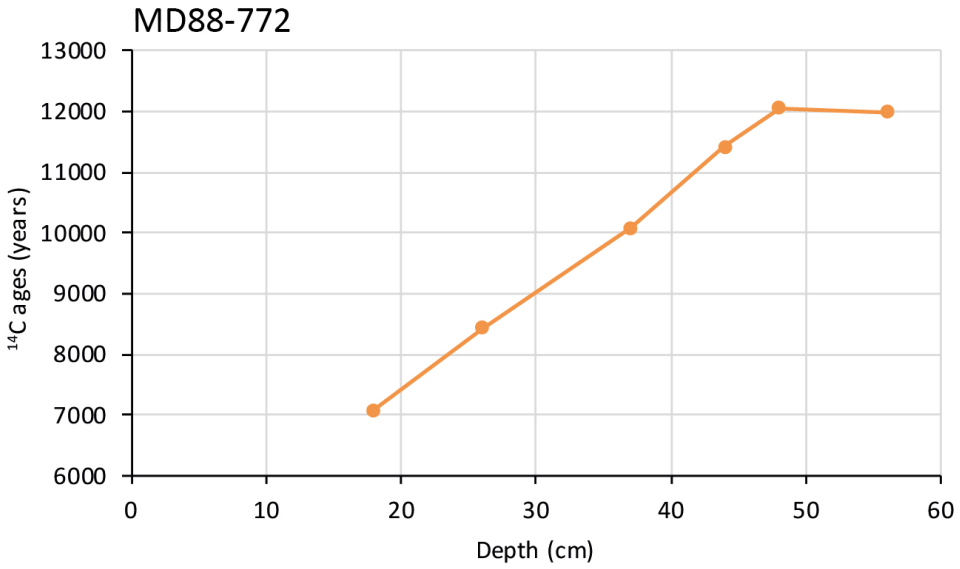

FIGURE 3.3: Uncalibrated 14C ages in MD88-772

dates of Southern Ocean planktic foraminifera may have apparent ages several thousand years old. It has been suggested that there has been little or no change to the Southern Ocean reservoir age throughout much of the Holocene (Hall et al., 2010). Hence, we used the ^{14}C dates later than 10 ka BP located at the top of the three cores to constrain the Holocene. For the remainder of the records we attempt to construct an age model using other stratigraphic tools noted below.

Oxygen isotope stratigraphy

Planktonic and benthic foraminifera (single species samples) were hand-picked from sieved (75 µM) and Milli-Q water washed bulk sediments. Published oxygen isotope ($\delta^{18}O$) records from several foraminiferal species were already available for MD84-551 (Labracherie et al., 1989; Pichon et al., 1992) across the entire record. 8 additional $\delta^{18}O$ measurements were performed on *N. pachyderma* samples beweem 115 cm and 157 cm.

As stated above, the calcium carbonate preservation in MD88-773 and MD88-772 is poor downcore. 27 $\delta^{18}O$ analyses on *N. pachyderma* were already published from MD88-773 (Francois et al., 1997) between 0 cm and 370 cm. An additional 12 measurements were performed on *N. pachyderma* between 150 cm and 335 cm. For MD88-772 no published $\delta^{18}O$ data was available. 30 $\delta^{18}O$ measurements on *N. pachderma* were performed on this core from 4 cm to 65 cm core depth.

The oxygen isotopic composition ($\delta^{18}O$) of foraminiferal calcium carbonate reflects the $\delta^{18}O$ composition and temperature of the water from which the foraminifera produced their tests, with a decrease in $\delta^{18}O$ indicating an increase in ambient temperatures or a decrease in the ambient $\delta^{18}O$. Because the deep ocean temperatures are already close to zero, much of the observed glacial-interglacial $\delta^{18}O$ variability from deep ocean benthic foraminifera records is thought to be solely due to changes in the deep ocean water $\delta^{18}O$ in response to the growth and collapse of large terrestrial ice sheets. On the other hand, planktic foraminifera experience larger changes in ambient temperature and may therefore reflect more localised climate variability.

In the Southern Ocean, planktonic $\delta^{18}O$ records have been commonly used to stratigraphically correlate records against the well-dated ice core records from Antarctica under the assumption of synchronous changes in sea surface temperature in the Southern Ocean and atmospheric temperature around Antarctica. However, the meandering of fronts may impart large changes in sea surface temperature and ambient water $\delta^{18}O$ in some cores, producing desynchronised changes in planktic foraminiferal $\delta^{18}O$. Aligning $\delta^{18}O$ records in the Southern Ocean should therefore be performed with caution and ideally accompanied by other stratigraphic tools.

The glacial-interglacial variability in benthic $\delta^{18}O$ is likely to be more homogenous across the Southern Ocean due to the muted influence of front movement and sea surface temperature variability. However, there is some evidence for inter-basin desynchronization during the deglaciation. For example, Stern and Lisieki (2014) produced a stack of $\delta^{18}O$ records from each of the three major oceanic basins (Atlantic, Indian and Pacific). The last glacial benthic $\delta^{18}O$ maximum and the onset of the deglacial decline in benthic $\delta^{18}O$ was found to be offset between the three basins, with the deep Indian stack exhibiting a later timing for both compared to the deep Pacific and deep Atlantic (Stern and Lisiecki, 2014). The reasons for this delay are currently unclear but may be due to later ventilation of parts of the deep ocean that are isolated from mixing due to bathymetric barriers (Sikes et al., 2017). The benthic foraminiferal (*Cibicides wellerstorfi*) $\delta^{18}O$ record of MD84-551 exhibits a maximum at 173 cm core depth and decreases thereafter towards the Holocene ^{14}C-dated section of the record. This benthic $\delta^{18}O$ maximum was used as a stratigraphic tie-point with an allocated age of 18 ka BP, corresponding to the observed $\delta^{18}O$ maximum in the nearby MD12-3396CQ (Figure 3.4). Because the benthic $\delta^{18}O$ record of MD84-551 is low resolution, there is significant uncertainty regarding this tie-point. However, the tie-point will only be used provisionally as a marker for the LGM (see text below).

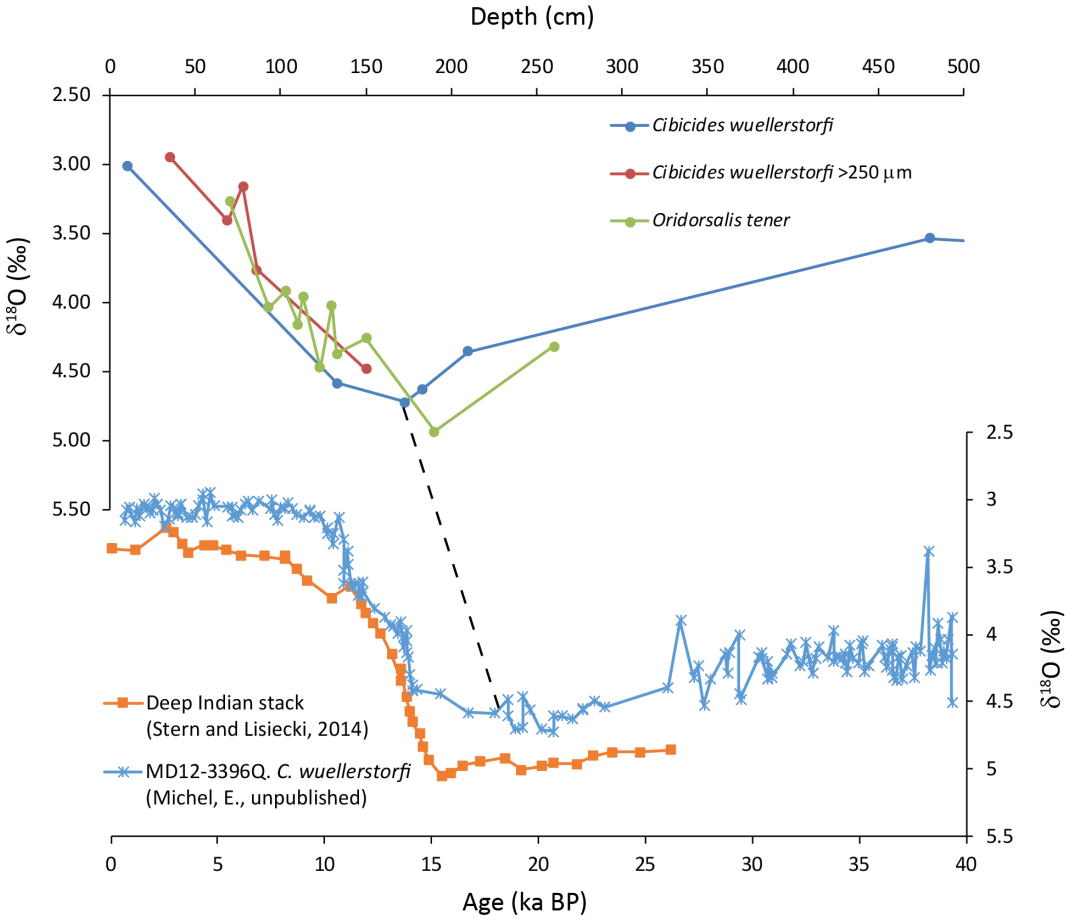

FIGURE 3.4: Benthic foraminifera (*Cibicides wuellerstorfi* and *Ordiorsalis tener*) $\delta^{18}O$ records from MD84-551 (top) (unpublished, E. Michel pers comms) with benthic foraminifera $\delta^{18}O$ records from MD12-3396CQ (unpublished, E. Michel pers comms) and the Deep Indian stack (Stern and Lisiecki, 2014) (bottom). The dashed line indicates an identified age control point. This control point was later rejected in favour of ^{14}C dates (see text and Table 3.4 for details).

After applying the benthic $\delta^{18}O$ tie-point described above and the Holocene ^{14}C age control points, a visual inspection of the planktonic foraminiferal $\delta^{18}O$ records of MD84-551 and MD12-3396CQ suggests comparable $\delta^{18}O$ variability through the last deglaciation. Notable features shared in both records include a small deglacial minimum at 13.3 – 14 ka BP in MD12-3396CQ and a late deglaciation cessation of the deglacial $\delta^{18}O$ decline at 10.7 ka BP in MD12-3396CQ. These two features were used as further stratigraphic tie-points for MD84-551 (Figure 3.5).

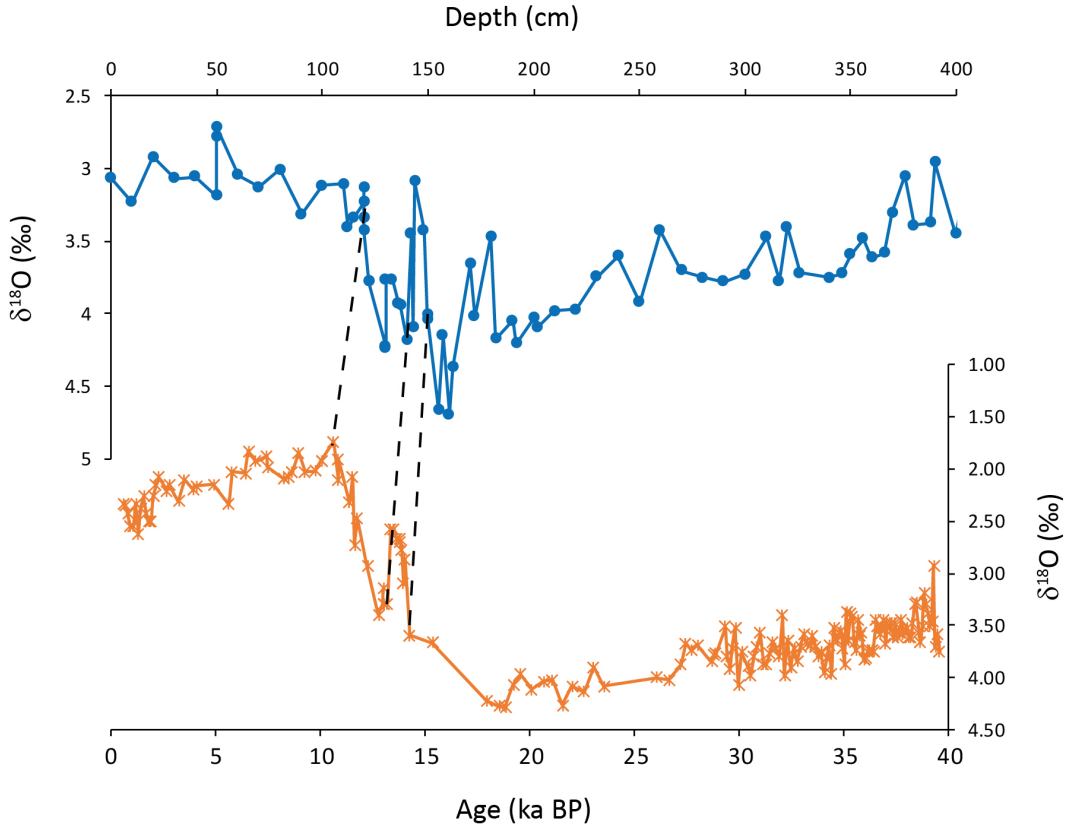

FIGURE 3.5: Planktic foraminifera (*N. pachyderma*) $\delta^{18}O$ records from MD84-551 (top) (Labracherie et al., 1989) and MD12-3396CQ (bottom) (unpublished, E. Michel pers comms). Dashed lines indicate identified age control points.

Due to the vicinity MD88-773 to the polar front and the location of MD88-772 within the polar front zone, it is more likely that migrations of the polar front between the last glacial maximum and the Holocene may have influenced these two records. Planktic $\delta^{18}O$ was not used to provide stratigraphy for MD88-772 and MD88-773.

Lithogenic detritus and magnetic susceptibility

Elements such as Fe, Al, Ti and ^{232}Th in marine sediments are most commonly associated with detrital material, which is transported to the sediments as wind-blown dust, fluvial sediments, ice-rafted debris or the reworking of marine topography. The strong deep ocean currents associated with the ACC generate thick and intense nepheloid (suspended particle) layers in the Southern Ocean that can transport particles significant distances (Dutkiewicz et al., 2016). Based on mineralogical analyses, much of the detrital material deposited in Indian sector through the last glacial cycle is suggested to have derived from erosion of

the basaltic Kerguelen Plateau (Bareille et al., 1994). The higher detrital flux noted in all sediment cores within the Indian sector during the last glacial period suggests erosion of the plateau was increased possibly due to a combination of glacial working and the more exposed shelf region during the lower sea level stand. The glacial-interglacial variability in detrital fluxes in Indian sector records approximately correlates with the dust flux records from the Antarctic, which suggests a shared control mechanism. One possibility is stronger westerly winds produced greater dust fluxes and a strengthened ACC, producing stronger bottom currents during glacial periods and thus more intense nepheloid layers. However, whether the strength of the ACC was enhanced during glacial periods remains contentious (Klinck and Smith, 1993; ; McCave et al., 2014; Lynch-Stieglitz et al., 2016).

The hypothesis that detrital fluxes in the Southern Ocean correlate with the glacial-interglacial variability in Antarctic dust fluxes has encouraged some researchers to stratigraphically align these records (Pugh et al., 2009). However, detrital records from the Indian sector display subtle differences compared with Antarctic dust flux between the LGM and Holocene, suggesting the two processes are not entirely coupled. However, the timing of detrital flux and magnetic susceptibility (which correlates to magnetite content) changes between numerous cores in the Indian sector appears to be synchronous, suggesting the glacial-interglacial variability in bottom water currents controls the sediment composition over a wide area (Mazaud et al., 2007).

Figure 3.6 displays the magnetic susceptibilities of three sediment records from the Indian sector located north-west of MD88-773 and MD88-772 (see Figure 3.7). The three cores are independently dated with ^{14}C-dates. In addition, MD94-103 is aligned to magnetic field reversal intervals (Mazaud et al., 2002) and both MD12-3396CQ and MD88-769 contains benthic δ^{18}O record that display a good fit to global benthic δ^{18}O stacks (Stern and Lisiecki, 2014). The magnetic susceptibility records from the three cores are highly comparable, suggesting regional changes in the flux of material derived from the Kerguelen Plateau (Mazaud et al., 2007).

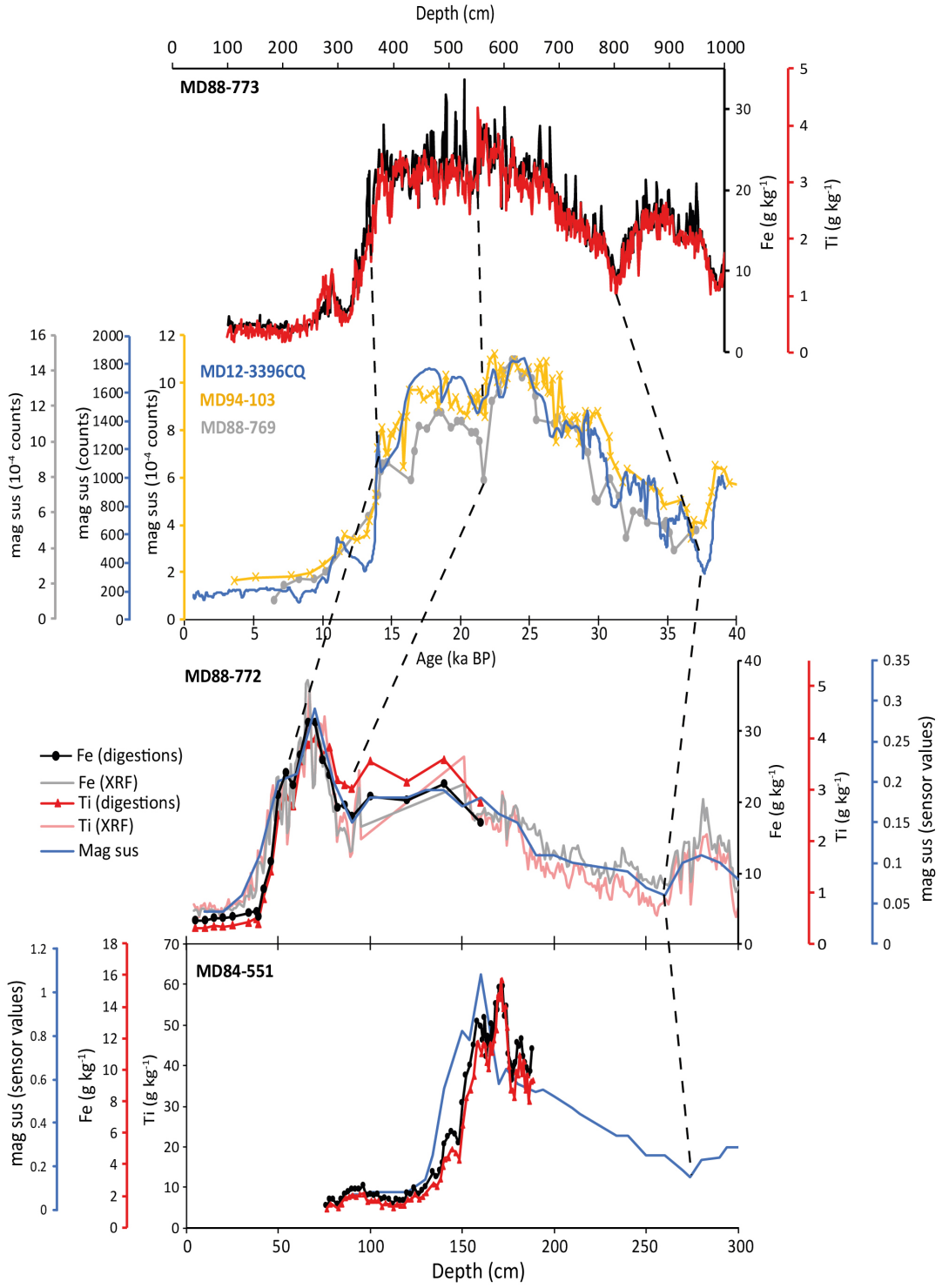

FIGURE 3.6: Lithogenic detritus records from Indian sector records (see Figure 3.6 for locations). Dashed lines indicated identified age control points.

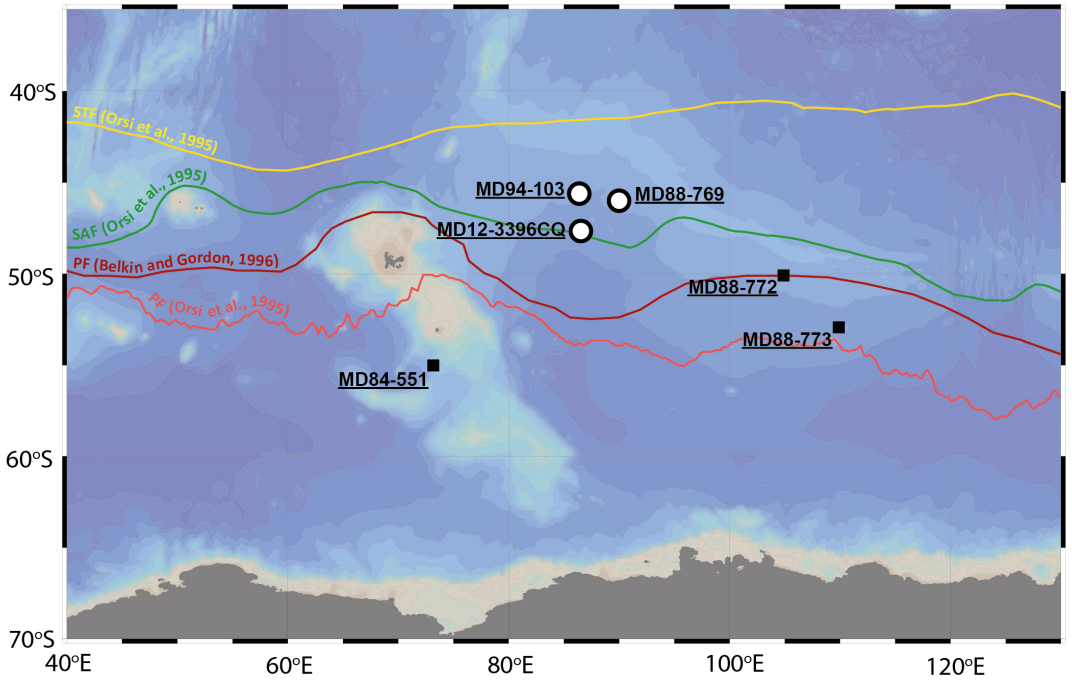

FIGURE 3.7: Map of the core locations used to construct the age models. Front positions estimated by the denoted reference material. Map produced using ODV software (Schlitzer, 2002).

A visual comparison between the Ti and Fe records of MD88-773 and MD88-772 with the three dated records suggests some features are shared between the records, reflecting a shared mechanism of detritus delivery to the east Indian sector. Included in Figure 3.6 is the magnetic susceptibility record for MD88-772, which correlates very well with the down-core Ti and Fe records. Magnetic susceptibility data are not available for MD88-773. The Al records of MD88-773 and MD88-772 also shared some broadly similar patterns to the Ti and Fe records, however, visual inspection of the Al records derived from XRF scanning suggest significant interferences in the analysis that produced highly noisy records. Hence, the Al records were not used for stratigraphy. Stratigraphic tie points were added to align the Fe and Ti records of MD88-773 and MD88-772 with the three dated records and are shown in Figure 3.6. A prominent feature in the MD88-773 Ti record that was not aligned to the three dated records was the small peak at approximately 10 ka BP. A similar peak appears to occur in MD12-3396CQ at approximately 11 ka BP, however, using this feature as a stratigraphic tie-point would conflict with the Holocene ^{14}C dates in MD88-773. Radiocarbon reservoir effects cannot explain this discrepancy as such a change would suggest the foraminifera were younger than the contemporaneous atmosphere. One possible reason for this misalignment is that there is a large change in biogenic material

(opal and carbonate) flux around this interval, which may produce dilution effects on the Ti record.

The magnetic susceptibility minimum at 37.5 ka BP in the three dated cores given above was aligned to a similar magnetic susceptibility minimum in MD84-551 (Figure 3.6). This feature is shared between many records in the Indian sector (Bareille et al., 1994), as well as the dust flux records of Antarctica. The remainder of the detritus record for MD84-551 was not used for stratigraphic alignment to the other cores east of the Kerguelen Islands as the detrital fluxes patterns may be different in this region.

3.2 Re-evaluation of the radiocarbon

Here we will now examine the ^{14}C dates older than the Holocene ($>$ 10 ka BP) in each of the cores with respect to their new, independently constrained age models. Figures 3.8-3.10 display the remaining ^{14}C dates as calibrated calendar ages for each of the three cores, applying the same reservoir correction as those in the Holocene. The deglacial ^{14}C dates of MD88-773 and MD88-772 appear to fit well with the current age model, suggesting little change in the reservoir age at these sites during the late deglaciation. One ^{14}C date in MD88-772 shows a small reversal and is anomalous with respect to the current age model (labelled in Figure 3.10). This ^{14}C date was discarded. The remaining ^{14}C dates of MD88-773 and MD88-772 were included as part of the overall age models of these two cores.

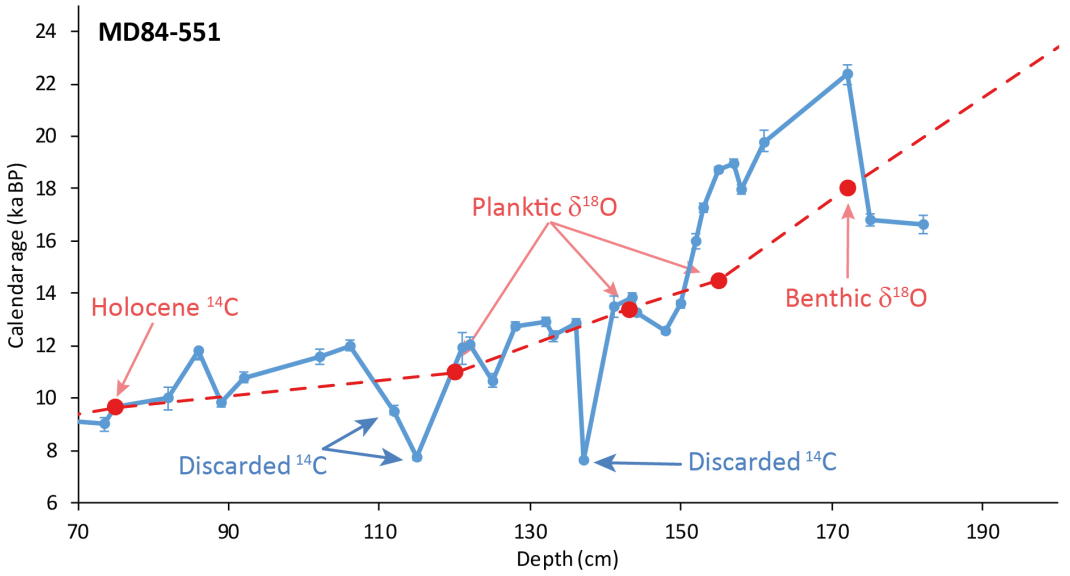

FIGURE 3.8: MD84-551 calibrated radiocarbon dates to calendar ages using the Calib 7.04 software, (Stuiver et al., 2018) (blue solid line). Error bards are $\pm 1\sigma$. The age model controls points are also displayed (red dashed line). Note that the benthic δ^{18}O control point was later rejected for ^{14}C dating. See the text, Figure 3.11 and Table 3.4 for details.

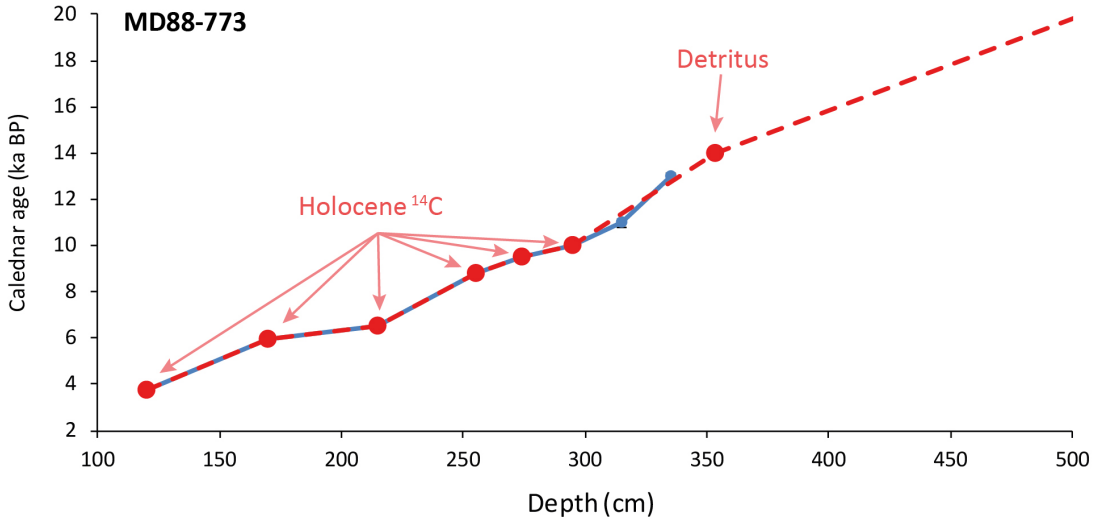

FIGURE 3.9: MD88-773 calibrated radiocarbon dates to calendar ages using the Calib 7.04 software, (Stuiver et al., 2018) (blue solid line). Error bards are $\pm 1\sigma$. The age model controls points are also displayed (red dashed line). See Table 3.5 for a list of the age control points.

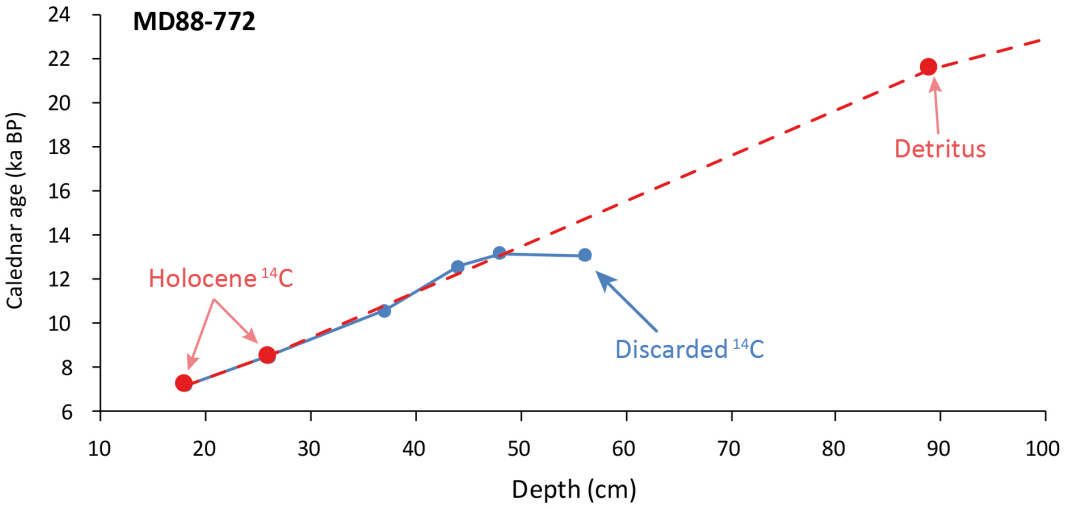

FIGURE 3.10: MD88-772 calibrated radiocarbon dates to calendar ages using the Calib 7.04 software, (Stuiver et al., 2018) (blue solid line). Error bards are $\pm 1\sigma$. The age model controls points are also displayed (red dashed line). See Table 3.6 for a list of the age control points.

The majority of the deglacial ^{14}C dates in MD84-551 fit reasonably well with the current age model (are within 1 kyr of the age model). Exceptions to this include five distinctly anomalous young radiocarbon dates (at 112 cm, 115 cm, 137 cm, 175 cm and 182 cm) and a series of anomalously old radiocarbon dates located at 152 – 172 cm core depth. The upper three anomalously young ^{14}C dates (112 cm, 115 cm and 137 cm) appear to be flyers with respect to the adjacent radiocarbon dates and were therefore discarded. It is less clear whether the lower two (175 cm and 182 cm) anomalously young ^{14}C dates are also flyers due to the scarcity of radiocarbon dates at that depth in the core. Due to the uncertainty of the two stratigraphic tie points at this depth in the core (benthic foraminifera δ^{18}O and detrital stratigraphy), the radiocarbon date that furthest downcore was incorporated into the age model. By default, the Holocene reservoir age of 1100 years was adopted for this ^{14}C date, however the true reservoir age of is unknown. Taken together the age model of MD84-551 at onset of the deglaciation and LGM is more poorly constrained than the remainder of the deglaciation. The new age model for MD84-551 is presented in Figure 3.11.

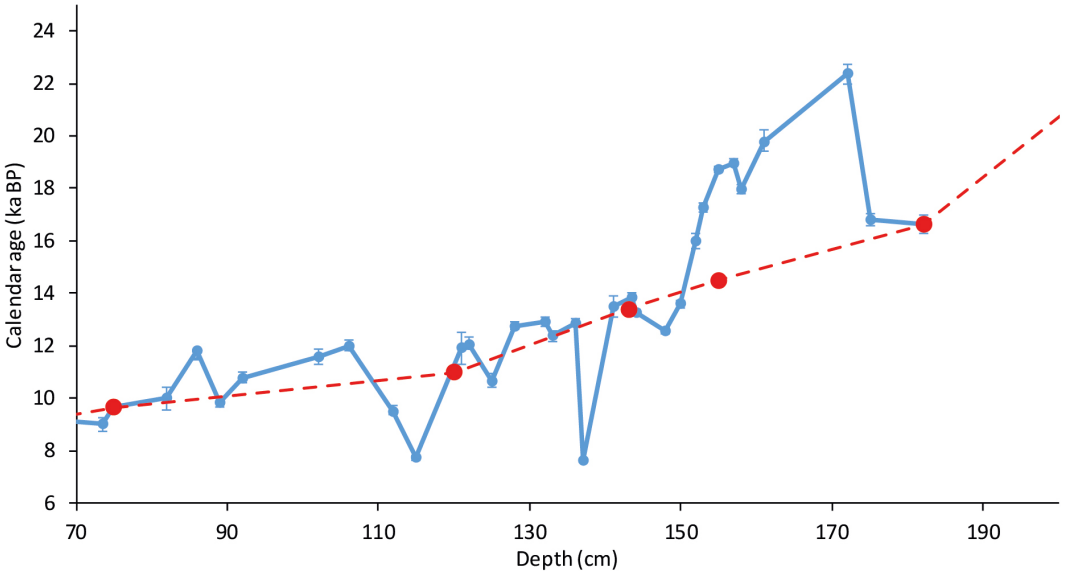

FIGURE 3.11: An update of Figure 3.8 tp include ^{14}C age control point (182 cm depth). This is the final age model for MD84-551 used through the remainder of this thesis. See Table 3.4 for a list of the age control points.

The series of anomalously old ^{14}C dates (152 – 172 cm) cannot be discarded as the number of comparable dates within the series suggests this is indeed a real feature of the radiocarbon record. However, fitting the age model to these radiocarbon dates would not only produce a large reversal between 172 cm and 175 cm, but would also produce large and abrupt changes in sedimentation rate that are not accompanied by a reciprocal change in mineralogy that one would expect.

The radiocarbon activity of multiple records can be evaluated using the Δ^{14}C notation, derived by the following equation from Stuiver and Polach (1977).

$$\Delta^{14}C = 1000\left(e^{\frac{^{14}C_{age}}{-8033}+\lambda t} - 1\right) \tag{3.1}$$

Where $^{14}C_{age}$ is the uncalibrated radiocarbon age, λ is the mean life of radiocarbon (1/8267) and t is the calendar age from the independently constrained age model. Because the radiocarbon activity of the atmosphere ($\Delta^{14}C_{atmos}$) varies over time, the difference between the radiocarbon activity of the sample and $\Delta^{14}C_{atmos}$ ($\Delta\Delta^{14}C$) is used to determine the degree of radiocarbon depletion within a record. $\Delta\Delta^{14}C$ values within MD84-551 (Figure 3.12) range between +52.9 ‰to -726 ‰(not including the three discarded anomalously young dates). The single positive $\Delta\Delta^{14}C$ value indicates either an incorrect age model or

analytical error. The age model was not adjusted, in favour of maintaining an age model independently constrained from radiocarbon across much of the deglaciation.

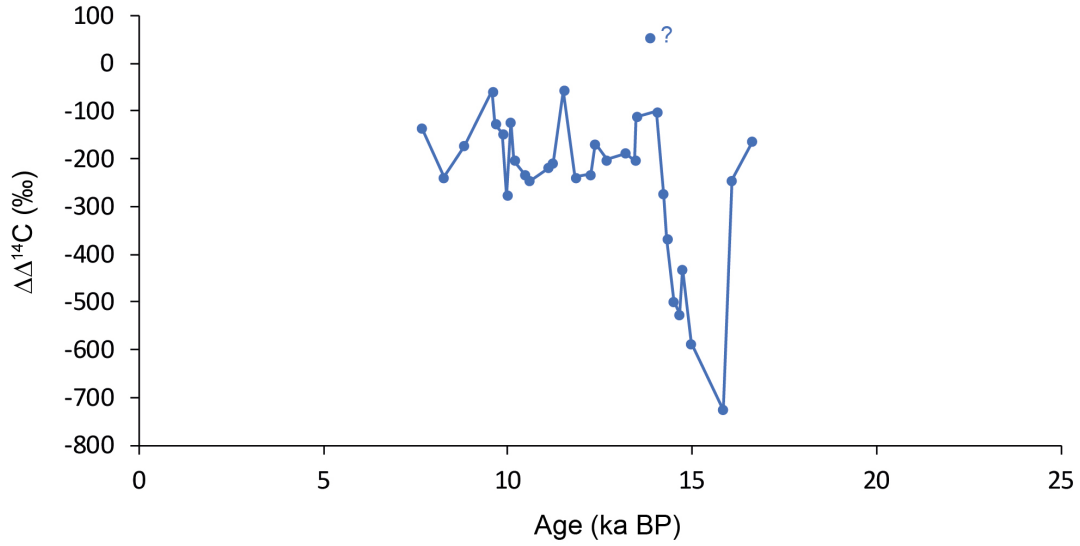

FIGURE 3.12: $\Delta\Delta^{14}C$ record from MD84-551, interpreted to be displaying the ^{14}C variability in Antarctic surface waters across the deglaciation.

The pattern of $\Delta\Delta^{14}C$ variability in MD84-551 (Figure 3.12) implies large variations of the surface radiocarbon reservoir age in the Antarctic across the last deglaciation. Such changes can be attributed to the upwelling of ^{14}C-depleted deep waters. A well-established hypothesis for explaining such old radiocarbon ages is that deep ocean mixing was sluggish and shallower during glacial periods, hence the deep waters became isolated from the atmosphere for longer periods and replenishment of radiocarbon was inhibited. It is thought that the deep waters were likely ventilated via the Southern Ocean and numerous recent studies have predicted such changes in the Antarctic surface radiocarbon content (Du et al., 2018; Zhao et al., 2018). However, this record is the first to substantiate these hypotheses.

Figure 3.13 displays the MD84-551 $\Delta\Delta^{14}C$ record in a global context of atmospheric CO_2 and $\Delta^{14}C_{atmos}$ variability. This figure demonstrates that periods of atmospheric CO_2 increase align well with the $\Delta\Delta^{14}C$ excursions, including the smaller $\Delta\Delta^{14}C$ excursion at approximately 12 ka BP. These intervals are coeval with an accelerated decline in $\Delta^{14}C_{atmos}$ (grey dashed line), supporting the argument that the release of ^{14}C-depleted carbon to the atmosphere from the Antarctic was responsible for the atmospheric CO_2 increase during the deglaciation.

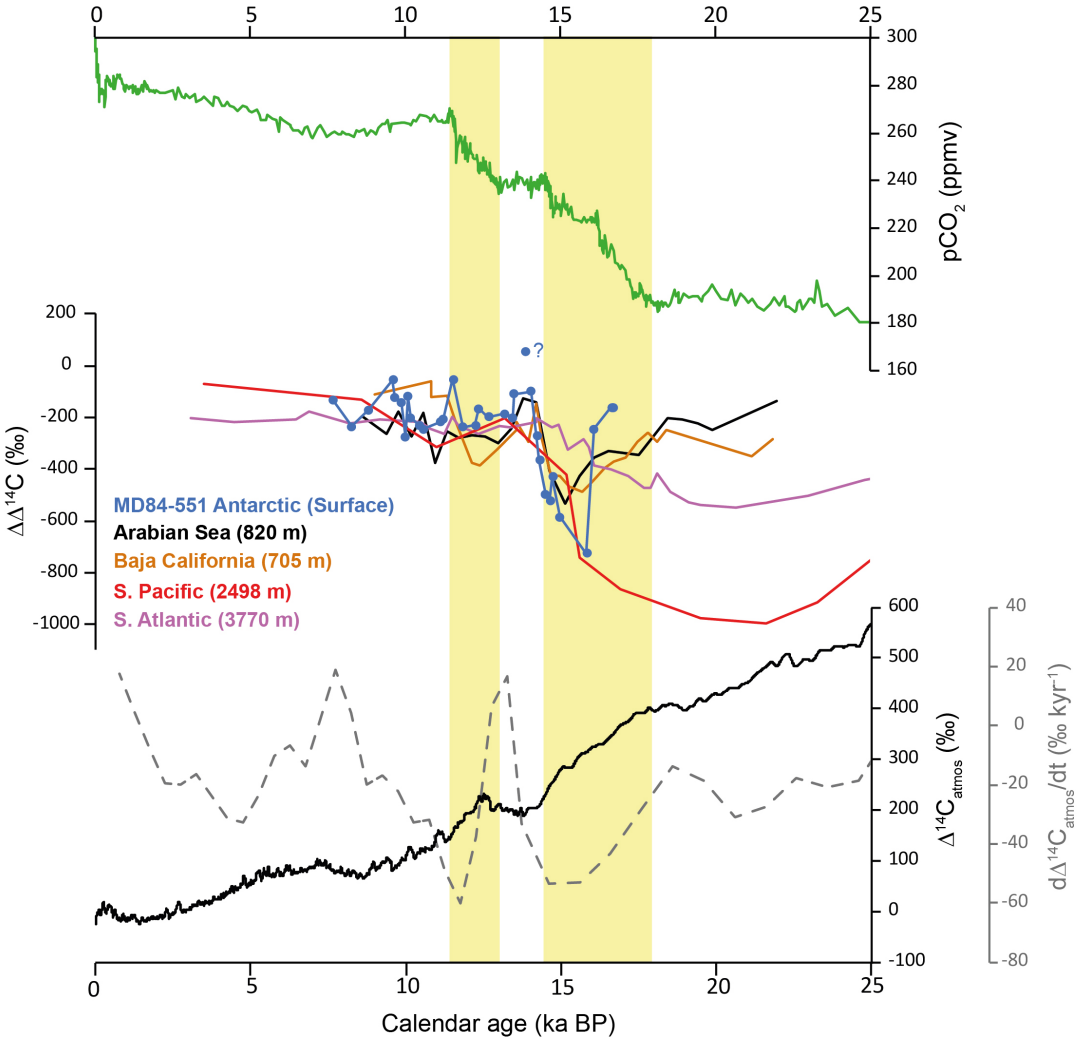

FIGURE 3.13: **Top**: Atmospheric pCO_2 record from EPICA Dome C (Monnin et al., 2001). **Middle**: Compilation of several $\Delta\Delta^{14}C$ records the Antarctic surface (MD84-551, this study), intermediate waters of the Arabian Sea (Bryan et al., 2010) and Baja California (Marchitto et al., 2007), deep waters of the south Pacific (Ronge et al., 2016) and south Atlantic (Skinner et al., 2010). **Bottom**: Atmospheric radiocarbon activity ($\Delta^{14}C_{atmos}$) from the IntCal13 curve (Reimer et al., 2013) (black solid line). 500 year smoothed first-order derivative of the IntCal13 curve (grey dashed line).

Also included in Figure 3.13 are reconstructions of $\Delta\Delta^{14}C$ from benthic foraminifera records. The $\Delta\Delta^{14}C$ of the South Atlantic record (Skinner et al., 2010) is more positive (younger) during the first interval of CO_2 increase (14.6 – 18 ka BP) than MD84-551, suggesting that the $\Delta\Delta^{14}C$ variability within MD84-551 was not entirely driven by ventilation of the deep Atlantic. Due to poor carbonate preservation, few radiocarbon records are available for the deep Pacific, Indian and Southern Oceans. Available $\Delta\Delta^{14}C$ records suggest the deep Pacific was extremely ^{14}C-depleted during the glacial period (Ronge et al., 2016; Sikes et

al., 2016), with $\Delta\Delta^{14}C$ records from UCDW depths that suggest comparable ^{14}C-depletion with MD84-551.

Anomalously ^{14}C-depleted benthic foraminifera records have also been observed at intermediate depths in low latitude regions such as Baja California (Marchitto et al., 2007) and the Arabian Sea (Bryan et al., 2010). These $\Delta\Delta^{14}C$ excursions within these records (Figure 3.13) exhibit a remarkable similarity in both magnitude and timing to the Antarctic surface record of MD84-551 constructed here. It has been suggested that the intermediate waters feeding these low latitude regions were derived from the Southern Ocean. Therefore, these low latitude $\Delta\Delta^{14}C$ excursions may be attributed to the supply of ^{14}C-depleted waters to Southern Ocean intermediate waters via the Antarctic. The preservation of the $\Delta\Delta^{14}C$ signal between the Antarctic surface and intermediate waters suggests that equilibration with the surface ocean and atmosphere may have been inhibited at this time. More extensive sea ice presence may have prevented efficient exchange (Jones et al., 2014) between the surface waters and atmosphere across the early deglaciation, allowing the upper Southern Ocean to remain ^{14}C-depleted and for the $\Delta\Delta^{14}C$ signal to be efficiently transferred to intermediate waters. The preservation of ^{14}C-depleted Southern Ocean surface waters is further supported by the coeval increase in the surface radiocarbon age noted in the Subantarctic Pacific (Siani et al., 2013), indicating that Ekman transport delivered the Antarctic surface $\Delta\Delta^{14}C$ signal to as far north as the SAZ.

3.3 Summary of the age models

The individual age control points for each of the cores is displayed in Tables 3.4 – 3.6.

Depth (cm)	Age (ka BP)	Description
35	7.667	^{14}C ($\Delta R = 700$ yrs)
75	9.655	^{14}C ($\Delta R = 700$ yrs)
120	11	Planktic $\delta^{18}O$
143	13.4	Planktic $\delta^{18}O$
155	14.5	Planktic $\delta^{18}O$
182	16.624	^{14}C ($\Delta R = 700$ yrs)
274	37.65	Magnetic susceptibility

TABLE 3.4: MD84-551 age control points

Depth (cm)	Age (ka BP)	Description
120	3.748	^{14}C (ΔR = 590 yrs)
170	5.922	^{14}C (ΔR = 590 yrs)
215	6.499	^{14}C (ΔR = 590 yrs)
255	8.787	^{14}C (ΔR = 590 yrs)
274	9.52	^{14}C (ΔR = 590 yrs)
295	9.975	^{14}C (ΔR = 590 yrs)
335	12.992	^{14}C (ΔR = 590 yrs)
353	14	Fe
550	21.8	Fe
803	37.65	Fe

TABLE 3.5: MD88-773 age control points

Depth (cm)	Age (ka BP)	Description
18	7.209	^{14}C (ΔR = 400 yrs)
26	8.489	^{14}C (ΔR = 400 yrs)
37	10.588	^{14}C (ΔR = 400 yrs)
44	12.571	^{14}C (ΔR = 400 yrs)
48	13.159	^{14}C (ΔR = 400 yrs)
89	21.8	Fe
260	37.65	Magnetic susceptibility

TABLE 3.6: MD88-772 age control points

The following figures present the stratigraphic data of the cores in their age models.

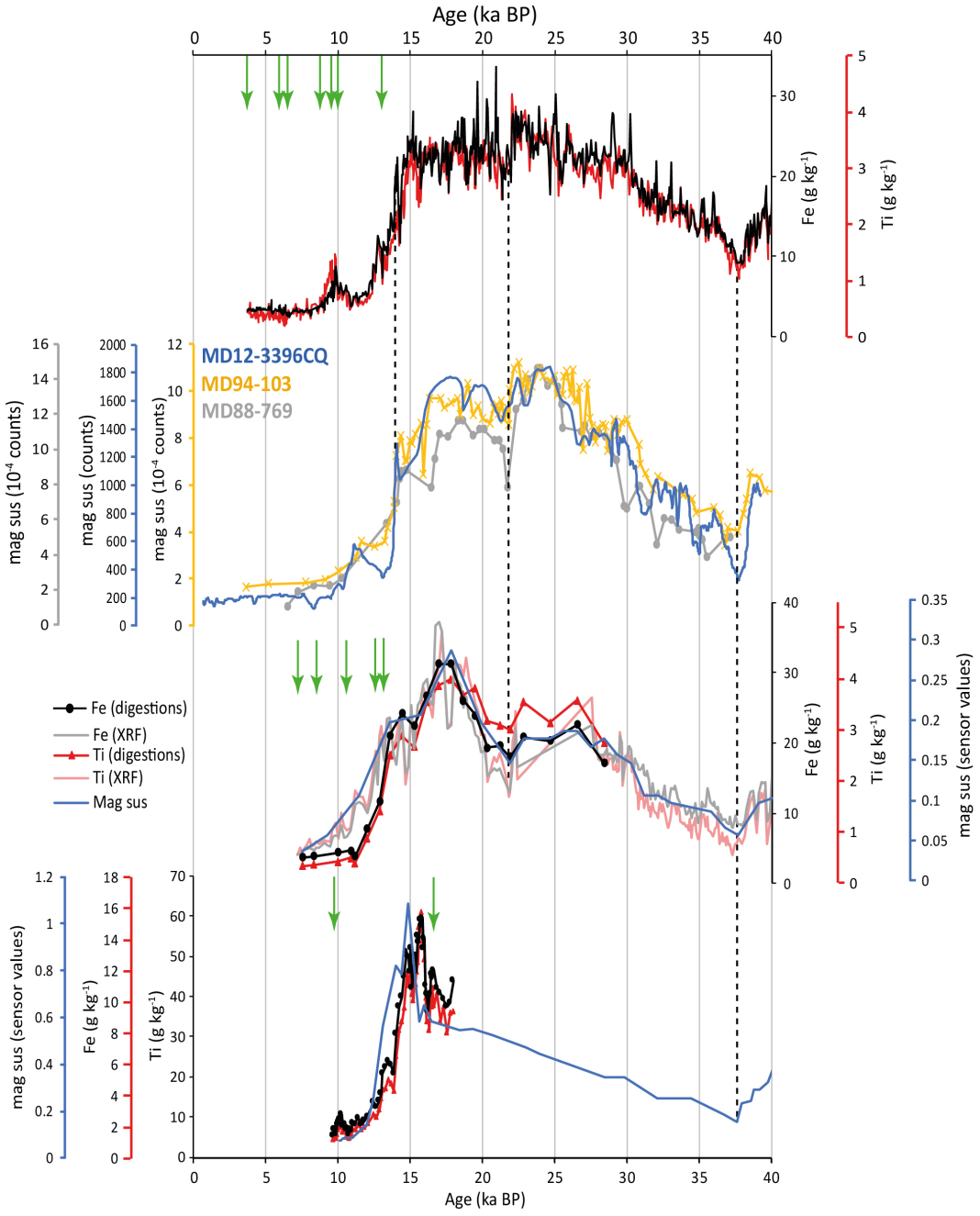

FIGURE 3.14: Lithogenic detritus records from the Indian sector cores placed on the final age models. Vertical dashed lines indicate the age control points (provided in Tables 3.4 – 3.6).

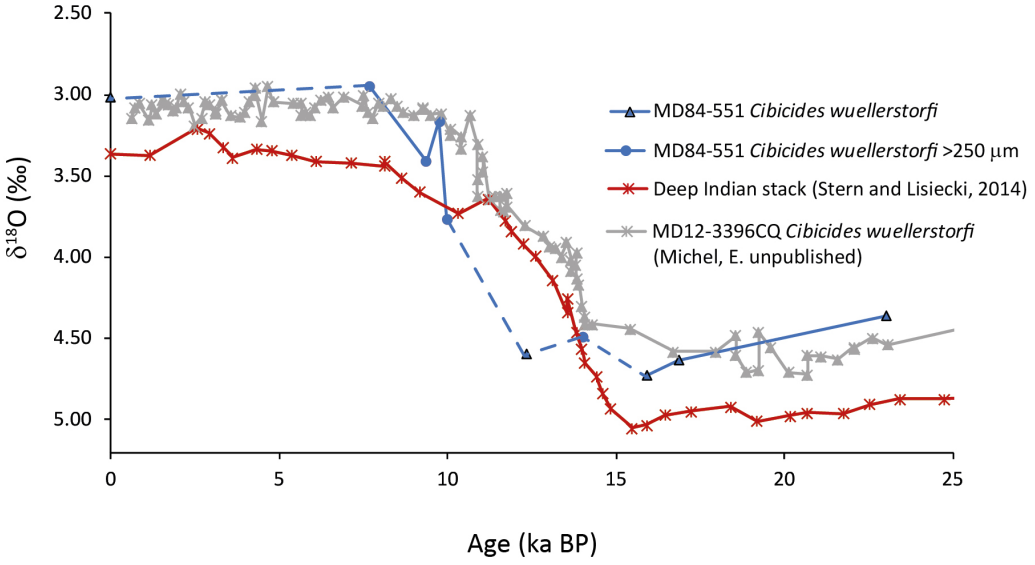

FIGURE 3.15: Benthic foraminifera (*Cibicides wuellerstorfi*) $\delta^{18}O$ record from MD84-551 placed on the final age model with benthic foraminifera $\delta^{18}O$ records from MD12-3396CQ and the Deep Indian stack (Stern and Lisiecki, 2014).

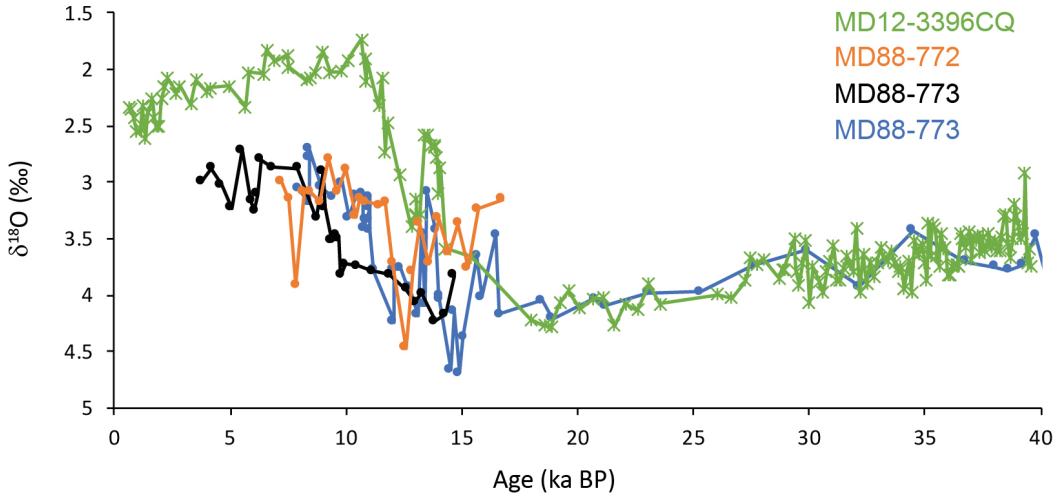

FIGURE 3.16: Planktic foraminifera $\delta^{18}O$ records from MD84-551 (*N. pachyderma*) (Labracherie et al., 1989), MD88-773 (*N. pachyderma*) (Francois et al., 1997), MD88-772 (*G. bulloides*) and MD12-3396CQ (*N. pachyderma*).

References

Anderson , R. F., Ali , S., Bradtmiller , L. I., Nielsen , S. H. H., Fleisher , M. Q., Anderson , B. E., and Burckle , L. H. Wind-driven upwelling in the Southern Ocean and the deglacial rise in atmospheric CO2. *Science (New York, N.Y.)*, 323(5920):1443–1448, mar 2009. doi: 10.1126/science.1167441.

Anderson , R., Barker , S., Fleisher , M. Q., Gesonde , R., Goldstein , S. L., Kuhn , G., Pahnke , K., and Sachs , J. P. Biological response to millennial variability of dust and nutrient supply in the Subantarctic South Atlantic Ocean. *Philosophical Transactions of the Royal Society A: Mathematical, Physical and Engineering Sciences*, 372, 2014.

Bard , E. Correction of accelerator mass spectrometry 14C ages measured in planktonic foraminifera: Paleoceanographic implications. *Paleoceanography*, 3(6):635–645, 1988.

Bareille , G., Grousset , F. E., Labracherie , M., Labeyrie , L. D., and Petit , J. Origin of detrital fluxes in the southeast Indian Ocean during the last climatic cycles. *Paleoceanography*, 9(6):799–819, 1994.

Belkin , I. M. and Gordon , A. L. Southern Ocean fronts from the Greenwich meridian to Tasmania. *Journal of Geophysical Research*, 101(C2):3675, 1996. doi: 10.1029/95JC02750.

Bryan , S. P., Marchitto , T. M., and Lehman , S. J. The release of 14C-depleted carbon from the deep ocean during the last deglaciation: Evidence from the Arabian Sea. *Earth and Planetary Science Letters*, 298(1-2):244–254, sep 2010. doi: 10.1016/j.epsl.2010.08.025.

Burckle , L. H. and Cooke , D. W. Late Pleistocene Eucampia antarctica abundance stratigraphy in the Atlantic sector of the Southern Ocean. *Micropaleontology*, 29(1):6–10, 1983.

Burke , A. and Robinson , L. F. The Southern Ocean's role in carbon exchange during the last deglaciation. *Science (New York, N.Y.)*, 335(6068):557–61, feb 2012. doi: 10.1126/science.1208163.

Crosta , X. and Shemesh , A. Reconciling down core anticorrelation of diatom carbon and nitrogen isotopic ratios from the Southern Ocean. *Paleoceanography*, 17(1):1–8, 2002.

Du , J., Haley , B. A., Mix , A. C., Walczak , M. H., and Praetorius , S. K. Flushing of the deep Pacific Ocean and the deglacial rise of atmospheric CO2 concentrations. *Nature Geoscience*, 2018. doi: 10.1038/s41561-018-0205-6.

Dutkiewicz , A., O'Callaghan , S., and Müller , R. Controls on the distribution of deep-sea sediments. *Geochemistry, Geophysics, Geosystems*, 17:3075–3098, 2016. doi: 10.1002/2016GC006428.Received.

Francois , R., Altabet , M. A., Yu , E.-f., Sigman , D. M., Bacon , M. P., Frank , M., Bohrmann , G., Bareille , G., and Labeyrie , L. D. Contribution of Southern Ocean surface-water stratification to low atmospheric CO 2 concentrations during the last glacial period. *Nature*, 389:929–935, 1997.

Hall , B. L., Henderson , G. M., Baroni , C., and Kellogg , T. B. Constant Holocene Southern-Ocean C reservoir ages and ice-shelf fl ow rates. *Earth and Planetary Science Letters*, 296(1-2):115–123, 2010. doi: 10.1016/j.epsl.2010.04.054.

Jones , D. C., Ito , T., Takano , Y., and Hsu , W.-c. Spatial and seasonal variability of the air-sea equilibration timescale of carbon dioxide. *Global Biogeochem. Cycles*, 28:1163–1178, 2014. doi: 10.1002/2014GB004813.Received.

Key , R. M., Kozyr , A., Sabine , C. L., Lee , K., Wanninkhof , R., Bullister , J. L., Feely , R. A., Millero , F. J., Mordy , C., and Peng , T. H. A global ocean carbon climatology: Results from Global Data Analysis Project (GLODAP). *Global Biogeochemical Cycles*, 18(4):1–23, 2004. doi: 10.1029/2004GB002247.

Klinck , J. M. and Smith , A. Effect of wind changes during the last glacial maximum on the circulation in the Southern Ocean. *Paleoceanography*, 8(4):427–433, 1993.

Labracherie , M., Labeyrie , L., Duprat , J., Bard , E., Arnold , M., Pichon , J.-J., and Duplessy , J. The last deglaciation in the Southern Ocean. *Paleoceanography*, 4(6):629–638, 1989.

Lynch-Stieglitz , J., Ito , T., and Michel , E. Antarctic density stratification and the strength of the

circumpolar current during the Last Glacial Maximum. *Paleoceanography*, 31(5):539–552, 2016. doi: 10.1002/2015PA002915.

Marchitto , T. M., Lehman , S. J., Ortiz , J. D., Flückiger , J., and van Geen , A. Marine radiocarbon evidence for the mechanism of deglacial atmospheric CO2 rise. *Science (New York, N.Y.)*, 316(5830): 1456–9, jun 2007. doi: 10.1126/science.1138679.

Mazaud , A., Kissel , C., Laj , C., Sicre , M. A., Michel , E., and Turon , J. L. Variations of the ACC-CDW during MIS3 traced by magnetic grain deposition in midlatitude South Indian Ocean cores: Connections with the northern hemisphere and with central Antarctica. *Geochemistry, Geophysics, Geosystems*, 8(5), 2007. doi: 10.1029/2006GC001532.

Mazaud , A., Sicre , M. A., Ezat , U., Pichon , J. J., Duprat , J., Laj , C., Kissel , C., Beaufort , L., Michel , E., and Turon , J. L. Geomagnetic-assisted stratigraphy and sea surface temperature changes in core MD94-103 (Southern Indian Ocean): Possible implications for North-South climatic relationships around H4. *Earth and Planetary Science Letters*, 201(1):159–170, 2002. doi: 10.1016/S0012-821X(02)00662-3.

McCave , I. N., Crowhurst , S. J., Kuhn , G., Hillenbrand , C. D., and Meredith , M. P. Minimal change in antarctic circumpolar current flow speed between the last glacial and holocene. *Nature Geoscience*, 7(2): 113–116, 2014. doi: 10.1038/ngeo2037.

Monnin , E., Indermühle , a., Dällenbach , a., Flückiger , J., Stauffer , B., Stocker , T. F., Raynaud , D., and Barnola , J. M. Atmospheric CO2 concentrations over the last glacial termination. *Science (New York, N.Y.)*, 291(5501):112–4, jan 2001. doi: 10.1126/science.291.5501.112.

Orsi , A., Whitworth , T., and Nowlin , W. On the meridional extent and fronts of the Antarctic Circumpolar Current. *Deep Sea Research Part I: Oceanographic Research Papers*, 42(5):641–673, 1995.

Pichon , J.-J., Labeyrie , L. D., Bareille , G., Labracherie , M., Duprat , J., and Jouzel , J. Surface water temperature changes in the high latitudes of the Southern Hemisphere. *Paleoceanography*, 7(3):289–318, 1992.

Pugh , R. S., McCave , I. N., Hillenbrand , C. D., and Kuhn , G. Circum-Antarctic age modelling of Quaternary marine cores under the Antarctic Circumpolar Current: Ice-core dust-magnetic correlation. *Earth and Planetary Science Letters*, 284(1-2):113–123, 2009. doi: 10.1016/j.epsl.2009.04.016.

Reimer , P., Bard , E., and Bayliss , A. IntCal13 and Marine13 radiocarbon age calibration curves 0–50,000 years cal BP. *Radiocarbon*, 55(4), 2013.

Robinson , R. S., Brzezinski , M. a., Beucher , C. P., Horn , M. G. S., and Bedsole , P. The changing roles of iron and vertical mixing in regulating nitrogen and silicon cycling in the Southern Ocean over the last glacial cycle. *Paleoceanography*, pages 1179–1195, 2014. doi: 10.1002/2014PA002686.Received.

Ronge , T. A., Tiedemann , R., Lamy , F., Köhler , P., Alloway , B. V., De Pol-Holz , R., Pahnke , K., Southon , J., and Wacker , L. Radiocarbon constraints on the extent and evolution of the South Pacific glacial carbon pool. *Nature Communications*, 7(May):1–12, 2016. doi: 10.1038/ncomms11487.

Schlitzer , R. Interactive analysis and visualization of geoscience data with Ocean Data View. *Computers & Geosciences*, 28(10):1211–1218, dec 2002. doi: 10.1016/S0098-3004(02)00040-7.

Siani , G., Michel , E., De Pol-Holz , R., Devries , T., Lamy , F., Carel , M., Isguder , G., Dewilde , F., and Lourantou , A. Carbon isotope records reveal precise timing of enhanced Southern Ocean upwelling during the last deglaciation. *Nature communications*, 4(May):2758, jan 2013. doi: 10.1038/ncomms3758.

Sikes , E. L., Cook , M. S., and Guilderson , T. P. Reduced deep ocean ventilation in the Southern Pacific

Ocean during the last glaciation persisted into the deglaciation. *Earth and Planetary Science Letters*, 438: 130–138, 2016. doi: 10.1016/j.epsl.2015.12.039.

Sikes , E. L., Samson , C. R., Guilderson , T. P., and Howard , W. R. Old radiocarbon ages in the southwest Pacific Ocean during the last glacial period and deglaciation. *Nature*, 405(6786):555–559, 2000. doi: 10.1038/35014581.

Skinner , L. C., Fallon , S., Waelbroeck , C., Michel , E., and Barker , S. Ventilation of the deep Southern Ocean and deglacial CO2 rise. *Science*, 328(5982):1147–51, may 2010. doi: 10.1126/science.1183627.

Stern , J. V. and Lisiecki , L. E. Termination 1 timing in radiocarbon-dated regional benthic δ18O stacks. *Paleoceanography*, 29(12):1127–1142, 2014. doi: 10.1002/2014PA002700.

Stuiver , M. and Polach , H. Discussion; reporting of C-14 data. *Radiocarbon*, 19(3):355–363, 1977.

Stuiver , M. and Reimer , P. J. Extended 14C Data Base and Revised CALIB 3.0 14C Age Calibration Program. *Radiocarbon*, 35(01):215–230, 1993. doi: 10.1017/S0033822200013904.

Stuiver , M., Reimer , P. J., and Reimer , R. W. CALIBR 7.1 [WWW program], 2018.

Zhao , N., Marchal , O., Keigwin , L., Amrhein , D., and Gebbie , G. A Synthesis of Deglacial Deep-Sea Radiocarbon Records and Their (In)Consistency With Modern Ocean Ventilation. *Paleoceanography and Paleoclimatology*, 33(2):128–151, 2018. doi: 10.1002/2017PA003174.

4

Controls on primary production

4.1 Introduction

Primary production and biological export are integral components of the biological pump, helping to maintain a vertical DIC gradient in the oceans and modulate atmospheric CO_2 (Broecker, 1982). Primary production is the rate of organic carbon production in the euphotic zone and is often tied to chlorophyll concentrations in the surface ocean. Much of the organic carbon produced is recycled within the mixed layer (Martin et al., 1987) and therefore has no impact on the biological pump. The fraction of sinking organic carbon that survives mixed-layer recycling is known as export production (or biological export).

Within the Southern Ocean, annual primary production and the seasonal evolution of phytoplankton biomass exhibit 'bottom-up' controls from light and nutrients (including micro-nutrients such as Fe) (Sverdrup, 1953; Thomalla et al., 2011). Consequently, changes in primary production through time reflected in primary productivity proxies are of a release from or restraint by certain limiting conditions that may ultimately dictate the strength of

the biological pump in the Southern Ocean. Here we will explore the factors that control primary productivity and biological export in the Southern Ocean over glacial-interglacial cycles and discuss the importance of these changing conditions on the biological pump.

The hydrography of the Southern Ocean is dominated by the Antarctic Circumpolar Current (ACC) which acts to longitudinally homogenise tracers supplied to the surface ocean. As a result, there are meridional patterns in the primary productivity regime that are reflected across the whole Southern Ocean. The Southern Ocean is often divided into broad ecological regions (e.g. marginal ice zone, transitional zone, seasonally ice-free zone, permanently open ocean zone) that consider the ecology rather than the hydrography and differ considerably between studies (Treguer and Jacques, 1992; Moore and Abbott, 2000; Thomalla et al., 2011). However, the focus in this work is how the changes in hydrography influence the cycling of nutrients and carbon in the Southern Ocean. Hence, to avoid confusion the numerous additional acronyms used to describe the ecological regions will not be used here; instead the front-delimited zonation (e.g. AZ, PFZ and SAZ) will continue to be used.

Within the AZ, deep upwelling supplies ample nutrients into the euphotic zone, but with a stoichiometric deficiency in iron (Boyd et al., 2012). As a result, primary production in the AZ that is not limited by light due to sea ice cover is limited by the lack of dissolved iron (Martin et al., 1990; Coale et al., 2004). This produces longitudinal gradients in primary productivity down-wind/-current from terrestrial iron sources such as continental shelves and islands (Sullivan et al., 1993). Using satellite remote-sensing data, Moore and Abbott (2000) identified a number of such naturally iron-fertilized regions including downstream of the Kerguelen Islands (50°E – 70°E), downstream of the Argentinian coastline and within the coastal waters of Antarctica.

An important feature with respect to Southern Ocean primary productivity and nutrient cycling is the opal belt (Burckle and Cirilli, 1987; Geibert et al., 2005), which is situated in the northern latitudes of the AZ . Here the phytoplankton community is dominated by large diatoms (Landry et al., 2002) that are highly silicifying in response to iron limitation (Brzezinski et al., 2003). Consequently, mean annual biogenic silica production, export flux and burial in the opal belt region are some of the highest observed in the global ocean (Nelson et al., 1995; Treguer and De le Roche, 2013). Sediment trap (Honjo et al., 2000; Trull et al., 2001; Nelson et al., 2002) and core-top studies (Geibert et al., 2005; Chase et al., 2015) show peak opal fluxes are situated just south of the polar front with a decline

northward corresponding to the decline in mixed layer DSi concentrations. Due to the iron-mediated change in diatom Si:C ratios this region (Chapter 2; Brzezinski et al., 2003), the high opal fluxes do not proportionately translate to high particulate organic carbon (POC) fluxes (Honjo et al., 2000; Nelson et al., 2002) and high chlorophyll concentrations (Moore et al., 2000). Non-silicifying algae species, particularly haptophytes (e.g. *Emiliana huxleyi* and *Phaeocystis antarctica*) outcompete diatoms to the north of the opal belt due to the low DSi concentrations (Iida and Odate et al., 2014).

North of the opal belt into the Subantarctic annual mean chlorophyll concentrations rise to a maximum within the SAZ before rapidly declining within the subtropical gyres (Moore and Abbott, 2000). However, annual POC fluxes have been found to decline through the Subantarctic (Honjo et al., 2000; Trull et al., 2001). This poor relationship between chlorophyll concentrations and annual POC fluxes has been attributed to a number of factors including plankton community structure and seasonality (Maiti et al., 2013). Although the factors controlling the relationship between primary production and POC export are still being explored (Le Moigne et al., 2015), it is apparent that diatoms control POC export in the AZ and PFZ (Honjo et al., 2000). Due to the blooming nature of diatoms in the AZ and PFZ, a higher proportion of the phytoplankton evade grazing pressure (Moore et al., 2000) and tend to form fast sinking aggregates (Boyd and Newton, 1999; Laurenceau-Cornec et al., 2015) that produce higher POC export fluxes than expected given the low overall chlorophyll and POC production in the surface waters (Jin et al., 2006).

Here two proxies (%opal and Ba_{xs}) will be used to discuss changes in the 'bottom-up' controls on primary production. %opal is a measure of the biogenic silica content of the sediment and can be related to the flux of diatomaceous matter. It should be stressed that downcore variations in %opal (and estimations of opal flux) may not be directly related to variations in POC flux due to the iron-mediated changes in Si:C ratio in diatoms (Hutchins and Bruland, 1998; Takeda, 1998; Pichevin et al., 2009). However, %opal changes are, theoretically, directly related to biogenic silica export from the surface ocean and can therefore provide a valuable insight into the cycling of silicon through time. Sedimentary Ba is susceptible to dissolution under low oxygen and opal is not hence collective use of these proxies are preferable.

Ba_{xs} is a measure of the terrigenous-corrected barite content of sediments and can be used as a proxy for POC flux that is independent of silica (Dymond et al., 1992; Francois et al.,

1995). Barite formation has been found to occur in the barium-saturated micro-environments of decaying plankton detritus (Dehairs et al., 1980; Ganeshram et al., 2003). Subsequently, barium flux through the water column and its burial within sediments has been shown to correlate well with export production (Dymond et al., 1992).

4.2 Methods

Weight percent opal (%opal) contents of sediment samples were determined by the heteropoly blue method adapted from Mortlock and Froelich (1989, see Methods for details. Opal preservation has been found to not be an important factor in controlling the spatial variability in opal fluxes in the global oceans (Pondaven et al., 2000). In addition, changes in preservation do not appear to be important drivers of opal flux variability through time in the Southern Ocean (Francois et al., 1997; Dezileau et al., 2003).

The barium contents of sediment samples were determined via ICP-OES (MD88-773 and MD88-772) and ICP-MS (MD84-551) after acid digestions, see Methods for details. An important factor controlling the preservation of biogenic barium in sediments is the redox conditions. The dissolution of biogenic barium in suboxic sediments has been attributed to the use of the sulphate within barite during bacterial sulphate reduction (McManus et al., 1998). Authigenic uranium accumulation has been found to correlate well with sulphate reduction and hence will be used where possible to qualitatively assess changes in barite preservation. Detrital additions of barium were corrected for using the average Ba/Ti ratio of Kerguelen basalts (Ba/Ti = 0.0128, Gautier et al., 1990), see Methods for a further discussion on this correction.

Syndepositional redistribution of sediments can significantly bias accumulation rate records, particularly in the strong bottom current regime of the Southern Ocean (Francois et al., 1993; Dezileau et al., 2000). Where possible, 230Th-normalisation (Francois et al., 2004) was applied to correct for the waxing and winnowing of sediments by bottom currents. 230Th-normalisation data is unavailable for MD88-772. MAR reconstructions interpreted from dry bulk density and sedimentation rate estimates may provide an indication of whether the changes in the bulk constituents are driven by changes in export production or preservation/dilution. However, unlike Th-normalised fluxes, MAR estimates do not account for changes in syndepositional sediment redistribution and so cannot be used quantitatively

in the turbulent Southern Ocean. Nevertheless, in a study comparing opal fluxes across the eastern Indian sector, Dezileau et al (2003) found that although MAR cannot be used quantitatively, overall the glacial-interglacial patterns observed in MAR records remained largely the same after Th-normalisation. Therefore, MAR will be used as a qualitative indicator of opal flux variability.

4.3 Results

The Ba_{xs} and opal data (fluxes and bulk sediment content) are presented in Figure 4.1. The Holocene sections of the three cores show a classical Antarctic - Subantarctic divide in %opal content with greater %opal within the two southern cores (MD84-551 = 70 – 80%, MD88-773 = 75 – 92%) than the northern core (MD88-772 = 17 – 40 %). Due to the nature of piston coring, the Holocene sections from each of the three cores are incomplete. However, the limited Holocene data that is available from these cores agrees well with the Holocene sections from nearby cores (Bareille et al., 1998; Dezileau et al., 2003).

Holocene Th-normalised opal fluxes in MD88-773 (0.35 – 1 g cm^{-2} kyr^{-1}) are in good agreement with core-tops and Holocene sections of other cores situated close to the PF, which have an average opal accumulation of 0.38 $\pm$ 0.32 ($\pm$ 1 σ) g cm^{-2} ka^{-1} (Chase et al., 2015). On the other hand, the Holocene opal flux in MD84-551 (2 g cm^{-2} ka^{-1}) is close to the highest modern open ocean opal accumulation rate recorded in the Southern Ocean. Similar opal fluxes ($\sim$2 g cm^{-2} ka^{-1}) were recorded in the nearby core, MD84-552 (Francois et al., 1997), suggesting the region south of the Kerguelen Islands is subject to very high opal export.

Unlike %opal, the Ba_{xs} content within the Holocene sections of each of the three cores was very similar (1 – 1.5 g/kg). Compilations of Southern Ocean Holocene and surface sediments show that sediments beneath the permanently ice-free ocean south of the STF have a typical Ba_{xs} content of 0.5 – 2 g kg^{-1} (Nurnberg et al., 1997; Fagel et al., 2002), in agreement with the data presented here. The low variability of Ba_{xs} content within Southern Ocean sediments in comparison to %opal appears to reflect the high silica export within the AZ compared to the Subantarctic (Honjo et al., 2000). The Th-noramlised fluxes of Ba_{xs} in MD88-773 and MD84-551 produce a similar pattern to that of opal, with greater Ba_{xs} fluxes in MD84-551 than in MD88-773.

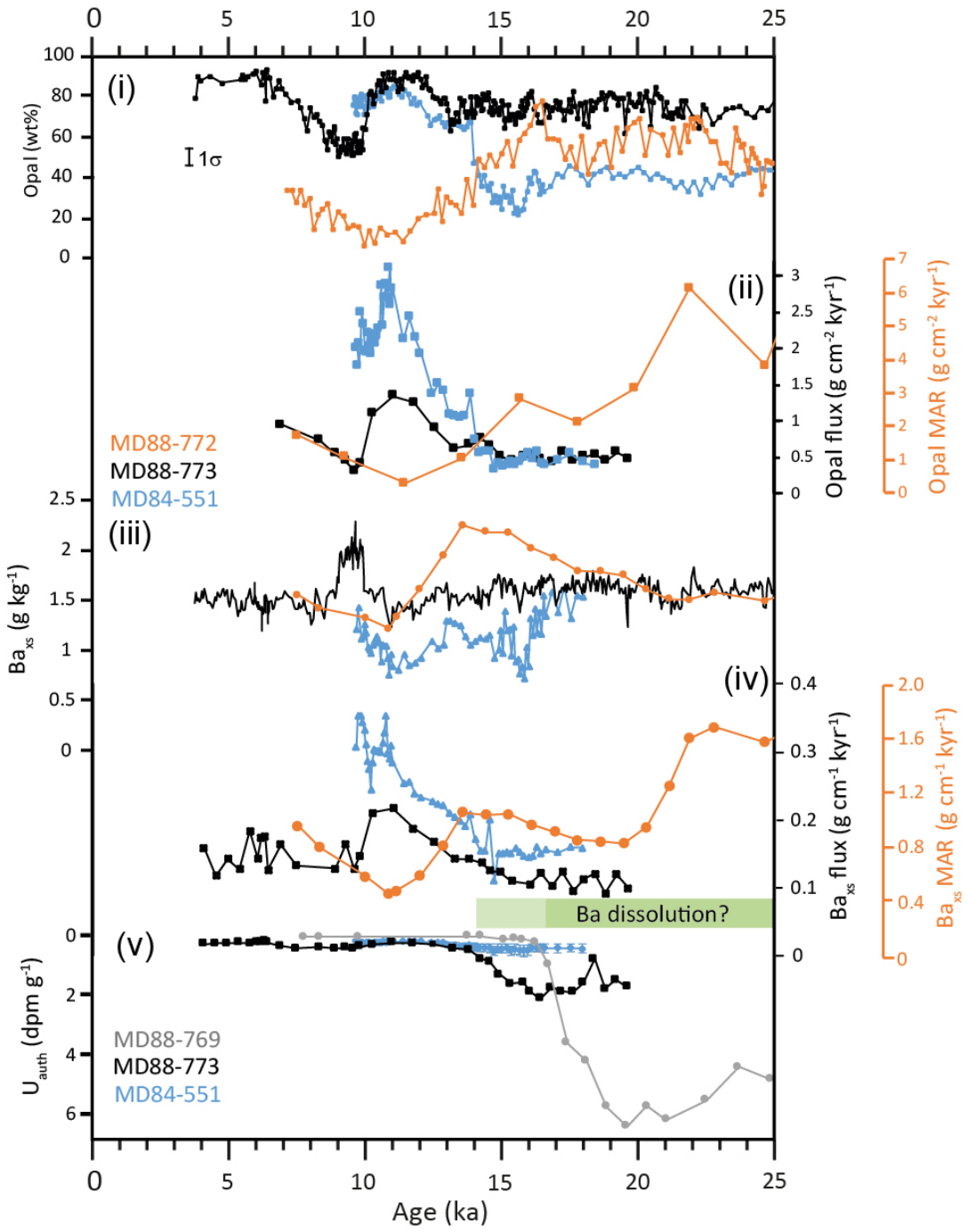

FIGURE 4.1: Primary productivity proxy data from the three Indian sector cores. **(i)** %opal from all records. **(ii)** Th-normalised opal flux from MD84-551 and MD88-773 (Th-normalisation data from Francois et al (1997). With opal mass accumulation rates from MD88-772. **(iii)** Ba_{xs} data from the three cores. **(iv)** Th-normalised Ba_{xs} fluxes from MD84-551 and MD88-773 (Th-normalisation data from Francois et al (1997). With Ba_{xs} mass accumulation rates from MD88-772. **(v)** U_{auth} data from MD88-769 (Rosenthal et al., 1995), MD88-773 (Francois et al., 1997) and MD84-551.

Between 18 and 25 ka BP there is little variability in either %opal or Ba_{xs} in any of the cores compared to the deglacial transition that follows. The overall glacial – interglacial

change in %opal and Th-normalised opal flux between the cores is reflective of the archetypal Antarctic - Subantarctic dipole (e.g. Charles et al., 1991; Mortlock et al., 1991), whereby the glacial-interglacial variability in opal flux patterns in the Southern Ocean are characterised by lower opal fluxes to Antarctic sediments and greater opal fluxes to Subantarctic sediments during glacial periods with the reverse trend during interglacials. MD84-551 displays the most marked reduction in opal flux and %opal at the glacial period relative to the Holocene, with the intermediate record (MD88-773) exhibiting only a small reduction in both %opal and opal flux. The %opal and opal MAR are greater during the glacial period in MD88-772 compared to the Holocene in agreement with other Subantarctic records (Kumar et al., 1995; Chase et al., 2003). North of MD88-772, both MD88-769 and MD88-770 exhibit an increase in %opal and Th-normalised opal flux during the glacial relative to the Holocene. Maximum LGM opal fluxes observed in MD88-769 and MD88-770 are 0.2 g cm^{-2} ka^{-1} and 0.56 g cm^{-2} ka^{-1}, respectively. These are lower than the average LGM opal flux in MD88-773 (0.64 g cm^{-2} ka^{-1}) and comparable to that of MD84-551 (0.43 g cm^{-2} ka^{-1}), suggesting that the opal belt was situated northwards during the last glacial period, but its core remained closer to MD88-773 than the SAZ cores, MD88-769 and MD88-770.

As during the Holocene, the glacial Ba_{xs} contents of the three cores (Figure 4.1iii) appear to be very similar, contrasting against the large differences in %opal. For the Holocene section, the decoupling of Ba_{xs} and %opal was attributed to high silicification of particles in the AZ. However, for the LGM suboxic conditions in the bottom waters may have led to poor preservation of biogenic barium in sediments (McManus et al., 1998). Authigenic uranium (a proxy for suboxia) data are available for MD88-773, MD84-551 and nearby SAZ core MD88-769 (Rosenthal et al., 1995) (Figure 4.1v). Glacial low oxygen conditions are most apparent in MD88-773 and MD88-769, with the cores exhibiting a Holocene-LGM Uauth enrichment by ~1.8 dpm/g and 6 dpm/g, respectively. No authigenic uranium data is available for MD88-772, however MD88-769 resides at a similar depth (3420 m) to MD88-772 (3240 m) suggesting that the waters at that depth were deoxygenated relative to the Holocene. Hence, barite dissolution may have occurred in the LGM sections of both MD88-773 and MD88-772. Indeed, the poor correspondence between %opal and Ba_{xs} prior to 14 ka BP in MD88-772 suggests suboxic conditions may have reduced the barite content at the LGM.

Suboxia is less apparent in the LGM section of MD84-551, which exhibits only a modest

increase in authigenic uranium content across the deglaciation. Further, the lower sedimentation rate of this core during this period would permit more diffusive oxygenation of the sediments, favouring better barite preservation (Francois et al., 1997). Nevertheless, a decoupling of opal from Ba_{xs} is evident in core MD84-551, which exhibits little change in Ba_{xs} content between the LGM and Holocene despite a large change in the opal content. This decoupling is manifested in the Th-normalised flux changes between the LGM and Holocene, which for opal increases from 0.45 g cm^{-2} ka^{-1} to 2.12 g cm^{-2} ka^{-1} (increase by a factor of 4.7) and for Ba_{xs} increases from 0.16 g cm^{-1} ka^{-1} to 0.31 g cm^{-1} ka^{-1} (increase by a factor of 1.9). The lower Ba_{xs} flux than expected given the opal flux within the well-oxygenated Holocene sediments argues against barite preservation as the primary cause. Instead, the data suggest a greater silicification of particles during the Holocene (higher Si:C ratio), which could have been a result of iron stressed diatom communities (e.g. Brzezinski et al., 2002; Pichevin et al., 2009).

Across the deglacial transition the %opal and opal Th-normalised flux/MAR records of MD88-772 and MD84-551 display a very apparent anti-phased relationship, with %opal and opal MAR decreasing in MD88-772 and while they increase in MD84-551 between the early deglaciation (15 – 16 ka BP) to the end of the deglaciation (10 – 11 ka BP). This anti-phasing is less apparent in the Ba_{xs} records, with MD88-772 displaying a broad peak in Ba_{xs} content across much of the early deglaciation before declining to a minimum at 11 ka BP. The opal and Ba_{xs} flux records from MD88-773 more closely correspond to MD84-551, showing a general increase across the deglaciation. This deglacial increase is not as apparent in the %opal and Ba_{xs} content data from MD88-773, suggesting an influence of dilution by increased carbonate preservation across the interval.

Figure 4.2 provides the opal and Ba_{xs} flux data with both regional and local reconstructions of sea ice and dust flux to the Indian sector of the Southern Ocean. The local sea ice presence data is derived from diatom transfer functions applied to diatom counts in MD84-551 and MD88-773. The local dust flux proxy used is from N-alkane fluxes to MD94-103 (45°35'S; 86°31'E) (Sicre et al., 2006), located in the SAZ between MD84-551 and MD88-772. Regional sea ice coverage is reconstructed from EPICA Dome C sea salt Na (ssNa) fluxes (Wolff et al., 2006), which are indicative of sea ice extent in the Indian sector of the Southern Ocean. Finally, regional dust fluxes are reconstructed from dust fluxes to EPICA Dome C (Lambert et al., 2012).

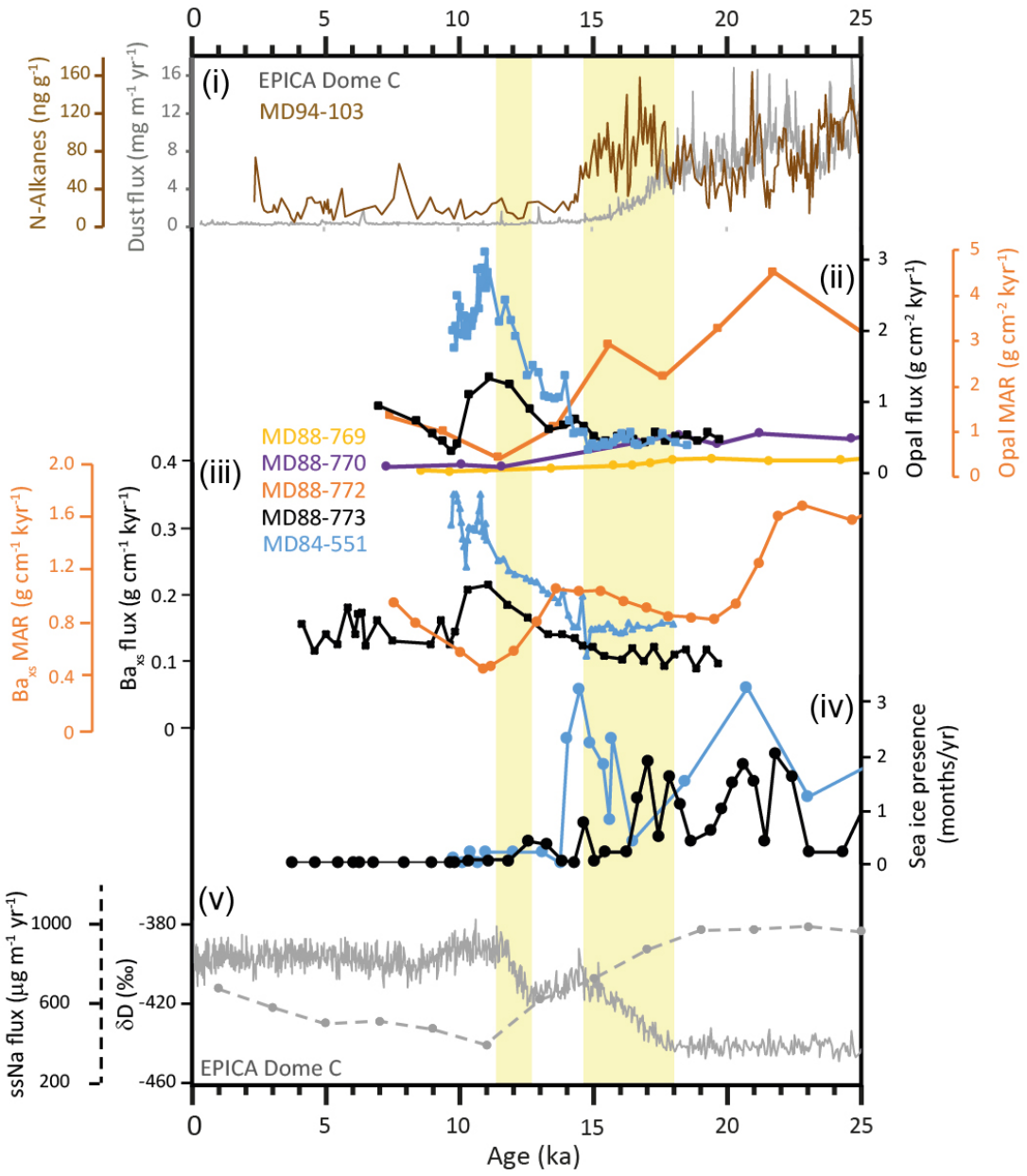

FIGURE 4.2: Deglacial productivity changes within the Indian sector along with proxies for their potential drivers. **(i)** Antarctic dust flux to EPICA Dome C (Lambert et al., 2012) and the N-alkane content of Indian sector core MD94-103 indicative of the input of terrestrial material and terrestrial aridity (Sicre et al., 2006). **(ii)** Th-normalised opal fluxes from cores across the Indian sector (MD88-769 and MD88-770: Dezileau et al., 2003) with opal MAR from MD88-772. **(iii)** Th-normalised Ba_{xs} fluxes from MD84-551 and MD88-773 (Th-normalisation data from Francois et al (1997). With Ba_{xs} mass accumulation rates from MD88-772. **(iv)** Diatom-based sea ice presence reconstructions from MD84-551 and MD88-773 (Crosta, X., unpublished). **(v)** Antarctic temperature (Parrenin et al., 2013) and sea ice extent (Wolff et al., 2006) proxies from EPICA Dome C.

The disparity between the EPICA Dome C dust flux and the MD94-103 n-alkane flux records has been attributed to different responses to terrestrial aridity by the two proxies. In this case,

increased aridity tends to reduce vegetation cover and thus n-alkane production, whereas it tends to increase dust transport (Sicre et al., 2006).

There is little correspondence between the productivity proxies from the three sediment cores and the evolution of dust flux across the deglacial transition. The transition from LGM to Holocene dust fluxes to EPICA Dome C occurs from 18 ka BP to 14.7 ka BP, approximately encompassing the first interval of Antarctic temperature rise. This is earlier than the productivity transitions (rise in opal and Ba_{xs} in MD84-551 and MD88-773, and vice versa for MD88-772) occurring within the three records, which begin between 14 ka BP and 16 ka BP and ends at approximately 11 – 11.5 ka BP within the three cores.

On the other hand, the regional sea ice reconstruction interpreted from ssNa accumulation within the EPICA Dome C ice core correlates well with the productivity transition with a minimum in sea ice extent occurring during the minimum in opal MAR in MD88-772 and maximum in opal flux in both MD88-773 and MD84-551 at 11 ka BP. This is followed by a gradual increase in ssNa flux through the Holocene, corresponding well with the increase in opal MAR in MD88-772 and the decrease in opal flux in MD84-551. Sea ice presence data from diatom counts in MD84-551 and MD88-773 do not correspond as well to the productivity data as the EPICA Dome C reconstructions. However, the initiation of the deglacial changes in the two productivity proxies coincides well with the abrupt reduction of sea ice presence in MD84-551 ($\sim$14 ka BP).

4.4 Discussion

Figure 4.3 provides a compilation of average Holocene and LGM opal fluxes from the different sectors of the Southern Ocean (adapted from Chase et al., 2003 and Diekmann, 2007) with the fluxes from MD84-551 and MD88-773 included. For the Holocene sections the estimated number of ice-free months ($<$ 15 % cover, Parkinson, 2002) and surface water (50 m depth) silicic acid concentrations (WOA 13, Garcia et al., 2013) are also given. The peak opal fluxes (i.e. the core of the opal belt) in each sector lie 2 °south of the PF, close to the edge of the winter sea ice maximum. It is suggested that sea ice imposes light limitation on diatom production south of this opal flux maximum (Chase et al., 2015).

The silicic acid concentration gradient is high within the region of high opal flux, indicating intensive drawdown. The northward decrease in opal fluxes in the Subantarctic flattens

by ∼10 uM, indicating the northern extent of the opal belt is governed by silicic acid concentrations.

As illustrated in Figure 4.3, the decrease in opal flux in the AZ and increase in the Subantarctic manifests as a northward shift of the opal belt during the LGM. There have been numerous factors attributed to the apparent glacial-interglacial changes in productivity in the Southern Ocean, including shifts in the westerly wind belt (Anderson et al., 2009), stratification of the Antarctic (Francois et al., 1997), light limitation by sea ice (Elderfield and Rickaby, 2000), and iron fertilization (Martin, 1990). These mechanisms are not necessarily mutually exclusive, however elucidating the importance of certain mechanisms may have implications for our understanding of glacial-interglacial variability in atmospheric CO_2.

The southern limit: sea ice and stratification

The productivity proxy data presented here (Figure 4.2) suggests sea ice exerted a control over the position of the opal belt between the LGM and Holocene, a conclusion shared by previous studies (Francois et al., 1997; Anderson et al., 2002; Chase et al., 2003; Ridgewell, 2007). However, the mechanism for how sea ice restricts productivity in the Antarctic during the LGM has remained contentious.

In the modern ocean the southern limit imposed by sea ice is largely due to light limitation (Chase et al., 2015). This has naturally led to the hypothesis, known hereon as the sea ice cap hypothesis, that the more extensive sea ice cover during the LGM ultimately limited phytoplankton growth in the Antarctic due to light limitation (Elderfield and Rickaby, 2000; Matsumoto et al., 2001; Anderson et al., 2002; Chase et al., 2003). This proposal allows for a similar vertical supply of nutrients to the AZ during the LGM as today, however the nutrients are poorly utilized due to the light limitation and are thus advected into the Subantarctic. This greater lateral supply of nutrients fuels the higher productivity observed in proxy reconstructions.

An alternative hypothesis, known hereon as the stratification hypothesis, proposes that the supply of nutrients into the AZ surface waters was restricted thus producing a nutrient-limited system (Francois et al., 1997; Sigman et al., 1999; Studer et al., 2015). A reduction in vertical nutrient supply can be achieved by a combination of reduced wind-driven mixing by the presence of sea ice itself (Liu et al., 2015) or northward displacement of the westerly

winds (Toggweiler et al., 2006), and/or the strengthening of the water column halocline due to the formation/melting of sea ice (Adkins et al., 2002). Complete utilisation of supplied macronutrients would have been aided by a greater supply of exogeneous iron both from increased dust flux (Lambert et al., 2012) and the melting sea ice (Wang et al., 2014). Importantly, this mechanism requires vertical supply of nutrients to the Subantarctic to have increased during the LGM (Beucher et al., 2007) to support the higher productivity observed there.

From a paleoceanographic perspective the distinction between these two hypotheses is important as it defines whether the entrapment of CO_2 in the deep Southern Ocean during the LGM was driven by water column stratification or the physical prevention of outgassing by sea ice capping (Keeling and Visbeck, 2001). From a biogeochemical perspective the sea ice cap hypothesis implies productivity in the Subantarctic was enhanced by reduced nutrient uptake in the Antarctic, whereas the stratification hypothesis must invoke increased vertical supply of nutrients to the Subantarctic relative to today. Furthermore, reduced nutrient supply to the Southern Ocean as suggested by the stratification hypothesis has implications for the nutrient transport to low latitude regions supplied by Subantarctic intermediate waters (Sarmiento et al., 2004).

$\delta^{15}N$ records used for reconstructing the relative uptake of supplied nitrate, suggest nitrate utilisation in the AZ was greater during the LGM than in the Holocene. The details of this process and reconstructions performed within these cores are provided in more detail in Chapter 5. In short, the greater degree of nitrate exhaustion within surface waters combined with reduced productivity strongly indicates a reduction in nutrient supply to the Southern Ocean during the LGM. Further evidence that stratification was likely important comes from the $\Delta\Delta^{14}C$ reconstructions in Chapter 3, which appear to show the presence of more aged water during the deglaciation. If sea ice were simply acting as a physical barrier to the CO_2 exchange with the atmosphere, one would expect such old ages to be observed through the LGM.

On the other hand, the responses of the productivity proxy records in the two AZ records (MD84-551 and MD88-773) are negligible across the first interval of CO_2 rise when stratification was apparently broken down. This implies that persistent sea ice presence may have continued to inhibit primary production in the Indian sector across this first Antarctic warming interval.

As shown in Figure 4.3, the increased opal fluxes in the Subantarctic during the last glacial did not entirely compensate for the reduced opal fluxes in the AZ. This is particularly apparent in the Indian and Pacific sectors. If, as the sea ice cap hypothesis implies, the Southern Ocean upwelling during the LGM was indeed similar to today (Matsumoto et al., 2001) then we would expect a quantitative displacement of the Southern Ocean productivity from the Subantarctic to the Antarctic across the deglaciation.

Taken together it is apparent that sea ice presence did reduce phytoplankton growth in the Antarctic more than the Holocene, probably due to light limitation. However, it also appears that deep upwelling was encumbered during the LGM, resulting in reduced nutrient supply and limited ventilation of the deep waters. In terms of the biological pump, both the sea ice cap and Antarctic stratification mechanisms may have been operating to reduce CO_2 outgassing from the deep ocean during the LGM. However, ultimately the the evidence described above suggests stratification of the AZ was more important in strengthening the vertical DIC gradient in the ocean, restricting nutrient supply to the AZ and permitting a greater drawdown of CO_2.

Subantarctic productivity: iron and nutrients

The evidence given above suggests the southern limit of the opal belt is controlled by Antarctic stratification, which is related to sea surface temperatures and sea ice extent. The factors controlling the northern limit of the opal belt are somewhat less clear. In their analysis of surface sediment opal fluxes across the Southern Ocean, Chase et al (2015) found a strong correspondence of the northern limit of the modern opal belt with sea surface temperatures. However, it was concluded that the true controlling factor was likely to be silicic acid availability, which may itself correlate with sea surface temperature, but silicic acid measurements are too sparse to provide a good statistical correlation. The absence of a clear correlation between opal flux and DSi availability may be due to the numerous co-limiting factors that become important in the Subantarctic.

North of the polar front mean annual mixed layer depths deepen (Rintoul and Trull, 2001; Montegut et al., 2004) favouring non-diatom phytoplankton such as *Phaeocystis antarctica* that are better adapted to variable and low light levels (Arrigo et al., 1999; Arrigo et al., 2010). In addition, iron limitation not only has a strong influence on phytoplankton growth in the Southern Ocean but also plays a role in determining stoichiometric Si uptake by

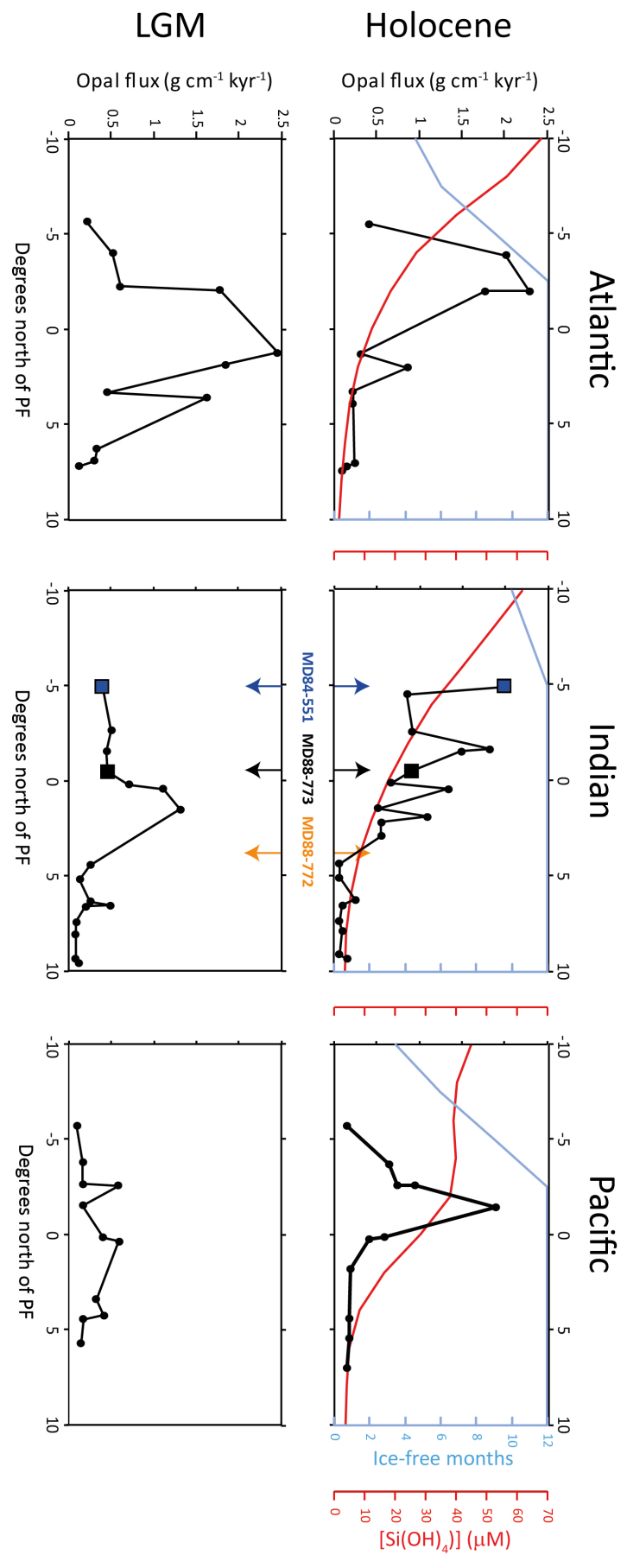

FIGURE 4.3: Compilation of opal flux data (black) from across the Atlantic (left two), Indian (middle two) and Pacific (right two) sectors with respect to the modern PF latitude. Includes data from Kumar et al (1995), Dezileau et al (2003) and Bradtmiller et al (2009). Holocene panels (top three) include estimates of mean sea ice extent based on Parkinon (2002) and surface water (10 m depth) silicic acid concentration from WOA13 (Garcia et al., 2013). Note the core of the opal belt (peak opal fluxes) occur immediately north of the winter sea ice extent minimum. Diatom production is light limited south of this point and becomes progressively iron and DSi limited northwards. During the LGM (bottom three panels) the opal belt has shifted just north of the modern PF position, suggesting greater sea ice presence to the south. Dust-borne iron fluxes from Patagonia produced a Atlantic-Indian-Pacific gradient in opal fluxes.

diatoms (Franck et al., 2000). Shipboard bottle-enrichment experiments (Franck et al., 2000; Hutchins et al., 2001), culture experiments (Hoffmann et al., 2008) and mesoscale experiments (Brzezinski et al., 2005) suggest that both Fe and Si availability are limiting factors on diatom growth in the Subantarctic. From these studies it has been hypothesised that the limits on phytoplankton growth may exhibit a seasonal progression. At the end of winter, the mixed layer begins to shoal and non-diatom algae such as Phaeocystis compete with the diatoms for the available Fe (Gall et al., 2001). As the surface Fe inventory diminishes the diatom community shifts towards higher Si:N uptake (Hutchin and Bruland, 1998; Takeda, 1998). By summer, Si limitation becomes a strong factor curtailing diatom growth and opal production (Bzezinski et al., 2005). Taken together it appears that the low availability of both Fe and Si limit diatom productivity in the Subantarctic and hence the northward extent of the modern opal belt.

As discussed in Chapter 6, δ^{30}Si data from the Southern Ocean during the LGM suggest that DSi availability was considerably greater than today from the seasonally ice-covered Antarctic to the northern limits of the ACC close to the STF (De La Rocha et al., 1998; Beuchar et al., 2007; Robinson et al., 2014). This indicates that Si limitation was not the primary control on the northern extent of the opal belt during the LGM. As discussed by Brzezinski et al (2002), iron fertilization during this period may have lowered the stoichiometric Si:N demand by diatoms and caused a shift towards N limitation in the Southern Ocean. As such, it is possible that the northern extent of the opal belt at the LGM was controlled by the availability of other macro nutrients such as nitrate or phosphate, although Fe limitation cannot be ruled out.

The absence of an obvious correlation between the productivity proxies in the three cores and the dust flux proxies is surprising given the importance of iron on DSi uptake by diatoms (e.g. Brzezinski et al., 2002). Productivity proxies in Subantarctic records from both the Atlantic (Anderson et al., 2014; Martinez-Garcia et al., 2014) and Pacific (Lamy et al., 2014) have shown a good correspondence with both Antarctica (Lambert et al., 2012) and local dust flux reconstructions, albeit at low resolutions. One possibility is that although the location of the opal belt is defined by Antarctic stratification, whereas the absolute productivity and opal flux across the Southern Ocean are modulated by dust-borne iron fluxes. Indeed, the deglacial decline of opal fluxes in SAZ cores, MD88-769 and MD88-770, far north of the opal belt during the LGM have a much closer fit to the decline in dust flux observed in the EPICA Dome C record (Figure 4.2; Dezileau et al., 2003). This supports

the notion suggested above, that the northern limit of the opal belt is defined by not only macro nutrient concentrations (Si during the Holocene and N/P during the LGM) but also the availability of iron.

The sensitivity of primary production to dust-borne iron inputs appears to have created distinct inter-basin differences in Subantarctic opal fluxes during the LGM, interpreted to be in response to differing distances from prominent dust sources (Chase et al., 2003; Dezileau et al., 2003). This inter-basin difference is depicted in Figure 4.3, with the highest opal fluxes observed in the Atlantic during the LGM and the lowest in the Pacific. The pattern of inter-basin opal fluxes may be explained by the distance of sites from prominent dust sources. There is strong evidence to suggest that the most important source regions of dust to the Southern Ocean and Antarctica during the LGM was Patagonia (Basile et al., 1997; Sugden et al., 2009; Noble et al., 2012; Gili et al., 2016). Hence, the Subantarctic Atlantic immediately downwind from Patagonia experienced the greatest increase in opal flux observed in the Southern Ocean at the LGM. Other dust source regions, such as South Africa and Australia may have contributed to the dust fluxes to the Indian and Pacific sectors, respectively. However, the spatially averaged total dust flux to these regions is expected to have been approximately an order of magnitude lower than that depositing in the Atlantic sector (Mahowald et al., 2006). Such inter-basin differences are not apparent in the Holocene, suggesting that the role of exogeneous iron inputs in controlling primary productivity became diminished by the Holocene.

A longitudinal iron availability gradient is unable to explain why the opal fluxes in the Atlantic Subantarctic during the LGM remained comparable to the Holocene Atlantic AZ opal fluxes, given that it suggested nutrient supply was reduced overall. Hence, an alternative or complimentary mechanism by which opal fluxes differ between the sectors of the Southern Ocean is that glacial Subantarctic upwelling strength was longitudinally heterogenous.

Deglacial upwelling and productivity maxima

The opal flux maxima in the two AZ cores (MD84-551 and MD88-773) is centred at approximately 11 ka BP, which corresponds well with the Antarctic temperature maximum (Parrenin et al., 2013) and sea ice minimum (Wolff et al. 2006). Other records across the Southern Ocean exhibit maximum opal fluxes at different periods during the deglaciation. For example, Anderson et al (2009) published an opal flux record from core TN057-13-4PC

situated in the Atlantic AZ (Figure 4.4). This recorded exhibits two prominent peaks in opal flux during the deglaciation, the first (∼14 – 17 ka BP) is approximately aligned with the first stage of Antarctic temperature rise, the second (∼9.5 – 13 ka BP) aligns well with the Antarctic temperature maximum and the opal peaks within the Indian sector records.

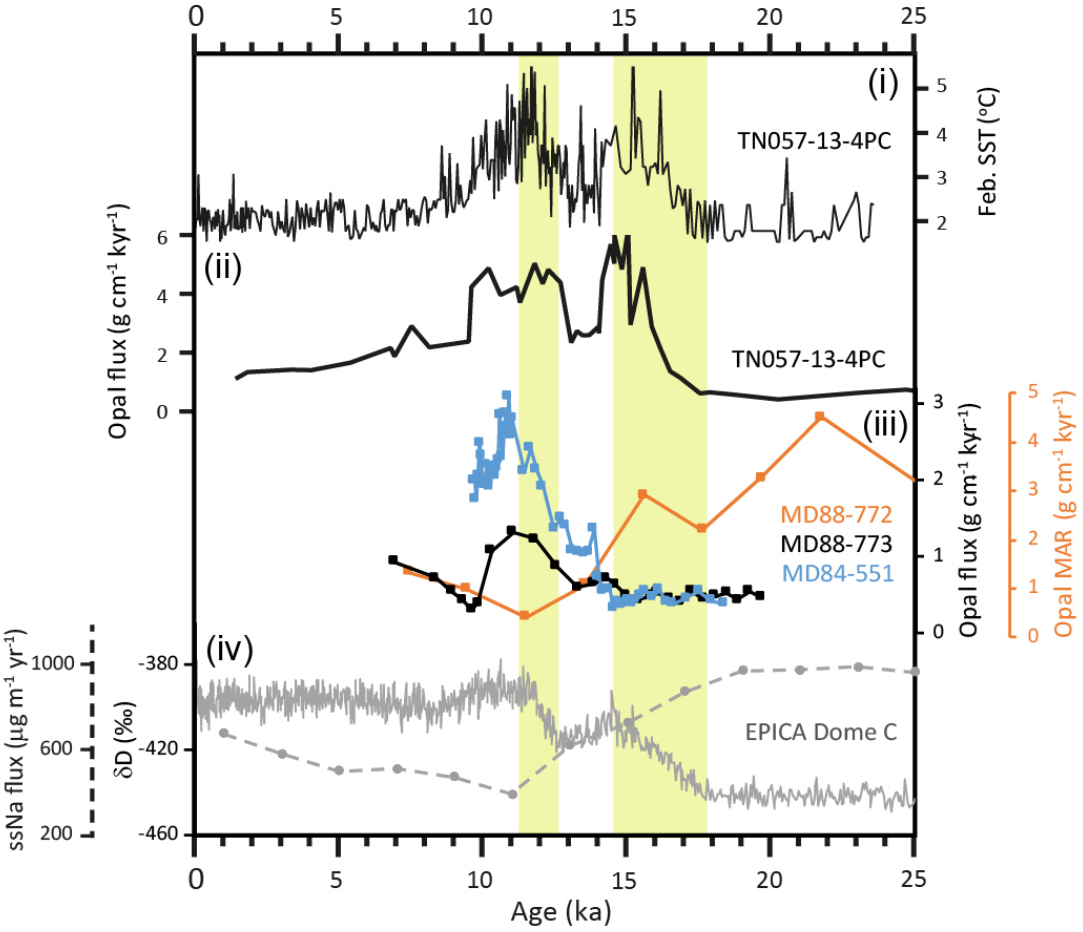

FIGURE 4.4: A comparison of the deglacial opal flux changes within the Atlantic and Indian sectors. **(i)** diatom-based sea surface temperature reconstruction from Atlantic sector core, TN057-13-4PC (Nielsen, 2004) illustrating the influence of the bipolar seesaw transfer of heat to the Southern Hemisphere during the deglaciation. **(ii)** Th-normalised opal flux data from TN057-13-4PC (Anderson et al., 2009) showing an earlier peak in opal fluxes in the Atlantic sector than the Indian sector. **(iii)** Th-normalised opal fluxes from MD84-551 and MD88-773 with opal MAR from MD88-772. **(iv)** Antarctic temperature (Parrenin et al., 2013) and sea ice extent (Wolff et al., 2006) proxies from EPICA Dome C. The better correlation between the opal fluxes in the Indian sector and the Antarctic temperature records suggests the Atlantic sector opal belt is more sensitive to North Atlantic climatic conditions.

Anderson et al (2009) attributed the opal flux peaks in TN057-13-4PC to increased upwelling during the deglaciation due to a southward shift of the westerly wind belt. The modern hydrographic regime of TN057-13-4PC is not dissimilar to that of MD84-551 and MD88-773, located beneath the ice-free waters of the AZ. Hence, we would expect the wind-driven

upwelling to similarly induce higher opal fluxes in the Indian sector records during the first deglacial warming interval. One possible explanation for this disparity is deglacial sea ice retreat and the subsequent shift of the opal belt was not uniform across the Southern Ocean. Indeed, sea surface temperature reconstruction from TN057-13-4PC displays two peaks coeval with the opal flux peaks observed in the same record (Anderson et al., 2009). Other Atlantic sector records recording abundances of warm foraminifera species indicate that sea surface temperatures may have been higher during the first deglacial warming interval than the early Holocene (Barker et al., 2009). Hence, the opal peaks may represent two successive progressions of the opal belt as it moved southward during the deglaciation, rather than the more monotonic transit observed in the Indian sector. The mechanism attributed to the anomalous South Atlantic warming during the deglaciation is suggested to derive from the bipolar seesawing of interhemispheric temperature exchange as the Atlantic meridional overturning oscillates in strength (Barker et al., 2009). Importantly, this seems to demonstrate that the hydrographical and thus ecological conditions within the Atlantic sector of the Southern Ocean are much more sensitive to North Atlantic forcings than other sectors of the Southern Ocean.

Nevertheless, the magnitude of the opal peaks observed within TN057-13-4PC cannot be explained entirely by two successive transits of the opal belt southward to the Atlantic AZ during the deglaciation because there is little evidence of a concomitant decrease in opal flux from a Atlantic PFZ records (Abelmann et al., 2015). At 4 – 6 g cm^{-2} kyr^{-1}, the opal flux peaks in TN057-13-4PC are larger than anywhere observed in the modern Southern Ocean (Chase et al., 2015). Hence, the transition of the opal belt must have been accompanied by a process that fertilized silica export during the deglacial transition. A large supply of nutrients may release the phytoplankton community from their glacial nutrient limitation during these warming intervals. The nutrient supply may have been longitudinally heterogenous as suggested for the glacial period in the text above. In addition, the higher sea surface temperatures in the Atlantic sector imply a greater retreat of sea ice relative to other sectors, which would promote greater wind-driven mixing, reduced salinity stratification and less light limitation. The latter opal peak ($\sim$11 ka BP) is more universally represented across AZ records, including those from the Indian sector, suggesting environmental conditions and nutrient supply were more balanced between the sectors later in the deglaciation.

4.5 Conclusions

The data from the three Indian sector cores presented here display a classic Antarctic-Subantarctic productivity dipole (Charles et al., 1991; Mortlock et al., 1991; Kumar et al., 1995; Chase et al., 2003; Ridgewell, 2007) between the last glacial maximum and the Holocene. The evolution of opal and Ba_{xs} accumulation within the three cores corresponds well with changes in sea ice extent and Antarctic temperature rise. Hence, it is suggested that glacial-interglacial productivity changes within the AZ and much of the PFZ are driven by changes in Southern Ocean stratification associated with sea ice formation and melting (Adkins et al., 2002).

The variability in the productivity proxies in the records presented here do not follow that of dust flux changes in Antarctica (Lambert et al., 2012), suggesting that the control on productivity by exogeneous iron fertilization in the Indian sector AZ and PFZ is muted. However, an observed decoupling of opal and Ba_{xs} that could not be attributed to preservation changes suggests that iron plays a role in modulating productivity and silica export within the AZ and PFZ across glacial-interglacial cycles.

In combination with previously published records, the opal flux proxies provide an account of the southward transit of the opal belt in response to the southward migration of the region of maximum upwelling. Attributing these observations to a southward shift of the westerly wind belt is avoided here, primarily because studies have yet to agree on the direction of the westerly wind movement (Rojas et al.,2008; Kohfeld et al., 2013). Nevertheless, reduced sea ice cover would increase the wind stress in the AZ across the deglaciation anyway (Liu et al., 2015), hence movement or strengthening of the westerly winds may not necessarily be required for altering mixing in the AZ. However, the increased productivity in the glacial Atlantic (Kumar et al., 1995) is in agreement with increased wind-driven mixing and nutrient supply to the Subantarctic.

Here it is suggested that superimposed onto the deglacial opal belt shift is an increase in opal flux associated with increased nutrient supply. However, the higher productivity is only observed towards the latter stages of the deglaciation (10 – 13 ka BP) in the Indian sector cores, possibly in response to the gradual retreat of sea ice across the deglacial period. From the perspective of the biological pump, the deglacial upwelling in the AZ would have led to improved exchange of carbon between the deep ocean and atmosphere, leading to a

weakening of the vertical DIC gradient and a rise in atmospheric CO_2. However, if sea ice retreat was not complete during the early deglaciation across much of the Southern Ocean then either through the persistence of sea ice mediated stratification or reduced air-sea gas exchange the deepest ocean water that upwell furthest south would have remained poorly ventilated. As the sea ice retreated further south during the late deglaciation the upwelling would have shifted towards denser isopycnals that ventilate deeper into the ocean interior (Ferrari et al., 2014). As a result, the deepest waters would have been exposed only towards the latter period of the deglaciation. The deepest waters of the world's oceans are the most enriched in silicic acid, due to the slow remineralisation rate of biogenic silica. Hence, the latter upwelling interval may have been an important factor in the delivery of silicic acid to the Southern Ocean during the deglaciation. This idea is explored in more detail in Chapter 6.

References

Abelmann , A., Gersonde , R., Knorr , G., Zhang , X., Chapligin , B., Maier , E., Esper , O., Friedrichsen , H., Lohmann , G., Meyer , H., and Tiedemann , R. The seasonal sea-ice zone in the glacial Southern Ocean as a carbon sink. *Nature communications*, 6:8136, 2015. doi: 10.1038/ncomms9136.

Adkins , J. F., Mcintyre , K., and Schrag , D. P. The Salinity, Temperature, and d18O of the Glacial Deep Ocean. *Science*, 298(November):1769–1774, 2002.

Anderson , R. F., Ali , S., Bradtmiller , L. I., Nielsen , S. H. H., Fleisher , M. Q., Anderson , B. E., and Burckle , L. H. Wind-driven upwelling in the Southern Ocean and the deglacial rise in atmospheric CO2. *Science (New York, N.Y.)*, 323(5920):1443–1448, mar 2009. doi: 10.1126/science.1167441.

Anderson , R., Barker , S., Fleisher , M. Q., Gesonde , R., Goldstein , S. L., Kuhn , G., Pahnke , K., and Sachs , J. P. Biological response to millennial variability of dust and nutrient supply in the Subantarctic South Atlantic Ocean. *Philosophical Transactions of the Royal Society A: Mathematical, Physical and Engineering Sciences*, 372, 2014.

Anderson , R. F., Chase , Z., Fleisher , M. Q., and Sachs , J. The Southern Ocean's biological pump during the Last Glacial Maximum. *Deep Sea Research Part II: Topical Studies in Oceanography*, 49(9-10): 1909–1938, jan 2002. doi: 10.1016/S0967-0645(02)00018-8.

Arrigo , K. R., Robinson , D. H., Worthen , D. L., Dunbar , R. B., DiTullio , G., VanWoert , M. L., and Lizotte , M. P. Phytoplankton Community Structure and the Drawdown of Nutrients and CO2 in the Southern Ocean. *Science*, 283(5400):365–367, jan 1999. doi: 10.1126/science.283.5400.365.

Arrigo , K. R., Mills , M. M., Kropuenske , L. R., and Dijken , G. L. V. Photophysiology in Two Major Southern Ocean Phytoplankton Taxa : Photophysiology in Two Major Southern Ocean Phytoplankton Taxa : Photosynthesis and Growth of Phaeocystis antarctica and Fragilariopsis cylindrus under Different Irradiance Levels. *Integrative and Comparative Biology*, 50(6):950–966, 2010. doi: 10.1093/icb/icq021.

Bareille , G., Labracherie , M., Bertrand , P., Labeyrie , L., Lavaux , G., and Dignan , M. Glacial–interglacial changes in the accumulation rates of major biogenic components in Southern Indian Ocean sediments. *Journal of Marine Systems*, 17(1-4):527–539, nov 1998. doi: 10.1016/S0924-7963(98)00062-1.

Barker , S., Diz , P., Vautravers , M. J., Pike , J., Knorr , G., Hall , I. R., and Broecker , W. S. Interhemispheric Atlantic seesaw response during the last deglaciation. *Nature*, 457(7233):1097–102, feb 2009. doi: 10.1038/nature07770.

Basile , I., Grousset , F. E., Revel , M., Petit , J. R., Biscaye , P. E., and Barkov , N. I. Patagonian origin of glacial dust deposited in East Antarctica (Vostok and Dome C) during glacial stages 2, 4 and 6. *Earth and Planetary Science Letters*, 146(3-4):573–589, 1997. doi: 10.1016/S0012-821X(96)00255-5.

Beucher , C. P., Brzezinski , M. a., and Crosta , X. Silicic acid dynamics in the glacial sub-Antarctic: Implications for the silicic acid leakage hypothesis. *Global Biogeochemical Cycles*, 21(3):1–13, sep 2007. doi: 10.1029/2006GB002746.

Boyd , P. W. and Newton , P. P. Does planktonic community structure determine downward particulate organic carbon flux in different oceanic provinces ? *Deep Sea Research I*, 46:63–91, 1999.

Boyd , P. W., Arrigo , K. R., Strzepek , R., and van Dijken , G. L. Mapping phytoplankton iron utilization: Insights into Southern Ocean supply mechanisms. *Journal of Geophysical Research*, 117(C6):C06009, jun 2012. doi: 10.1029/2011JC007726.

Broecker , W. Glacial to interglacial changes in ocean chemistry. *Progress in Oceanography*, 11:151–197, 1982.

Brzezinski , M., Pride , C., Franck , V. M., Sigman , D. M., Sarmiento , J. L., Matsumoto , K., Gruber , N., Rau , G. H., and Coale , K. H. A switch from Si (OH) 4 to NO3 depletion in the glacial Southern Ocean. *Geophysical Research Letters*, 29(12):3–6, 2002.

Brzezinski , M. A., Dickson , M.-l., Nelson , D. M., and Sambrotto , R. Ratios of Si , C and N uptake by microplankton in the Southern Ocean. *Deep Sea Research Part II: Topical Studies in Oceanography*, 50: 619–633, 2003.

Brzezinski , M. A., Jones , J. L., and Demarest , M. S. Control of silica production by iron and silicic acid during the Southern Ocean Iron Experiment (SOFeX). *Limnol. Oceanogr*, 50(3):810–824, 2005.

Burckle , L. H. and Cirilli , J. Origin of diatom ooze belt in the Southern Ocean : for late Quaternary Implications paleoceanography. *Micropaleontology*, 33(1):82–86, 1987.

Charles , C., Froelich , P., Zibello , M., Mortlock , R., and Morley , J. Biogenic opal in Southern Ocean sediments over the last 450,000 years: Implications for surface water chemistry and circulation. *Paleoceanography*, 6(6):697–728, 1991.

Chase , Z., Anderson , R. F., Fleisher , M. Q., and Kubik , P. W. Accumulation of biogenic and lithogenic material in the Pacific sector of the Southern Ocean during the past 40,000 years. *Deep Sea Research Part II: . . .*, 50:799–832, 2003.

Chase , Z., Kohfeld , K. E., and Matsumoto , K. Controls on biogenic silica burial in the Southern Ocean. *Global Biogeochemical Cycles*, 29:1599–1616, 2015. doi: 10.1002/2014GB004979.Received.

Coale , K. H., Johnson , K. S., Chavez , F. P., Buesseler , K. O., Barber , R. T., Brzezinski , M. a., Cochlan , W. P., Millero , F. J., Falkowski , P. G., Bauer , J. E., Wanninkhof , R. H., Kudela , R. M., Altabet , M. a., Hales , B. E., Takahashi , T., Landry , M. R., Bidigare , R. R., Wang , X., Chase , Z., Strutton , P. G., Friederich , G. E., Gorbunov , M. Y., Lance , V. P., Hilting , A. K., Hiscock , M. R., Demarest , M.,

Hiscock , W. T., Sullivan , K. F., Tanner , S. J., Gordon , R. M., Hunter , C. N., Elrod , V. a., Fitzwater , S. E., Jones , J. L., Tozzi , S., Koblizek , M., Roberts , A. E., Herndon , J., Brewster , J., Ladizinsky , N., Smith , G., Cooper , D., Timothy , D., Brown , S. L., Selph , K. E., Sheridan , C. C., Twining , B. S., and Johnson , Z. I. Southern Ocean iron enrichment experiment: carbon cycling in high- and low-Si waters. *Science (New York, N.Y.)*, 304(5669):408–14, apr 2004. doi: 10.1126/science.1089778.

De La Rocha , C. and Brzezinski , M. Silicon-isotope composition of diatoms as an indicator of past oceanic change. *Nature*, 395(October):28–31, 1998.

Dehairs , F., Chesselet , R., and Jedwab , J. DISCRETE SUSPENDED PARTICLES OF BARITE AND THE BARIUM CYCLE IN THE OPEN OCEAN. *Earth and Planetary Science Letters*, 49:528–550, 1980.

Dezileau , L., Bareille , G., Reyss , J. L., and Lemoine , F. Evidence for strong sediment redistribution by bottom currents along the southeast Indian ridge. *Deep-Sea Research Part I: Oceanographic Research Papers*, 47(10):1899–1936, 2000. doi: 10.1016/S0967-0637(00)00008-X.

Dezileau , L., Reyss , J., and Lemoine , F. Late Quaternary changes in biogenic opal fluxes in the Southern Indian Ocean. *Marine Geology*, 202(3-4):143–158, nov 2003a. doi: 10.1016/S0025-3227(03)00283-4.

Dezileau , L., Bareille , G., and Reyss , J. The 231Pa/230Th ratio as a proxy for past changes in opal fluxes in the Indian sector of the Southern Ocean. *Marine Chemistry*, 81(3-4):105–117, apr 2003b. doi: 10.1016/S0304-4203(02)00070-1.

Diekmann , B. Sedimentary patterns in the late Quaternary Southern Ocean. *Deep-Sea Research Part II: Topical Studies in Oceanography*, 54(21-22):2350–2366, 2007. doi: 10.1016/j.dsr2.2007.07.025.

Dymond , J., Suess , E., and Lyle , M. Barium in deep-sea sediment: A geochemical proxy for paleoproductivity. *Paleoceanography*, 7(2):163–181, 1992.

Elderfield , H. and Rickaby , R. Oceanic Cd/P ratio and nutrient utilization in the glacial Southern Ocean. *Nature*, 405(6784):305–10, may 2000. doi: 10.1038/35012507.

Fagel , N., Bareille , G., Monnin , C., Fagel , N., Dehairs , F., and Andre , L. Ba distribution in surface Southern Ocean sediments and export production estimates. *Paleoceanography*, 17(2), 2002.

Franck , V. M., Brzezinski , M. A., Coale , K. H., and Nelson , D. M. Iron and silicic acid concentrations regulate Si uptake north and south of the Polar Frontal Zone in the Pacific Sector of the Southern Ocean. *Deep Sea Research Part II: Topical Studies in Oceanography*, 47:3315–3338, 2000.

Francois , R., Altabet , M. A., Yu , E.-f., Sigman , D. M., Bacon , M. P., Frank , M., Bohrmann , G., Bareille , G., and Labeyrie , L. D. Contribution of Southern Ocean surface-water stratification to low atmospheric CO 2 concentrations during the last glacial period. *Nature*, 389:929–935, 1997.

Francois , R., Bacon , M. P., Altabet , M. A., and Labeyrie , L. D. Glacial/Interglacial changes in sediment rain rate in the SW Indian sector of Subantarctic waters as recorded by 230Th, 231Pa, U, and d15N. *Paleoceanography*, 8(5):611–629, 1993.

Francois , R., Frank , M., Rutgers van der Loeff , M. M., and Bacon , M. P. 230 Th normalization: An essential tool for interpreting sedimentary fluxes during the late Quaternary. *Paleoceanography*, 19(1): n/a–n/a, mar 2004. doi: 10.1029/2003PA000939.

Francois , R., Honjo , S., Manganini , J., and Ravizza , E. Biogenic barium fluxes to the deep sea: Implications for paleoproductivity reconstruction. *Global Biogeochemical Cycles*, 9(2):289–303, 1995.

Gall , M. P., Boyd , P. W., Hall , J., Sa , K. A., and Chang , H. Phytoplankton processes . Part 1 : Community structure during the Southern Ocean Iron RElease Experiment (SOIREE). *Deep Sea Research*

II, 48:2551–2570, 2001.

Ganeshram , R. S., François , R., Commeau , J., and Brown-Leger , S. L. An experimental investigation of barite formation in seawater. *Geochimica et Cosmochimica Acta*, 67(14):2599–2605, jul 2003. doi: 10.1016/S0016-7037(03)00164-9.

Garcia , H. E., Locarnini , R. A., Boyer , T. P., Antonov , J. I., Baranova , O. K., Zweng , M., Reagan , J. R., and Johnson , D. R. World Ocean Atlas 2013, Volume 4: Dissolved Inorganic Nutrients (phosphate, nitrate, silicate). In Levitus , S. and Mishonov , A. V., editors, *NOAA Atlas NESDIS 76*. 2013.

Gautier , I., Weis , D., Mennessier , J. P., Vidal , P., Giret , A., and Loubet , M. Petrology and geochemistry of the Kerguelen Archipelago basalts (South Indian Ocean): evolution of the mantle sources from ridge to intraplate position. *Earth and Planetary Science Letters*, 100(1-3):59–76, 1990. doi: 10.1016/0012-821X(90)90176-X.

Geibert , W., Rutgers van der Loeff , M. M., Usbeck , R., Gersonde , R., Kuhn , G., and Seeberg-Elverfeldt , J. Quantifying the opal belt in the Atlantic and southeast Pacific sector of the Southern Ocean by means of 230 Th normalization. *Global Biogeochemical Cycles*, 19(4):n/a–n/a, dec 2005. doi: 10.1029/2005GB002465.

Gili , S., Gaiero , D. M., Goldstein , S. L., Chemale , F., Koester , E., Jweda , J., Vallelonga , P., and Kaplan , M. R. Provenance of dust to Antarctica: A lead isotopic perspective. *Geophysical Research Letters*, 43 (5):2291–2298, 2016. doi: 10.1002/2016GL068244.

Hoffmann , L., Peeken , I., and Lochte , K. Iron , silicate , and light co-limitation of three Southern Ocean diatom species. *Polar Biology*, 2008. doi: 10.1007/s00300-008-0448-6.

Honjo , S., Francois , R., and Manganini , S. Particle fluxes to the interior of the Southern Ocean in the Western Pacific sector along 170 W. *Deep Sea Research Part II: Topical Studies in Oceanography*, 47, 2000.

Hutchins , D. and Bruland , K. Iron-limited diatom growth and Si: N uptake ratios in a coastal upwelling regime. *Nature*, 393(June):65–68, 1998.

Hutchins , D., Sedwick , P., DiTullio , G., Boyd , P., Queguiner , B., Griffiths , F., and Crossley , C. Control of phytoplankton growth by iron and silicic acid availability in the subantarctic Southern Ocean: Experimental results from the SAZ Project. *Journal of Geophysical Research*, 106(C12), 2001.

Iida , T. and Odate , T. Seasonal variability of phytoplankton biomass and composition in the major water masses of the Indian Ocean sector of the Southern Ocean. *Polar Science*, 8(3):283–297, 2014. doi: 10.1016/j.polar.2014.03.003.

Jin , X., Gruber , N., Dunne , J. P., Sarmiento , J. L., and Armstrong , R. A. Diagnosing the contribution of phytoplankton functional groups to the production and export of particulate organic carbon , CaCO 3 , and opal from global nutrient and alkalinity distributions. *Global Biogeochem. Cycles*, 20:1–17, 2006. doi: 10.1029/2005GB002532.

Keeling , R. F. and Visbeck , M. Palaeoceanography: Antarctic stratification and glacial CO2. *Nature*, 412: 605–606, 2001.

Kumar , N., Anderson , R., Mortlock , R., Froelich , P., Kubik , P., Dittrich-Hannen , B., and Suter , M. Increased biological productivity and export production in the glacial Southern Ocean. *Nature*, 378: 678–680, 1995.

Lambert , F., Bigler , M., Steffensen , J. P., Hutterli , M., and Fischer , H. Centennial mineral dust variability

in high-resolution ice core data from Dome C, Antarctica. *Climate of the Past*, 8(2):609–623, mar 2012. doi: 10.5194/cp-8-609-2012.

Lamy , F., Gersonde , R., Winckler , G., Esper , O., Jaeschke , a., Kuhn , G., Ullermann , J., Martinez-Garcia , a., Lambert , F., and Kilian , R. Increased dust deposition in the Pacific Southern Ocean during glacial periods. *Science (New York, N.Y.)*, 343(6169):403–7, jan 2014. doi: 10.1126/science.1245424.

Laurenceau-Cornec , E., Trull , T. W., Davies , D. M., Bray , S. G., Doran , J., Planchon , F., and Carlotti , F. The relative importance of phytoplankton aggregates and zooplankton fecal pellets to carbon export : insights from free-drifting sediment trap deployments in naturally iron-fertilised waters near the Kerguelen Plateau. *Biogeosciences*, 12:1007–1027, 2015. doi: 10.5194/bg-12-1007-2015.

Liu , W., Lu , J., Leung , L. R., Xie , S. P., Liu , Z., and Zhu , J. The de-correlation of westerly winds and westerly-wind stress over the Southern Ocean during the Last Glacial Maximum. *Climate Dynamics*, 45 (11-12):3157–3168, 2015. doi: 10.1007/s00382-015-2530-4.

Mahowald , N. M., Muhs , D. R., Levis , S., Rasch , P. J., Yoshioka , M., Zender , C. S., and Luo , C. Change in atmospheric mineral aerosols in response to climate: Last glacial period, preindustrial, modern, and doubled carbon dioxide climates. *Journal of Geophysical Research*, 111(D10):D10202, 2006. doi: 10.1029/2005JD006653.

Maiti , K., Charette , M. a., Buesseler , K. O., and Kahru , M. An inverse relationship between production and export efficiency in the Southern Ocean. *Geophysical Research Letters*, 40(8):1557–1561, apr 2013. doi: 10.1002/grl.50219.

Martin , J. Glacial-interglacial CO2 change: The iron hypothesis. *Paleoceanography*, 5(1):1–13, 1990.

Martin , J., Knauer , G., Karl , D., and Broenkow , W. VERTEX: carbon cycling in the northeast Pacific. *Deep Sea Research Part A. Oceanographic Research Papers*, 34(2):267–285, 1987.

Martin , J. H., Fitzwater , S. E., and Gordon , R. M. Iron deficiency limits phytoplankton growth in Antarctic waters. *Global Biogeochemical Cycles*, 4(1):5–12, 1990.

Martínez-García , A., Sigman , D. M., Ren , H., Anderson , R. F., Straub , M., Hodell , D. a., Jaccard , S. L., Eglinton , T. I., and Haug , G. H. Iron fertilization of the Subantarctic ocean during the last ice age. *Science (New York, N.Y.)*, 343(6177):1347–50, mar 2014. doi: 10.1126/science.1246848.

Matsumoto , K., Lynch-Stieglitz , J., and Anderson , R. F. Similar glacial and Holocene Southern Ocean hydrography. *Paleoceanography*, 16(5):445–454, 2001.

McManus , J., Berelson , W., Klinkhammer , G. P., Johnson , K. S., Coale , K. H., Anderson , R. F., Kumar , N., Burdige , D. J., Hammond , D. E., Brumsack , H.-j., Mccorkle , D. C., and Rushdi , A. Geochemistry of barium in marine sediments: Implications for its use as a paleoproxy. *Geochimica et Cosmochimica Acta*, 62(21):3453–3473, 1998.

Montegut , d. B., Madec , G., Fischer , A. S., Lazar , A., and Iudicone , D. Mixed layer depth over the global ocean : An examination of profile data and profile-based climatology. *Journal of Geophysical Research*, 109(April), 2004. doi: 10.1029/2004JC002378.

Moore , J. K. and Abbott , M. R. Phytoplankton chlorophyll distributions and primary production in the Southern Ocean. *Journal of Geophysical Research*, 105(C12):28709, 2000. doi: 10.1029/1999JC000043.

Moore , J., Abbott , M., Richman , J. D., and Nelson , D. M. The Southern Ocean at the last glacial maximum: A strong sink for atmospheric carbon dioxide. *Global Biogeochemical Cycles*, 14(1), 2000.

Mortlock , R. and Froelich , P. A simple method for the rapid determination of biogenic opal in pelagic marine sediments. *Deep Sea Research Part A. Oceanographic Research Papers*, 36(9):1415–1426, 1989.

Mortlock , R. a., Charles , C. D., Froelich , P., Zibello , M., Saltzman , J., Hays , J., and Burckle , L. H. Evidence for lower productivity in the Antarctic Ocean during the last glaciation. *Nature*, 351, 1991.

Nelson , D. M., Trrguer , P., Brzezinski , M. A., Leynaert , A., and Queginer , B. Production and dissolution of biogenic silica in the ocean : Revised global estimates , comparison with regional data and relationship to biogenic sedimentation. *Global Biogeochem. Cycles*, 9(3):359–372, 1995.

Nielsen , S. *Southern Ocean climate variability*. PhD thesis, University of Tromso, 2004.

Noble , T. L., Piotrowski , A. M., Robinson , L. F., McManus , J. F., Hillenbrand , C.-D., and Bory , A. J.-M. Greater supply of Patagonian-sourced detritus and transport by the ACC to the Atlantic sector of the Southern Ocean during the last glacial period. *Earth and Planetary Science Letters*, 317-318:374–385, feb 2012. doi: 10.1016/j.epsl.2011.10.007.

Nürnberg , C., Bohrmann , G., and Schluter , M. Barium accumulation in the Atlantic sector of the Southern Ocean: Results from 190,000-year records. *Paleoceanography*, 12(4):594–603, 1997.

Parkinson , C. L. Trends in the length of the Southern Ocean sea-ice season ,. *Annals of Glaciology*, 34: 435–440, 2002.

Parrenin , F., Masson-Delmotte , V., Köhler , P., Raynaud , D., Paillard , D., Schwander , J., Barbante , C., Landais , a., Wegner , a., and Jouzel , J. Synchronous change of atmospheric CO2 and Antarctic temperature during the last deglacial warming. *Science (New York, N.Y.)*, 339(6123):1060–3, mar 2013. doi: 10.1126/science.1226368.

Pichevin , L. E., Reynolds , B. C., Ganeshram , R. S., Cacho , I., Pena , L., Keefe , K., and Ellam , R. M. Enhanced carbon pump inferred from relaxation of nutrient limitation in the glacial ocean. *Nature*, 459 (7250):1114–7, jun 2009. doi: 10.1038/nature08101.

Pondaven , P., Ragueneau , O., Treguer , P., Hauvespre , a., Dezileau , L., and Reyss , J. Resolving the 'opal paradox' in the Southern Ocean. *Nature*, 405(6783):168–72, may 2000. doi: 10.1038/35012046.

Ridgwell , A. J. Application of sediment core modelling to interpreting the glacial-interglacial record of Southern Ocean silica cycling. *Climate of the Past*, 3(3):387–396, 2007. doi: 10.5194/cp-3-387-2007.

Rintoul , R. and Trull , W. Seasonal evolution of the mixed layer in the Subantarctic Zone south of Australia. *Journal of Geophysical Research*, 106, 2001.

Robinson , R. S., Brzezinski , M. a., Beucher , C. P., Horn , M. G. S., and Bedsole , P. The changing roles of iron and vertical mixing in regulating nitrogen and silicon cycling in the Southern Ocean over the last glacial cycle. *Paleoceanography*, pages 1179–1195, 2014. doi: 10.1002/2014PA002686.Received.

Rosenthal , Y., Boyle , E. A., Labeyrie , L. D., and Oppo , D. W. Glacial enrichments of authigenic Cd and U in Subantarctic. *Paleoceanography*, 10(3):395–413, 1995.

Sarmiento , J. L., Gruber , N., Brzezinski , M. A., and Dunne , J. P. High-latitude controls of thermocline nutrients and low latitude biological productivity. *Nature*, 427:56–60, 2004. doi: 10.1038/nature02204.1.

Sicre , M. A., Labeyrie , L., Ezat , U., Mazaud , A., and Turon , J. L. A 27 kyr terrestrial biomarker record in the southern Indian Ocean. *Geochemistry, Geophysics, Geosystems*, 7(7), 2006. doi: 10.1029/2005GC001234.

Sigman , M., Altabet , M. A., Francois , R., Mccorkle , D. C., and Gaillard , J.-F. The isotopic composition of diatom-bound nitrogen in Southern Ocean sediments. *Paleoceanography*, 14(2):118–134, 1999.

Studer , A. S., Sigman , D. M., Martínez-García , A., Benz , V., Winckler , G., Kuhn , G., Esper , O.,

Lamy , F., Jaccard , S. L., Wacker , L., Oleynik , S., Gersonde , R., and Haug , G. H. Antarctic Zone nutrient conditions during the last two glacial cycles. *Paleoceanography*, pages n/a–n/a, 2015. doi: 10.1002/2014PA002745.

Sugden , D. E., McCulloch , R. D., Bory , A. J.-M., and Hein , A. S. Influence of Patagonian glaciers on Antarctic dust deposition during the last glacial period. *Nature Geoscience*, 2(4):281–285, 2009. doi: 10.1038/ngeo474.

Sullivan , A. C. W., Arrigo , K. R., Mcclain , C. R., Comiso , J. C., Firestone , J., Sullivan , C. W., Arrigo , K. R., Mcclain , C. R., Comiso , J. C., and Firestone , J. Distributions of Phytoplankton Blooms in the Southern Ocean. *Science*, 262(5141):1832–1837, 1993.

Sverdrup , H. On conditions for the vernal blooming of phytoplankton. *Journal du Conseil*, 18:287–295, 1953. doi: 10.4319/lom.2007.5.269.

Takeda , S. Influence of iron availability on nutrient consumption ratio of diatoms in oceanic waters. *Nature*, 393(JUNE):774–777, 1998.

Thomalla , S. J., Fauchereau , N., Swart , S., and Monteiro , P. M. S. Regional scale characteristics of the seasonal cycle of chlorophyll in the Southern Ocean. *Biogeosciences*, 8(10):2849–2866, 2011. doi: 10.5194/bg-8-2849-2011.

Toggweiler , J. R., Russell , J. L., and Carson , S. R. Midlatitude westerlies, atmospheric CO 2 , and climate change during the ice ages. *Paleoceanography*, 21(2), 2006. doi: 10.1029/2005PA001154.

Treger , P. and Jaques , G. Dynamics of nutrients and phytoplankton, and flluxes of carbon, nitrogen, and silicon in the Antartic Ocean. *Polar Biology*, 12(1992):149–162, 1992. doi: 10.1007/BF00238255.

Tréguer , P. J. and De La Rocha , C. L. The world ocean silica cycle. *Annual review of marine science*, 5: 477–501, jan 2013. doi: 10.1146/annurev-marine-121211-172346.

Trull , T., Bray , S., Manganini , S. J., Honjo , S., and Francois , R. Moored sediment trap measurements of carbon export in the Subantarctic and Polar Frontal Zones of the Southern Ocean, south of Australia. *Journal of Geophysical Research*, 106(2000), 2001.

Wang , S., Bailey , D., Lindsay , K., Moore , J. K., and Holland , M. Impact of sea ice on the marine iron cycle and phytoplankton productivity. *Biogeosciences*, 11(17):4713–4731, sep 2014. doi: 10.5194/bg-11-4713-2014.

Wolff , E. W., Fischer , H., Fundel , F., Ruth , U., Twarloh , B., Littot , G. C., Mulvaney , R., Röthlisberger , R., de Angelis , M., Boutron , C. F., Hansson , M., Jonsell , U., Hutterli , M. a., Lambert , F., Kaufmann , P., Stauffer , B., Stocker , T. F., Steffensen , J. P., Bigler , M., Siggaard-Andersen , M. L., Udisti , R., Becagli , S., Castellano , E., Severi , M., Wagenbach , D., Barbante , C., Gabrielli , P., and Gaspari , V. Southern Ocean sea-ice extent, productivity and iron flux over the past eight glacial cycles. *Nature*, 440 (7083):491–6, mar 2006. doi: 10.1038/nature04614.

5

The Southern Ocean soft-tissue pump and the global nitrogen cycle

5.1 Introduction

During glacial periods, atmospheric CO_2 was lowered by approximately 80 ppm relative to interglacials (Monnin et al., 2001). This variability has been attributed to the sequestration of carbon in the deep ocean that became isolated from the surface ocean and atmosphere (Sigman and Boyle, 2000; Toggweiler et a., 2006; Skinner et al., 2010; Shakun et al., 2012). Today the deep ocean is ventilated through the Southern Ocean, therefore it has been suggested that stratification of the Southern Ocean could have inhibited communication between the deep ocean and atmosphere (Toggweiler, 1999; Adkins et al., 2002; Burke and Robinson, 2012). The deglaciation marks the transition between the peak glacial conditions of deep ocean isolation and the well-mixed Southern Ocean similar to today. Previous studies have suggested that the deglacial invigoration of Southern Ocean overturning occurred in

two phases, coeval with the two main periods of atmospheric CO_2 rise (Burke and Robinson, 2012).

At the same time there was the reduction in dust fluxes to Antarctica (Lambert et al., 2012) and the Southern Ocean (Martinez-Garcia et al., 2014). Greater dust fluxes during glacial periods has been attributed to various mechanisms, including a shift in position or strength of the westerly winds, decreased in vegetation cover in dust source regions and a reduced hydrological cycle (Mahowald et al., 1999). Since the Iron Hypothesis, proposed by Martin (1990), it has been suggested that the deglacial decrease in dust-borne iron flux to the Southern Ocean may have led to a weakening of the biological pump, which could have contributed to the deglacial rise in atmospheric CO_2.

As described in Chapter 1, the biological pump is the vertical DIC gradient produced by the export of organic matter from the surface ocean, counteracted by vertical mixing. In the previous chapter we discussed changes in export production using proxies such as opal and Baxs flux. However, these tools are insufficient for reconstructing the biological pump as they provide no information on the resupply of DIC to the surface ocean through mixing. In other words, all else being equal an increase in export production would strengthen the biological pump, however, should the rate of DIC supply more than compensate for the increase in export production then the biological pump would weaken.

Reconstructing the balance between DIC supply and export directly is very challenging due to the constant equilibration of carbon between the ocean and atmosphere. Therefore, paleoceanographers have turned to the reconstruction of nutrients as an indirect approach. This is achieved by assuming that the DIC pumped int the deep ocean by exported organic carbon is stoichiometrically balanced by the regenerated nutrients (Redfield, 1963). Hence, if the nutrients supplied to the surface ocean are not completely used by phytoplankton and exported to the deep ocean then a stoichiometrically equivalent proportion of the DIC also remains. In the case of upwelling regions, DIC in the form of dissolved CO_2 is contained at high partial pressures in the rising deep waters and will subsequently degas upon reaching the surface. If the upwelled nutrients are not completely utilised then the resultant export production would not sufficiently offset this CO_2 emission (Eppley and Peterson, 1979; Broecker, 1982a,b).

The iron limitation of the modern Southern Ocean results in a large proportion of the upwelled nutrients (nitrate and phosphate) going unutilized. Consequently, the Southern

Ocean is termed a high-nutrient, low-chlorophyll region and today much of the surface ocean south of the polar front provides a net efflux of CO_2 to the atmosphere (Mikaloff Fletcher et al., 2007; Lovenduski et al., 2007). An increase in the proportion of nutrients utilised by phytoplankton in the Southern Ocean would stem this leak of CO_2 to the atmosphere and thus may explain the lower glacial atmospheric CO_2. Here we will use the nitrogen isotope geochemistry to reconstruct the relative uptake (utilisation) of nitrate in the Southern Ocean by diatoms, which are the dominant phytoplankton group across much of the Southern Ocean (Ida and Odate, 2014). We will also explore how the nutrient uptake dynamics in the Southern Ocean evolve across the deglaciation, comparing the reconstructions of N uptake with those of dust flux (iron input) and Southern Ocean upwelling.

In addition to an assessment of the Southern Ocean's biological pump, we will also consider the glacial-interglacial variability in the N-cycle. The budget of nitrate in the pre-industrial ocean is governed by N2 fixation as a source, and denitrification as a sink. Denitrification is the bacterially-mediated process by which nitrate is used as an electron acceptor in the oxidation of organic matter. Due to the energetic inefficiency of this process, denitrification in the marine environment is most prominently found within deoxygenated zones in sediments (benthic denitrification) and the water column (pelagic denitrification). Benthic denitrification is widespread throughout the oceans, although it is most important within the high POC flux regions on continental shelves (Middelburg et al., 1996). On the other hand, pelagic denitrification is focused to three distinct oxygen minimum zones (OMZs): the Arabian Sea, the eastern tropical north Pacific (ETNP) and eastern tropical southern Pacific (ETSP), where high POC fluxes combine with poor water column ventilation to produce suboxic (< 5 µM) conditions in the water column at 150 – 500 m water depth (Codispoti et al., 2001).

Changes in the relative importance of N2 fixation versus denitrification will influence the global marine nitrate inventory. Because much of the low latitude ocean is nitrate limited, it has been proposed that changes in the nitrate inventory of the oceans could influence the global biological pump and hence atmospheric CO_2 drawdown (McElroy, 1983; Ganeshram et al., 2000). In addition, N fixation and denitrification operate as part of negative feedback loops, preventing catastrophic swings in the marine nitrate inventory and atmospheric CO_2. For example, if the N inventory of the ocean increases (due to increased input from rivers, for instance) the more productive ocean would place a greater oxygen demand on the subsurface ocean and cause an expansion of OMZs, leading to greater denitrification and a

rebalance of the N budget. Likewise, if the global N inventory is depleted (for example, due to greater organic N burial), N fixers such as *Trichodesmium* will be able to out-compete other organisms for the available phosphate and iron, eventually leading to a greater supply of nitrate to the ocean and a rebalance of the N budget (Ganeshram et al., 2002).

During the last glacial period the deep ocean became deoxygenated, a result of reduced deep ocean mixing (Jaccard et al., 2011). Upon the deglaciation, these deoxygenated deep waters were ventilated by the Southern Ocean (Burke and Robinson, 2012). Simultaneously, primary production increased throughout the Antarctic, increasing the oxygen demand in subsurface waters through greater organic carbon respiration. We will explore whether the compounding influences of low oxygen waters and high oxygen demand influenced denitrification rates in the Southern Ocean during the deglaciation. In doing so, we will discuss the role of changes in deep circulation on the N-cycle through glacial-interglacial cycles.

5.2 Methods

Nitrogen Isotope Geochemistry

Two stable isotopes exist in the natural world, ^{14}N (99.6 % abundance) and ^{15}N (0.4 % abundance) (Lide, 2002). Due their differences in atomic mass, identical molecules containing different N-isotopes will have different zero-point energies. During chemical processes this manifests as isotopic fractionation, whereby molecules containing one of the isotopes undergo a chemical process in greater proportion or at a faster rate than molecules containing the other. In the case of nitrogen, isotopic fractionation occurs during almost all processes within the biologically-mediated nitrogen cycle. Primary producers, such as diatoms, discriminate against the heavier isotope (^{15}N) upon assimilation of dissolved reactive nitrogen. The degree to which fractionation occurs is defined by the isotopic effect, ε. As a result, N-bearing compounds within primary producers will have an N-isotopic composition ($\delta^{15}N$) that is lighter than the stock of dissolved nitrogen from which they are drawing from. As the dissolved nitrogen stock depletes, the isotopic composition of the primary producers approaches that of the initial dissolved nitrogen stock. Therefore, if the $\delta^{15}N$ of the initial N stock is known, the $\delta^{15}N$ of fossil organic matter can provide information on the extent to which the N stock was utilised.

Two models can be applied to reconstruct the N-isotopic fractionation system (Figure 5.1). The 'closed system' is applied when the dissolved nitrogen stock is not replenished during the fractionation process (i.e. the N stock is limited), whilst the 'open system' assumes the total dissolved nitrogen stock is continuously replenished such that a steady state is reached between the supply of the dissolved nitrogen and its uptake by phytoplankton. The equations used for each of the two models are displayed in Figure 5.1 along with graphical representations of their output. In most cases the 'closed system' model is applied to dissolved nitrogen uptake by phytoplankton as the vertical supply of nitrate into the mixed layer during summer is often negligible.

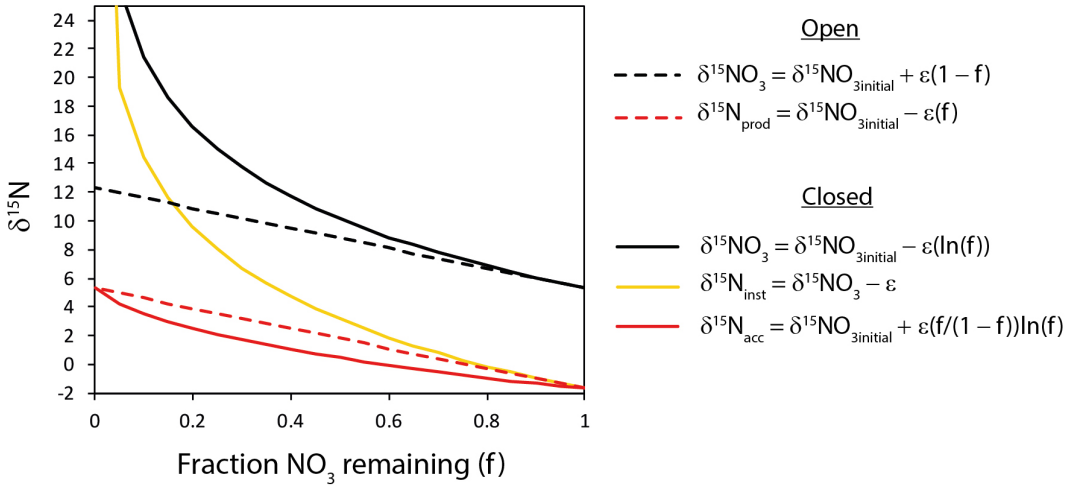

FIGURE 5.1: Illustration of the fractionation kinetics of nitrogen isotopes along with the two models (open or closed) applied to natural systems.

From Figure 5.1 it is possible to see that, assuming constant values for ε and $\delta^{15}N_{initial}$ (this assumption will be discussed later), changes in $\delta^{15}N_{prod}$ or $\delta^{15}N_{acc}$ can be interpreted in terms of relative uptake of the dissolved nitrogen pool. In this case, greater values of $\delta^{15}N_{prod}$ or $\delta^{15}N_{acc}$ indicate more complete nutrient utilisation and thus a greater proportion of upwelled DIC being pumped back into the deep ocean.

Palaeoceanographic reconstructions of $\delta^{15}N$

Reconstructing changes in $\delta^{15}N_{prod}$ or $\delta^{15}N_{acc}$ through time requires the isotopic analysis of organic matter derived from sinking phytoplankton within sediment records. Figure 5.2 displays the results of two surface sediment $\delta^{15}N$ transects across the Indian sector of the Southern Ocean (Altabet and Franois, 1994). The isotopic composition of the bulk sediment

was determined via the now well-adopted combustion method (e.g. Altabet et al., 1995; Francois et al., 1997). The northward ^{15}N enrichment in the sediments of the Southern Ocean tracks the depletion of nitrate in the surface ocean away from the upwelling source in the AZ, confirming that the proxy is a good indicator of N utilization. One caveat that was realised during this study was that buried sediments were more ^{15}N-enriched (isotopically heavier) than expected given the uptake in the surface ocean (black line in Figure 5.2) and the $\delta^{15}N$ of particles suspended within the surface ocean (Wada et al., 1987; Altabet and Fracois, 1994). This offset was found to be most pronounced in the diatomaceous sediments of the Southern Ocean and was hence suggested that the organic compounds incorporated into the frustules of diatoms are ^{15}N-enriched and selective preservation of diatoms within the Southern Ocean would result in a ^{15}N-enrichment of the bulk sediment (Shemesh et al., 1993; Altabet and Francois, 1994). Nevertheless, core-top studies such as the one presented in Figure 5.2 suggest that the use of sedimentary $\delta^{15}N$ appears to be a suitable, albeit qualitative indicator of changes in N utilisation.

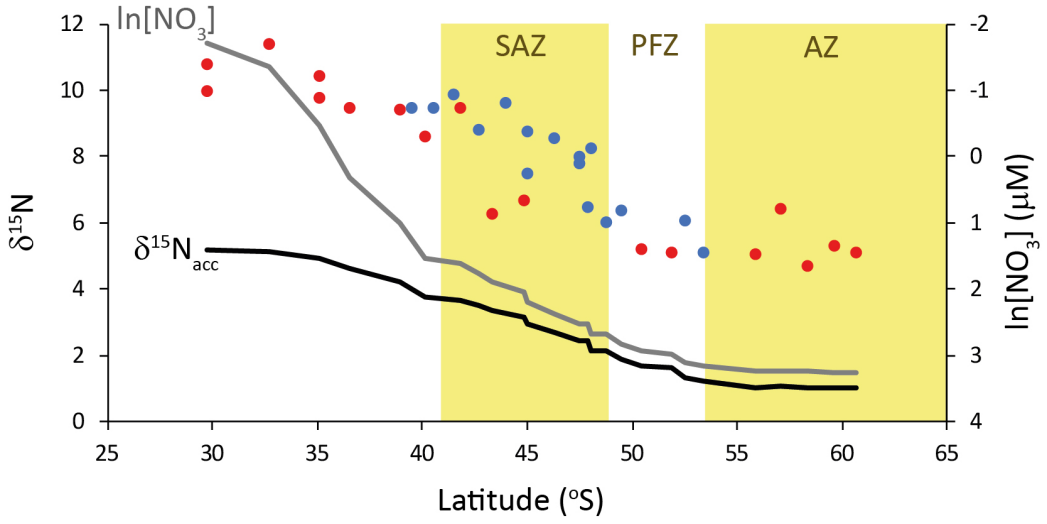

FIGURE 5.2: Blue and red data bulk sediment $\delta^{15}N$ measurements within two transects across the Indian sector of the Southern Ocean (red = eastern, blue = western from Altabet and Francois, 1994). The grey line is an estimation of the late summer (March) surface nitrate concentrations across the same region (WOA13, Garcia et al., 2013). The black line is the predicted sedimentary $\delta^{15}N$ ($\delta^{15}N_{acc}$) assuming the progressive consumption of the surface nitrate pool northwards and an $\delta^{15}N_{initial}$ of 5.3‰.

Recent developments have permitted the isolation and isotopic analysis of the diatom-bound organic matter (Sigman et al., 1999; Robinson et al., 2004). The advantages of using this material are two-fold: Firstly, although the offset between the expected $\delta^{15}N$ and the measured $\delta^{15}N$ described above is maintained, biases related to variations in sediment

mineralogy (i.e. changes in opal content) through time and would be reduced. Secondly, biases derived from diagenetic alteration are also mitigated against. The organic matter encased within diatom frustules is relatively N-rich and consist of mostly of polyamines and proteins (Swift and Wheeler, 1992, Kroger et al., 1999; Kroger et al., 2000; Kroger et al., 2002; Ingalls et al., 2004) but also include amino acids (predominantly glycine) (Shemesh et al., 1993; Ingalls et al., 2003). It is argued that these labile compounds encased within the diatom frustules are protected from diagenetic alteration. This has been corroborated by studies demonstrating that the amino acid composition in Southern Ocean diatom-bound organic matter varies little between the surface ocean and the sediments (Ingalls et al., 2003), and this composition is maintained in LGM sediments (Shemesh et al., 1993). Further, these hydrolysable amino acids remain resistant to harsh chemical treatment (perchloric acid and hydrogen peroxide oxidation) until they are released from the opal frustule (Kroger et al., 1999; Ingalls et al., 2003; Ingalls et al., 2004), with little evidence to suggest partial dissolution of diatom frustules results in N-isotopic fractionation (Ren et al., 2013).

Here the $\delta^{15}N$ analysis of diatom-bound material ($\delta^{15}N_{DB}$) is employed to reconstruct the N utilisation of phytoplankton in the Southern Ocean. Because the organic content within diatom frustules is so small ($\sim$10 μmol N/g opal, Robinson et al., 2004) a large mass of diatomaceous material is required for N-isotopic analysis using traditional combustion techniques. Such a large mass of material can lead to inefficient combustion of the sample material, resulting in the production of carbon monoxide, increasing isobaric interferences with N_2 (Beaumont et al., 1994). Further, it has been suggested that the highly porous diatomaceous material may trap a reservoir of atmospheric N_2 which fractionates upon combustion producing further interferences (Robinson et al., 2004). These issues are circumvented by the employment of the persulphate-denitrifier technique (Sigman et al., 2001; Robinson et al., 2004). The full details of this method are described in the Methods. In short, pure diatomaceous matter is separated from the bulk sediment through step-wise physical separation and chemical cleaning. The resultant purified diatomaceous material is then digested in a sodium persulphate solution to quantitatively oxidise the diatom-bound organic nitrogen to nitrate. This nitrate product is then reduced to N_2O gas by bacterial denitrification and injected into a continuous flow GC-IRMS system.

For the analyses performed on the three cores presented here; a total, 124 unique samples were analysed, 91 of which were triplicated from the denitrifier stage onwards and 50 were measured in duplicate or triplicate from the persulphate digestion stage onwards. Average

errors calculated via the regression method given in the Methods Chapter were ±0.33 ‰(1σ), better than previously published errors (Robinson et al., 2014). The errors for individual samples are displayed as error bars in Figure 5.3.

5.3 Results and interpretation

Holocene

The $\delta^{15}N_{DB}$ data from the three cores are presented in Figure 5.3. Due to the nature of piston coring, the core top of MD84-551 was lost and so much of the Holocene from this record is absent. Nearby core MD84-552 (54.9167°S, 73.8333°E, 1780 m depth) has a preserved Holocene section and has been analysed in low resolution for $\delta^{15}N$ as both the bulk method (Francois et al., 1997) as well as the same persulphate denitrifier method used here (Robinson et al., 2004). A comparison of the $\delta^{15}N_{DB}$ data is given in Figure 5.3, which shows a reasonable similarity, albeit at a low resolution. Hence, the Holocene section of MD84-552 was spliced onto the MD84-551 record so that comparisons with the Holocene can be made.

In the modern Southern Ocean, the surface water $\delta^{15}NO_3$ increases northward from the region of greatest $[NO_3]$ supply in the AZ to the oligotrophic subtropical gyres where primary productivity is predominantly fuelled by regenerated N (Sigman et al., 1999; Altabet and Francois, 2001; DiFiore et al., 2006). A northward gradient in $\delta^{15}N_{DB}$ is not exhibited during the late deglaciation and Holocene between the three records presented here. Numerous studies (Altabet and Francois, 2001; Robinson and Sigman, 2008; Difiore et al., 2010) have noted a shift in the isotopic effect, ε, in modern Southern Ocean waters from approximately 5 ‰south of the Southern ACC Front (SACCF) to 8 ‰towards the SAF. This εshift appears to also be expressed in the $\delta^{15}N_{DB}$ of surface sediments, with $\delta^{15}N_{DB}$ decreasing between the PF and SAF by 2 ‰along an Indian sector transect (Robinson et al., 2004). This transition correlates well with the deepening of the summer mixed layer depth and has been suggested to be a result of changes in light availability (Needoba and Harrison, 2004; Difiore et al., 2010). The difference between MD88-551/2 and MD88-772 during the Holocene is approximately 1 ‰, well within the range of the observed εvariability. This εbias is exacerbated by the relatively weak surface $[NO_3]$ gradient observed in the Southern Ocean south of the SAZ as demonstrated in Figure 5.2. It should be noted that because $\delta^{15}N_{DB}$

offsets caused by differences in ε approach zero as N utilisation increases, offsets in $\delta^{15}N_{DB}$ related to variable ε become less important outside of the Holocene N utilisation minimum. We therefore attribute the irregular $\delta^{15}N_{DB}$ gradient observed between the records during the Holocene to differences in ε but this mechanism cannot explain the gradient observed during periods of high N utilisation prior to the Holocene.

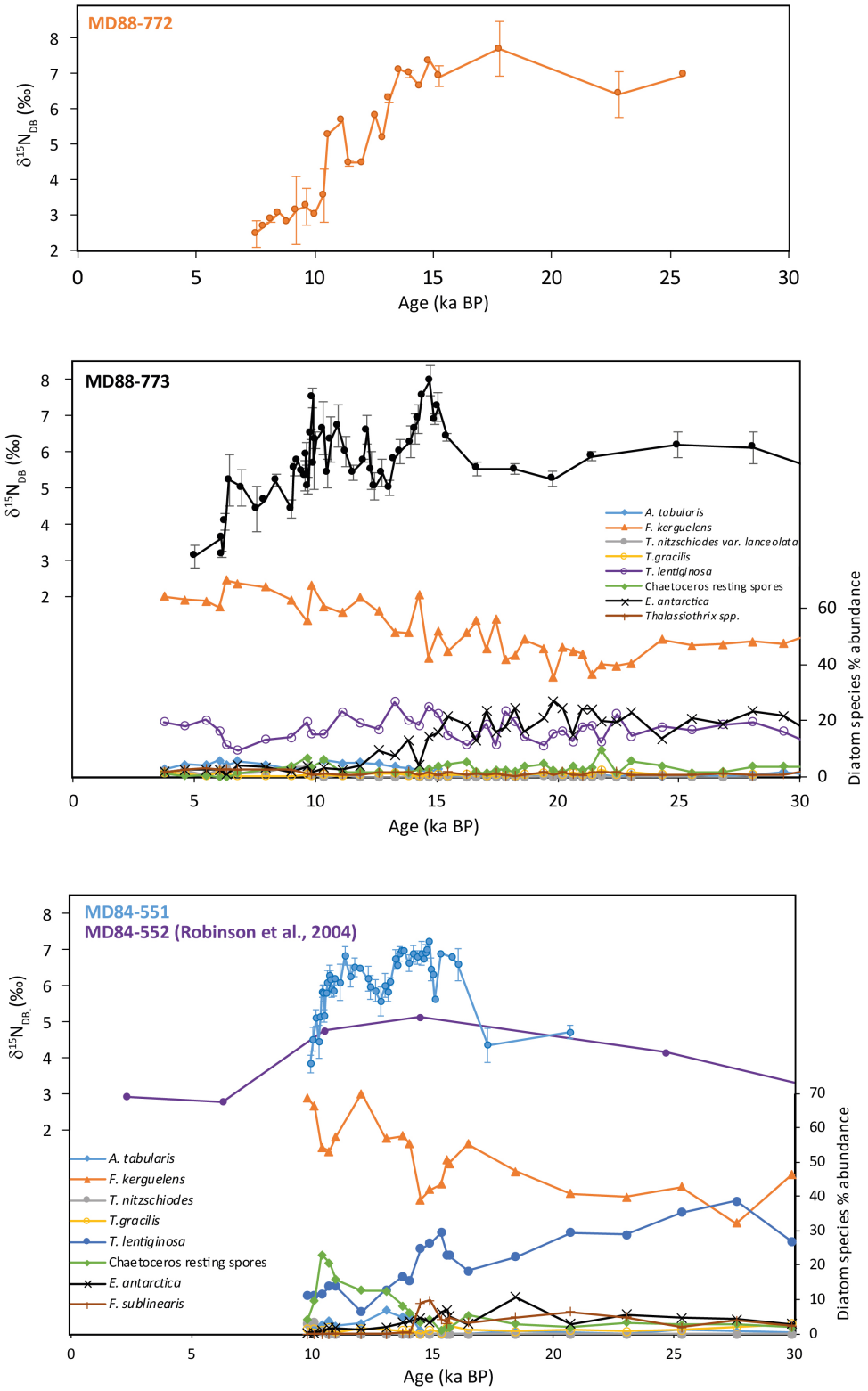

FIGURE 5.3: $\delta^{15}N_{DB}$ data from MD88-772 (top), MD88-773 (middle) and MD84-551 (bottom) along with a comparison with diatom assemblage data from MD84-551 and MD88-773 (Crosta, X. unpublished). $\delta^{15}N_{DB}$ data from nearby MD84-552 is also presented for comparison (Robinson et al., 2004).

The last glacial period: The Antarctic Zone and the Biological Pump

All three records can be characterised by higher $\delta^{15}N_{DB}$ during the LGM (18 – 23 ka BP) relative to the Holocene, with an overall decrease of 1 – 5.2 ‰. The magnitudes of these changes are within the range of other Southern Ocean records (e.g. Crosta et al., 2005; Horn et al., 2011 Robinson et al., 2014) and comparable to the variability observed in Southern Ocean deep sea corals (4.5 ‰) that feed from the organic matter settling out of the surface ocean (Wang et al., 2017).

The LGM-Holocene $\delta^{15}N_{DB}$ variability differs markedly between the three records, with the smallest overall change observed in the southern-most record, MD84-551 ($\sim$1 ‰), and the greatest observed in the northern-most core, MD88-772 ($\sim$5 ‰). The small overall LGM-Holocene change observed in MD84-551 is within the range of εvariability observed in the modern ocean (Difiore et al., 2010) and therefore may in fact reflect changes in MLD. It is therefore unclear whether N utilisation changed within this region between the LGM and today.

What factor or mechanisms could trigger an increase in N utilisation during the LGM relative to the present? Two competing scenarios have been widely discussed in the literature over the last few decades: increased relative utilisation of N due to lower supply from below (lower upwelling or stratification due to the presence of ice) (Francois et al., 1997) or a more efficient N utilisation stimulated by greater Fe availability (Martin, 1990). In the Southern Ocean the primary drivers of changes in N utilisation are the stoichiometric availability of iron relative to N and light availability (Mitchell et al., 1991; Boyd et al., 1999; Sedwick et al., 2002). An increase in the Fe:NO_3 ratio of the surface ocean will drive an increase in N utilisation (Boyd et al., 2000; Coale et al., 2004). An increase in the Fe:NO_3 ratio of the surface ocean can be brought about by a greater exogenous bioavailable Fe flux to the surface ocean. In addition, since the deep waters upwelling to the AZ are stoichiometrically deficient in Fe relative to NO_3 (Boyd and Ellwood, 2010; Tagliabue et al., 2017) a reduction in deep upwelling would also drive a relative increase in the Fe:NO_3 ratio of the surface ocean even if exogenous Fe supply remained unchanged. On the other hand, a decrease in light availability in response to increased sea ice cover could lower N utilisation. Therefore, light availability is not a good candidate to explain the observed changes.

Distinguishing between lower N supply or greater N consumption by biota can be resolved by interpreting the productivity proxies in the cores presented here (Chapter 4) and more broadly

in the Southern Ocean. The lower productivity observed in glacial sections of Antarctic records can be driven by either lower nutrient or lower light availability. A productivity decrease driven entirely by light limitation would yield lower N utilisation than today and thus a lower $\delta^{15}N_{DB}$, which is not observed in MD84-551. The increased sea ice extent during the LGM (Gersonde et al. 2005; Wolff et al., 2006) may have shortened the growing season at MD84-551, thus limiting the nutrient utilisation somewhat. However, the dominance of open ocean species such as *F. kerguelensis* and *T. lentiginosa* throughout the record (Figure 5.3) indicates that the region surrounding MD84-551 remained ice-free through the summer months, in agreement with the poleward position of the summer sea ice limit from MD84-551 based on reconstructions by Gersonde et al (2005).

This description of productivity and nutrient uptake in the glacial AZ contradicts some interpretations given by other authors. Abelmann et al (2006) suggested that the diatom assemblage changes in the Atlantic AZ may in fact be driving both the nutrient utilisation and productivity proxy variability. It was suggested that the biome dominated by lightly silicifying *Chaetoceros* and the haptophyte, *Phaeocystis antarctica* shifted northward to occupy the glacial AZ and the heavily silicifying *F. kerguelensis* shifted into the Subantarctic. Consequently, it was argued that the glacial AZ became a high-carbon, low-silica export region, whilst the Subantarctic became high-silica, low-carbon due to these shifts in species assemblage. It was suggested that opal flux would therefore not be a good productivity proxy in the glacial AZ due to the dominance of non- or lightly-silicifying phytoplankton and other productivity proxies such as barium flux have inherent biases (Abelmann et al., 2006). Furthermore, *Phaeocystis antarctica* have a higher N demand than diatoms, which may explain the higher N utilisation detected in the AZ during the LGM (Arrigo et al., 1999; Abelmann et al., 2006).

Chaetoceros resting spores dominate diatom assemblages in surface sediments downstream from the Antarctic Peninsula today (Crosta et al., 1997). This biome seems to have extended further into the Atlantic sector during the LGM (Abelmann et al., 2006) and therefore may have influenced the productivity and nutrient uptake regime there. However, changes in phytoplankton assemblage cannot explain the productivity and nutrient utilisation proxies within MD84-551. The highly silicifying species, *F. keguelensis* is the most abundant diatom species from the assemblage data across the LGM (40 – 47 %), whilst Chaetoceros resting spores are significantly rarer (2 – 3 %). Furthermore, we suggest based on U_{auth} analyses that the Ba_{xs} proxy data in MD84-551 does not seem to have undergone diagenetic alteration

(see Chapter 4), therefore the record is indeed indicating lower export production during the LGM. Because *Phaeocystis* do not preserve in sediments it is difficult to substantiate whether they did dominate AZ ecosystems during glacial periods. However, the good agreement between Ba_{xs} and opal flux in MD84-551 seems to suggest that diatoms were controlling carbon export across the last glacial cycle as they are in the AZ today (Honjo et al., 2000). On balance, these evidences suggest that productivity and biogenic export were slightly lower during the LGM compared to today in the AZ despite reported greater Fe supply and points to decreased upwelling-driven nitrate supply to the surface as responsible for the observed increase in $\delta^{15}N$. This agrees with existing interpretations by Francois et al. (1997).

This interpretation has significant implications for the explanation for glacial-interglacial changes in atmospheric CO_2. Global atmospheric CO_2 has been suggested to be particularly sensitive to changes in the efficiency of the biological pump within the AZ (Sigman et al., 2010). Since carbon and nutrients in upwelled waters are stoichiometrically tied to the composition of marine organisms (Redfield, 1963; Eppley and Peterson, 1979), nutrients going unutilized in the AZ before being subducted into the deep ocean represent a leak in the biological pump, allowing carbon to degas to the atmosphere without being offset by biological draw down. Because the AZ ventilates a large proportion of the ocean interior the total global unutilised (preformed) nutrient subduction to the deep ocean is largely controlled by inputs from the AZ (Knox and McElroy, 1984; Sigman et al., 2010). The minor change in $\delta^{15}N_{DB}$ between the LGM and the Holocene in MD84-551 implies only a small or even no change in the utilisation of the upwelled N pool within the AZ itself, leaving much of the poleward nitrate to re-enter the ocean interior as glacial AABW. This suggests that the importance of dust-borne iron in controlling the biological pump in the AZ (and the preformed nutrient content of the ocean interior) was minor in comparison to changes in nutrient supply. Hence, these data favour deep upwelling strength in the AZ as an ultimate control changes in the exchange of CO_2 between the ocean and atmosphere through glacial-interglacial cycles (Francois et al., 1997; Toggweiler, 1999).

The last glacial period: Nutrient dynamics of the Southern Ocean

Further to the north, the larger $\delta^{15}N_{DB}$ gradient (~ 3 ‰) between MD84-551 and MD88-772 during the LGM strongly suggests that nitrate utilisation increased between the core sites

(Figure 5.4) compared to today. Cores MD88-769 (central SAZ, 46°04'S) and MD97-2101 (northern SAZ, 43°30'S) (see locations in Figure 5.5) have associated $\delta^{15}N_{DB}$ data (Crosta et al., 2005, Figure 5.4) that can be used to extend the meridional transect across the remainder of the Subantarctic from 55°S (MD84-551 to 43°30'S (MD97-2101). An important caveat to consider is the apparent inter-laboratory $\delta^{15}N_{DB}$ variability produced by differing analytical techniques (Robinson et al., 2004; Crosta et al., 2005). Nevertheless, comparisons can be made between the $\delta^{15}N_{DB}$ changes observed within cores (i.e. the LGM-Holocene $\delta^{15}N$ change) as well as gradients between cores analysed by the same analytical technique.

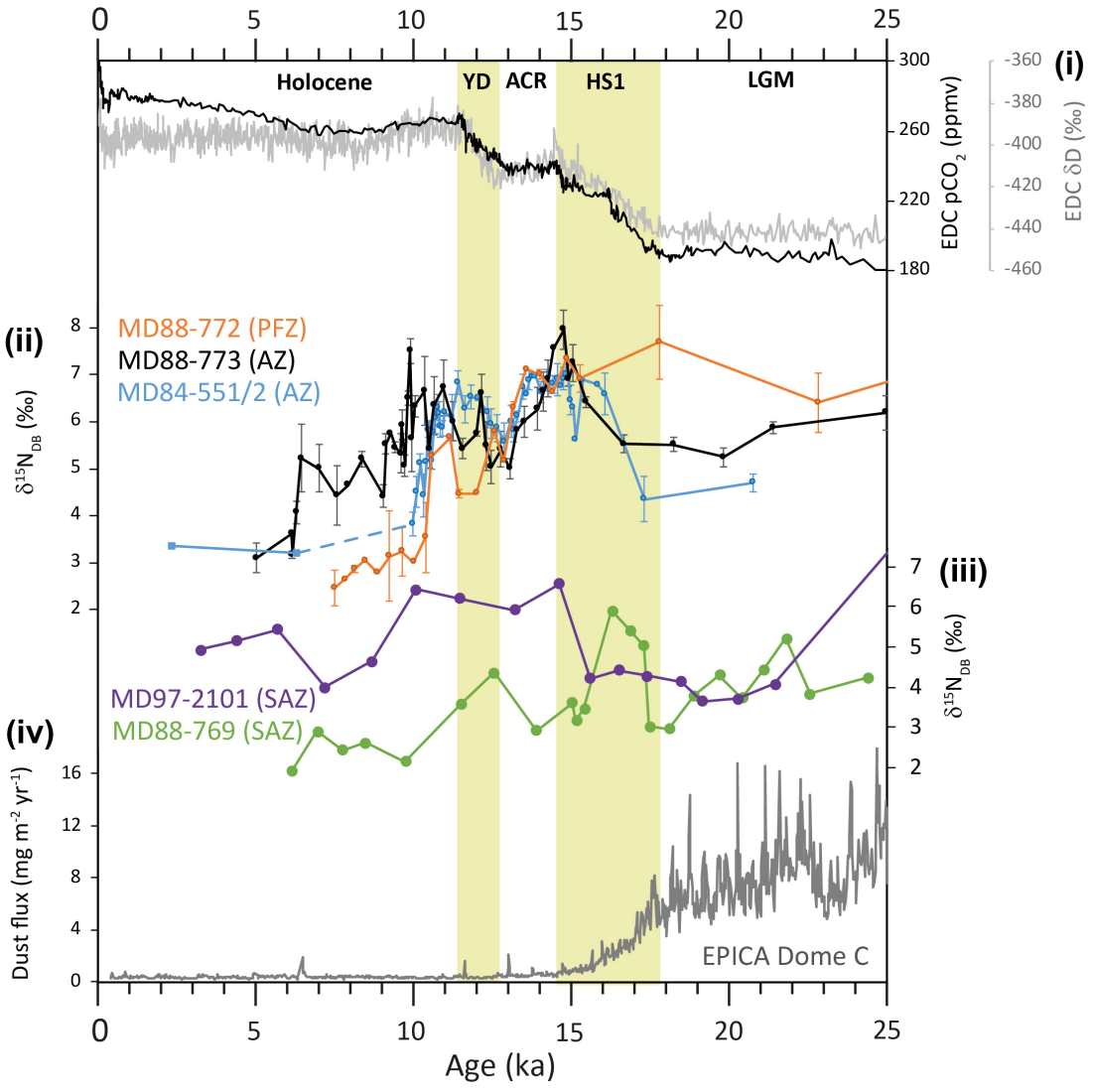

FIGURE 5.4: **(i)** Atmospheric CO_2 (Monnin et al., 2001) and Antarctic temperature proxy (Parrenin et al., 2013) data from EPICA Dome C. **(ii)** $\delta^{15}N_{DB}$ data from the three Indian sector cores. The dashed line indicates the splicing between MD84-551 and MD84-552 (Robinson et al., 2004). **(iii)** $\delta^{15}N_{DB}$ data from two Indian sector SAZ records (see Figure 5.5) (Crosta et al., 2005). Dust flux to Antarctica recorded in EPICA Dome C (Lambert et al., 2012).

MD88-769 and MD97-2101 are located closer to the modern N front in the Southern Ocean (Figure 5.5), which is expressed in the records as a large $\delta^{15}N_{DB}$ gradient (2 – 3.5 ‰) between the two records during the Holocene. In contrast to the $\delta^{15}N_{DB}$ data from our records, the gradient between MD88-769 and MD97-2101 reduces to zero during the LGM. This contradicts the notion that the diatoms were supplied from an advected source of nitrate that was more utilized during the LGM, as this would have produced a larger gradient.

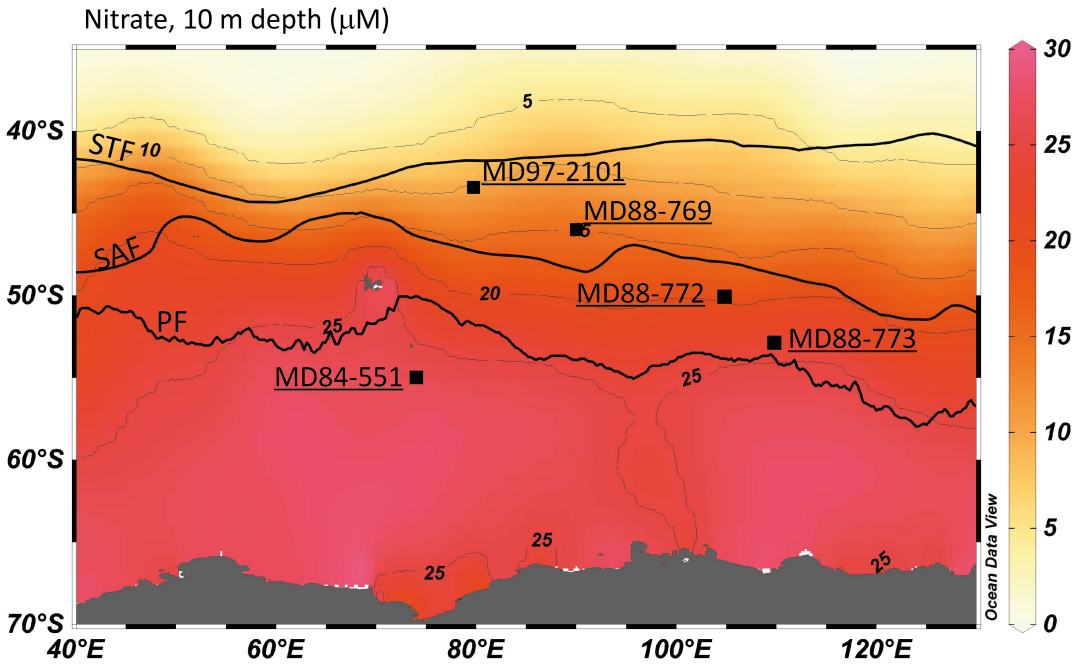

FIGURE 5.5: Map of the core locations shown in Figure 5.4 on a background of gridded surface water nitrate concentrations. Nitrate data from WOA13 (Garcia et al., 2013). Front locations based on Orsi et al (1995). Produced using ODV software (Schlitzer, 2002).

However, in the modern Southern Ocean, the thermocline water in the SAZ mix with the subtropical surface waters to the north (Sigman et al., 1999; Difiore et a., 2006). This changes little with respect to the $\delta^{15}NO_3$ gradient because the nitrate derived from the south overwhelms the $\delta^{15}NO_3$ signal nitrate-poor subtropical waters. Hence, as argued by Crosta et al (2005), the lack of an LGM-Holocene $\delta^{15}N_{DB}$ change in MD97-2101 can be attributed to a change in the source of nitrate being utilized by the diatoms. Reducing the Antarctic supply of nitrate due to Antarctic stratification and iron fertilization would have placed a greater importance on the supply of nitrate from the subtropics. Therefore, the removal of a $\delta^{15}N_{DB}$ gradient between MD88-769 and MD97-2101 could be due to a

shift towards oligotrophic conditions in the SAZ and the nitrate pool delivered by Ekman transport from the south became largely depleted.

The development of the $\delta^{15}N_{DB}$ gradient between MD84-551 and MD88-772 during the LGM suggests that the N front had indeed shifted southwards from its position in the SAZ today closer to the modern polar front position. Based on the assessment of productivity proxies in Chapter 4, it was argued that the centre of the opal belt was located close to MD88-772 and MD88-773 during the LGM. Therefore, the location of the LGM opal belt (just north of the modern PF, see Chapter 4) appears to more closely correspond with the N front during the LGM, which contrasts with modern conditions, whereby the opal belt corresponds to the Si front (Chase et al., 2003). This supports the notion that the Southern Ocean as a whole was characterised by nitrate limitation during the LGM as opposed to the current situation where diatom production is constrained by Fe-Si co-limitation. This shif in the nutrient status of the Southern Ocean was driven by a shift in the Si and N demand of diatoms under changing Fe availability (Brzezinski et al., 2002).

N-cycling across the last deglaciation

While our $\delta^{15}N$ and productivity records corroborate and refine the previously proposed interpretations that Southern Ocean upwelling-controlled CO_2 efflux and nutrient cycling at glacial-interglacial timescales (Francois et al., 1997), they record $\delta^{15}N$ changes during the deglaciation with unprecedented resolution, enabling the detailed study of marine nitrate cycling during this highly dynamic time period.

The onset of the last deglaciation occurs at 18 ka BP and is marked in Antarctic ice cores by the initiation of atmospheric CO_2 and Antarctic temperature rise (Parrenin et al., 2013) as well as an abrupt decline in Antarctic dust flux (Lambert et al., 2012). Across the deglacial period there are two major intervals of atmospheric CO_2 rise, referred to here as HS1 (14.5 – 18 ka BP) and YD (11.5 – 12.8 ka BP) due to their association with the respective North Atlantic cooling events. The pause in CO_2 rise separating these two intervals is the Antarctic Cold Reversal (Bølling-Allerød), which we will refer to as the ACR hereon.

It has been proposed that much of the CO_2 rise across both HS1 and the YD was a response to the removal of glacial stratification in the Southern Ocean, allowing the aged deep waters to ventilate at the surface and degas CO_2. The nutrient content of these glacial deep waters

is unknown; however, we would expect the greater overturning during these periods to contrast with the LGM conditions described in the previous section that are characterised by low N supply through stratification.

Illustrated in Figure 5.6, the deglacial transition in $\delta^{15}N_{DB}$ progresses in markedly different fashions between the three cores. The northern core, MD88-772, displays an abrupt decline in $\delta^{15}N_{DB}$ from its LGM values beginning at approximately 13.6 ka BP and ending at $\sim$ 10 ka BP with a brief pause at 10.5 - 12.5 ka BP. The two AZ cores (MD84-551 and MD88-773) exhibit overall greater $\delta^{15}N_{DB}$ values during the deglaciation compared to the LGM. The early deglacial increase in $\delta^{15}N_{DB}$ reaches peak $\delta^{15}N_{DB}$ values by $\sim$ 14.8 ka BP. The 1 – 3 ‰elevation in $\delta^{15}N_{DB}$ above LGM values is interrupted in both cores by a brief decline between 13 ka BP and 14.5 ka BP, approximately coinciding with the ACR. Subsequently the $\delta^{15}N_{DB}$ value of both cores elevates once again through the late deglaciation, approximately coinciding with the YD interval and the pause in $\delta^{15}N_{DB}$ decline observed in MD88-772.

The deglacial pattern of $\delta^{15}N_{DB}$ decline in all three of the cores is puzzling as it does not appear to agree with the assumption that N utilisation in the Southern Ocean is governed by the Fe:NO_3 availability in the surface ocean. As discussed in Chapter 4, during the intervals of deglacial CO_2 rise, Antarctic stratification was removed leading to intensified deep upwelling. Deep waters today are stoichiometrically depleted in Fe relative to NO_3 due to Fe scavenging (Boyd and Ellwood, 2010). Therefore, this deep upwelling should have encouraged a decrease in N utilisation and therefore a drop in $\delta^{15}N$ during these intervals. Further, based on Antarctic dust flux reconstructions the exogeneous Fe supply to the Southern Ocean also decreased during this period, which would have further decreased N utilisation leading to a decline in $\delta^{15}N_{DB}$. The pattern of deglacial dust flux to the Indian sector of the Southern Ocean is unknown, however, it is suggested that Patagonia was a dominant source to the Southern Ocean as a whole (Mahowald et al., 2006). Therefore, the aridity of this dust source region likely influenced dust fluxes to both the Antarctic continent and Indian sector. N-alkane data from MD94-103, north-west of MD88-772, indicate the dust source regions to the Indian sector likely reached Holocene-like conditions by 14 ka BP (Figure 5.6. Sicre et al., 2006), suggesting an approximate concordance with the Antarctic dust flux record (Figure 5.6).

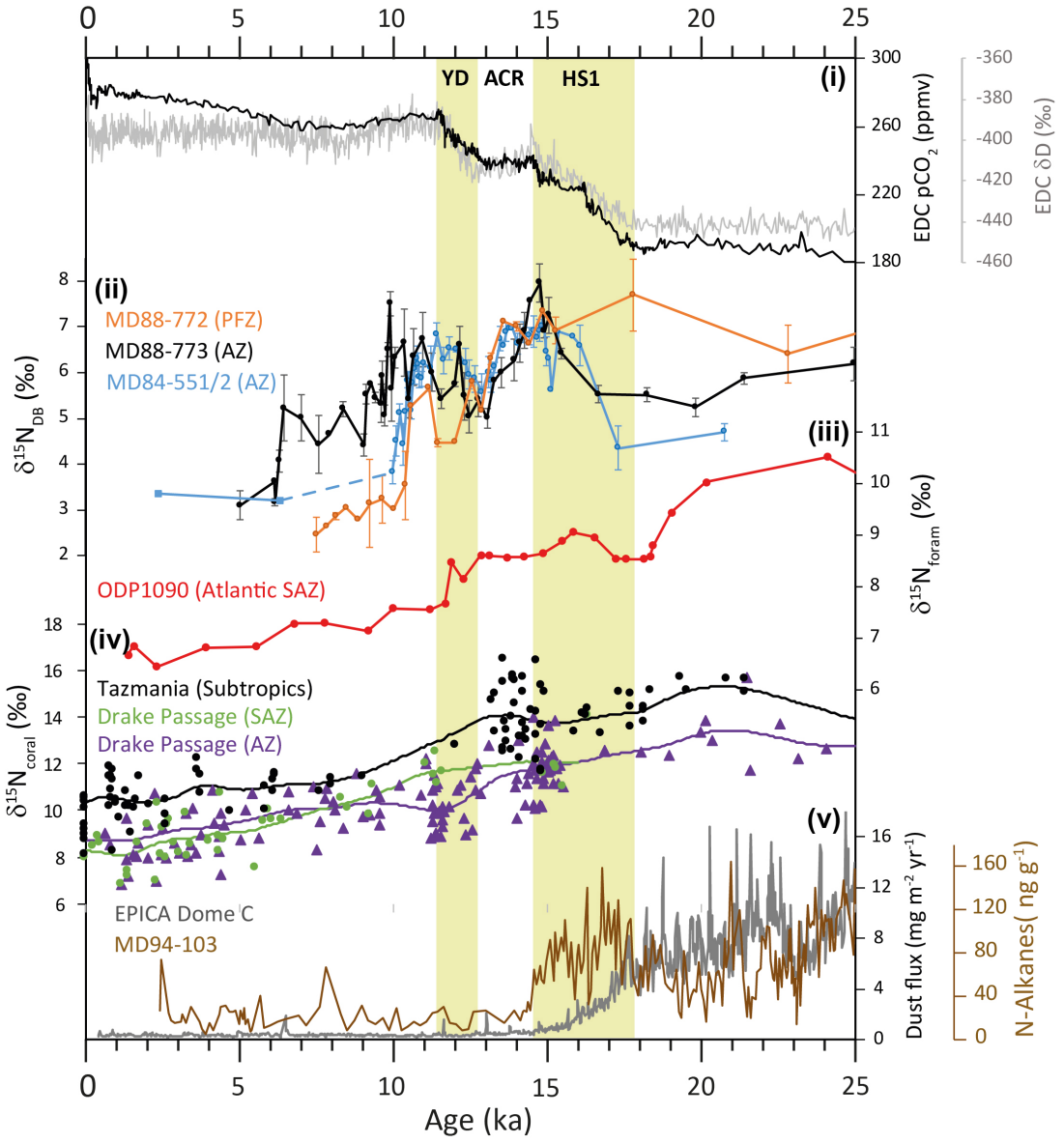

FIGURE 5.6: Plot of nitrogen isotope data from various Southern Ocean records demonstrating the delayed decline in nitrogen isotopes compared to the decline in dust flux. **(i)** Atmospheric CO_2 (Monnin et al., 2001) and Antarctic temperature proxy (Parrenin et al., 2013) data from EPICA Dome C. **(ii)** $\delta^{15}N_{DB}$ data from the three Indian sector cores. The dashed line indicates the splicing between MD84-551 and MD84-552 (Robinson et al., 2004). **(iii)** Foraminifera-bound $\delta^{15}N$ record from the Atlantic sector (Martinez-Garcia et al., 2014). **(iv)** Coral-bound $\delta^{15}N$ records from the various regions of the Southern Ocean (Wang et al., 2017). **(v)** Dust flux to Antarctica recorded in EPICA Dome C (Lambert et al., 2012) and N-alkane content of Indian sector core MD94-103 (Sicre et al., 2006).

As demonstrated in Figure 5.6, rather than a clear decline in $\delta^{15}N_{DB}$ as expected, the three cores presented here display an increase or no change in $\delta^{15}N_{DB}$ during the period of dust flux decline (14 – 18 ka BP) and the two periods of CO_2 rise (11.5 – 13 ka BP and 14.5 – 18 ka BP). The unexpectedly high $\delta^{15}N_{DB}$ values during these events are more apparent in

the Antarctic cores (MD84-551 and MD88-773). However, the primary periods of decline in MD88-772 (10 – 11 ka BP and 12.5 – 13.5 ka BP) are also not aligned to the intervals given above, rather, they occur during periods of minimal dust flux and relatively unchanging atmospheric CO_2. These misalignments cannot be attributed to errors in the age model as the entire deglacial decline in $\delta^{15}N_{DB}$ bracketed by radiocarbon dates. For example, the offset between the onset of the $\delta^{15}N_{DB}$ decline in MD88-773 (13.57 ka BP) and the end of the dust flux decline (14 ka BP) cannot be resolved by changes in the radiocarbon reservoir age (see Chapter 3).

Numerous $\delta^{15}N$ records from across the Southern Ocean also exhibit either a positive excursion or a pause in the $\delta^{15}N$ decline across the deglaciation. For example, Wang et al (2017) presented $\delta^{15}N$ records from deep sea corals collected from near Tasmania and the Drake Passage which showed negligible decline between the LGM and ∼14 ka BP and decreased by approximately 4 ‰thereafter (Figure 5.6) Another example is the foraminifera-bound $\delta^{15}N$ record in ODP1090 presented by Martinez-Garcia et al (2014), which correlates well with down-core dust flux proxies with the exception being a positive excursion at 12 – 17 ka BP (Figure 5.6). Both of these studies attribute the delayed decline in $\delta^{15}N$ during the deglaciation to an increase in the lateral supply of isotopically fractionated NO_3 from the AZ. It is suggested that vertical NO_3 supply to the Subantarctic, where the records from these two studies are located, overwhelmed lateral supply during the LGM due to stratification of the AZ. Upon the deglaciation, initiation of upwelling in the AZ would place a greater importance on laterally advected NO_3 from the AZ that has undergone isotopic fractionation through utilisation.

The same mechanism cannot be used to explain the $\delta^{15}N_{DB}$ excursions observed in the Antarctic records here. In the modern Southern Ocean, nitrate supply in the Antarctic is dominated by vertical mixing of deep waters. Conversely, lateral contributions from the south act to lighten the $\delta^{15}NO_3$ supplied to the more northern AZ mixed layer due to the lower initial $\delta^{15}NO_3$ supplied to the more polar regions by LCDW (∼4.8 ‰) as well as the effect of a lower εon $^{15}NO_3$ fractionation (Sigman et al., 1999a,b; Difiore et al., 2010). Therefore, it is unlikely that a lateral supply mechanism could have driven an increase in the $\delta^{15}N_{DB}$ in the AZ records. Further, an increase in the importance of lateral supply of fractionated NO_3 would produce a divergence of the $\delta^{15}N_{DB}$ gradients between the records presented here. Instead we observe a reduction in the meridional $\delta^{15}N_{DB}$ gradient from the LGM into the deglaciation, suggesting that N utilisation between the cores was reduced.

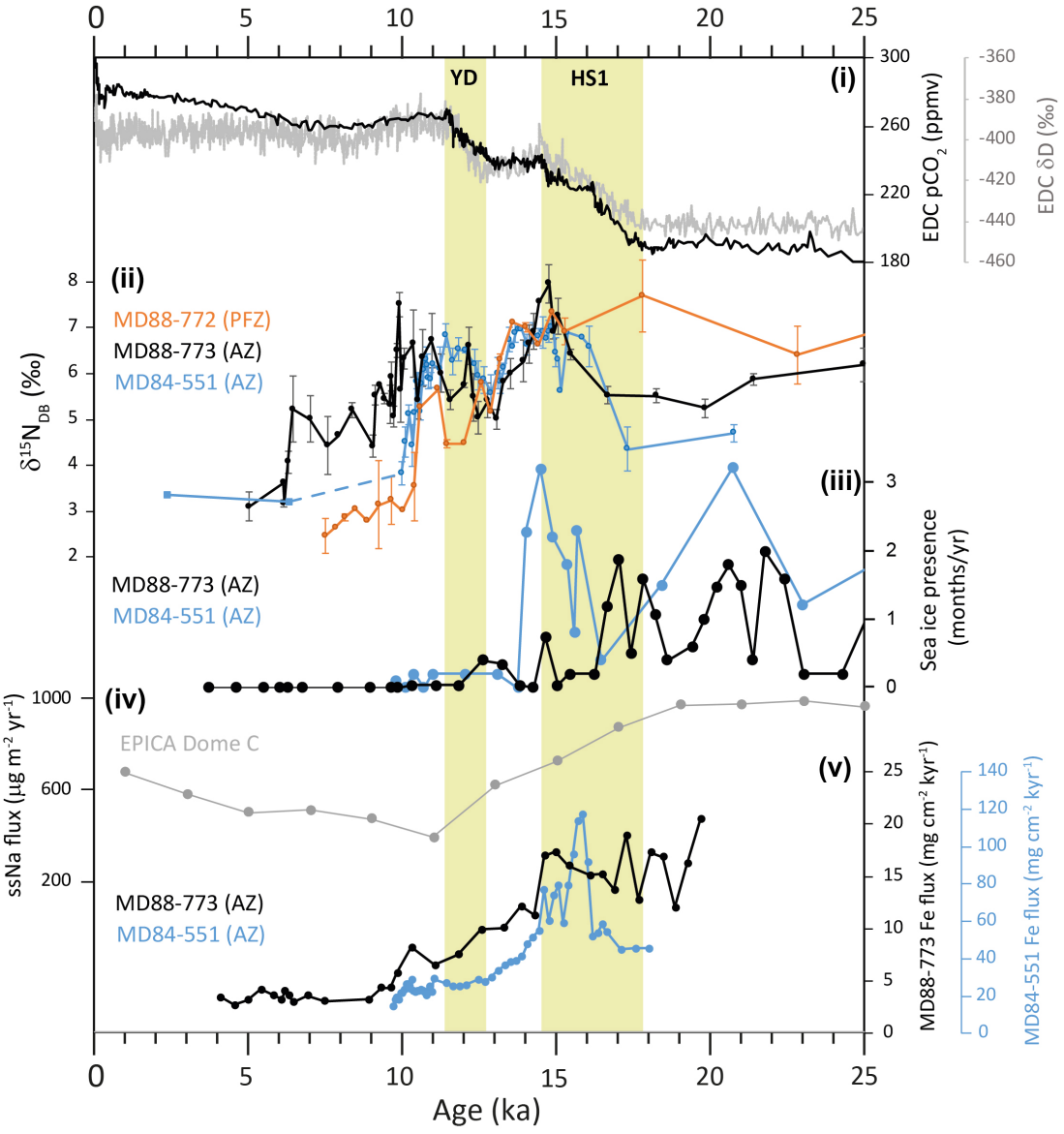

FIGURE 5.7: Records of potential climatic drivers of the $\delta^{15}N_{DB}$ variability observed. **(i)** Atmospheric CO_2 (Monnin et al., 2001) and Antarctic temperature proxy (Parrenin et al., 2013) data from EPICA Dome C. **(ii)** $\delta^{15}N_{DB}$ data from the three Indian sector cores. The dashed line indicates the splicing between MD84-551 and MD84-552 (Robinson et al., 2004). **(iii)** Diatom-based reconstructions of sea ice extent from MD84-551 and MD88-773 (Crosta, X, unpublished). **(iv)** Regional sea ice extent proxy from EPICA Dome C (Wolff et al., 2006). These three sea ice records demonstrate that sea ice and limited nutrient supply by stratification are unlikely drivers of the deglacial increase in $\delta^{15}N_{DB}$.**(v)** Th-normalised iron fluxes in MD84-551 and MD88-773 (Th/U data from Francois et al., 1997). These records suggest iron fertilization cannot explain the deglacial peaks in $\delta^{15}N_{DB}$.

Since it appears that N utilisation in MD84-551 may have been constrained by light limitation during the LGM, an explanation for the increase in N utilisation may be a release from light limitation as the sea ice extent retreats. However, the local reconstructions of sea ice presence from diatom transfer functions (Figure 5.7) as well as a more regional proxy for sea

ice extent from EPICA Dome C (Wolff et al., 2006) do not display a good relationship with the $\delta^{15}N_{DB}$ records (whereby sea ice extent decreases monotonically from 18 ka BP to 11 ka BP). Furthermore, as with the lateral advection mechanisms described above, increased utilisation would be expected to yield expanded $\delta^{15}N_{DB}$ gradients, particularly between the AZ cores and MD88-772, which is not observed during the deglaciation.

Another possible mechanism for the observed $\delta^{15}N_{DB}$ increase during the deglaciation is a localised increase in iron fertilization inducing greater local N utilisation. The most obvious source of local iron fertilization would be from erosion of the Kerguelen Islands, which naturally fertilize a downstream region today (Blain et al., 2007; 2015). However, there are several factors that argue against this mechanism:

1) Given the distal location of MD88-773 relative to the Kerguelen Islands, greater eastward transport would likely have been required to either fertilize a greater area of the Southern Ocean or transport the iron-fertilized diatoms to the core site. It is unlikely that such an increase in eastward transport would also permit the fertilized diatoms to be deposited at MD84-551, which is located immediately south of the islands.

2) Greater Fe fertilization of the Indian sector of the Southern Ocean would need to be supported by greater erosion of the Kerguelen Islands during this interval. Hence, we would expect some correspondence between $\delta^{15}N_{DB}$ and Fe accumulation in affected records. However, the Fe accumulation records of MD84-551 and MD88-773 and numerous other records from across the Indian sector (Bareille et al., 1994; Dezileau et al., 2000) do not correlate well with the $\delta^{15}N_{DB}$ data, particularly during the late deglaciation (11 – 13 ka BP) (Figure 5.7).

3) As part of the KEOPS2 campaign, a study was carried out to determine the $\delta^{15}N$ of particles produced in the water column within the iron fertilized region downstream of the islands (Trull et al., 2015). The open ocean (i.e. not shallow coastal) sites produced particles with a maximum $\delta^{15}N$ of 2.35 ‰, whilst the unfertilized reference station produced particles with an average $\delta^{15}N$ of 1.03 ‰(Trull et al., 2015). This 1.32 ‰$\delta^{15}N$ enrichment is less than half of that observed between the Holocene and the peak deglacial $\delta^{15}N_{DB}$ values in MD84-551 and MD88-773. This suggests that the two cores would have needed to have been influenced by more intense iron fertilization during the deglaciation than that observed immediately downstream from the Kerguelen Islands today. Given the lack of evidence for

increased erosion from the Fe accumulation records, such intense iron fertilization appears unlikely.

Denitrification and deep ocean deoxygenation

It is possible that the observed peak deglacial $\delta^{15}N_{DB}$ values are not caused by changes in utilization, but by an increase in the source $\delta^{15}NO_3$ signal supplied to the Antarctic. One such mechanism for enriching the supplied $\delta^{15}NO_3$ is water column denitrification, which today primarily occurs within the oxygen minimum zones (OMZs) surrounding low latitude upwelling. As an introduction, following text will provide a short description of denitrification, its role in the marine nitrogen cycle and its influence on sedimentary $\delta^{15}N$ records.

The isotopic fractionation during pelagic denitrification (ε= 20 – 30 ‰, Sigman et al., 2001) is highly distinct from both N_2 fixation (adds nitrate with a $\delta^{15}N$ of -1 ‰, Wada and Hattori, 1976) and benthic denitrification, which has negligible impact on the isotopic composition of nitrate (Brandes and Devol, 1997) As a result, the global mean isotopic composition of nitrate will reflect the balance of importance between pelagic denitrification and the other two processes. For example, if pelagic denitrification were to increase whilst N_2 fixation and benthic denitrification remained constant, the mean $\delta^{15}NO_3$ will increase although this system will not be in steady state due to the imbalance between N_2 fixation and total denitrification. If pelagic denitrification were to increase and benthic denitrification decrease (i.e. a steady state is maintained) then the global mean $\delta^{15}NO_3$ would also rise (Deutsch et al., 2004; Galbraith et al., 2013).

The powerful isotopic fractionation by the pelagic denitrification process leaves a distinct signal on nitrate in the water column. The $\delta^{15}NO_3$ of nitrate within the OMZs has been found to be enriched to ∼20 ‰(global average $\delta^{15}NO_3$ ∼5 ‰) (Altabet et al., 1999). Dilution of this ^{15}N-enriched nitrate with ambient nitrate occurs as it is transported away from the OMZ. Nevertheless, phytoplankton growing in waters in the vicinity of denitrification zones will assimilate nitrate that has been isotopically altered by the denitrification. The $\delta^{15}N$ of organic matter accumulating in sediments surrounding the OMZs will thus reflect changes in the intensity of denitrification within the OMZ through time (as well as any other changes related to N utilisation). Sediment records from the three major OMZs (Arabian Sea, ETNP and ETSP) all display glacial-interglacial variability in $\delta^{15}N$ that has been

attributed to a diminishment of denitrification zones during glacial periods and expansion during interglacials (Figure 5.8) (Altabet et al., 1995; 1999; Ganeshram et al., 1995; Emmer and Thunell, 2000; Pichevin et al., 2010). It has been suggested that such a reduction of denitrification during glacials would have increased the global N inventory thus promoting greater primary production and carbon drawdown (Ganeshram et al., 1995). However, the extent of N inventory changes may have been limited by the strong internal negative feedbacks associated with N fixation and denitrification (Deutsch et al., 2004).

During the deglaciation, $\delta^{15}N$ records from the OMZs records display increasing values indicating an enhanced rate of pelagic denitrification (Ganeshram et al., 2000). The onset of the deglacial $\delta^{15}N$ rise in the Pacific OMZs (ETNP and ETSP) approximately corresponds to the onset of deglacial temperature rise in the Antarctic ($\sim$17 ka BP), whilst the Arabian Sea $\delta^{15}N$ increase is delayed ($\sim$14 ka BP), exhibiting an increase in-phase with Greenland temperature proxies. The $\delta^{15}N$ reconstructions from the Pacific provinces indicate that denitrification rates were greater during the deglaciation than the late Holocene, with the ETSP standing out as the most intense denitrification signal overall (De Pol Holz et al., 2006).

It is argued that the deglacial enhancement of pelagic denitrification in the three OMZs altered the balance between pelagic denitrification, benthic denitrification and N fixation such that the global mean $\delta^{15}NO_3$ increased (Deutsch et al., 2004; Galbraith et al., 2013). Small deglacial peaks in $\delta^{15}N$ (up to 1.5 ‰) from sediment records in the Caribbean (Ren et al., 2009) and South China Sea (Ren et al., 2012) (Figure 5.8) have been attributed to this increase in global mean $\delta^{15}NO_3$.

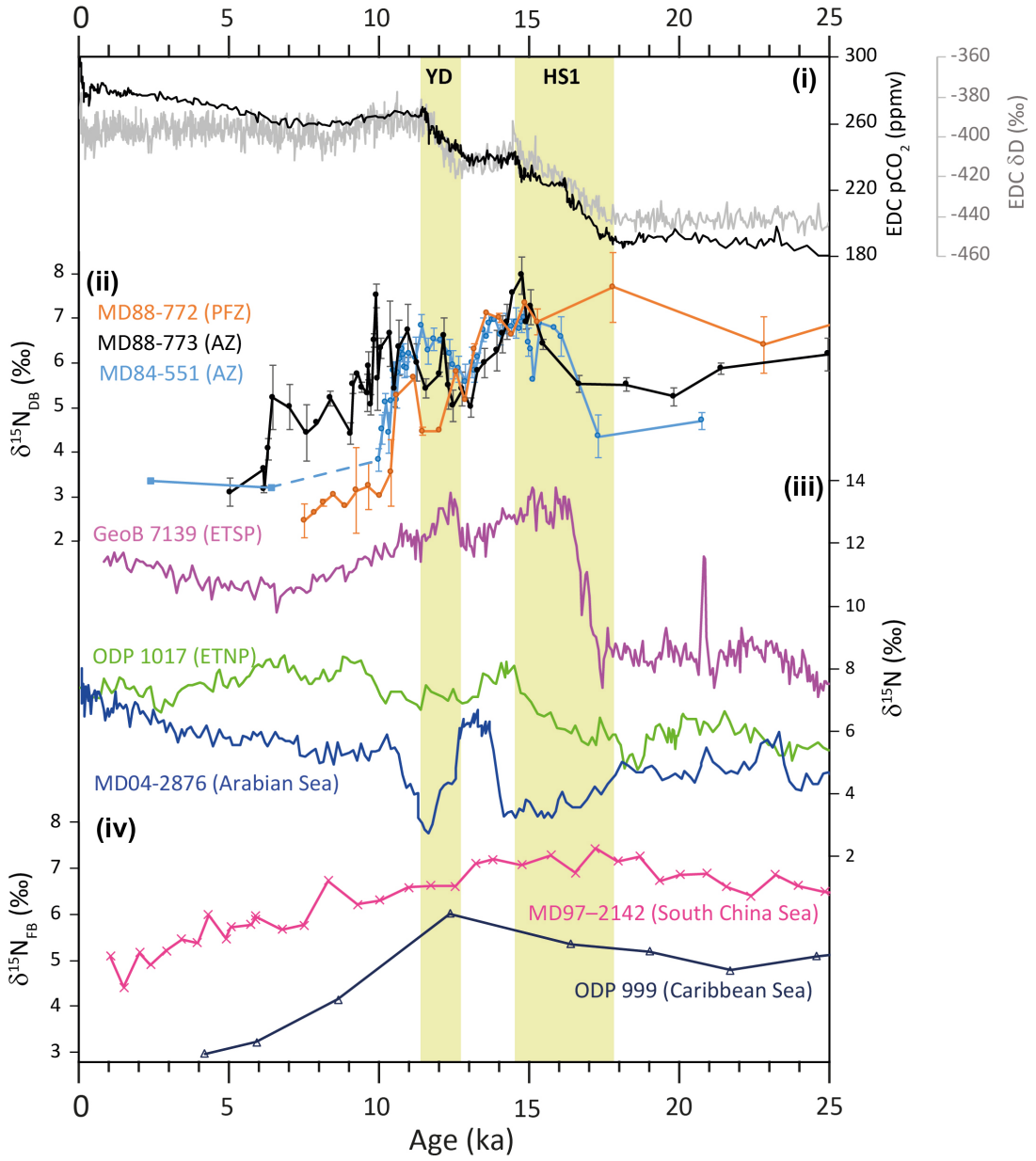

FIGURE 5.8: Plot demonstrating global denitrification changes across the deglaciation. **(i)** Atmospheric CO_2 (Monnin et al., 2001) and Antarctic temperature proxy (Parrenin et al., 2013) data from EPICA Dome C. **(ii)** $\delta^{15}N_{DB}$ data from the three Indian sector cores. The dashed line indicates the splicing between MD84-551 and MD84-552 (Robinson et al., 2004). **(iii)** Bulk sediment $\delta^{15}N$ records taken close to the three major OMZs (ETSP: De Pol-Holz et al (2007), ETNP: Hendy et al(2004), Arabian Sea: Pichevin et al (2007)). **(iv)** Foraminifera-bound $\delta^{15}N$ records away from the denitrification regions in the South China Sea (Ren et al., 2012) and Caribbean Sea (Ren et al., 2009), demonstrating changes in the global mean $\delta^{15}NO_3$.

Could an increase in global mean $\delta^{15}NO_3$ forced by enhanced low latitude denitrification during the deglaciation have caused the deglacial $\delta^{15}N_{DB}$ peaks observed in the Southern Ocean records presented here? The magnitude of the deglacial $\delta^{15}N_{DB}$ change (LGM to

peak $\delta^{15}N_{DB}$) in MD84-551 and MD88-773 is 2 – 3 ‰. This change is comparable to the deglacial $\delta^{15}N$ increases observed in the OMZ records. Given that the influence of the denitrification source signal attenuates due to dilution away from the denitrification sources, it seems unlikely that low latitude denitrification changes were the cause of the Southern Ocean $\delta^{15}N_{DB}$ peaks.

An alternative explanation is that the deglacial $\delta^{15}N$ peaks observed in the Southern Ocean were produced by ^{15}N-enriched nitrate advected more directly from an OMZ. Although modern water column denitrification is primarily restricted to the three major OMZs, water column deoxygenation may have created new regions of denitrification during the glacial period or deglaciation. One candidate is the deep Pacific, from which deep waters upwelling to the Southern Ocean are derived. Today, these depths are occupied by Antarctic Bottom Water and Pacific/Indian Deep Water, the latter of which being the precursor of UCDW (Talley, 2013). Therefore, denitrification within these waters would be detectable by phytoplankton growing in the AZ.

In the modern ocean, the North Pacific oxygen minimum resides above 2000 m rather than in the abyssal waters due to the strong ventilation from well-oxygenated AABW. Stratification of the Southern Ocean (Adkins et al., 2002; Sigman et al., 2010) would have inhibited the ventilation of the deep Pacific by AABW during the LGM (Hain et al., 2010). Oxygenation proxy records are sparse for waters $>$ 2000 m in the Pacific, however those that are available indicate that the oxygen minimum deepened to below 2000 m during the LGM (Bradtmiller et al., 2010; Jaccard et al., 2011). These proxy data are corroborated by earth system model simulations that predict an average decrease of dissolved oxygen concentrations by 15.1 µmol m^{-3} in the deep ocean at the LGM relative to the present (Bopp et al., 2017). Likewise, available subsurface radiocarbon reconstructions suggest reduced ventilation of the deep Pacific during the LGM (Shackleton et al., 1988; Keigwin and Legman, 2015; Ronge et al., 2016; Sikes et al., 2016). The only hint that denitrification may have indeed occurred in the deep Pacific comes from a pore-water $\delta^{15}NO_3$ study by Hartwell (2013). In this study the authors observed a shift in the $\delta^{15}N$ and $\delta^{18}O$ within pore-water nitrate (corrected for in situ nitrate regeneration) extracted from cores within the abyssal Pacific (5410 m and 5819 m depth) towards values resembling modern tropical Pacific intermediate waters that are influenced by denitrification (Hartwell, 2013). Due to the much lower POC input at these depths, it is unlikely that denitrification rates would have been comparable to those in modern OMZs. However, the extended residence time of waters within the deep ocean

during the LGM may have allowed even slow denitrification to have significantly influenced the isotopic composition of the ambient nitrate.

If denitrification did indeed occur within these abyssal waters during the LGM, then the $\delta^{15}N_{DB}$ signal detected within the Indian sector cores presented here agrees with the well-established hypothesis, that the deep poorly-ventilated ocean was upwelled through the Southern Ocean upon the deglaciation (Burke and Robinson., 2012; Siani et al., 2013). In this case, the ^{15}N-enriched waters would have been associated with the contemporaneous Southern Ocean overturning and CO_2 outgassing. Indeed, the redox proxy, U_{auth} record from MD88-773 indicate periods of oxygenation of the deep Southern Ocean during the early deglaciation. This is coeval with the aged 14C reservoir interval detected in the 14C record of MD84-551 (Figure 5.9). A stable level of oxygenation appeared to be met in these cores by $\sim$14 ka BP, which agrees with other redox records from the Southern Ocean (Jaccard et al., 2016). This suggests the latter $\delta^{15}N_{DB}$ excursion (10 - 12.5 ka BP) may not be explained by Southern Ocean ventilation. However, it appears that the deep Pacific (Sikes et al., 2016) and Indian (Stern and Lisieki, 2014) basins remained poorly ventilated until after 14 ka BP, suggesting the source waters may have been derived from the either of these basins.

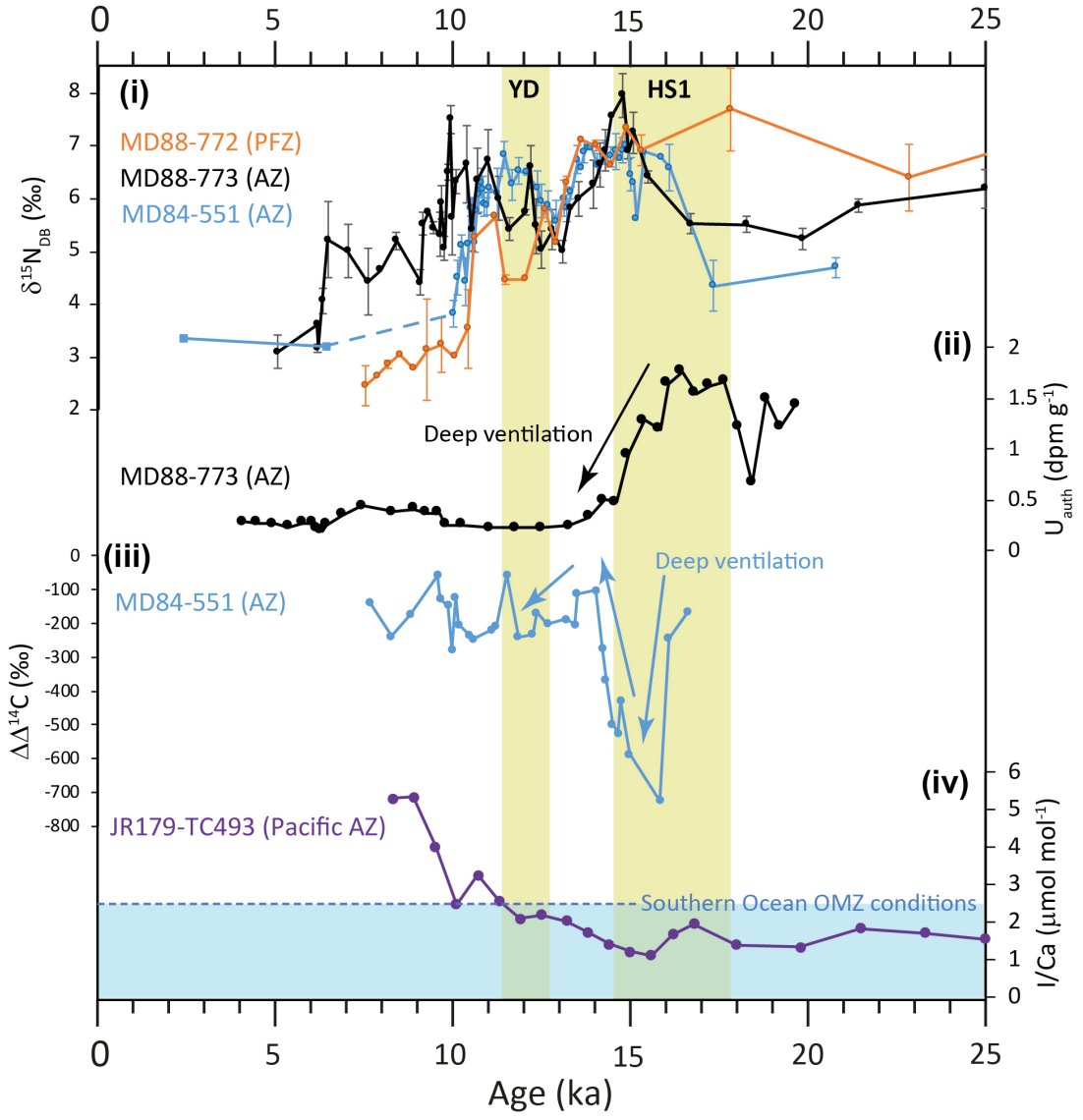

FIGURE 5.9: Evidence for deep deoxygenation driving enhanced denitrification within the Southern Ocean. **(i)** $\delta^{15}N_{DB}$ data from the three Indian sector cores. The dashed line indicates the splicing between MD84-551 and MD84-552 (Robinson et al., 2004). **(ii)** U_{auth} content of MD88-773 (Francois et al., 1997). **(iii)** Planktic foraminifera $\Delta\Delta^{14}C$ record from MD84-551. **(iv)** Planktic foraminifera I/Ca in JR179-TC493 in the Pacific Antarctic (Lu et al., 2016). Shaded area indicates OMZ conditions recorded by I/Ca (Lu et al., 2010).

The second possible explanation for the heavy $\delta^{15}N_{DB}$ signal observed in the Southern Ocean records is that the upwelling of deoxygenated deep waters during the deglaciation induced local denitrification in the upper Southern Ocean, thus creating an OMZ in the Southern Ocean comparable to modern OMZs. A relatively new method for reconstructing water column oxygenation is the I/Ca ratio of calcifying organisms such as foraminifera. This proxy utilises the redox-sensitive speciation of iodine, which is only incorporated into

the carbonate structure as IO^{3-} but is converted to I- when oxygen is depleted. As result, foraminifera producing their tests within deoxygenated waters record a lower I/Ca ratio (Lu et al., 2010), with I/Ca ratios of < 2.5 indicative of OMZ conditions. Figure 5.9 displays a planktonic foraminifer (*N. pachyderma*) I/Ca record from a core within the Pacific AZ (Lu et al., 2016). This record suggests this part of the Southern Ocean experienced OMZ conditions through the last glacial maximum and much of the deglaciation. It should be noted that the age model of this core is not well constrained across the deglaciation. However, I/Ca ratios only rise above 2.5 (blue shaded area) by the early Holocene, which is reasonably well constrained by benthic $\delta^{18}O$ stratigraphy (Lu et al., 2016), suggesting the Southern Ocean indeed had the capacity to experience OMZ conditions during the glacial period and deglaciation.

The result of this study is surprising, primarily because the Southern Ocean water column is one of the most well-oxygenated regions of the ocean today (Garcia et al., 2014) maintained by the strong wind-driven mixing and a high oxygen solubility in the cold surface waters. However, the increased productivity (see Chapter 4) and the deoxygenation of deep upwelling waters may have fostered the suboxic conditions necessary for denitrification. We are unable to distinguish between the above scenarios (deep or shallow Southern Ocean denitrification) with the current data available. Further efforts aimed at reconstructing water column oxygenation in the Southern Ocean across the deglaciation may aid in determining whether local denitrification may be the cause.

The above hypotheses provide explanations for the mechanism behind the enhanced denitrification observed in the low latitude OMZs during the deglaciation. A widely agreed explanation for these signals local productivity enhancements due to increased wind-driven upwelled (Altabet et al., 1995; Ganeshram et al., 2000). However, some studies have found poor correlation between upwelling (sea-surface temperature and productivity) proxies and the deglacial expansion of the OMZs detected by sedimentary $\delta^{15}N$ and redox proxies, particularly in the ETSP (Higginson and Altabet, 2004; De Pol-Holz et al., 2006) but also the ETNP (Hendy and Pedersen, 2006). These studies suggest that water column deoxygenation in the low latitude OMZs was not entirely caused by greater local oxygen demand, but by a lower oxygen content of the water mass in which the OMZs reside. Importantly, all of the low latitude OMZs are bathed in the intermediate waters derived from the Southern Ocean. This has led some to suggest that the glacial-interglacial variability in low latitude denitrification may be attributed to changes in oxygenation of these water mass in the Southern Ocean

(Galbraith et al., 2004). Specifically, the cooler sea surface temperatures of the glacial Southern Ocean would induce greater oxygenation of the subducted intermediate waters, thus supplying more oxygen to the low latitude OMZs. However, this temperature control on intermediate water oxygenation cannot explain the deglacial denitrification maxima as sea surface temperatures throughout much of the Southern Ocean were not greater during the deglaciation than today as one would expect (Crosta et al., 2004).

It is hypothesized here that the deglacial enhancement of low latitude denitrification in the Pacific was at least partially caused by the same suboxic water mass that produced the $\delta^{15}N_{DB}$ maxima observed in the Southern Ocean. Some of the deglacial $\delta^{15}N$ signal observed globally could be attributed to the deoxygenation of intermediate waters thus forcing an expansion of the tropical denitrification zones as detected by redox proxy records from intermediate depths (Hendy and Pedersen, 2006). This deoxygenation could have been caused by vertical exchange between intermediate waters and the suboxic deep waters that were poorly ventilated through the glacial period. In addition, the isotopically heavy nitrate either produced in the upper Southern Ocean or the deep ocean may have been advected to the low latitudes providing additional ^{15}N-enriched waters to the OMZs and thus exacerbating the deglacial $\delta^{15}N$ increase. Indeed, the production of ^{15}N-enriched waters from the Southern Ocean would help explain the coeval peaks in sedimentary $\delta^{15}N$ observed in regions distant from denitrification zones but supplied by Southern Ocean waters, such as the Nicaragua margin (Pichevin et al., 2010), the Namibia margin (Pichevin et al., 2005) and the southern Chile margin (Martinez et al., 2006) (Figure 5.10).

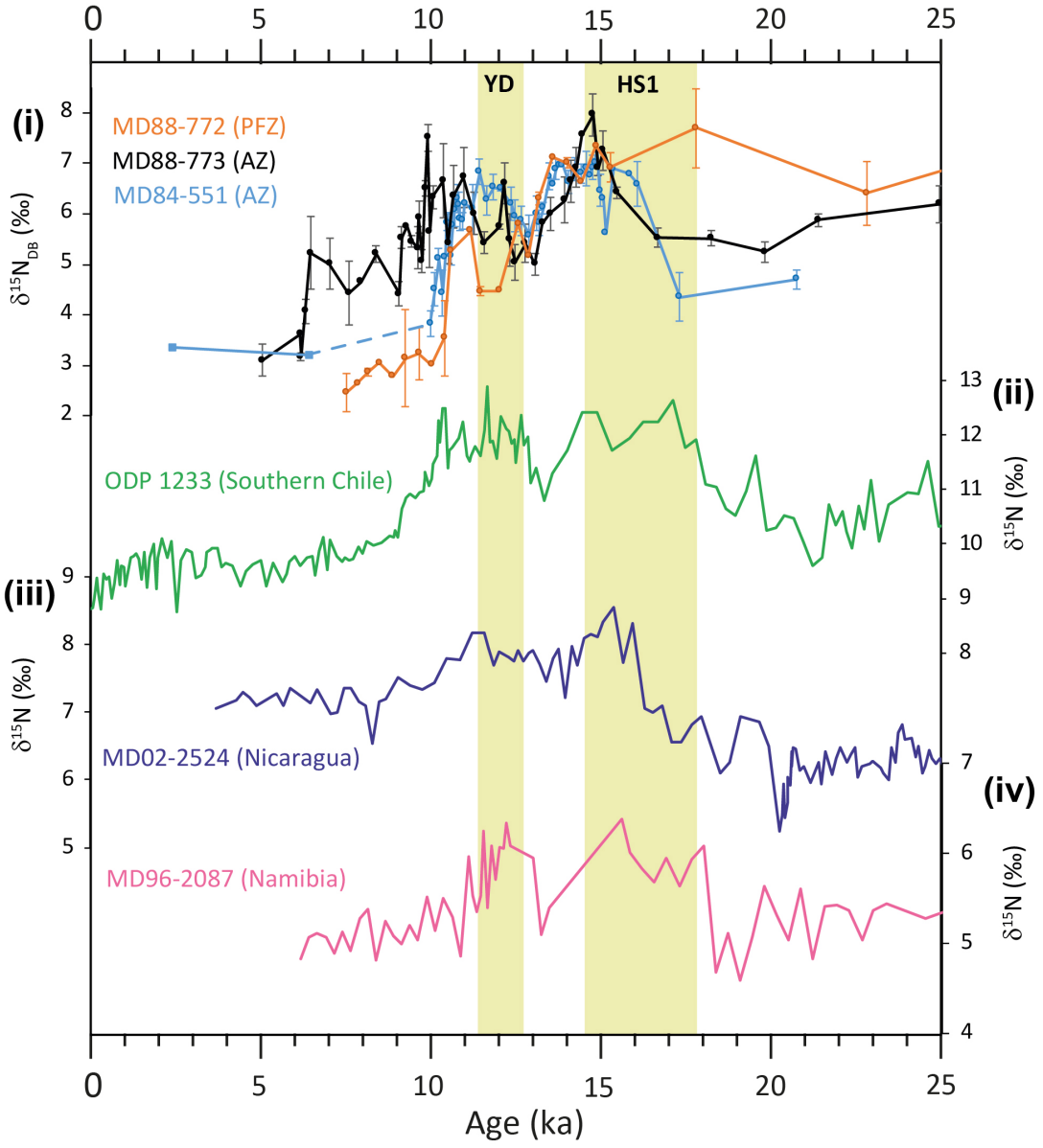

FIGURE 5.10: Demonstration of the distal influence of the Southern Ocean/deep ocean denitrification during the deglaciation. **(i)** $\delta^{15}N_{DB}$ data from the three Indian sector cores. The dashed line indicates the splicing between MD84-551 and MD84-552 (Robinson et al., 2004). Along with bulk sediment $\delta^{15}N$ records from the margins of **(ii)** Southern Chile (Martinez et al., 2006), **(iii)** Nicaragua (Pichevin et al., 2010), and **(iii)** Namibia (Pichevin et al., 2005).

The implications of these findings on the global nitrogen cycle and atmospheric CO_2 depend on whether the denitrification source was from the deep ocean or locally within the Southern Ocean. These will be discussed separately in the text below.

Implications: Deep denitrification

If the Southern Ocean peaks in $\delta^{15}N_{DB}$ to have been produced by the upwelling of denitrified waters from the deep ocean, it is probable that the rate of denitrification was slow and that the denitrified signal was produced over the extended period in which the waters resided in the deep ocean during glacial periods. With regards to the global N budget, it is assumed that pelagic denitrification was reduced overall during the glacial period due to diminishment of the low latitude OMZs. Because benthic denitrification is concentrated on continental shelves, it is suggested that the eustatic sea level drop during glacials would have also decreased benthic denitrification (Christiansen, 1994). As described above, the fraction of total denitrification that occurs in the sediments versus in the water column defines the global mean isotopic composition of nitrate. Due to the multitude of factors that control the variability of sedimentary $\delta^{15}N$ records, reconstructing the global mean $\delta^{15}NO_3$ is challenging. Foraminifera-bound $\delta^{15}N$ records from the Caribbean (Ren et al., 2009) and South China Sea (Ren et al., 2012) exhibit a 1.8 ‰and 1.2 ‰greater $\delta^{15}N$ content during the last glacial period. The authors suggest that this change is unlikely to be due to a whole-ocean increase in the mean $\delta^{15}NO_3$ because of the reduction in low latitude pelagic denitrification during the glacial period. However, if pelagic denitrification was maintained in the deep ocean, at least part of this glacial-interglacial $\delta^{15}N$ signal may be attributed to a whole ocean $\delta^{15}NO_3$ change.

The residence time of nitrate in the global ocean is approximately 3000 years (Brandes and Devol, 2002), the result of which is that internal negative feedbacks will act to balance the global N budget towards a steady state over glacial-interglacial timescales. Hence, it is thought that the loss of total denitrification during glacial periods was likely met by a concomitant reduction in N fixation (Ganeshram et al., 2002; Ren et al., 2009). This is despite the greater availability of iron in the global oceans during glacials, which would have acted to fertilise diazotrophs (Falkowski, 1997). Continuation of pelagic denitrification in the deep glacial ocean as suggested as a possibility here would imply N fixation would not have been forced to decline during glacial periods by as much as previously thought.

Implications: Shallow Southern Ocean denitrification

In this scenario, the Southern Ocean becomes a denitrifying OMZ only during the intervals of deep upwelling that are coeval with both the rise in atmospheric CO_2 and Antarctic temperature rise. During the deglaciation the global mean $\delta^{15}NO_3$ increased, which is interpreted as a response to the early increase in pelagic denitrification relative to benthic denitrification, to which the Southern Ocean denitrification may have contributed to.

The relatively short residence time of oceanic nitrate ($\approx$ 3000 years, Brandes and Devol, 2002) could enable large changes in the global N inventory over millennial timescales. A global enhancement of denitrification during the deglaciation in response to both productivity enhancements and exposure to deoxygenated deep waters could temporarily tip the marine N cycle into a transient state, before internal negative feedbacks have time to respond. Hence, the deglacial global peak $\delta^{15}N$ (Deutsch et al., 2004; Galbraith et al., 2013) could represent a transient period of N loss from the ocean. This loss of nitrate could induce two negative feedbacks, an increase in N fixation in response to the shift in global N/P ratios, and a decrease in denitrification due to increased N limitation of primary production (Deutsch et al., 2004). However, since it is argued here that the deglacial denitrification enhancements are at least partially due to the ventilation of deoxygenated deep waters, the latter of these two feedbacks was probably less important.

The transient loss of N from the oceans during the deglaciation may be thought of an adjustment of the N cycle to a restructuring of nutrients in the global ocean. We can think of the ocean circulation as being compartmentalised, with a more rapidly overturning upper circulation cell, and a sluggish deep cell. During the glacial period the deep cell became enriched in DIC because of reduced ventilation. The coupling of N and DIC in the biological pump would result in a proportional enrichment of nutrients such as nitrate in the deep ocean. This would have caused a global reduction of primary productivity, for which there is little evidence for across much of the world's oceans during the LGM. Hence, any enrichment of nitrate (and phosphate) in the deep ocean would need to have been balanced by an adjustment of the nutrient budgets in the upper ocean (for instance, a decrease in denitrification during glacials). Upon the deglaciation the stratification between the deep and upper cells was removed, which produced an injection CO_2 into the atmosphere as well as an abundant supply of nutrients to the surface ocean. Evidence in support of this enhanced supply of nutrients to the upper ocean comes from productivity records in the Southern

Ocean (Chapter 4), low latitude upwelling regions (Pichevin et l., 2009; Meckler et al., 2013) and nutrient content reconstructions of AAIW (Poggemann et al., 2016). The increase in upper ocean nutrient availability would have activated the negative feedbacks that act to mitigate such changes. It can be hypothesised that the enhanced global denitrification during the deglaciation was a response to the greater nutrient inventory of the upper ocean during this interval. If N fixation rates do not change across the deglaciation, or even decrease in response to the lower iron availability (Falkowski, 1997) then enhanced denitrification during the deglaciation would have resulted in a net decrease in the global N inventory during the deglaciation. Such a decrease is hypothesised in box model experiments (e.g. Eugster et al., 2013), although, these do not account for the glacial-interglacial changes in global circulation that would act to restructure the global distribution of nutrients. The gradual reduction of the global N inventory would have acted to weaken the biological pump during the deglaciation in a similar fashion to that proposed by Ganeshram et al (1995). This may have contributed to the atmospheric CO_2 rise across the deglaciation.

5.4 Conclusions

To conclude, the $\delta^{15}N_{DB}$ data from the three Indian sector cores presented here document the weakening of the Southern Ocean biological pump across the last deglaciation, although much of this weakening appears to have been driven by changes in physical overturning rather than greater carbon export. These data suggest little overall change in N utilization between the LGM and Holocene within the Indian sector AZ. Considering the large decrease in productivity at the LGM compared to the Holocene in MD84-551, the small change was likely brought about by lower N supply combined with light limitation due to greater sea ice presence. Overall the lower nutrient delivery would have reduced the preformed nutrient content entering the nutrient interior, likely resulting in a stemming of the leak in the biological pump at the LGM and a lowering of atmospheric CO_2.

In the Subantarctic, the expanded $\delta^{15}N_{DB}$ gradient between the three records during the LGM indicates a poleward position of the surface nitrate gradient in the Southern Ocean at that time. The convergence of the opal belt (Chapter 4) and the nitrate gradient during the LGM highlights the decrease in Si:N uptake ratio by diatoms driven by higher iron availability (Brzezinski et al., 2002).

References

Abelmann , A., Gersonde , R., Cortese , G., Kuhn , G., and Smetacek , V. Extensive phytoplankton blooms in the Atlantic sector of the glacial Southern Ocean. *Paleoceanography*, 21(1):n/a–n/a, mar 2006. doi: 10.1029/2005PA001199.

Adkins , J. F., Mcintyre , K., and Schrag , D. P. The Salinity, Temperature, and d18O of the Glacial Deep Ocean. *Science*, 298(November):1769–1774, 2002.

Altabet , A., Murray , D. W., and Prell , W. L. Climatically linked oscillations in Arabian Sea denitrification over the past 1 m.y.: Implications for the marine N cycle. *Paleoceanography*, 14(6):732–743, 1999.

Altabet , M., Francois , R., Murray , D., and Prell , W. Climate-related variations in denitrification in the Arabian Sea from sediment 15N/14N ratios. *Nature*, 373(6514):506–509, 1995.

Altabet , M. A. and Francois , R. Nitrogen isotope biogeochemistry of the Antarctic Polar Frontal Zone at 170W. *Deep-Sea Research II*, 48:4247–4273, 2001.

Arrigo , K. R., Robinson , D. H., Worthen , D. L., Dunbar , R. B., DiTullio , G., VanWoert , M. L., and Lizotte , M. P. Phytoplankton Community Structure and the Drawdown of Nutrients and CO2 in the Southern Ocean. *Science*, 283(5400):365–367, jan 1999. doi: 10.1126/science.283.5400.365.

Bareille , G., Grousset , F. E., Labracherie , M., Labeyrie , L. D., and Petit , J. Origin of detrital fluxes in the southeast Indian Ocean during the last climatic cycles. *Paleoceanography*, 9(6):799–819, 1994.

Beaumont , V., Agrlnier , P., Robert , F., De , L., Paris , U., Cedex , P., Mineralogie , L. D., and Naturelle , H. Determination of the CO Contribution to the 15N / 14N Ratio Measured by Mass Spectrometry. *Analytical Chemistry*, 66(13):2187–2189, 1994. doi: 10.1021/ac00085a039.

Blain , S., Capparos , J., Guéneuguès , A., Obernosterer , I., and Oriol , L. Distributions and stoichiometry of dissolved nitrogen and phosphorus in the iron-fertilized region near Kerguelen (Southern Ocean). *Biogeosciences*, 12(2):623–635, 2015. doi: 10.5194/bg-12-623-2015.

Blain , S., Quéguiner , B., Armand , L., Belviso , S., Bombled , B., Bopp , L., Bowie , A., Brunet , C., Brussaard , C., Carlotti , F., Christaki , U., Corbière , A., Durand , I., Ebersbach , F., Fuda , J. L., Garcia , N., Gerringa , L., Griffiths , B., Guigue , C., Guillerm , C., Jacquet , S., Jeandel , C., Laan , P., Lefèvre , D., Lo Monaco , C., Malits , A., Mosseri , J., Obernosterer , I., Park , Y. H., Picheral , M., Pondaven , P., Remenyi , T., Sandroni , V., Sarthou , G., Savoye , N., Scouarnec , L., Souhaut , M., Thuiller , D., Timmermans , K., Trull , T., Uitz , J., Van Beek , P., Veldhuis , M., Vincent , D., Viollier , E., Vong , L., and Wagener , T. Effect of natural iron fertilization on carbon sequestration in the Southern Ocean. *Nature*, 446(7139):1070–1074, 2007. doi: 10.1038/nature05700.

Bopp , L., Resplandy , L., Untersee , A., Le Mezo , P., and Kageyama , M. Ocean (de)oxygenation from the Last Glacial Maximum to the twenty-first century: Insights from Earth System models. *Philosophical Transactions of the Royal Society A: Mathematical, Physical and Engineering Sciences*, 375(2102), 2017. doi: 10.1098/rsta.2016.0323.

Boyd , P. W., Watson , a. J., Law , C. S., Abraham , E. R., Trull , T., Murdoch , R., Bakker , D. C., Bowie , a. R., Buesseler , K. O., Chang , H., Charette , M., Croot , P., Downing , K., Frew , R., Gall , M., Hadfield , M., Hall , J., Harvey , M., Jameson , G., LaRoche , J., Liddicoat , M., Ling , R., Maldonado , M. T., McKay , R. M., Nodder , S., Pickmere , S., Pridmore , R., Rintoul , S., Safi , K., Sutton , P., Strzepek , R., Tanneberger , K., Turner , S., Waite , a., and Zeldis , J. A mesoscale phytoplankton bloom

in the polar Southern Ocean stimulated by iron fertilization. *Nature*, 407(6805):695–702, oct 2000. doi: 10.1038/35037500.

Boyd , P. W. and Ellwood , M. J. The biogeochemical cycle of iron in the ocean. *Nature Geoscience*, 3(10): 675–682, sep 2010. doi: 10.1038/ngeo964.

Boyd , P., Laroche , J., Gall , M., Frew , R., Mckay , R. M. L., and Phytoplankton , A. Role of iron, light, and silicate in controlling algal biomass in subantarctic waters SE of New Zealand. *Journal of Geophysical Research*, 104:395–408, 1999.

Bradtmiller , L. I., Anderson , R. F., Sachs , J. P., and Fleisher , M. Q. A deeper respired carbon pool in the glacial equatorial Pacific Ocean. *Earth and Planetary Science Letters*, 299(3-4):417–425, 2010. doi: 10.1016/j.epsl.2010.09.022.

Brandes , J. A. and Devol , A. H. Isotopic fractionation of oxygen and nitrogen in coastal marine sediments. *Geochimica et Cosmochimica Acta*, 61(9):1793–1801, 1997. doi: 10.1016/S0016-7037(97)00041-0.

Brandes , J. A. and Devol , A. H. A global marine-fixed nitrogen isotopic budget: Implications for Holocene nitrogen cycling. *Global Biogeochemical Cycles*, 16(4):67–1–67–14, 2002. doi: 10.1029/2001GB001856.

Broecker , W. Glacial to interglacial changes in ocean chemistry. *Progress in Oceanography*, 11:151–197, 1982a.

Broecker , W. Ocean chemistry during glacial time. *Geochimica et Cosmochimica Acta*, 46:1689–1705, 1982b.

Bronk , D. A., Lomas , M. W., Glibert , P. M., Schukert , K. J., and Sanderson , M. P. Total dissolved nitrogen analysis: Comparisons between the persulfate, UV and high temperature oxidation methods. *Marine Chemistry*, 69(1-2):163–178, 2000. doi: 10.1016/S0304-4203(99)00103-6.

Brunelle , B. G., Sigman , D. M., Cook , M. S., Keigwin , L. D., Haug , G. H., Plessen , B., Schettler , G., and Jaccard , S. L. Evidence from diatom-bound nitrogen isotopes for subarctic Pacific stratification during the last ice age and a link to North Pacific denitrification changes. *Paleoceanography*, 22(1):1–17, 2007. doi: 10.1029/2005PA001205.

Brzezinski , M., Pride , C., Franck , V. M., Sigman , D. M., Sarmiento , J. L., Matsumoto , K., Gruber , N., Rau , G. H., and Coale , K. H. A switch from Si (OH) 4 to NO3 depletion in the glacial Southern Ocean. *Geophysical Research Letters*, 29(12):3–6, 2002.

Burke , A. and Robinson , L. F. The Southern Ocean's role in carbon exchange during the last deglaciation. *Science (New York, N.Y.)*, 335(6068):557–61, feb 2012. doi: 10.1126/science.1208163.

Cartapanis , O., Bianchi , D., Jaccard , S. L., and Galbraith , E. D. Global pulses of organic carbon burial in deep-sea sediments during glacial maxima. *Nature Communications*, 7:10796, 2016. doi: 10.1038/ncomms10796.

Chase , Z., Anderson , R. F., Fleisher , M. Q., and Kubik , P. W. Accumulation of biogenic and lithogenic material in the Pacific sector of the Southern Ocean during the past 40,000 years. *Deep Sea Research Part II: ...*, 50:799–832, 2003.

Cline , J. D. and Kaplan , I. R. Isotopic fractionation of dissolved nitrate during denitrification in the eastern tropical north pacific ocean. *Marine Chemistry*, 3(4):271–299, 1975. doi: 10.1016/0304-4203(75)90009-2.

Coale , K. H., Johnson , K. S., Chavez , F. P., Buesseler , K. O., Barber , R. T., Brzezinski , M. a., Cochlan , W. P., Millero , F. J., Falkowski , P. G., Bauer , J. E., Wanninkhof , R. H., Kudela , R. M., Altabet , M. a., Hales , B. E., Takahashi , T., Landry , M. R., Bidigare , R. R., Wang , X., Chase , Z., Strutton ,

P. G., Friederich , G. E., Gorbunov , M. Y., Lance , V. P., Hilting , A. K., Hiscock , M. R., Demarest , M., Hiscock , W. T., Sullivan , K. F., Tanner , S. J., Gordon , R. M., Hunter , C. N., Elrod , V. a., Fitzwater , S. E., Jones , J. L., Tozzi , S., Koblizek , M., Roberts , A. E., Herndon , J., Brewster , J., Ladizinsky , N., Smith , G., Cooper , D., Timothy , D., Brown , S. L., Selph , K. E., Sheridan , C. C., Twining , B. S., and Johnson , Z. I. Southern Ocean iron enrichment experiment: carbon cycling in high- and low-Si waters. *Science (New York, N.Y.)*, 304(5669):408–14, apr 2004. doi: 10.1126/science.1089778.

Codispoti , L. A., Brandes , J. A., Christensen , J. P., Devol , A. H., Naqvi , S. A., Paerl , H. W., and Yoshinari , T. The oceanic fixed nitrogen and nitrous oxide budgets: Moving targets as we enter the anthropocene? *Scientia Marina*, 65(S2):85–105, 2001. doi: 10.3989/scimar.2001.65s285.

Crosta , X., Shemesh , a., Etourneau , J., Yam , R., Billy , I., and Pichon , J. J. Nutrient cycling in the Indian sector of the Southern Ocean over the last 50,000 years. *Global Biogeochemical Cycles*, 19(3): n/a–n/a, sep 2005. doi: 10.1029/2004GB002344.

Crosta , X., Pichon , J. J., and Labracherie , M. Distribution of Chaetoceros resting spores in modern peri-Antarctic sediments. *Marine Micropaleontology*, 29(3-4):283–299, 1997. doi: 10.1016/S0377-8398(96)00033-3.

Crosta , X., Sturm , A., Armand , L., and Pichon , J.-J. Late Quaternary sea ice history in the Indian sector of the Southern Ocean as recorded by diatom assemblages. *Marine Micropaleontology*, 50(3-4):209–223, 2004. doi: 10.1016/S0377-8398(03)00072-0.

De La Rocha , C. L. Opal-based isotopic proxies of paleoenvironmental conditions. *Global Biogeochem. Cycles*, 20(May):1–11, 2006. doi: 10.1029/2005GB002664.

De Pol-holz , R. D., Ulloa , O., Lamy , F., Dezileau , L., Sabatier , P., and Hebbeln , D. Late Quaternary variability of sedimentary nitrogen isotopes in the eastern South Pacific Ocean. *Paleoceanography*, 22: 1–16, 2007. doi: 10.1029/2006PA001308.

Deutsch , C., Sigman , D. M., Thunell , R. C., Meckler , A. N., and Haug , G. H. Isotopic constraints on glacial / interglacial changes in the oceanic nitrogen budget. *Global Biogeochemical Cycles*, 18, 2004. doi: 10.1029/2003GB002189.

Dezileau , L., Bareille , G., Reyss , J. L., and Lemoine , F. Evidence for strong sediment redistribution by bottom currents along the southeast Indian ridge. *Deep-Sea Research Part I: Oceanographic Research Papers*, 47(10):1899–1936, 2000. doi: 10.1016/S0967-0637(00)00008-X.

Difiore , P. J., Sigman , D. M., Karsh , K. L., Trull , T. W., Dunbar , R. B., and Robinson , R. S. Poleward decrease in the isotope effect of nitrate assimilation across the Southern Ocean. *Geophysical Research Letters*, 37(17):1–5, 2010. doi: 10.1029/2010GL044090.

DiFiore , P. J., Sigman , D. M., Trull , T. W., Lourey , M. J., Karsh , K., Cane , G., and Ho , R. Nitrogen isotope constraints on subantarctic biogeochemistry. *Journal of Geophysical Research: Oceans*, 111 (August 2005):1–19, 2006. doi: 10.1029/2005JC003216.

Emmer , E. and Thunell , R. C. Nitrogen isotope variations in Santa Barbara Basin sediments : Implications for denitrification in the eastern tropical North Pacific during the last 50 , 000 years in Santa fill the Santa zone in the the nitrate in these waters has a • SN value During of. *Paleoceanography*, 15(4):377–387, 2000.

Eppley , R. W. and Peterson , B. Particulate organic matter flux and planktonic new production in the deep ocean. *Nature*, 282:677–680, 1979.

Eugster , O., Gruber , N., Deutsch , C., Jaccard , S. L., and Payne , M. R. The dynamics of the marine nitrogen cycle across the last deglaciation. *Paleoceanography*, 28(1):116–129, 2013. doi: 10.1002/palo.20020.

Falkowski , P. Evolution of the nitrogen cycle and its influence on the biological sequestration of CO2 in the ocean. *Nature*, 387:272–275, 1997.

Francois , R., Altabet , M. A., Yu , E.-f., Sigman , D. M., Bacon , M. P., Frank , M., Bohrmann , G., Bareille , G., and Labeyrie , L. D. Contribution of Southern Ocean surface-water stratification to low atmospheric CO 2 concentrations during the last glacial period. *Nature*, 389:929–935, 1997.

Galbraith , E. D., Kienast , M., Albuquerque , A. L., Altabet , M. a., Batista , F., Bianchi , D., Calvert , S. E., Contreras , S., Crosta , X., De Pol-Holz , R., Dubois , N., Etourneau , J., Francois , R., Hsu , T.-C., Ivanochko , T., Jaccard , S. L., Kao , S.-J., Kiefer , T., Kienast , S., Lehmann , M. F., Martinez , P., McCarthy , M., Meckler , A. N., Mix , A., Möbius , J., Pedersen , T. F., Pichevin , L., Quan , T. M., Robinson , R. S., Ryabenko , E., Schmittner , A., Schneider , R., Schneider-Mor , A., Shigemitsu , M., Sinclair , D., Somes , C., Studer , A. S., Tesdal , J.-E., Thunell , R., and Terence Yang , J.-Y. The acceleration of oceanic denitrification during deglacial warming. *Nature Geoscience*, 6(7):579–584, jun 2013. doi: 10.1038/ngeo1832.

Galbraith , E. D., Kienast , M., Pedersen , T. F., and Calvert , S. E. Glacial-interglacial modulation of the marine nitrogen cycle by high-latitude O2 supply to the global thermocline. *Paleoceanography*, 19 (December 2003):1–12, 2004. doi: 10.1029/2003PA001000.

Galbraith , E. D., Jaccard , S. L., Pedersen , T. F., Sigman , D. M., Haug , G. H., Cook , M., Southon , J. R., and Francois , R. Carbon dioxide release from the North Pacific abyss during the last deglaciation. *Nature*, 449(7164):890–3, oct 2007. doi: 10.1038/nature06227.

Ganeshram , R., Pedersen , T. F., Calvert , S. E., and Murray , J. Large changes in oceanic nutrient inventories from glacial to interglacial periods. *Nature*, 376:755–759, 1995.

Ganeshram , R., Pedersen , T., Calvert , S., and François , R. Reduced nitrogen fixation in the glacial ocean inferred from changes in marine nitrogen and phosphorus inventories. *Nature*, 415(January):1–4, 2002.

Ganeshram , S., Pedersen , F., Calvert , E., Mcneill , W., and Fontugne , M. R. Glacial-interglacial variability in denitrification in the world's oceans: Causes and consequences. *Paleoceanography*, 15(4):361–376, 2000.

Garcia , H. E., Locarnini , R. A., Boyer , T. P., Antonov , J. I., Baranova , O. K., Zweng , M., Reagan , J. R., and Johnson , D. R. World Ocean Atlas 2013, Volume 4: Dissolved Inorganic Nutrients (phosphate, nitrate, silicate). In Levitus , S. and Mishonov , A. V., editors, *NOAA Atlas NESDIS 76*. 2013a.

Garcia , H. E., Locarnini , R. A., Boyer , T. P., Antonov , J. I., Baranova , O. K., Zweng , M., Reagan , J. R., and Johnson , D. R. World Ocean Atlas 2013, Volume 3: Dissolved Oxygen, Apparent Oxygen Utilization, and Oxygen Saturation. In Levitus , S. and Mishonov , A., editors, *NOAA Atlas NESDIS 75*, page 27. 2013b.

Gersonde , R., Crosta , X., Abelmann , A., and Armand , L. Sea-surface temperature and sea ice distribution of the Southern Ocean at the EPILOG Last Glacial Maximum—a circum-Antarctic view based on siliceous microfossil records. *Quaternary Science Reviews*, 24(7-9):869–896, apr 2005. doi: 10.1016/j.quascirev.2004.07.015.

Gray , W. R., Rae , J. W. B., Wills , R. C. J., Shevenell , A. E., Taylor , B., Burke , A., Foster , G. L., and Lear , C. H. Deglacial upwelling, productivity and CO2 outgassing in the North Pacific Ocean. *Nature*

Geoscience, 11(May):1, 2018. doi: 10.1038/s41561-018-0108-6.

Hartwell , A. M. *A Reconstruction of d15N of Deep Ocean Nitrate in the Past Using Pore Fluid*. PhD thesis, University of Rhode Island, 2013.

Hendy , I. L. and Pedersen , T. F. Oxygen minimum zone expansion in the eastern tropical North Pacific during deglaciation. *Geophysical Research Letters*, 33(February):1–5, 2006. doi: 10.1029/2006GL025975.

Higginson , M. J. and Altabet , M. Initial test of the silicic acid leakage hypothesis using sedimentary biomarkers. *Geophysical Research Letters*, 31(18), 2004. doi: 10.1029/2004GL020511.

Honjo , S., Francois , R., and Manganini , S. Particle fluxes to the interior of the Southern Ocean in the Western Pacific sector along 170 W. *Deep Sea Research Part II: Topical Studies in Oceanography*, 47, 2000.

Horn , M. G., Beucher , C. P., Robinson , R. S., and Brzezinski , M. a. Southern ocean nitrogen and silicon dynamics during the last deglaciation. *Earth and Planetary Science Letters*, 310(3-4):334–339, oct 2011a. doi: 10.1016/j.epsl.2011.08.016.

Horn , M. G., Robinson , R. S., Rynearson , T. a., and Sigman , D. M. Nitrogen isotopic relationship between diatom-bound and bulk organic matter of cultured polar diatoms. *Paleoceanography*, 26(3), sep 2011b. doi: 10.1029/2010PA002080.

Iida , T. and Odate , T. Seasonal variability of phytoplankton biomass and composition in the major water masses of the Indian Ocean sector of the Southern Ocean. *Polar Science*, 8(3):283–297, 2014. doi: 10.1016/j.polar.2014.03.003.

Ingalls , A. E., Anderson , R. F., and Pearson , A. Radiocarbon dating of diatom-bound organic compounds. *Marine Chemistry*, 92:91–105, 2004. doi: 10.1016/j.marchem.2004.06.019.

Ingalls , A. E., Lee , C., Wakeham , S. G., and Hedges , J. I. The role of biominerals in the sinking flux and preservation of amino acids in the Southern Ocean along 1701W. *Deep-Sea Research*, 50:713–738, 2003.

Jaccard , S. L. and Galbraith , E. D. Large climate-driven changes of oceanic oxygen concentrations during the last deglaciation. *Nature Geoscience*, 5(2):151–156, 2011. doi: 10.1038/ngeo1352.

Jaccard , S. L., Galbraith , E. D., Martínez-Garcia , A., and Anderson , R. F. Covariation of abyssal Southern Ocean oxygenation and pCO2 throughout the last ice age. *Nature*, 530(7589):207–210, 2016. doi: 10.1038/nature16514.

Kao , S. J., Liu , K. K., Hsu , S. C., Chang , Y. P., and Dai , M. H. North Pacific-wide spreading of isotopically heavy nitrogen during the last deglaciation : Evidence from the western Pacific. *Biogeosciences*, 5:1641–1650, 2008.

Keigwin , L. and Lehman , S. Radiocarbon evidence for a possible abyssal front near 3.1 km in the glacial equatorial Pacific Ocean. *Earth and Planetary Science Letters*, 425:93–104, 2015. doi: 10.1016/j.epsl.2015.05.025.

Kienast , M. Unchanged nitrogen isotopic composition of organic matter in the South China Sea during the last climatic cycle: Global implications. *Paleoceanography*, 15(2):244–253, 2000.

Knapp , A. N., Sigman , D. M., and Lipschultz , F. N isotopic composition of dissolved organic nitrogen and nitrate at the Bermuda Atlantic Time-series Study site. *Global Biogeochemical Cycles*, 19(1):n/a–n/a, 2005. doi: 10.1029/2004GB002320.

Knox , F. and McElroy , M. B. Changes in Atmospheric Influence of the Marine Biota at High Latitude. *Journal of Geophysical Research*, 89(D3):4629–4637, 1984.

Kohfeld , K. E. and Chase , Z. Controls on deglacial changes in biogenic fluxes in the North Pacific Ocean. *Quaternary Science Reviews*, 30(23-24):3350–3363, 2011. doi: 10.1016/j.quascirev.2011.08.007.

Kroger , N., Deutzmann , R., Bergsdorf , C., and Sumper , M. Species-specific polyamines from diatoms control silica morphology. *Biochemistry*, 97(26):14133–14138, 2000.

Kroger , N., Deutzmann , R., and Sumper , M. Polycationic Peptides from Diatom Biosilica That Direct Silica Nanosphere Formation. *Science*, 286(November):1129–1133, 1999.

Kroger , N., Lorenz , S., Brunner , E., and Sumper , M. Self-Assembly of Highly Phosphorylated Silaffins and Their Function in Biosilica Morphogenesis. *Science*, 298(October):584–587, 2002.

Lambert , F., Bigler , M., Steffensen , J. P., Hutterli , M., and Fischer , H. Centennial mineral dust variability in high-resolution ice core data from Dome C, Antarctica. *Climate of the Past*, 8(2):609–623, mar 2012. doi: 10.5194/cp-8-609-2012.

Langner , C. L. and Hendrix , P. F. Evaluation of a persulfate digestion method for particulate nitrogen and phosphorus. *Water Research*, 16(10):1451–1454, 1982. doi: 10.1016/0043-1354(82)90243-3.

Lide , D. *CRC Handbook of Chemistry and Physics*. CRC Press, Boca Raton, FL, 83rd edition, 2002. ISBN 0-8493-0483-0.

Lourey , M. J., Trull , T. W., and Sigman , D. M. N of nitrate, surface suspended and deep sinking particulate nitrogen to seasonal nitrate depletion in the Southern Ocean. *Global Biogeochemical Cycles*, 17(3):1–18, 2003. doi: 10.1029/2002GB001973.

Lovenduski , N. S., Gruber , N., Doney , S. C., and Lima , I. D. Enhanced CO 2 outgassing in the Southern Ocean from a positive phase of the Southern Annular Mode. *Global Biogeochem. Cycles*, 21(April):1–14, 2007. doi: 10.1029/2006GB002900.

Lu , Z., Hoogakker , B. A. A., Hillenbrand , C.-d., Zhou , X., Thomas , E., Gutchess , K. M., Lu , W., Jones , L., and Rickaby , R. E. M. Oxygen depletion recorded in upper waters of the glacial Southern Ocean. *Nature communications*, 7(May 2015), 2016. doi: 10.1038/pj.2016.37.

Lu , Z., Jenkyns , H. C., and Rickaby , R. E. M. Iodine to calcium ratios in marine carbonate as a paleo-redox proxy during oceanic anoxic events. *Geology*, 38(12):1107–1110, 2010. doi: 10.1130/G31145.1.

Mahowald , N., Kohfeld , K., Hansson , M., Balkanski , Y., Harrison , S. P., Prentice , I. C., Schulz , M., and Rodhe , H. Dust sources and deposition during the last glacial maximum and current climate: A comparison of model results with paleodata from ice cores and marine. *Journal of Geophysical Research*, 104(D13):15,895–15,916, 1999.

Mahowald , N. M., Muhs , D. R., Levis , S., Rasch , P. J., Yoshioka , M., Zender , C. S., and Luo , C. Change in atmospheric mineral aerosols in response to climate: Last glacial period, preindustrial, modern, and doubled carbon dioxide climates. *Journal of Geophysical Research*, 111(D10):D10202, 2006. doi: 10.1029/2005JD006653.

Martin , J. Glacial-interglacial CO2 change: The iron hypothesis. *Paleoceanography*, 5(1):1–13, 1990.

Martinez , P., Lamy , F., Robinson , R. R., Pichevin , L., and Billy , I. Atypical δ15N variations at the southern boundary of the East Pacific oxygen minimum zone over the last 50 ka. *Quaternary Science Reviews*, 25(21-22):3017–3028, 2006. doi: 10.1016/j.quascirev.2006.04.009.

Martínez-García , A., Sigman , D. M., Ren , H., Anderson , R. F., Straub , M., Hodell , D. a., Jaccard , S. L., Eglinton , T. I., and Haug , G. H. Iron fertilization of the Subantarctic ocean during the last ice age. *Science (New York, N.Y.)*, 343(6177):1347–50, mar 2014. doi: 10.1126/science.1246848.

McElroy , M. Marine biological controls on atmospheric CO2 and climate. *Nature*, 302:328–329, 1983.

Mikaloff Fletcher , S. E., Gruber , N., Jacobson , A. R., Gloor , M., Doney , S. C., Dutkiewicz , S., Gerber , M., Follows , M., Joos , F., Lindsay , K., Menemenlis , D., Mouchet , A., and Mu , S. A. Inverse estimates of the oceanic sources and sinks of natural CO 2 and the implied oceanic carbon transport. *Global Biogeochemical Cycles*, 21:1–19, 2007. doi: 10.1029/2006GB002751.

Mitchell , B. G., Brody , E. A., Holm-Hansen , O., McClain , C., and Bishop , J. Light limitation of phytoplankton biomass and macronutrient utilization in the Southern Ocean, 1991.

Monnin , E., Indermühle , a., Dällenbach , a., Flückiger , J., Stauffer , B., Stocker , T. F., Raynaud , D., and Barnola , J. M. Atmospheric CO2 concentrations over the last glacial termination. *Science (New York, N.Y.)*, 291(5501):112–4, jan 2001. doi: 10.1126/science.291.5501.112.

Needoba , J. A. and Harrison , P. J. INFLUENCE OF LOW LIGHT AND A LIGHT : DARK CYCLE ON NO – INTRACELLULAR NO 3 , AND NITROGEN ISOTOPE FRACTIONATION BY and. *Journal of Phycology*, 516(September 2003):505–516, 2004. doi: 10.1111/j.1529-8817.2004.03171.x.

Nydahl , F. On the peroxodisulphate oxidation of total nitrogen in waters to nitrate. *Water Research*, 12 (1974), 1978.

Parrenin , F., Masson-Delmotte , V., Köhler , P., Raynaud , D., Paillard , D., Schwander , J., Barbante , C., Landais , a., Wegner , a., and Jouzel , J. Synchronous change of atmospheric CO2 and Antarctic temperature during the last deglacial warming. *Science (New York, N.Y.)*, 339(6123):1060–3, mar 2013. doi: 10.1126/science.1226368.

Pichevin , L. E., Ganeshram , R. S., Francavilla , S., Arellano-Torres , E., Pedersen , T. F., and Beaufort , L. Interhemispheric leakage of isotopically heavy nitrate in the eastern tropical Pacific during the last glacial period. *Paleoceanography*, 25(1):1–15, feb 2010. doi: 10.1029/2009PA001754.

Pichevin , L., Martinez , P., Bertrand , P., Schneider , R., Giraudeau , J., and Emeis , K. Nitrogen cycling on the Namibian shelf and slope over the last two climatic cycles: Local and global forcings. *Paleoceanography*, 20(2):1–13, 2005. doi: 10.1029/2004PA001001.

Poggemann , D. W., Hathorne , E. C., Nürnberg , D., Frank , M., Bruhn , I., Reißig , S., and Bahr , A. Rapid deglacial injection of nutrients into the tropical Atlantic via Antarctic Intermediate Water. *Earth and Planetary Science Letters*, 463:118–126, 2017. doi: 10.1016/j.epsl.2017.01.030.

Praetorius , S. K., Mix , A. C., Walczak , M. H., Wolhowe , M. D., Addison , J. A., and Prahl , F. G. North Pacific deglacial hypoxic events linked to abrupt ocean warming. *Nature*, 527(7578):362–366, 2015. doi: 10.1038/nature15753.

Redfield , A., Ketchum , B. H., and Richards , F. A. The influence of organisms on the composition of sea water. *The sea*, 1963.

Ren , H., Brunelle , B. G., Sigman , D. M., and Robinson , R. S. Diagenetic aluminum uptake into diatom frustules and the preservation of diatom-bound organic nitrogen. *Marine Chemistry*, 155:92–101, sep 2013. doi: 10.1016/j.marchem.2013.05.016.

Ren , H., Sigman , D. M., Chen , M.-t., and Kao , S.-j. Elevated foraminifera-bound nitrogen isotopic composition during the last ice age in the South China Sea and its global and regional implications. *Global Biogeochem. Cycles*, 26:1–13, 2012. doi: 10.1029/2010GB004020.

Robinson , R. S., Martinez , P., Pena , L. D., and Cacho , I. Nitrogen isotopic evidence for deglacial changes in nutrient supply in the eastern equatorial Pacific. *Paleoceanography*, 24(October 2008):1–12, 2009. doi:

10.1029/2008PA001702.

Robinson , R. S., Brunelle , B. G., and Sigman , D. M. Revisiting nutrient utilization in the glacial Antarctic: Evidence from a new method for diatom-bound N isotopic analysis. *Paleoceanography*, 19(3), sep 2004. doi: 10.1029/2003PA000996.

Robinson , R. S. and Sigman , D. M. Nitrogen isotopic evidence for a poleward decrease in surface nitrate within the ice age Antarctic. *Quaternary Science Reviews*, 27(9-10):1076–1090, may 2008. doi: 10.1016/j.quascirev.2008.02.005.

Robinson , R. S., Sigman , D. M., DiFiore , P. J., Rohde , M. M., Mashiotta , T. a., and Lea , D. W. Diatom-bound 15 N/ 14 N: New support for enhanced nutrient consumption in the ice age subantarctic. *Paleoceanography*, 20(3), sep 2005. doi: 10.1029/2004PA001114.

Robinson , R. S., Brzezinski , M. a., Beucher , C. P., Horn , M. G. S., and Bedsole , P. The changing roles of iron and vertical mixing in regulating nitrogen and silicon cycling in the Southern Ocean over the last glacial cycle. *Paleoceanography*, pages 1179–1195, 2014. doi: 10.1002/2014PA002686.Received.

Robinson , R. S., Kienast , M., Albuquerque , A. L., Altabet , M., Contreras , S., Holz , R. D. P., Dubois , N., Francois , R., Galbraith , E., Hsu , T.-c., Ivanochko , T., Jaccard , S., Kao , S.-j., Kiefer , T., Kienast , S., Lehmann , M., Martinez , P., Mccarthy , M., Möbius , J., Pedersen , T., Quan , T. M., Ryabenko , E., Schmittner , A., Schneider , R., and Schneider-mor , A. A review of nitrogen isotopic alteration in marine sediments. *Paleoceanography*, 27(PA4203), 2012. doi: 10.1029/2012PA002321.

Ronge , T. A., Tiedemann , R., Lamy , F., Köhler , P., Alloway , B. V., De Pol-Holz , R., Pahnke , K., Southon , J., and Wacker , L. Radiocarbon constraints on the extent and evolution of the South Pacific glacial carbon pool. *Nature Communications*, 7(May):1–12, 2016. doi: 10.1038/ncomms11487.

Sedwick , P. N., Blain , S., Quéguiner , B., Griffiths , F. B., Fiala , M., Bucciarelli , E., and Denis , M. Resource limitation of phytoplankton growth in the Crozet Basin, Subantarctic Southern Ocean. *Deep-Sea Research Part II: Topical Studies in Oceanography*, 49(16):3327–3349, 2002. doi: 10.1016/S0967-0645(02)00086-3.

Shackleton , N., Duplessy , J., and Arnold , M. Radiocarbon age of last glacial Pacific deep water. *Nature*, 335:708–711, 1988.

Shakun , J. D., Clark , P. U., He , F., Marcott , S. a., Mix , A. C., Liu , Z., Otto-Bliesner , B., Schmittner , A., and Bard , E. Global warming preceded by increasing carbon dioxide concentrations during the last deglaciation. *Nature*, 484(7392):49–54, apr 2012. doi: 10.1038/nature10915.

Shemesh , A., Macko , S., Charles , C., and Rau , G. Isotopic evidence for reduced productivity in the glacial Southern Ocean. *Science*, 262(5132):407–410, 1993.

Siani , G., Michel , E., De Pol-Holz , R., Devries , T., Lamy , F., Carel , M., Isguder , G., Dewilde , F., and Lourantou , A. Carbon isotope records reveal precise timing of enhanced Southern Ocean upwelling during the last deglaciation. *Nature communications*, 4(May):2758, jan 2013. doi: 10.1038/ncomms3758.

Sicre , M. A., Labeyrie , L., Ezat , U., Mazaud , A., and Turon , J. L. A 27 kyr terrestrial biomarker record in the southern Indian Ocean. *Geochemistry, Geophysics, Geosystems*, 7(7), 2006. doi: 10.1029/2005GC001234.

Sigman , D. M., Altabet , M. a., McCorkle , D. C., Francois , R., and Fischer , G. N of nitrate in the Southern Ocean: Nitrogen cycling and circulation in the ocean interior. *Journal of Geophysical Research*, 105:19599, 1999a. doi: 10.1029/2000JC000265.

Sigman , D. M., Karsh , K. L., and Casciotti , K. L. Nitrogen Isotopes in the Ocean. *Encyclopedia of Ocean Sciences*, (1997):40–54, 2001a. doi: 10.1016/B978-012374473-9.00632-9.

Sigman , D. M. and Boyle , E. A. Glacial/interglacial variation in atmospheric carbon dioxide. *Nature*, 407: 859–869, 2000.

Sigman , D. M., Hain , M. P., and Haug , G. H. The polar ocean and glacial cycles in atmospheric CO(2) concentration. *Nature*, 466(7302):47–55, jul 2010. doi: 10.1038/nature09149.

Sigman , D. M., M. a , A., McCorkle , D. C., Francois , R., and Fischer , G. The d15N of nitrate in the Southern Ocean: Nitrate consumption in surface waters. *Global Biogeochemical Cycles*, 13(4):1149–1166, 1999b. doi: 10.1029/1999GB900038.

Sigman , D., Casciotti , K., Andreani , M., Barford , C., Galanter , M., and Bohlke , J. K. A bacterial method for the nitrogen isotopic analysis of nitrate in seawater and freshwater. *Analytical Chemistry*, 73 (17):4145–4153, 2001b.

Sigman , M., Altabet , M. A., Francois , R., Mccorkle , D. C., and Gaillard , J.-F. The isotopic composition of diatom-bound nitrogen in Southern Ocean sediments. *Paleoceanography*, 14(2):118–134, 1999c.

Sikes , E. L., Cook , M. S., and Guilderson , T. P. Reduced deep ocean ventilation in the Southern Pacific Ocean during the last glaciation persisted into the deglaciation. *Earth and Planetary Science Letters*, 438: 130–138, 2016. doi: 10.1016/j.epsl.2015.12.039.

Skinner , L. C., Fallon , S., Waelbroeck , C., Michel , E., and Barker , S. Ventilation of the deep Southern Ocean and deglacial CO2 rise. *Science*, 328(5982):1147–51, may 2010. doi: 10.1126/science.1183627.

Stern , J. V. and Lisiecki , L. E. Termination 1 timing in radiocarbon-dated regional benthic δ18O stacks. *Paleoceanography*, 29(12):1127–1142, 2014. doi: 10.1002/2014PA002700.

Swift , D. M. and Wheeler , A. P. EVIDENCE OF AN ORGANIC MATRIX FROM DIATOM BIOSILICA. *Journal of Phycology*, 28:202–210, 1992.

Tagliabue , A., Bowie , A. R., Boyd , P. W., Buck , K. N., Johnson , K. S., and Saito , M. A. The integral role of iron in ocean biogeochemistry. *Nature*, 543(7643):51–59, 2017. doi: 10.1038/nature21058.

Talley , L. D. Closure of the global overturning circulation through the Indian, Pacific and Southern Oceans: schematics and transports. *Oceanography*, 26(1):80–97, 2013.

Toggweiler , J. R., Russell , J. L., and Carson , S. R. Midlatitude westerlies, atmospheric CO 2 , and climate change during the ice ages. *Paleoceanography*, 21(2), 2006. doi: 10.1029/2005PA001154.

Toggweiler , J. Variation of atmospheric CO2 by ventilation of the ocean's deepest water. *Paleoceanography*, 14(5), 1999.

Trull , T. W., Davies , D. M., Dehairs , F., Cavagna , A. J., Lasbleiz , M., Laurenceau-Cornec , E. C., D'Ovidio , F., Planchon , F., Leblanc , K., Quéguiner , B., and Blain , S. Chemometric perspectives on plankton community responses to natural iron fertilisation over and downstream of the Kerguelen Plateau in the Southern Ocean. *Biogeosciences*, 12(4):1029–1056, 2015. doi: 10.5194/bg-12-1029-2015.

Wada , E. and Hattori , A. Natural abundance of 15N in particulate organic matter in the North Pacific Ocean. *Geochimica et Cosmochimica Acta*, 40(2):249–251, 1976. doi: 10.1016/0016-7037(76)90183-6.

Wang , X. T., Sigman , D. M., Prokopenko , M. G., Adkins , J. F., Robinson , L. F., Hines , S. K., Chai , J., Studer , A. S., Martínez-García , A., Chen , T., and Haug , G. H. Deep-sea coral evidence for lower Southern Ocean surface nitrate concentrations during the last ice age. *Proceedings of the National Academy of Sciences*, (March):201615718, 2017. doi: 10.1073/pnas.1615718114.

Wolff , E. W., Fischer , H., Fundel , F., Ruth , U., Twarloh , B., Littot , G. C., Mulvaney , R., Röthlisberger , R., de Angelis , M., Boutron , C. F., Hansson , M., Jonsell , U., Hutterli , M. a., Lambert , F., Kaufmann

, P., Stauffer , B., Stocker , T. F., Steffensen , J. P., Bigler , M., Siggaard-Andersen , M. L., Udisti , R., Becagli , S., Castellano , E., Severi , M., Wagenbach , D., Barbante , C., Gabrielli , P., and Gaspari , V. Southern Ocean sea-ice extent, productivity and iron flux over the past eight glacial cycles. *Nature*, 440 (7083):491–6, mar 2006. doi: 10.1038/nature04614.

6

Glacial-interglacial redistribution of marine DSi

6.1 Introduction

Ice-core records have revealed that global atmospheric pCO_2 varies by approximately 80 ppm through glacial-interglacial cycles (Monnin et al., 2001; Lüthi et al., 2008). Lower atmospheric CO_2 during glacials has been attributed to strengthened deep stratification, which isolated the deep ocean promoting the sequestration of respired carbon (Francois et al., 1997; Toggweiler, 1999; Sigman et al., 2010). During glacial terminations, reinvigorated vertical overturning in the Southern Ocean enabled these deep waters to ventilate, releasing the CO_2 back to the atmosphere (Skinner et al., 2010; Burke and Robinson, 2012). However, this hypothesis does not account for the response of the silicon cycle to changes in deep mixing, and the subsequent effect this would have on the biological pump and oceanic carbon uptake.

Dissolved silicon (DSi) is an essential nutrient for diatoms that secrete opaline frustules. The supply of DSi to the surface ocean controls the degree of dominance of diatoms over

other phytoplankton groups (Egge and Aksnes, 1992; Dugdale et al., 1995). Consequently, a change in the supply of DSi to the surface ocean would alter the average Corg:CaCO3 ratio of settling particles (Matsumoto et al., 2002; Matsumoto and Sarmiento, 2008), which controls relative strengths of the soft-tissue and carbonate pumps (Volk and Hoffert, 1985; Sigman et al., 1998) that are antagonistic with respect to their influence on atmospheric CO_2 drawdown. Sinking biogenic silica detritus delivers silica to the deep ocean more efficiently than other nutrients such as N and P due to its relatively slow remineralisation rate (Gnanadesikan, 1999). The influence of this remineralisation offset can be observed in the depth distributions of DSi and NO_3 in the world's oceans (Figure 6.1), which demonstrate that throughout much of the ocean maximum [NO_3] is reached by $\sim$1000 m depth whereas maximum [$Si(OH)_4$] is not reached until 2000 m. Importantly, this depth differential places the nutrient maxima on either side of the 27.9 kg m^{-3} isopycnal (dashed line in Figure 6.1). This isopycnal outcrops in the Southern Ocean approximately the air-sea buoyancy flux changes sign (Ferrari et al., 2014), dividing waters bound for the northern and southern limbs of the meridional overturning circulation. During the LGM it has been suggested that NADW shoaled above this divide, reducing the mixing between the two limbs. Further, salinity stratification of the Southern Ocean would restrict an important pathway for DSi transport to the northern limb. It is therefore expected that the isolation of deep water during glacial periods would favour enhanced storage of DSi in the deep sea, potentially reducing DSi availability in the upper ocean. The subsequent ecological shift toward calcifying phytoplankton would have operated as a negative feedback, reducing the efficiency of the biological pump and raising atmospheric CO_2. Hence, further insight into the response of the silicon cycle to glacial-interglacial perturbations is necessary in understanding the drivers of atmospheric CO_2 variability.

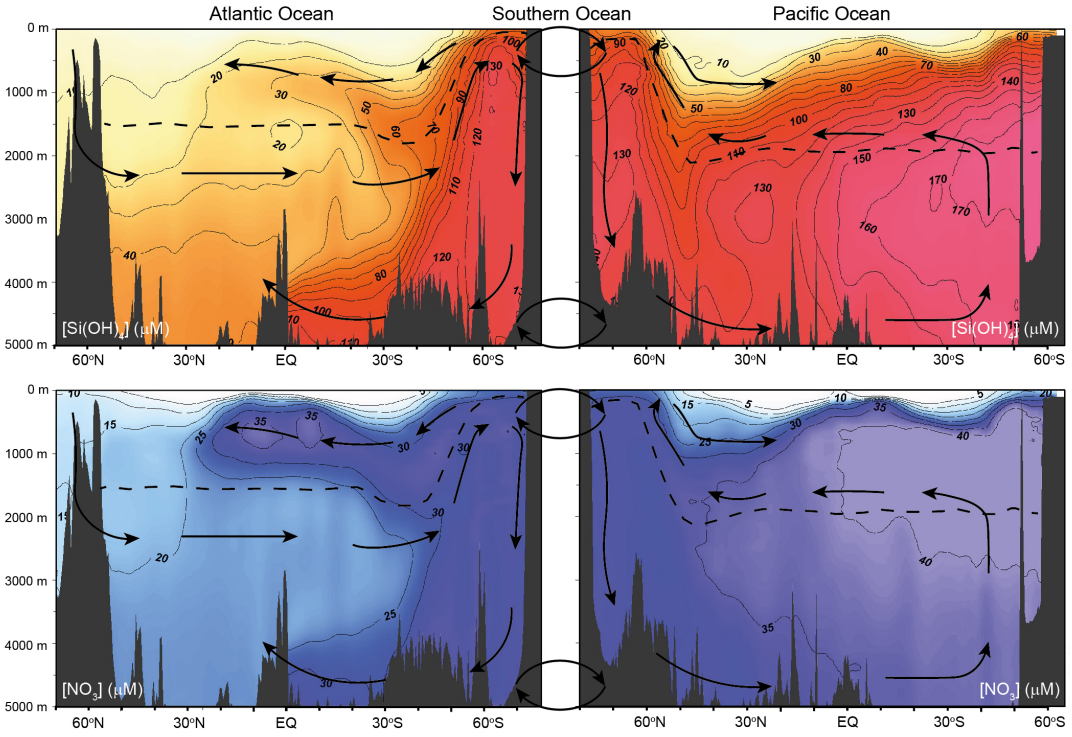

FIGURE 6.1: Profiles of silicic acid (top) and nitrate (bottom) across the world's ocean. Constructed using WOA13 data (Garcia et al., 2013) with ODV software (Schlitzer, 2002). The dashed line represents the 27.9 kg m^{-3} isopycnal. As noted by Ferrari et al (2014) this isopycnal approximately intersects the surface of the Southern Ocean where the buoyancy flux changes sign. Hence, on approaching the Southern Ocean water above this isopycnal (UCDW today) will be transported northwards and water below the line (UCDW and LCDW today) will tend to flow southward. This promotes the mixing of silica-rich deep waters of the Pacific through the Southern Ocean and into the North Atlantic. However, if mixing across this line were to be reduced, the redistribution of silica would be limited.

Owing to tilted isopycnals and deep vertical mixing, the Southern Ocean provides an important pathway for deep waters to resupply DSi to the surface ocean. However, the redistribution of DSi from the Southern Ocean to low latitude surface waters is limited due to the exhaustive demand for DSi by diatoms growing within the northern limb of Southern Ocean surface waters. Such high DSi uptake is driven by heavy silicification of diatoms under iron stress (Hutchins and Bruland, 1998; Takeda, 1998; Brzezinski et al., 2003). The resultant high opal export of the Southern Ocean combined with the deep remineralisation of biogenic silica act to trap DSi within the deep Southern Ocean and enrich the deep Pacific through which the deep southern-sourced waters circulate (Sarmiento et al., 2007; Holzer et al., 2014; De Souza et al., 2014). The relaxation of this silicon trap during glacial periods in response to greater iron availability has been discussed previously (Matsumoto et al., 2002; Matsumoto et al., 2014). However, there has been little suggestion that sluggish deep

mixing during glacials may have strengthened the trapping of DSi within the deep waters isolated from the surface ocean during these periods. Upon deglaciation, the isolated waters were released partly through the Southern Ocean, exposing the deep glacial waters to the surface. Here we will investigate whether DSi storage in the deep ocean was enhanced during the last glacial maximum and subsequently released through the Southern Ocean during the deglaciation in response to changes in deep overturning. In doing so, we will address whether the resultant removal of DSi from the upper ocean impacted on glacial-interglacial changes in the biological pump.

DSi availability in the surface ocean can be inferred from the isotopic composition of diatom biogenic silica ($\delta^{30}Si_{diat}$) (De La Rocha et al., 1997; 1998). Here we will present $\delta^{30}Si_{diat}$ reconstructions from the three Indian Sector cores. The DSi supplied to the surface waters above the core sites is sourced from upper circumpolar deep water (Cardinal et al., 2005; Fripiat et al., 2011), which upwells within the AZ and delivers DSi to the PFZ by Ekman transport. The endmember DSi properties of AAIW reflect surface waters close to the PF (Fripiat et al., 2011). Therefore, DSi reconstructions from the three cores presented here provide an indication of both the DSi supply to the Southern Ocean as well as that exported through intermediate waters to low latitudes (Sarmiento et al., 2004).

6.2 Methods

The $\delta^{30}Si_{diat}$ protocol is described in detail in the Methods Chapter. Briefly, isolated diatom samples were produced from bulk sediment through mechanical separation and chemically cleaning following that of Shemesh et al (1998) and Robinson et al (2008). The quality of the cleaning procedure was assessed by inspection through scanning electron microscopy. The procedure produced samples that appeared to contain $>$98% diatoms, with the remaining fraction consisting of silicoflaggelates, radiolaria fragments and sponge spicule fragments. The clay fraction was reduced such that $< 0.5\%$ of the surface area of samples inspected by SEM were clay.

The method for $\delta^{30}Si$ analysis follows that of Georg et al (2006). 10 ml of cleaned diatoms suspended in Milli-Q water were digested in 0.1 M suprapure NaOH before neutralisation with 1 M double-distilled HCl and dilution to 20 ppm. 0.5 ml of the DSi analyte was then loaded into a pre-cleaned 1.8 ml BioRad AG 50W-X8 catio exchange resin column and

eluted with Milli-Q water. Isotopic compositions of samples were analysed by MC-ICP-MS on a Nu Plasma II instrument at the University of Edinburgh using sample-standard bracketing with isotopic reference material, NBS28. All $\delta^{30}Si$ values quoted are with respect to NBS28. Average internal reproducibility at 1$\sigma$is 0.06 ‰(n $\leq$ 3 per sample, total 124 samples including repeats). Average external reproducibility at 1s is 0.09 ‰(n $\leq$ 3 per sample, total 14 samples).

The theory behind the use of silicon isotopes is similar to that described in the previous chapter on nitrogen isotope fractionation during N assimilation. In nature, there are three stable silicon isotopes: ^{28}Si (92.2 % abundance), ^{29}Si (4.7 % abundance) and ^{30}Si (3.1 % abundance) (Audi et al., 2003). During the uptake of DSi, diatoms discriminate against the heavier isotopes. The fractionation process can be described in terms of the relative uptake of the DSi pool much like that for nitrogen, with two model options to choose based on whether the system can be described as open or closed.

Unlike $\delta^{15}N_{DB}$, core-top studies have found a good correspondence between the isotopic composition of sediments, the isotopic composition of filtered diatoms in the surface ocean and the expected isotopic composition based on Rayleigh fractionation kinetics (Egan et al., 2012). The good similarity between the $\delta^{30}Si$ of buried ($\delta^{30}Si_{diat}$) and suspended diatoms is demonstrated in Figure 6.2, which is adapted from the Southern Ocean core-top study by Egan et al (2012). The tops of the three Indian sector cores presented here have been added to the plot. It should be noted that due to the nature of piston coring, the tops of the cores were not recovered, therefore these data represent mid to early Holocene samples. However, the $\delta^{30}Si$ variability within the Holocene sections of sediment records has been found to be minimal in comparison to the deglaciation (Horn et al., 2011; Robinson et al., 2014). From these core-top and seawater sample studies the silicon isotopic effect (ϵ) in diatoms has been found to be -1.1 ‰, and relatively invariable across the Southern Ocean (De la Rocha et al., 1997; Varela et al., 2004; Egan et al., 2012). Hence, $\delta^{30}Si_{diat}$ records can theoretically be used quantitatively reconstruct DSi utilisation in past environments.

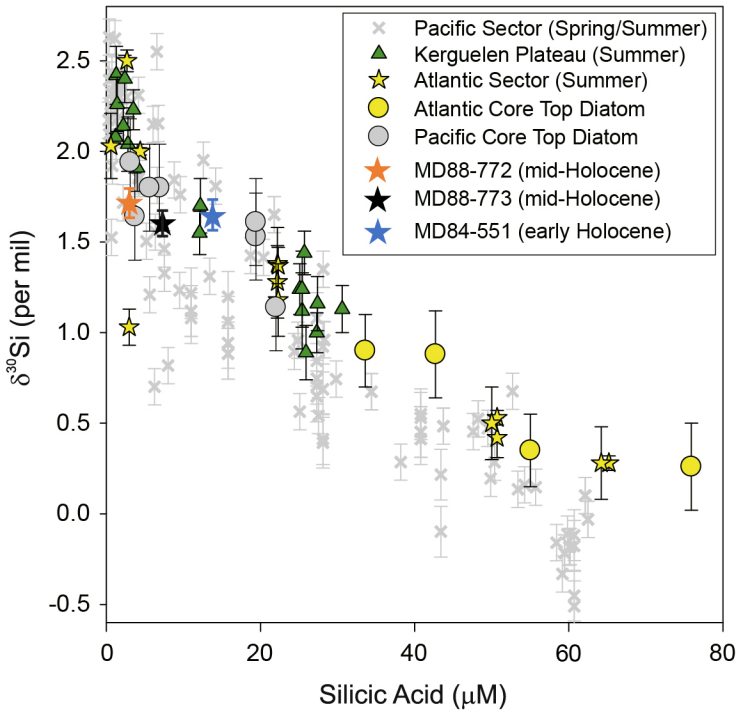

FIGURE 6.2: Adapted from Egan et al (2012). Core top and seawater $\delta^{30}Si$ samples from a Southern Ocean calibration study. Holocene $\delta^{30}Si_{diat}$ from MD84-551, MD88-773 and MD88-772 are included and closely fit the core-top and seawater data. Surface ocean silicic acid concentration data for the three Indian sector cores was estimated using WOA13 (Garcia et al., 2013).

One potential caveat of the use of $\delta^{30}Si_{diat}$ is the finding that lighter isotopes are preferentially lost from biogenic opal upon dissolution. Thus, it has been found that opal may increase in $\delta^{30}Si$ by as much as 0.55 ‰whilst settling through the water column (Demarest et al., 2009). However, this effect appears to be limited to the surface ocean where opal dissolution is greatest (Nelson et al., 2002; Demarest et al., 2009). Indeed, little evidence has been found for a depth-dependent effect on the isotopic composition of opal (Fripiat et al., 2012; Egan et al., 2012; Wetzel et al., 2014; Hendry and Brzezinski, 2014). Hence, it is likely that any isotopic bias related to dissolution is unimportant in driving the $\delta^{30}Si_{diat}$ changes observed in sediment records.

An additional bias that has been highlighted in previous studies is the influence of species-dependent fractionation, whereby the isotopic signal through a sediment record may be influenced by a change in the diatom species assemblage (Sutton et al., 2013). This appears to contradict core-top studies that find little variability in the mean isotopic effect across a variety of ecological regions with different diatom assemblages within the Southern Ocean

(Egan et al., 2012). In their culture-based study, Sutton et al (2013) noted the most extreme difference in isotopic effect between two species were *Chaetoceros brevis* (ε= -2.09 $\pm$ 0.09 ‰) and *Fragilariopsis kerguelensis* (ε= -0.53 $\pm$ 0.11 ‰). They argued that the change in relative abundance of these two species through Southern Ocean records may have driven much of the glacial-interglacial $\delta^{30}Si_{diat}$ variability. However, as noted in the previous chapter, the large glacial-interglacial variability of *Chaetoceros* resting spore abundance appears to be restricted to the Atlantic sector and is unlikely to be an important factor in other regions. Further, we found little correspondence between the variability in the diatom assemblage data of MD84-551 and MD88-773 and their respective $\delta^{30}Si_{diat}$ records (Figures 6.3 and 6.4). Hence, any species-dependent changes in $\varepsilon$are unlikely to have played an important role in the deglacial $\delta^{30}Si_{diat}$ variability within the Indian sector records.

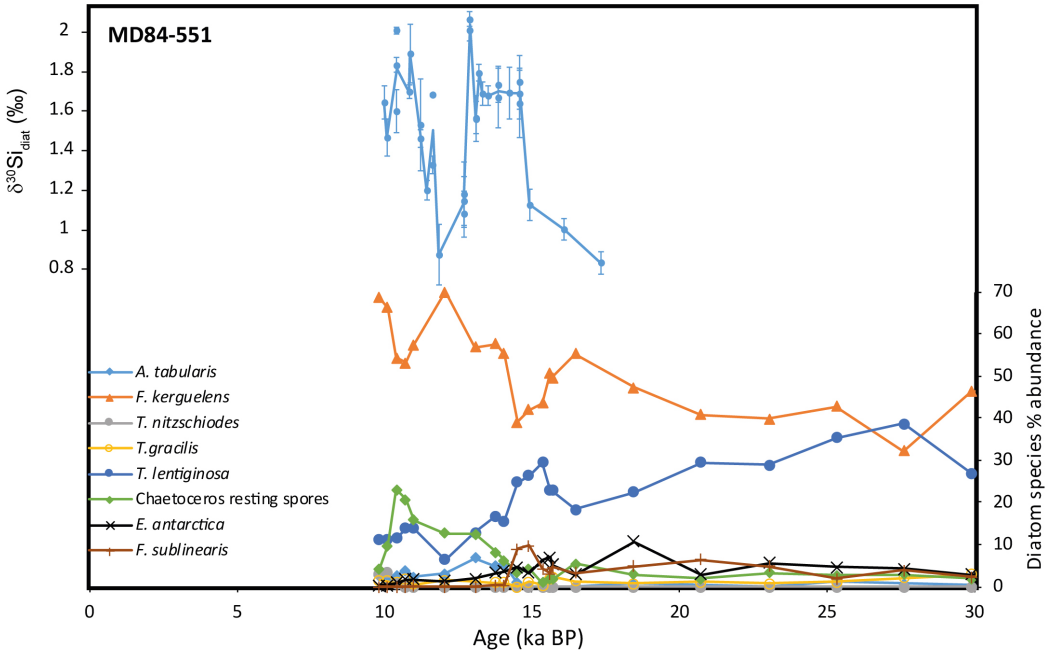

FIGURE 6.3: $\delta^{30}Si_{diat}$ data from MD84-551 along with a comparison with diatom assemblage data (Crosta, X. unpublished).

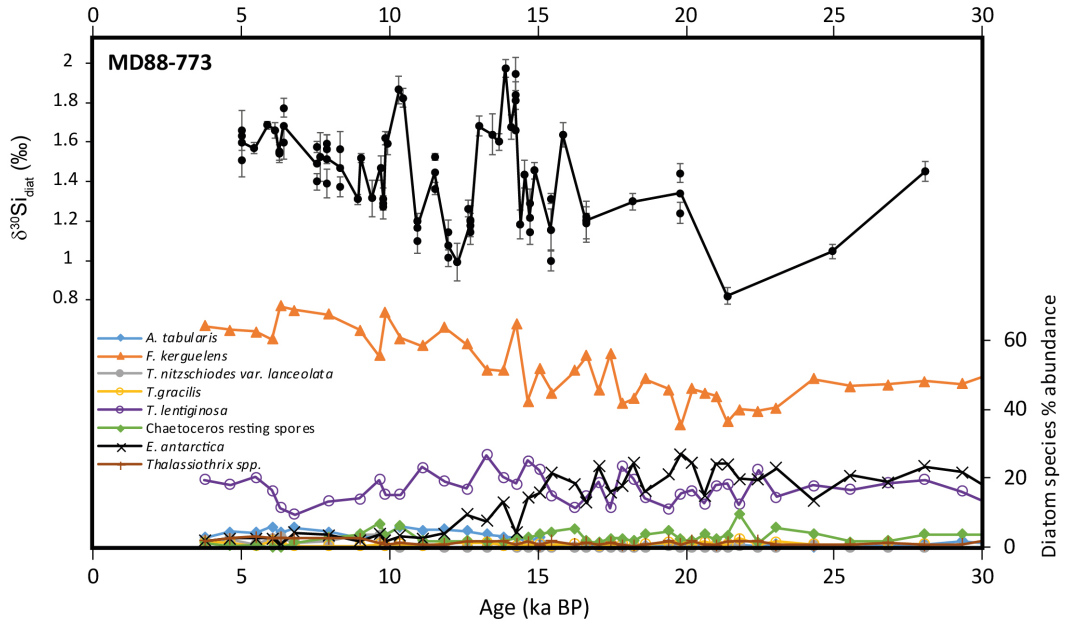

FIGURE 6.4: $\delta^{30}Si_{diat}$ data from MD88-773 along with a comparison with diatom assemblage data (Crosta, X. unpublished)

6.3 Results and interpretation

The $\delta^{30}Si_{diat}$ records (Figure 6.5) display an overall LGM – Holocene $\delta^{30}Si$ increase by 0.65 – 0.86 ‰, characteristic of Southern Ocean records (e.g. De la Rocha et al., 1998; Beuchar et al., 2007; Horn et al., 2011 Robinson et al., 2014). The heavy Holocene $\delta^{30}Si_{diat}$ values result from low Fe availability in the modern Southern Ocean, causing the more intense silicification of iron-stressed diatom communities and exhaustive uptake of DSi (Bzezinski et al., 2002). By contrast, during the LGM dust-borne iron fluxes were higher across the globe (Mahowald et al., 2006; Albani et al., 2016) permitting diatoms to reduce their DSi demand, producing lighter $\delta^{30}Si_{diat}$ values (Bzezinski et al., 2002; Beuchar et al., 2007).

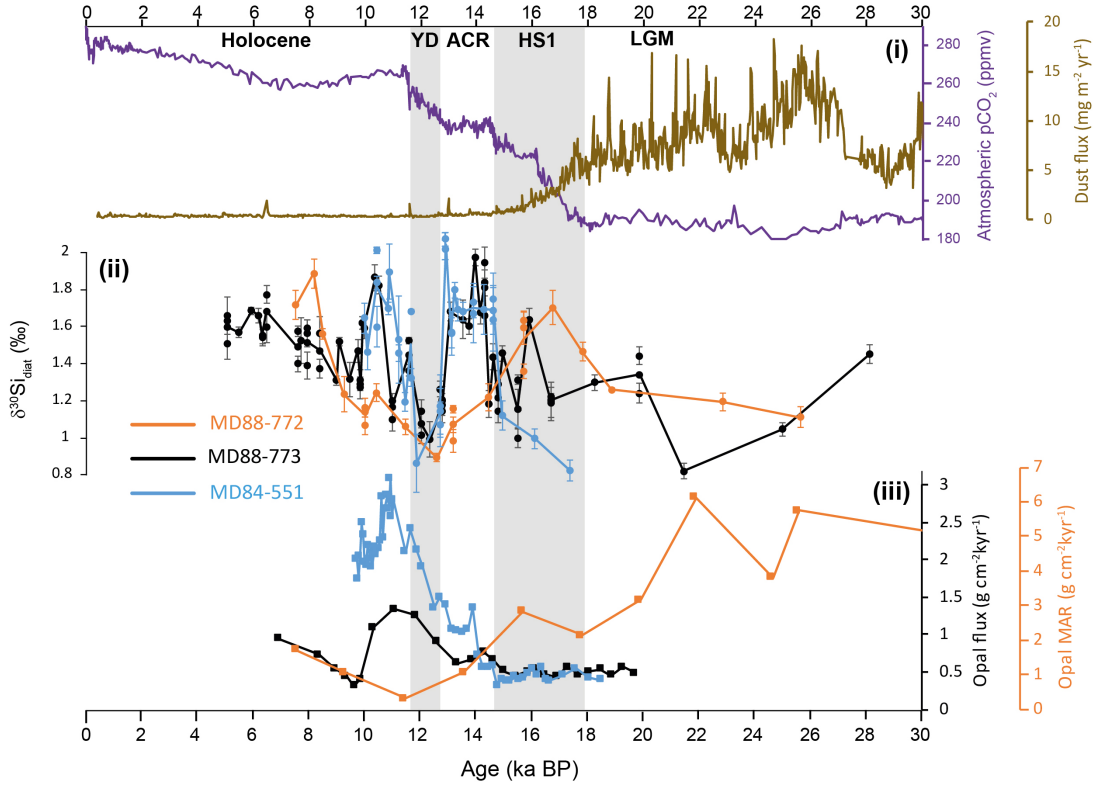

FIGURE 6.5: Changes in silicon cycling within the Indian sector across the deglaciation. **(i)** Atmospheric CO_2 (Monnin et al., 2001) and Antarctic dust flux (Lambert et al., 2012) recorded in EPICA Dome C. **(ii)** $\delta^{30}Si_{diat}$ data from MD84-551, MD88-773 and MD88-772. Note that the $\delta^{30}Si_{diat}$ tend to increase between the LGM and ACR in aggreement with and iron-mediated change in DSi demand. However, the $\delta^{30}Si_{diat}$ minimum at the YD cannot be explained by this process. **(iii)** Th-normalised opal flux records from MD84-551 and MD88-773 (Th-normalisation data from Francois et al., 1997) and opal MAR in MD88-772.

In addition, sea ice cover expanded (Crosta et al., 2004; Gersonde et al., 2005) which imposed a reduced supply of nutrients to the AZ through stratification (see Chapter 5; Francois et al., 1997) and shifted the belt of peak opal flux northwards (see Chapter 4; Chase et al., 2003; Dezileau et al., 2003; Ridgwell, 2007; Bradtmiller et al., 2009).

The initial $\delta^{30}Si_{diat}$ rise observed from the LGM through the first Antarctic warming interval ($\sim$15 – 23 ka) can be attributed to a reduction in dust-borne iron flux (Lambert et al., 2012; Martinez-Garcia et al., 2014) and gradual progression towards iron limitation, which would act to increase the DSi demand of the diatom community. This would operate in combination with the reduction in sea ice cover (Crosta et al., 2004; Wolff et al., 2006), increasing diatom productivity poleward of the core locations and fractionating the DSi pool prior to the core sites. At the Antarctic Cold Reversal (ACR, 13 – 14.7 ka BP), the Antarctic underwent a period of surface stratification (Burke and Robinson, 2012) and sea

ice expansion (Pedro et al., 2015), curtailing the DSi availability in the AZ. This drove the DSi pool in the AZ towards complete utilisation, raising the $\delta^{30}Si_{diat}$ of the southern sites (MD88-773 and MD84-551). Further north, strong vertical mixing may have been continued with the northward position of the wind belt, providing a greater supply of DSi and producing a lower $\delta^{30}Si_{diat}$ in MD88-772.

Following the early deglacial rise in $\delta^{30}Si_{diat}$, all the records exhibit a pronounced reversal, centred at approximately 12.5 ka BP. This large excursion ($\sim$0.75 ‰) does not correspond to regional reconstructions of dust flux (Lambert et al., 2012) so to invoke iron fertilization, nor other factors like diatoms assemblage changes (Figures 6.3 and 6.4). Opal flux records indicate that absolute silica uptake was similar or greater than during the Holocene (Fig.5; Dezileau et al., 2003; Anderson et al., 2009). Therefore, we suggest the $\delta^{30}Si_{diat}$ minimum reflects a combination of overwhelming DSi supply and a lighter $\delta^{30}Si_{diat}$ source.

An enhanced DSi supply is supported by the compilation of Southern Ocean $\delta^{30}Si_{diat}$ records. The pronounced minimum is common feature in Southern Ocean records and the values tend to converge during this interval towards $\sim$ 1‰, as shown in Figure 6.3. Such regional uniformity implies a flattening of the meridional DSi gradients produced by a large-scale supply of DSi to the Southern Ocean: the large influx of DSi overwhelmed the increasing DSi demand levied on the diatom community as the dust-borne iron supply approached its Holocene minimum (Lambert et al., 2012).

The timing of the $\delta^{30}Si_{diat}$ excursion supports the hypothesis that vertical (Jaccard and Galbraith, 2013; Sikes et al., 2016) and inter-basin (Sikes et al., 2017) ventilation was incomplete during the initial pCO_2 rise (15 – 18 ka BP) and that a portion of the deep ocean remained isolated until after HS1 (Stern and Lisieki, 2014). Indeed, sponge-based reconstructions (Figure 6.6) suggest the Pacific DSi content was enhanced during the LGM relative to today and this enrichment continued until the late deglaciation (Ellwood et al., 2010). The deglacial evolution of the inter-basin DSi gradient agrees well with inter-basin comparisons of $\delta^{13}C$ records (Sikes et al., 2017). These data therefore suggest that the restricted mixing across sills such as the Drake Passage may also partition nutrients as well as carbon between oceanic basins. Only after the resumption of interglacial NADW formation during the BA/ACR (McManus et al., 2004) and further retreat of Antarctic sea ice (Stephens and Keeling, 2000; Wolff et al., 2006) was deep mixing strong enough to remove the deep DSi gradients formed during the LGM.

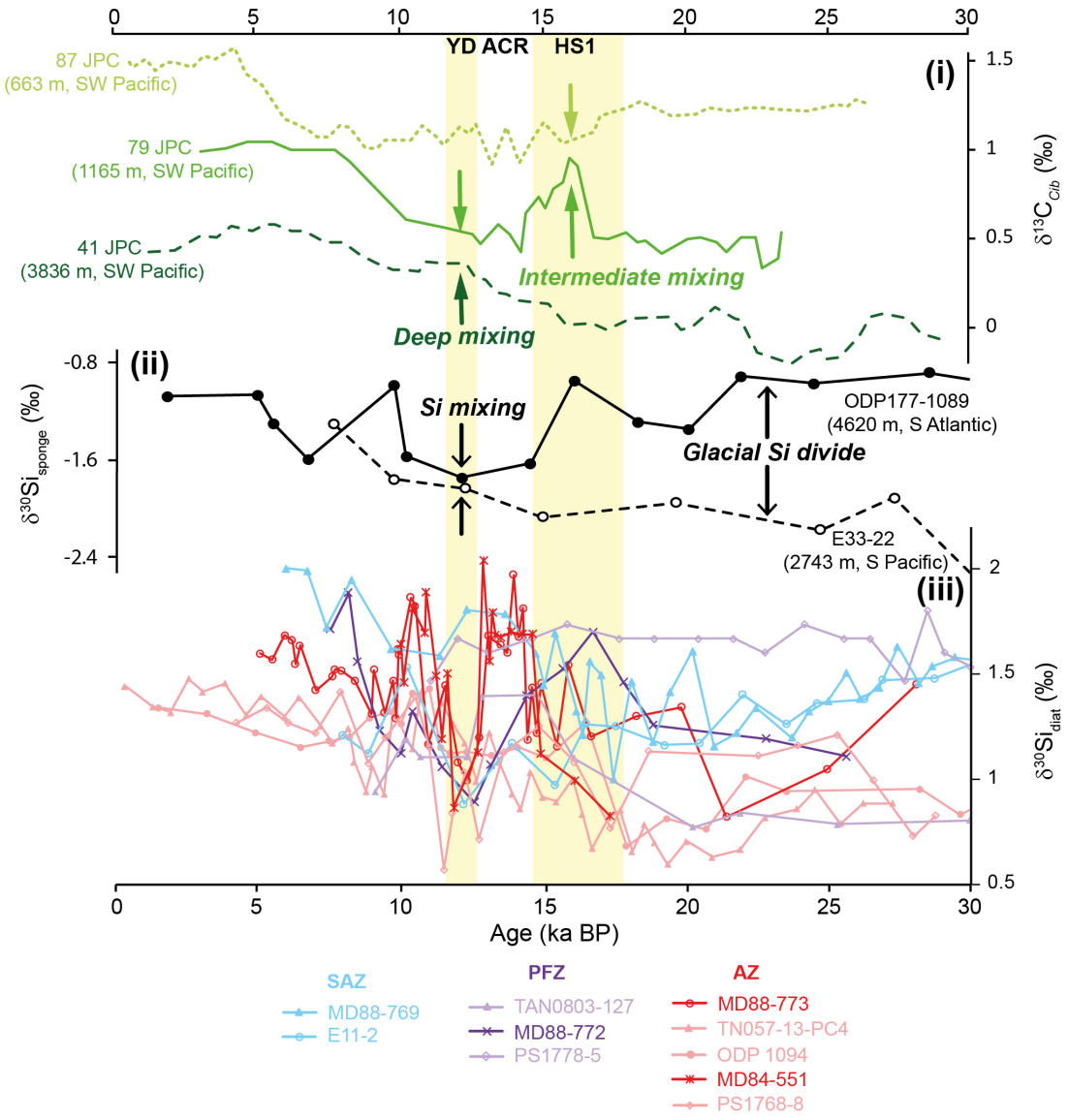

FIGURE 6.6: Plot demonstrating the correlation between deep ocean mixing during the YD and the Southern Ocean $\delta^{30}Si_{diat}$ records. **(i)** $\delta^{13}C$ of benthic foraminifera (*Cibicidoides wuellerstorfi*) within three southwest Pacific records (Sikes et al., 2016). These records demonstrate the evolution of deep ocean chemical gradients during the deglaciation. Note the homogenisation of deep and intermediate $\delta^{13}C$ at the YD, suggesting deep mixing during this interval. **(ii)** $\delta^{30}Si_{sponge}$ records from the south Atlantic and south Pacific (Ellwood et al., 2010) used as proxies for deep water DSi concentration. Note the separation of the $\delta^{30}Si_{sponge}$ data at the LGM relative to the Holocene, suggesting higher DSi concentrations were found in the deep Pacific at this time. The convergence of the Atlantic and Pacific $\delta^{30}Si_{sponge}$ data at the YD coincides with the deep/intermediate $\delta^{13}C$, suggesting both inter-basin and vertical mixing increased at this interval. **(iii)** A compilation of $\delta^{30}Si_{diat}$ records from across the SAZ (blue), PFZ (purple) and AZ (red). MD88-769: Beucher et al (2007). E11-2: Robinson et al (2005). TAN0803-127: Rousseau et al (2016). PS1778-5 & PS1768-8: (Abelmann et al., 2015). TN057-13-PC4: Horn et al (2011). ODP1094: Robinson et al (2014). Note the convergence of the $\delta^{30}Si_{diat}$ records, particularly the AZ records, at the YD, coeval with the $\delta^{30}Si_{sponge}$ and $\delta^{13}C$ homogenisation in the deep ocean.

PANDORA box model

We can demonstrate the conceptual framework by which the deep Pacific waters became enriched in DSi during glacials by adapting the PANDORA circulation model. The box model setup is based on the PANDORA architecture of Peng et al (1993) and Reynolds (2009). A major change is the inclusion of an abyssal Southern Ocean/Pacific box that will be used to simulate the isolation of deep waters. The water fluxes between boxes for the control (Holocene) setup have been taken from Peng et al (1993), with the Southern Ocean outputs re-routed through the Abyssal box (Figure 6.7).

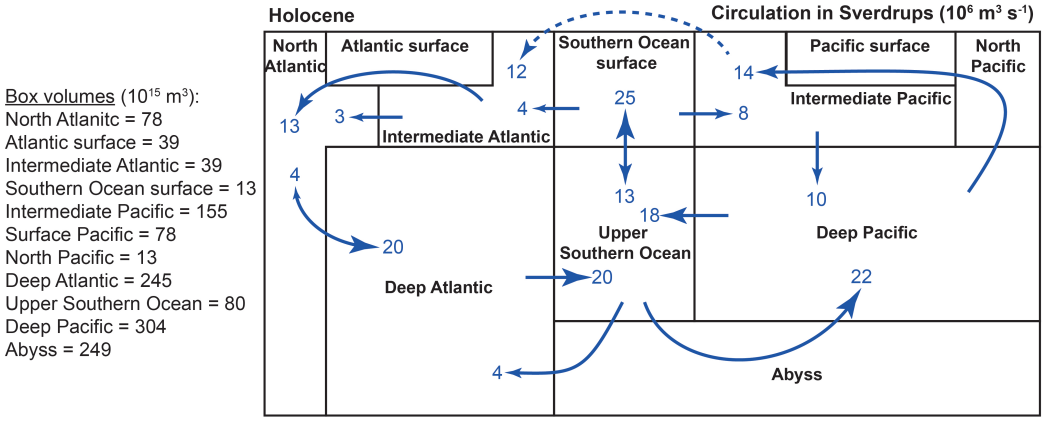

FIGURE 6.7: PANDORA box model water flux architecture for the Holocene (control).

The silica flux model operates by removing a prescribed fraction of DSi from the upper boxes at each time step and performing isotopic fractionation based on the closed system Rayleigh fractionation equation:

$$\delta^{30}Si = \delta^{30}Si(OH)_{4init} - \epsilon\frac{fln(f)}{1-f} \tag{6.1}$$

Where $\delta^{30}Si$ is the isotopic composition of the biogenic silica, $\delta^{30}Si(OH)_{4init}$ is the starting isotopic composition of the DSi pool, ϵ is the isotopic effect (-1.1 ‰) and f is the fraction of the DSi that remains unutilized. The amount of DSi uptake is prescribed by assigning a value of f to each box. This value is chosen iteratively to produce modern surface ocean DSi and $\delta^{30}Si(OH)_4$ distribution as well as modern $\delta^{30}Si$ values for exported biogenic opal. After the fraction of Si uptake is calculated, 56 % of the utilised silica is remineralised

back into the same box from which it was removed, representing dissolution prior to export (Treguer and De La Rocha, 2013). The remaining 44 % is exported to be remineralised in the ocean interior. The partitioning of the silica remineralisation into subsurface boxes is closely based on the profiles given by Reynolds (2009) but is adapted to incorporate the Abyssal box and produce modern DSi and δ^{30}Si distributions. The steady-state solution of the Si cycle is displayed in Figure 6.8.

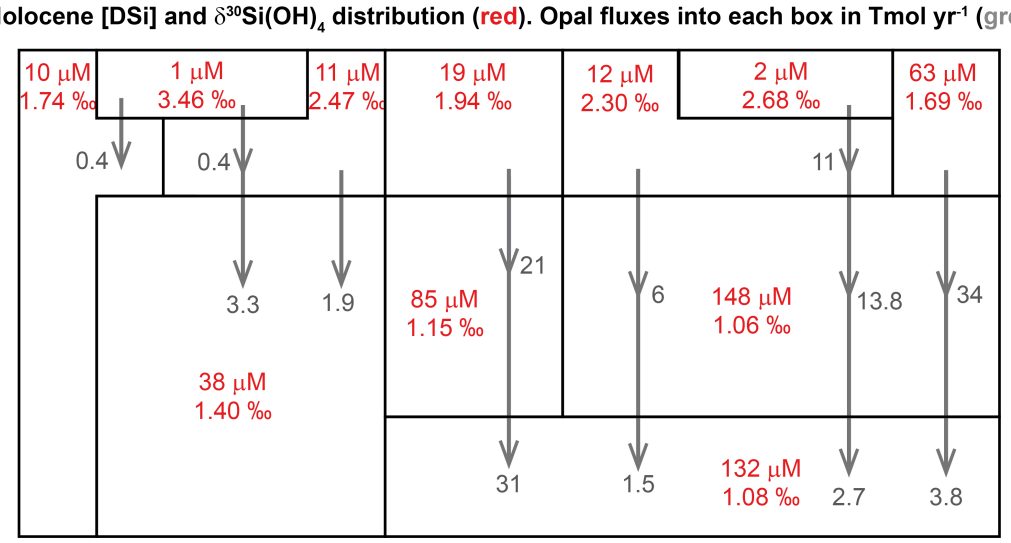

FIGURE 6.8: PANDORA box model silicon cycling architecture for the Holocene (control).

The LGM scenarios presented here are not intended to be reconstructions of the marine silicon cycle during the LGM but rather a demonstration of the mechanisms by which DSi may be enriched in the deep ocean and how the silicon isotopes are redistributed as a result. The circulation is re-ordered such that water fluxes through the Abyss box to the Deep Atlantic ($F_{SO-Abyss-Atl}$) or Deep Pacific ($F_{SO-Abyss-Pac}$) are redirected to become exchanges with the upper Southern Ocean box instead. This simulates reduced communication between the upper and abyssal ocean. An example of the circulation architecture is presented in Figure 6.9, whereby $F_{SO-Abyss-Atl} = 1$ and $F_{SO-Abyss-Pac} = 5$.

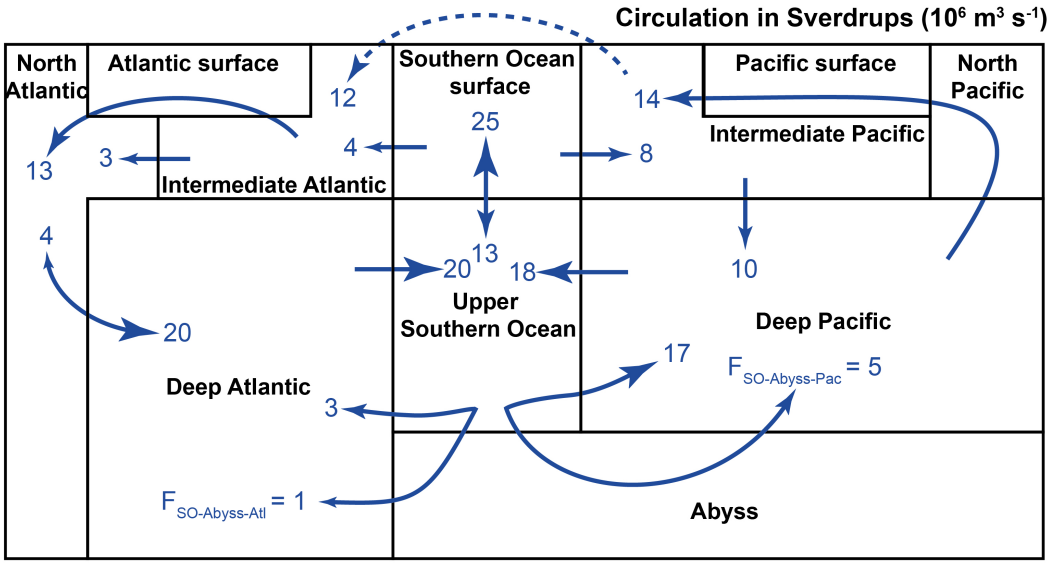

FIGURE 6.9: PANDORA box model water flux architecture demonstrating the sensativity experiment setup whereby water fluxes from the Upper Southern Ocean box were directed between the Deep Pacific, Abyss and Deep Atlantic boxes. In this example the flux between the Upper Southern Ocean, Abyss then Deep Atlantic ($F_{SO-Abyss-Atl}$) was reduced from its Holocene value of 4 to 1 Sv and the flux between the Upper Southern Ocean, Abyss then Deep Pacific ($F_{SO-Abyss-Pac}$) was reduced from 22 to 5 Sv.

Figures 6.10(A) and 6.10(B) display the results of a sensitivity test comparing the DSi concentrations (A) and δ^{30}Si compositions (B) of the Abyssal box and remainder of the ocean. The upper Southern Ocean – Abyss – Deep Pacific water flux ($F_{SO-Abyss-Pac}$) was varied from 1 to 22 Sv (x-axis) and the upper Southern Ocean – Abyss – Deep Atlantic water flux ($F_{SO-Abyss-Atl}$) was varied from 1 to 4 Sv (coloured series). It is apparent that reducing the exchange between the Abyss and Atlantic or Pacific tends to increase the DSi content of the Abyssal box. Changes in the distribution of Si isotopes are minimal in these scenarios as the Si utilization remains high throughout. Thus, the silica exported to the Abyss has a relatively high isotopic composition and increases as the upper ocean DSi content is depleted.

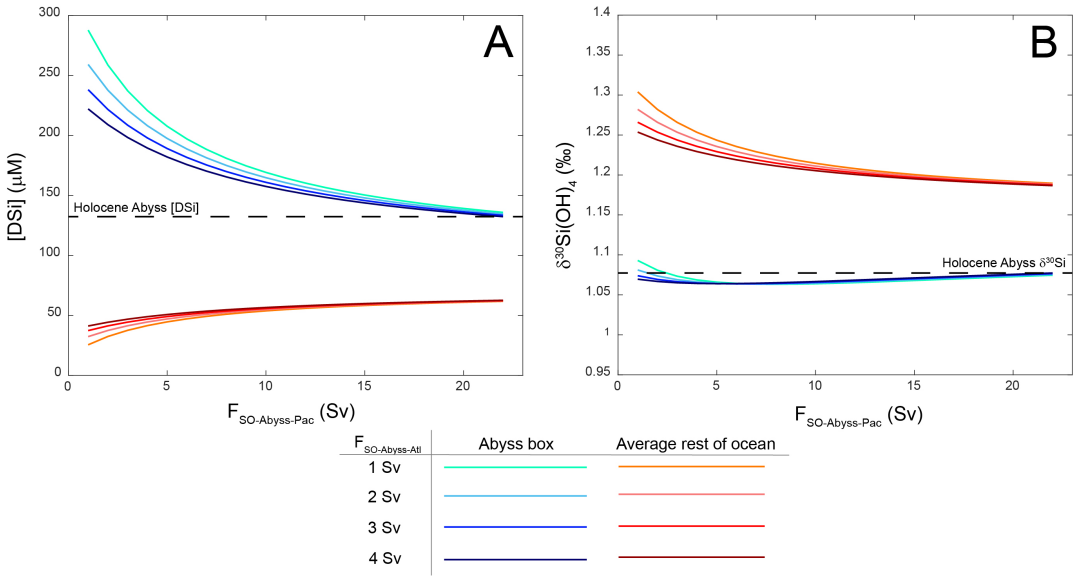

FIGURE 6.10: Plots of steady-state outputs from a series of sensitivity experiments varying the deep mixing only. **A** shows the effect of deep mixing on DSi concentrations in the Abyss box (blue lines) and the rest of the ocean (red lines). **A** shows the effect of deep mixing on the $\delta^{30}Si(OH)_4$ of the Abyss box (blue lines) and the rest of the ocean (red lines). Note that thus demonstrates that any reduction in mixing in the deep ocean would tend to result in the accumulation of DSi.

Figures 6.11(A) and 6.11(B) display results from a similar sensitivity test as above, however in these tests the fractional utilization of DSi in the Southern Ocean was lowered to approximately match the Holocene – LGM range in $\delta^{30}Si$ observed ($\sim 0.7‰$). For simplicity the same value of f was applied to every test, which produced $\delta^{30}Si$ values for the opal exported from the Southern Ocean from 0.58 ‰to 0.75 ‰lower than the control (Holocene). As an example of the model output, Figures 6.12 and 6.13 display the steady-state solutions of the silicon cycling for the circulation given in Figure 6.9 (i.e. $F_{SO-Abyss-Atl} = 1$ and $F_{SO-Abyss-Pac} = 5$) without and with the changes to Si utilization in the Southern Ocean, respectively. What is apparent is that reduced utilization in the Southern Ocean permits leakage of DSi to the remainder of the upper ocean. This allows opal fluxes to be sustained at or above Holocene levels as observed in equatorial Atlantic sediment records (Bradtmiller et al., 2007).

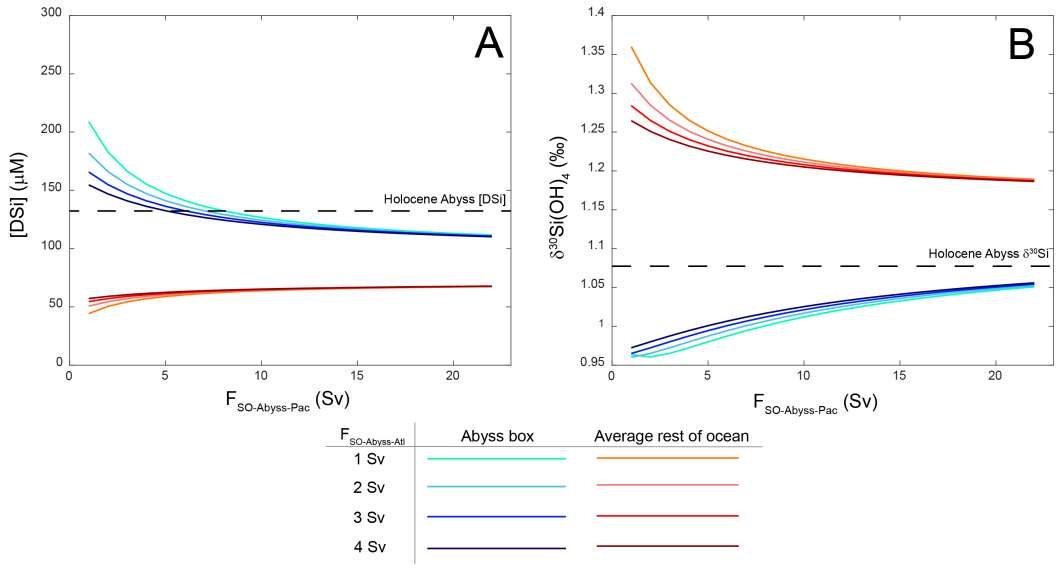

FIGURE 6.11: Plots of steady-state outputs from a series of sensitivity experiments varying the deep mixing but also with a reduction in Southern Ocean Si utilisation that matches observations. **A** shows the effect of deep mixing on DSi concentrations in the Abyss box (blue lines) and the rest of the ocean (red lines). **A** shows the effect of deep mixing on the $\delta^{30}Si(OH)_4$ of the Abyss box (blue lines) and the rest of the ocean (red lines). Note that in **A**, the Abyss box DSi concentration is lowererd when using the Holocene (control) circulation scheme. High concentrations are only obtained by reduced mixing. However, this acts to partition the $\delta^{30}Si(OH)_4$ between the Abyss and rest of the ocean, lowering the $\delta^{30}Si(OH)_4$ of the Abyss (**B**).

The decreased Si utilization in the Southern Ocean reduces the sensitivity of the DSi content of the Abyss box to changes in deep circulation. In turn this increase the ocean's sensitivity to changes in the distribution of Si isotopes. Greater residence times of water within the Abyss box tend to increase the importance of the isotopically light biogenic silica inputs over the heavier preformed DSi inputs from the Southern Ocean. The result is the generation of a pool of isotopically light DSi in the Abyss. The real magnitude of the change in the deep $\delta^{30}Si(OH)_4$ and DSi content is unknown and this model simply demonstrates the conceptual framework for how such a change can occur. However, it should be noted that this model highlights how reduced utilization in the Southern Ocean tends to reduce the DSi concentration in the deep waters (also known as Si leakage). Sponge-based DSi reconstructions suggest the deep Pacific DSi concentrations were in fact greater than today (Ellwood et al., 2010). As shown in Figure 6.11(A), greater-than-Holocene DSi concentrations in the deep would only be obtained through very sluggish mixing in our simulations, which tend to decrease the deep sea $\delta^{30}Si(OH)_4$. Further sponge-based

reconstructions combined with more data-constrained modelling approaches should be explored to quantify such changes.

In summary, by simply reducing deep water exchange, the isolated waters act as a sink for DSi. Although other nutrients, as well as carbon likely accumulated in this water mass during glacials, the effect would have been exacerbated for silica due to its efficient export into deeper waters relative to other nutrients (N, P and C). As demonstrated in the model outputs (Figure 6.12), sequestration of DSi into the deep sea reduces its availability in the upper ocean compared to the Holocene control scenario (Figure 6.8), lowering the productivity of diatoms and the export of silica. This contradicts observations that some low latitude regions supported similar or greater opal export during the LGM (e.g. Bradtmiller et al., 2007). Moreover, δ^{30}Si records from important regions for opal export including the Southern Ocean (Chapter 4, Robinson et al., 2014), equatorial Pacific (Pichevin et al., 2009) and north Pacific (Maier et al., 2015) all suggest that DSi availability in the upper ocean was in fact greater during the LGM than through the Holocene.

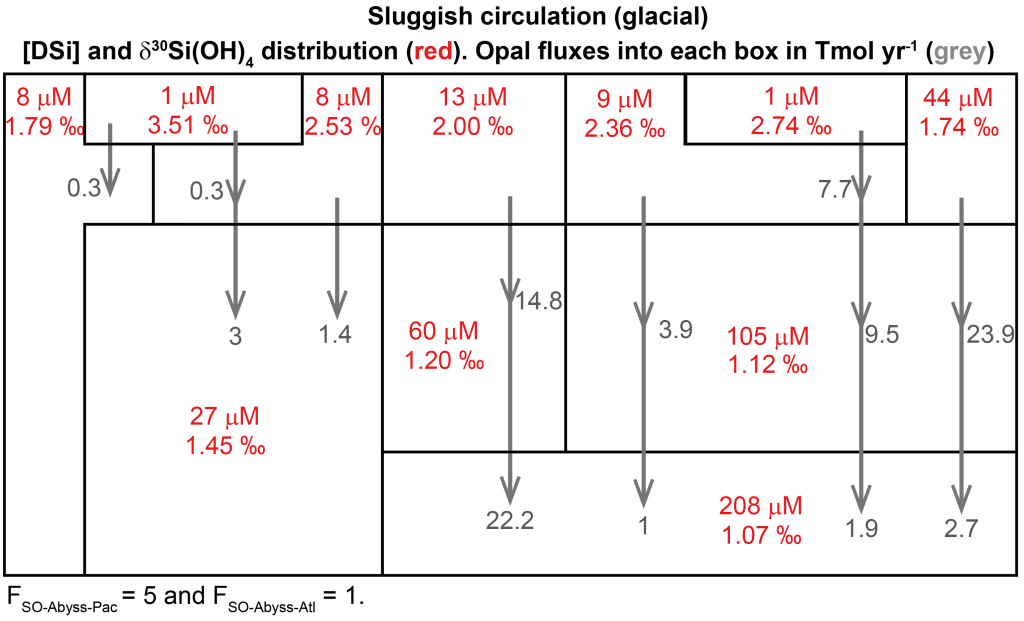

FIGURE 6.12: Output from a PANDORA box model experiment with a circulation architecture given in Figure 6.9 and no change in Si utilisation. Note the very high DSi concentrations in the Abyss box.

This paradox can be resolved by considering the effect of iron on diatom growth. Because the stoichiometric Si demand by diatoms decreases with increasing iron availability (Brzezinski et al., 2002) the additional dust-borne iron to the Southern Ocean and other iron limited

regions during glacials would provide a leakage of unused DSi to the remainder of the upper ocean. This would help maintain the availability of DSi in the upper glacial ocean, despite the tendency for sequestration in the deep. This effect is demonstrated in a further PANDORA model output (Figure 6.13) where we both alter the DSi utilization by the diatoms, fitting glacial δ^{30}Si observations, and reduce the overturning in the Southern Ocean to simulate surface stratification. In doing so, low latitude opal export is sustained, as observed in sedimentary records.

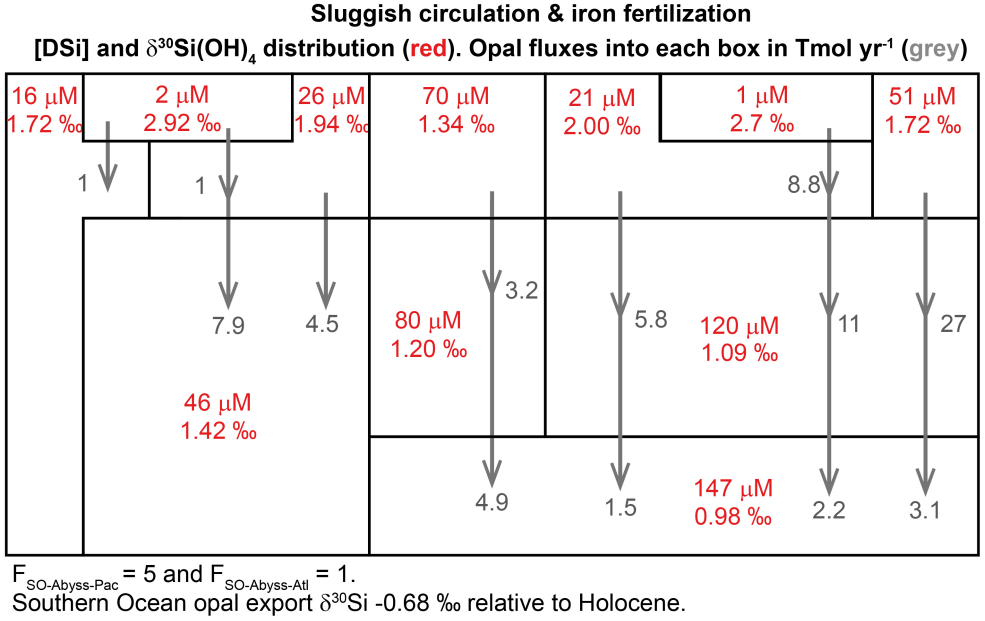

FIGURE 6.13: Output from a PANDORA box model experiment with a circulation architecture given in Figure 6.9 but with a reduction in Si utilisation. Note the DSi concentration of the Abyss box is lower than in Figure 6.12 but as is the $\delta^{30}Si(OH)_4$.

A further consequence of the reduced utilization is a steepening of the subsurface δ^{30}Si gradients along the path of deep water transport (Figure 6.13). This effect is largely absent from the modern Pacific due to the near complete DSi utilization in the surface and relatively strong mixing. Incomplete DSi utilization during glacial periods would result in isotopically light opal being exported into the deep ocean. Isolation of deep waters would promote a higher proportion of the comprising DSi to be derived from the isotopically light regenerated source rather than from heavier preformed DSi, decreasing the δ^{30}Si of the isolated waters. The deglacial upwelling of these isotopically light waters may have contributed to the low $\delta^{30}Si_{diat}$ values we observe in our sediment records after dust fluxes to Antarctica reached a minimum. Indeed, the magnitude of the excursion ($\sim$0.75 ‰) is very large with respect to the maximum range achievable through changes in utilization alone, dictated by the

fractionation factor (-1.1 ‰). Hence, we suggest that such a large change implies some contribution from a lightening of the source $\delta^{30}Si(OH)_4$.

The view of glacial marine silicon cycling presented here emphasises the importance of the trapping of biogenic silica in the deep ocean and is illustrated in Figure 6.14. The global distribution of DSi is sensitive to changes in deep mixing, which was sluggish during glacial periods. Our data suggests the reorganisation of the global DSi distribution towards modern conditions occurred primarily towards the latter stages of the deglaciation, possibly in response to reinvigoration of the Atlantic meridional overturning circulation and further retreat of Southern Ocean sea ice (Stephens and Keeling, 2000; McManus et al., 2004; Wolff et al., 2006). The glacial trapping of DSi in the deep ocean should have decreased the availability of DSi in the surface ocean, thus lowering the diatom dominance and raising the CaCO3:Corg rain ratio (Figure 6.14B). This would act as a negative feedback, promoting the rise of atmospheric CO_2. However, DSi depletion of the upper ocean was avoided because iron fertilization reduced the silicon demand by diatoms (Figure 6.14C). Consequently, the degree of diatom dominance observed today in upwelling regions may have been maintained or even enhanced during glacial periods (Bradtmiller et al., 2007). The efficient soft-tissue pump sustained by a strong diatom dominance would favour the sequestration of CO_2 into the deep sea during glacial periods acting in concert with the reduced ventilation of the deep ocean. This highlights the important role that iron plays with respect to modulating both the marine silicon cycle and productivity in high-nutrient, low-chlorophyll regions that together have a profound influence on the global biological pump.

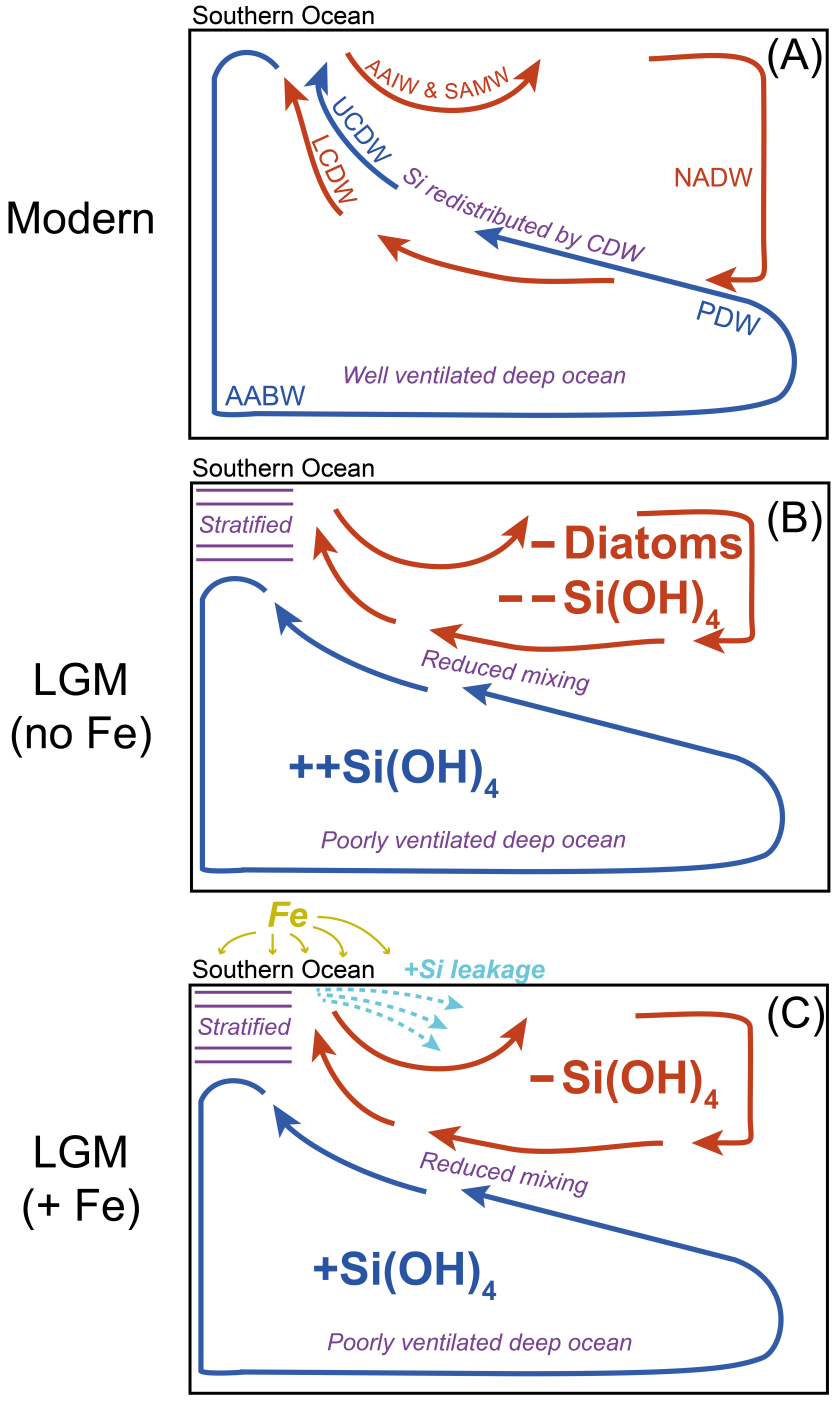

FIGURE 6.14: Schematic diagrams of proposed iron/circulation-driven redistribution of DSi between the Holocene and LGM. During the Holocene **(A)** the ocean circulation encourages deep mixing between the Atlantic and Pacific basins. However at the LGM **(B&C)** the shoaling of the boundary between the southern- and northern-source waters as well as the strengthening on salinity stratification reduced mixing between the two overturning cells. This promoted the sequestration of DSi in the deeper cell due to the slow remineralisation rate of opal. Without iron **(B)** this DSi sequestration would have reduced diatom productivity in the glacial surface ocean, which is not observed. The greater iron flux during the LGM **(C)** lowered the DSi demand by diatoms, enabling a greater leakage of DSi from the Southern Ocean to low latitudes, sustaining diatom productivity.

Deglacial Si leakage to low latitudes

Nutrients transported equatorward by Ekman drift and exiting the Antarctic contribute to the nutrient inventories and nutrient isotopic compositions of the intermediate water masses (AAIW and SAMW) that form in the Subantarctic (Sloyan and Rintoul, 2001; Fripiat et al., 2011). The exhaustive DSi utilization within the modern Southern Ocean results in a depletion of DSi in AAIW (∼20 µM) and SAMW (∼8 µM) relative to that of upwelled UCDW (70 – 100 µM) (Fripiat et al., 2011). Furthermore, the high Si:N uptake by iron-stressed diatoms in the Southern Ocean imprints a low DSi content on the intermediate waters relative to other nutrients. This is visualised in Figure 6.15, which shows intermediate waters derived from the Southern Ocean as having a lower DSi content than nitrate.

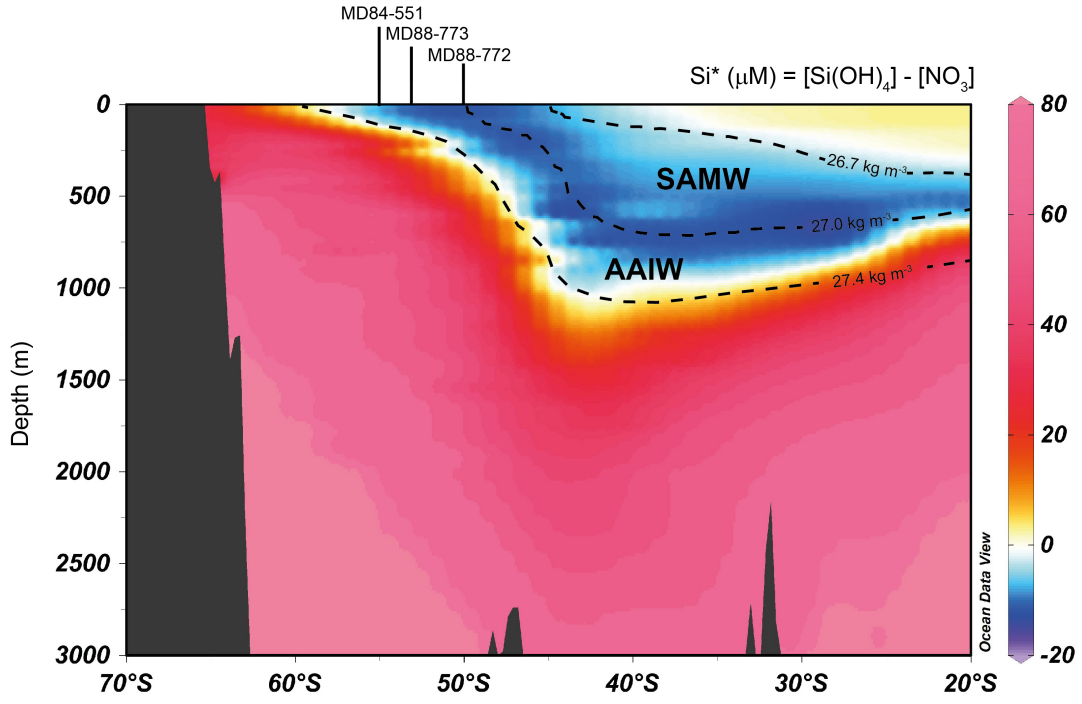

FIGURE 6.15: Gridded profile of Si* along 90°E. Silicic acid and nitrate data from WOA13 (Garcia et al., 2013). The 27.4 kg m^{-3}, 27.0 kg m^{-3} and 26.0 kg m^{-3} are shown to note the approximate location of AAIW and SAMW in the Indian sector (Herraiz-Borreguero and Rintoul, 2011). Produced using ODV software (Schlitzer, 2002).

The Southern Ocean intermediate waters, particularly SAMW, ventilate the low latitude thermocline, supporting the primary production within low latitude upwelling regions such as the eastern equatorial Pacific (Sarmiento et al., 2004). Because the nutrient inventory of the intermediate waters reflects the nutrient supply and export in the Southern Ocean surface waters, primary production in the low latitudes is modulated by physical and biogeochemical

processes occurring in the Southern Ocean. Based on this premise, it has been proposed that the lower DSi utilisation in the Southern Ocean during glacial periods could have increased the DSi:NO_3 supply ratio to the lower latitudes thus fertilizing diatom productivity (Brzezinski et al., 2002; Matsumoto et al., 2002; Matsumoto and Sarmiento, 2010). Because diatoms are efficient exporters of organic carbon to the deep sea, a shift towards diatom dominance may have contributed to the lower atmospheric CO_2 concentrations during glacial periods.

The lower $\delta^{30}Si$ and higher $^{15}N_{DB}$ (Chapter 5) during the LGM within the three records presented here indicates the DSi:NO_3 ratio remaining in AZ and PFZ waters to be incorporated into Southern Ocean intermediate waters was increased during the LGM. To demonstrate these changes a simple two-box model was constructed that was closely based on that produced by Beuchar et al (2007), with the boxes representing surface waters either side of the PF (i.e. the Antarctic and Subantarctic). Figure 6.16 displays the box model configurations for the Holocene and LGM. This setup is unchanged from that presented by Beuchar et al (2007). No updates to this model were deemed necessary as both the $\delta^{30}Si_{diat}$ data from the three cores presented here are comparable to the original $\delta^{30}Si$ outputs of the model.

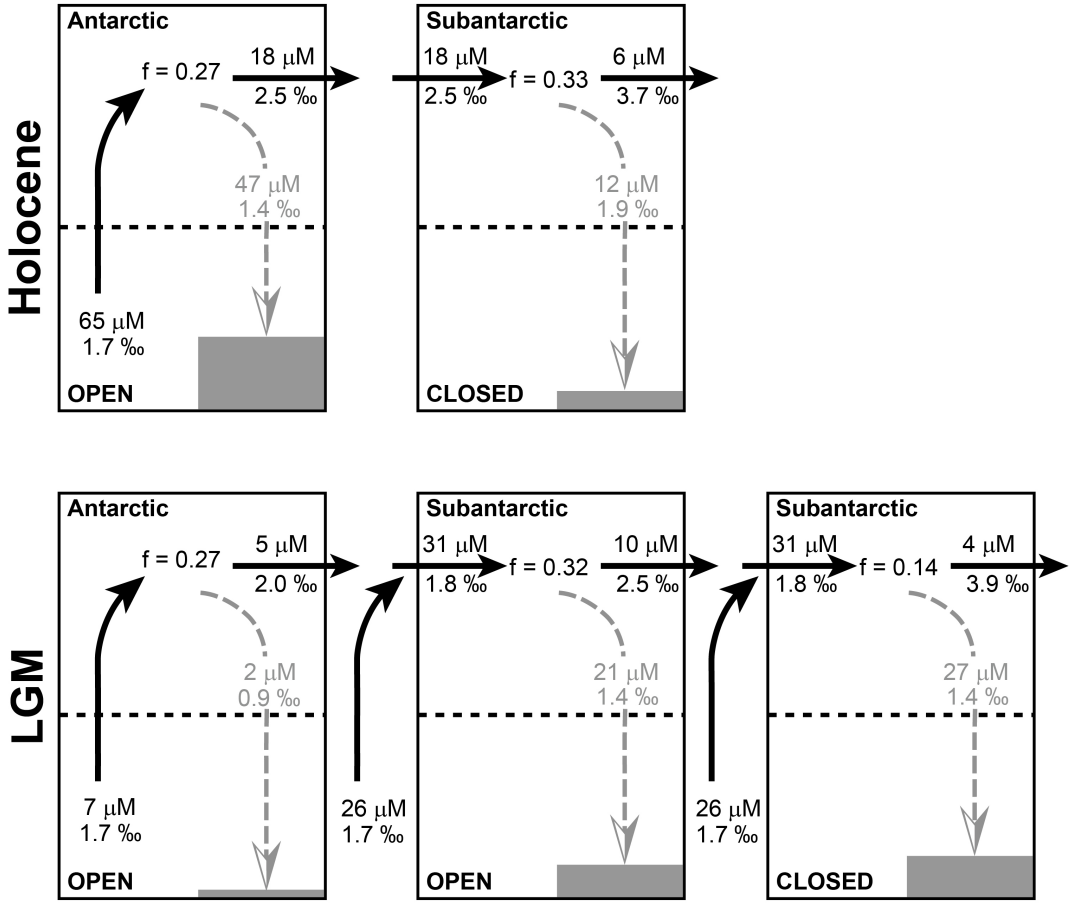

FIGURE 6.16: Box model setups based on Beuchar et al (2007).

In the modern Antarctic the supply of DSi into the Antarctic surface waters does not cease during summer (Fripiat et al., 2011). Hence, the isotopic fractionation in the Antarctic more closely fits that of an open system, whereas the modern Subantarctic is best described as a closed system as vertical supply during summer is negligible. For the LGM, Beuchar et al (2007) found an addition supply of DSi into the Subantarctic was required in order to produce higher opal fluxes during the LGM. Whether the Antarctic and Subantarctic behaved as open or closed systems during the LGM is unknown. A strong stratification in the Antarctic favours a closed system interpretation. However, the difference in output between the two fractionation models for the Antarctic has no impact on the overall interpretation, as contribution of DSi from the Antarctic to the Subantarctic is always small relative to the additional vertical mixing input into the Subantarctic. Both open and closed systems are presented for the Subantarctic box. As concluded by Beuchar et al (2007), the results of this Holocene – LGM box model comparison can be interpreted as suggesting greater

DSi leakage to the lower latitudes during the LGM. The overall LGM – Holocene change in unutilized DSi exiting the Subantarctic box is small (+4 μM and – 1.5 μM relative to the Holocene for an open and closed Subantarctic, respectively), however, more exhaustive utilization of nitrate due to iron fertilization would increase the DSi:NO_3 content of waters exiting the Subantarctic. Consequently, higher diatom productivity would be favoured in the low latitude upwelled regions (Bradtmiller et al., 2007), despite the lower overall DSi transport via upwelling to the Southern Ocean surface during the LGM (Matsumoto and Sarmiento, 2008).

This box model can be adapted to reconstruct the input of DSi to the Southern Ocean during the deglaciation, thus providing an indication of the change in DSi transport to lower latitudes during this interval. We aim to find a set of $\delta^{30}Si(OH)_4$ and [DSi] values that can produce a given opal flux in each of the boxes during the upwelling interval associated with the YD that is interpreted as an influx of [DSi] enriched deep waters. The Indian sector records suggest opal fluxes during the YD were comparable to the Holocene (Figure 6.5, Chapter 4), therefore, the opal fluxes used in the Holocene box model were used for simplicity and comparability. YD opal fluxes that were greater than during the Holocene have been found in some records from the Southern Ocean (Anderson et al., 2009; Abelmann et al., 2015), which would require a greater [DSi] supply than that presented in the box models here. Hence, the upwelled [DSi] applied could be considered an underestimate if opal fluxes across the Southern Ocean were indeed greater during the YD than the Holocene.

Again, the isotopic fractionation model (open or closed) applicable to either the Antarctic or Subantatctic during the YD is unknown. Given the hypothesised removal of Antarctic stratification during the YD interval, we suggest the open system model used to describe the modern Antarctic is most fitting. This would also provide a more direct comparison with the Holocene box model. For the Subantarctic the closed system was chosen to allow for a more direct comparison with the Holocene box model. It should be noted that applying an open system in the Subantarctic would require a lower Si utilization to produce the same opal flux output as the closed system. In this regard, the use of the closed system here can be thought of as conservative with respect to estimating the changes in DSi leakage from the Southern Ocean during the YD.

Because we suggest both the upwelling [DSi] and $\delta^{30}Si(OH)_4$ may have been subject to change across the deglaciation there are multiple solutions to the box model (different

combinations of [DSi] and $\delta^{30}Si(OH)_4$ inputs) that can produce the same opal fluxes and $\delta^{30}Si_{diat}$. The output $\delta^{30}Si_{diat}$ parameters for the Antarctic and Subantarctic boxes were estimated using by interpolating the Southern Ocean $\delta^{30}Si_{diat}$ records to find the $\delta^{30}Si_{diat}$ at 12 ka BP. The mean $\delta^{30}Si_{diat}$ at 12 ka BP for the Antarctic and Subantarctic records was estimated to be 1.0 ‰and 1.3 ‰, respectively. The constraints on the DSi input to the Antarctic were based on the Holocene values, with maximum $\delta^{30}Si(OH)_4$ and minimum [DSi] no different from the Holocene (1.7 ‰and 65 µM, respectively). Additional Subantarctic vertical mixing like that applied in the LGM box model will be considered separately.

Figure 6.17 presents a range of box model solutions. Solution A has the identical input parameters to the Holocene model. The Antarctic opal fluxes for this solution are lower than the Holocene, whilst the Subantarctic opal fluxes are higher. The opal fluxes do not agree with observations; therefore, this solution is rejected. Solution B has increased Antarctic [DSi] input such that the Antarctic opal export is identical to the Holocene and thus more closely agrees with observations. However, the opal flux in the Subantarctic is much greater than the Holocene, conflicting with observations. Solution C is opposite in the scenario range to solution B in that the input [DSi] is kept constant but the input $\delta^{30}Si(OH)_4$ is reduced. Subantarctic opal fluxes are too low in this solution without additional vertical mixing in suppling DSi to the Subantarctic. The $\delta^{30}Si(OH)_4$ and [DSi] parameters for any additional vertical supply to the Subantarctic are unknown. Solution C (+vertical mixing) presents one possible solution whereby addition DSi is supplied at an isotopic composition of 1.7 ‰. Solution D presents an intermediate between solution B and C. In this solution both the Antarctic and Subantarctic (no vertical mixing) opal fluxes match those in the Holocene model.

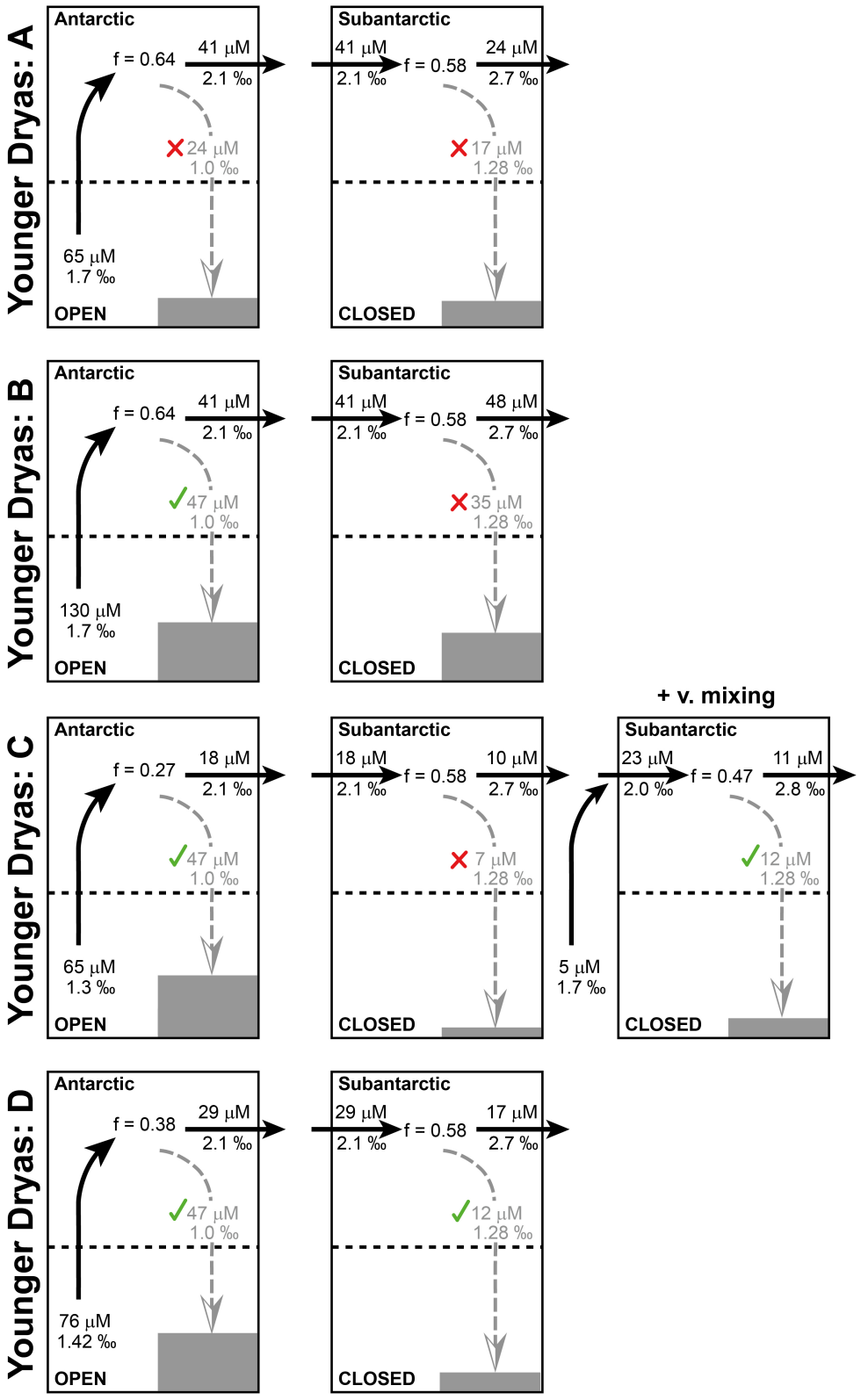

FIGURE 6.17: Box model setups based on Beuchar et al (2007) and adapted for the YD. Here the observations that there was lower $\delta^{30}Si_{diat}$ but similar opal accumulation used as a basis for reconstructing the DSi and $\delta^{30}Si(OH)_4$ cycling across this interval. **A** applies the same parameters as the Holocene setup (Figure 6.18) but the lower apparent Si utilisation in the Antarctic lowers the opal accumulation below the Holocene, which is not observed. **B** increases the DSi input to produce identical opal export in the Antarctic as the Holocene. However, this increases the Subantarctic opal flux above the Holocene. **C** lowers the input $\delta^{30}Si(OH)_4$ but this can only be reconciled by an increase in Subantarctic vertical DSi input relative to the Holocene. **D** lowers the $\delta^{30}Si(OH)_4$ and increases the DSi of upwelled water.

Both solutions C and D are viable box models based on the similar opal fluxes produced by the models in comparison to the Holocene box model (Antarctic = 47 µM, Subantarctic = 12 µM). Based on these box model experiments, it is suggested that the waters upwelling to the Antarctic surface during the YD had a maximum [DSi] content of 74 µM (+9 µM relative to the Holocene) and a minimum $\delta^{30}Si(OH)_4$ of 1.3 ‰(-0.4 ‰relative to the Holocene). All solutions suggest Si utilization decreased in the Southern Ocean during the YD, a situation that has been found to occur in Si-enrichment experiments in Southern Ocean waters without the addition of iron (Franck et al., 2000). The box model reconstructions demonstrate that a lowering of the supplied $\delta^{30}Si(OH)_4$ is required to produce the deglacial $\delta^{30}Si_{diat}$ variability. In all cases the [DSi] exiting the Subantarctic box was higher than the Holocene, suggesting enhanced Si leakage at this time. Further, the modelled $\delta^{30}Si(OH)_4$ exiting the Subantarctic box in solutions C and D (2.8 - 2.9 ‰) are approximately 0.9 ‰lighter than the Holocene (3.7 ‰). This lighter isotopic signal would have been transported to lower latitudes with the potential of producing light $\delta^{30}Si$ records.

There is considerable evidence that from low latitude records for an increase in DSi delivery within Subantarctic intermediate waters (AAIW and SAMW). A $\delta^{30}Si_{sponge}$ record presented by Hendry et al (2012) and shown in Figure 6.18 from the Brazilian Margin indicates a large increase in [DSi] within AAIW during the YD. The [DSi] of AAIW at this core site was estimated using the relationship provided by Hendry and Robinson (2012). At the YD, this record suggests that AAIW contained up to 102 µM of [DSi], much greater than at present (25 µM) and greater than we suggest entered the Southern Ocean surface waters during the YD (up to 78.5 µM). Therefore, this value appears to be unrealistically large. A potential solution to this outlier is that the $\delta^{30}Si_{sponge}$ to [DSi] calibration assumes no change in the ambient $\delta^{30}Si(OH)_4$. A lowering of the $\delta^{30}Si(OH)_4$ by 0.9 ‰, as estimated by the box model outputs given above, would reduce this [DSi] estimate to just 49 µM (+24 µM relative to today). This estimate is lower than our modelled [DSi] input to the Southern Ocean and therefore more agreeable with the interpretation here.

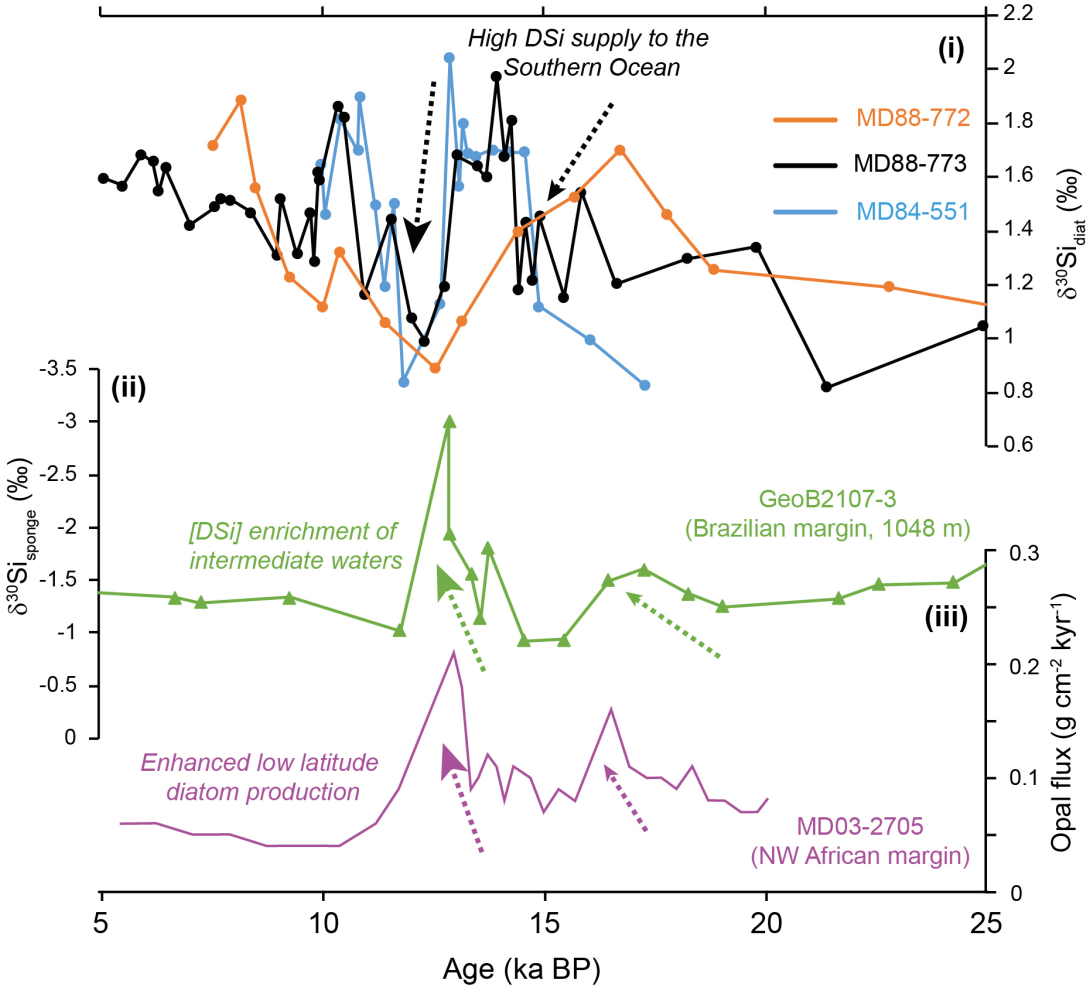

FIGURE 6.18: Plot demonstrating the leakage of DSi from the Southern Ocean, through intermediate waters and to low latitude upwelling regions such as the NW African margin during the deglaciation. **(i)** $\delta^{30}Si_{diat}$ data from the three Indian sector records. **(ii)** $\delta^{30}Si_{sponge}$ data from the Brazilian Margin (Hendry et al., 2012). This record indicates pulses of DSi enrichment occurred within AAIW during the deglaciation, likely derived from the Southern Ocean. **(iii)** Th-normalised opal flux record from the NW African margin (Meckler et al., 2013). This record highlights to strong link between DSi supply to the Southern Ocean and low latitude diatom production via the connecting intermediate waters.

The hypothesis presented here that a greater magnitude of DSi was delivered to intermediate waters via the Southern Ocean surface during the deglaciation is accompanied by other studies that interpret an increase in nutrient content of intermediate waters during the same interval (Came et al., 2003). For example, Poggemann et al (2017) attributed the increase in benthic foraminifera Cd/Ca in sediment records from the intermediate Atlantic as indicating an injection of macro-nutrients into intermediate waters during both HS1 and the YD Antarctic warming intervals. They attributed this injection to a see-sawing of Atlantic meridional overturning, such that during the HS1 and YD intervals there was a reduction in

the contribution of low-nutrient NADW to the Southern Ocean with a concomitant increase in high-nutrient PDW contribution. However, as noted by De Souza et al (2012), the influence of NADW on the $\delta^{30}Si(OH)_4$ of modern CDW is minimal (< 0.05 ‰). Therefore, we suggest it is unlikely that a decrease in the contribution of NADW to CDW during the deglaciation could have produced the $\delta^{30}Si_{diat}$ minima we observe.

Similarly, the silicic acid ventilation hypothesis presented by Hendry and Brzezinski (2014) argues that the increased DSi delivery to intermediate waters during the deglaciation was a response to an acceleration of the southern limb of the meridional overturning circulation during southern hemispheric warming events associated with a strong positive southern annular mode (SAM). In such a scenario, a greater supply of DSi to the Southern Ocean would be driven by stronger Ekman upwelling in the Antarctic, accompanied by a stronger and more southerly position of the westerly winds (Saenko et al., 2005; Ayers and Strutton, 2013). However, there is considerable debate over whether such an increase in wind-stress would increase residual mean flow required to increase nutrient supply to the surface ocean (Ito et al., 2005). Instead invigorated winds may simply produce increased mesoscale eddy transport or be compensated for by an increase in the counter-acting eddy-driven overturning known as eddy compensation (Straub, 1993; Morrison and Hogg, 2013; Lauderdale et al., 2017). Furthermore, there is little evidence that the strength of the westerlies (Bjorck et al., 2012; Mayr et al., 2013; Saunders et al., 2018) nor the strength of the ACC (Roberts et al., 2017) were greater during the YD and HS1 than during the Holocene, as would be expected under a strengthened positive SAM. Rather, we suggest the enhancement of the DSi content of intermediate waters during the deglaciation derives from the upwelling of deep waters that were enriched in DSi relative to today.

Alternative explanations for the apparent increase in nutrient content of intermediate waters during the deglaciation interpreted from nutrient proxies (Cd/Ca and $\delta^{13}C$ etc.) include an enhancement of intermediate water production during the Antarctic warming events at the expense of NADW production (Pahnke et al., 2008; Jung et al., 2009; Pena et al., 2013). There is still much debate concerning the changes in intermediate water production during the deglaciation (Oppo et al., 2012; Meckler et al., 2013; Romahn et al., 2014). Nevertheless, the variability of the proxies, ϵ_{Nd} and $^{231}Pa/^{230}Th$, used to identify the deglacial changes in water mass transport imply that perturbation on circulation was less intense during the YD than HS1 (McManus et al., 2004; Pahnke et al., 2008) However, proxies that can be used to interpret the nutrient inventory of intermediate waters suggest

the YD interval was marked by similar or greater nutrient enrichment of intermediate waters relative to HS1 (Romahn et al., 2014; Poggemann et al., 2015). This suggests that although enhanced production of intermediate waters may have occurred during the deglaciation, the changes in nutrient content were not entirely driven by intermediate circulation changes but also by increased delivery of nutrients to the Southern Ocean at that time.

The intermediate waters of the Southern Ocean supply the thermocline waters at low latitudes and subsequently the upwelling regions that bring DSi to the surface ocean. Hence, DSi enrichment of these intermediate waters during the deglaciation as suggested above would be expected to fertilize diatom production in the low latitude upwelling regions. Several studies from various upwelling regions including the equatorial Pacific (Pichevin et al., 2009; Pena et al., 2013) and NW African margin (Meckler et al., 2013; Bradtmiller et al., 2016) provide evidence for greater diatom productivity during the deglaciation (see Figure 6.18), agreeing with the interpretation given above, that DSi transport to low latitudes was increased during the deglaciation.

6.4 Conclusions

In summary, the $\delta^{30}Si_{diat}$ data presented here from the three Indian sector cores suggest the upwelling waters to the Antarctic during the deglaciation were more enriched in [DSi] and were isotopically lighter than the waters upwelling today. Sluggish deep mixing during the last glacial period acted to sequester DSi into the deep ocean, whilst the increased input of iron to the surface ocean at least partially counteracted the sequestration by relaxing the Southern Ocean silicon trap and permitting leakage of DSi to lower latitudes. A secondary consequence of these changes was that the silicon isotopes were partitioned between the upper and lower oceans. The light isotopes entering the deep ocean as remineralised opal acted to lower the isotopic composition of the DSi within the isolated deep waters, enhancing the $\delta^{30}Si(OH)_4$ gradient along the path of meridional overturning circulation. The upwelling of the Si-rich deep waters began in earnest during the Younger Dryas interval, with the lower $\delta^{30}Si(OH)_4$ composition and higher [DSi] content of the upwelling waters both contributing to the $\delta^{30}Si_{diat}$ minimum observed in the three Indian sector records.

Diatom production in the Indian sector appeared unresponsive to the increased availability of DSi, which may be attributed to iron limitation. The large increase in opal flux in the

Atlantic sector during this period (Anderson et al., 2009) suggests that proximity to dust sources may be required to increase DSi uptake in Antarctic waters, despite the heavier silicification of diatoms under iron-stress. The incomplete export of the upwelled DSi permitted greater DSi leakage to lower latitudes during the deglaciation, increasing diatom productivity within upwelling regions.

The implications of these findings are that the global distribution of DSi is intimately connected to both global oceanic circulation and the availability of iron in surface waters. Through glacial-interglacial cycles, these two processes are coupled, such that iron availability regulates the DSi availability in the surface ocean, allowing more DSi leakage during glacial periods when DSi deliver to the surface is reduced and increasing DSi removal during interglacials when overturning is invigorated. In this regard, iron plays an important role in controlling the efficiency of carbon export that diatoms contribute to the marine biological pump thus permitting a greater removal of atmospheric CO_2 to the deep ocean during glacial periods.

References

Abelmann , A., Gersonde , R., Knorr , G., Zhang , X., Chapligin , B., Maier , E., Esper , O., Friedrichsen , H., Lohmann , G., Meyer , H., and Tiedemann , R. The seasonal sea-ice zone in the glacial Southern Ocean as a carbon sink. *Nature communications*, 6:8136, 2015. doi: 10.1038/ncomms9136.

Albani , S., Mahowald , N. M., Murphy , L. N., Raiswell , R., Moore , J. K., Anderson , R. F., Mcgee , D., Bradtmiller , L. I., Delmonte , B., Hesse , P. P., and Mayewski , P. A. Paleodust variability since the Last Glacial Maximum and implications for iron inputs to the ocean. *Geophysical Research Letters*, 43: 3944–3954, 2016. doi: 10.1002/2016GL067911.

Anderson , R. F., Ali , S., Bradtmiller , L. I., Nielsen , S. H. H., Fleisher , M. Q., Anderson , B. E., and Burckle , L. H. Wind-driven upwelling in the Southern Ocean and the deglacial rise in atmospheric CO2. *Science (New York, N.Y.)*, 323(5920):1443–1448, mar 2009. doi: 10.1126/science.1167441.

Audi , G., Bersillon , O., Blachot , J., and Wapstra , A. H. The NUBASE evaluation of nuclear and decay properties. *Nuclear Physics A*, 729:3–128, 2003.

Ayers , J. M. and Strutton , P. G. Nutrient variability in Subantarctic Mode Waters forced by the Southern Annular Mode and ENSO. *Geophysical Research Letters*, 40(13):3419–3423, 2013. doi: 10.1002/grl.50638.

Beucher , C. P., Brzezinski , M. a., and Crosta , X. Silicic acid dynamics in the glacial sub-Antarctic: Implications for the silicic acid leakage hypothesis. *Global Biogeochemical Cycles*, 21(3):1–13, sep 2007. doi: 10.1029/2006GB002746.

Björck , S., Rundgren , M., Ljung , K., Unkel , I., and Wallin , Å. Multi-proxy analyses of a peat bog on Isla de los Estados, easternmost Tierra del Fuego: A unique record of the variable Southern

Hemisphere Westerlies since the last deglaciation. *Quaternary Science Reviews*, 42:1–14, 2012. doi: 10.1016/j.quascirev.2012.03.015.

Bradtmiller , L. I., Anderson , R. F., Fleisher , M. Q., and Burckle , L. H. Opal burial in the equatorial Atlantic Ocean over the last 30 ka: Implications for glacial-interglacial changes in the ocean silicon cycle. *Paleoceanography*, 22(4), dec 2007. doi: 10.1029/2007PA001443.

Bradtmiller , L. I., Anderson , R. F., Fleisher , M. Q., and Burckle , L. H. Comparing glacial and Holocene opal fluxes in the Pacific sector of the Southern Ocean. *Paleoceanography*, 24(2):1–20, jun 2009. doi: 10.1029/2008PA001693.

Bradtmiller , L. I., McGee , D., Awalt , M., Evers , J., Yerxa , H., Kinsley , C. W., and DeMenocal , P. B. Changes in biological productivity along the northwest African margin over the past 20,000 years. *Paleoceanography*, 31(1):185–202, 2016. doi: 10.1002/2015PA002862.

Brzezinski , M., Pride , C., Franck , V. M., Sigman , D. M., Sarmiento , J. L., Matsumoto , K., Gruber , N., Rau , G. H., and Coale , K. H. A switch from Si (OH) 4 to NO3 depletion in the glacial Southern Ocean. *Geophysical Research Letters*, 29(12):3–6, 2002.

Brzezinski , M. A., Dickson , M.-l., Nelson , D. M., and Sambrotto , R. Ratios of Si , C and N uptake by microplankton in the Southern Ocean. *Deep Sea Research Part II: Topical Studies in Oceanography*, 50: 619–633, 2003.

Burke , A. and Robinson , L. F. The Southern Ocean's role in carbon exchange during the last deglaciation. *Science (New York, N.Y.)*, 335(6068):557–61, feb 2012. doi: 10.1126/science.1208163.

Came , R. E., Oppo , D. W., and Curry , W. B. Atlantic Ocean circulation during the Younger Dryas: Insights from a new Cd/Ca record from the western subtropical South Atlantic. *Paleoceanography*, 18(4): 1–9, 2003. doi: 10.1029/2003PA000888.

Cardinal , D., Alleman , L. Y., Dehairs , F., Savoye , N., Trull , T. W., and André , L. Relevance of silicon isotopes to Si-nutrient utilization and Si-source assessment in Antarctic waters. *Global Biogeochemical Cycles*, 19(2):n/a–n/a, 2005. doi: 10.1029/2004GB002364.

Chase , Z., Anderson , R. F., Fleisher , M. Q., and Kubik , P. W. Accumulation of biogenic and lithogenic material in the Pacific sector of the Southern Ocean during the past 40,000 years. *Deep Sea Research Part II: . . .*, 50:799–832, 2003.

Crosta , X., Sturm , A., Armand , L., and Pichon , J.-J. Late Quaternary sea ice history in the Indian sector of the Southern Ocean as recorded by diatom assemblages. *Marine Micropaleontology*, 50(3-4):209–223, 2004. doi: 10.1016/S0377-8398(03)00072-0.

De La Rocha , C. L., Brzezinski , M. a., and DeNiro , M. J. Fractionation of silicon isotopes by marine diatoms during biogenic silica formation. *Geochimica et Cosmochimica Acta*, 61(23):5051–5056, dec 1997. doi: 10.1016/S0016-7037(97)00300-1.

De La Rocha , C. L., Brzezinski , M. A., DeNiro , M. J., and Shemesh , A. Silicon-isotope composition of diatoms as an indicator of diatoms as an indicator of past oceanic change. *Nature*, 395(October):28–31, 1998.

de Souza , G. F., Reynolds , B. C., Johnson , G. C., Bullister , J. L., and Bourdon , B. Silicon stable isotope distribution traces Southern Ocean export of Si to the eastern South Pacific thermocline. *Biogeosciences*, 9(11):4199–4213, nov 2012. doi: 10.5194/bg-9-4199-2012.

De Souza , G. F., Slater , R. D., Dunne , J. P., and Sarmiento , J. L. Deconvolving the controls on the deep

ocean's silicon stable isotope distribution. *Earth and Planetary Science Letters*, 398:66–76, 2014. doi: 10.1016/j.epsl.2014.04.040.

Demarest , M. S., Brzezinski , M. A., and Beucher , C. P. Fractionation of silicon isotopes during biogenic silica dissolution. *Geochimica et Cosmochimica Acta*, 73(19):5572–5583, 2009. doi: 10.1016/j.gca.2009.06.019.

Dezileau , L., Reyss , J., and Lemoine , F. Late Quaternary changes in biogenic opal fluxes in the Southern Indian Ocean. *Marine Geology*, 202(3-4):143–158, nov 2003. doi: 10.1016/S0025-3227(03)00283-4.

Dugdale , R. C., Wilkerson , F. P., and Minas , H. J. The role of a silcate pump in driving new production. *Deep-Sea Research I*, 42:697–719, 1995.

Egan , K. E., Rickaby , R. E., Leng , M. J., Hendry , K. R., Hermoso , M., Sloane , H. J., Bostock , H., and Halliday , A. N. Diatom silicon isotopes as a proxy for silicic acid utilisation: A Southern Ocean core top calibration. *Geochimica et Cosmochimica Acta*, 96:174–192, nov 2012. doi: 10.1016/j.gca.2012.08.002.

Egge , J. and Aksnes , D. Silicate as regulating nutrient in phytoplankton competition. *Marine ecology progress series*, 83(July 1988):281–289, 1992.

Ellwood , M. J., Wille , M., and Maher , W. Glacial silicic acid concentrations in the Southern Ocean. *Science (New York, N.Y.)*, 330(6007):1088–1091, 2010. doi: 10.1126/science.1194614.

Ferrari , R., Jansen , M. F., Adkins , J. F., Burke , A., Stewart , A. L., and Thompson , A. F. Antarctic sea ice control on ocean circulation in present and glacial climates. *Proceedings of the National Academy of Sciences of the United States of America*, 111(24):8753–8, jun 2014. doi: 10.1073/pnas.1323922111.

Francois , R., Altabet , M. A., Yu , E.-f., Sigman , D. M., Bacon , M. P., Frank , M., Bohrmann , G., Bareille , G., and Labeyrie , L. D. Contribution of Southern Ocean surface-water stratification to low atmospheric CO 2 concentrations during the last glacial period. *Nature*, 389:929–935, 1997.

Fripiat , F., Cavagna , a. J., Dehairs , F., De Brauwere , a., André , L., and Cardinal , D. Processes controlling the Si-isotopic composition in the Southern Ocean and application for paleoceanography. *Biogeosciences*, 9(7):2443–2457, 2012. doi: 10.5194/bg-9-2443-2012.

Fripiat , F., Cavagna , a. J., Dehairs , F., Speich , S., Andr?? , L., and Cardinal , D. Silicon pool dynamics and biogenic silica export in the Southern Ocean inferred from Si-isotopes. *Ocean Science*, 7(5):533–547, 2011. doi: 10.5194/osd-8-639-2011.

Gersonde , R., Crosta , X., Abelmann , A., and Armand , L. Sea-surface temperature and sea ice distribution of the Southern Ocean at the EPILOG Last Glacial Maximum—a circum-Antarctic view based on siliceous microfossil records. *Quaternary Science Reviews*, 24(7-9):869–896, apr 2005. doi: 10.1016/j.quascirev.2004.07.015.

Gnanadesikan , A. A global model of silicon cycling : Sensitivity to eddy parameterization and dissolution. *Global Biogeochemical Cycles*, 13(1):199–220, 1999.

Hendry , K. R., Robinson , L. F., Meredith , M. P., Mulitza , S., Chiessi , C. M., and Arz , H. Abrupt changes in high-latitude nutrient supply to the Atlantic during the last glacial cycle. *Geology*, 40(2): 123–126, 2012. doi: 10.1130/G32779.1.

Hendry , K. R. and Brzezinski , M. a. Using silicon isotopes to understand the role of the Southern Ocean in modern and ancient biogeochemistry and climate. *Quaternary Science Reviews*, 89:13–26, apr 2014. doi: 10.1016/j.quascirev.2014.01.019.

Hendry , K. R. and Robinson , L. F. The relationship between silicon isotope fractionation in sponges and silicic acid concentration: Modern and core-top studies of biogenic opal. *Geochimica et Cosmochimica*

Acta, 81:1–12, mar 2012. doi: 10.1016/j.gca.2011.12.010.

Herraiz-Borreguero , L. and Rintoul , S. R. Subantarctic mode water : Distribution and circulation. *Ocean Dynamics*, 61(1):103–126, 2011. doi: 10.1007/s10236-010-0352-9.

Holzer , M., Primeau , F. W., DeVries , T., and Matear , R. The Southern Ocean silicon trap: Data-constrained estimates of regenerated silicic acid, trapping efficiencies, and global transport paths. *Journal of Geophysical Research: Oceans*, 119(1):313–331, jan 2014. doi: 10.1002/2013JC009356.

Horn , M. G., Beucher , C. P., Robinson , R. S., and Brzezinski , M. a. Southern ocean nitrogen and silicon dynamics during the last deglaciation. *Earth and Planetary Science Letters*, 310(3-4):334–339, oct 2011. doi: 10.1016/j.epsl.2011.08.016.

Hutchins , D. and Bruland , K. Iron-limited diatom growth and Si: N uptake ratios in a coastal upwelling regime. *Nature*, 393(June):65–68, 1998.

Ito , T., Parekh , P., Dutkiewicz , S., and Follows , M. J. The Antarctic Circumpolar Productivity Belt. *Geophysical Research Letters*, 32(13):L13604, 2005. doi: 10.1029/2005GL023021.

Jaccard , S. L. and Galbraith , E. D. Direct ventilation of the North Pacific did not reach the deep ocean during the last deglaciation. *Geophysical Research Letters*, 40(1):199–203, 2013. doi: 10.1029/2012GL054118.

Jung , S. J., Kroon , D., Ganssen , G., Peeters , F., and Ganeshram , R. Enhanced Arabian Sea intermediate water flow during glacial North Atlantic cold phases. *Earth and Planetary Science Letters*, 280(1-4): 220–228, apr 2009. doi: 10.1016/j.epsl.2009.01.037.

Kohfeld , K., Graham , R., a.M. de Boer , Sime , L., Wolff , E., Le Quéré , C., and Bopp , L. Southern Hemisphere westerly wind changes during the Last Glacial Maximum: paleo-data synthesis. *Quaternary Science Reviews*, 68:76–95, may 2013. doi: 10.1016/j.quascirev.2013.01.017.

Lambert , F., Bigler , M., Steffensen , J. P., Hutterli , M., and Fischer , H. Centennial mineral dust variability in high-resolution ice core data from Dome C, Antarctica. *Climate of the Past*, 8(2):609–623, mar 2012. doi: 10.5194/cp-8-609-2012.

Lauderdale , J. M., Williams , R. G., Munday , D. R., and Marshall , D. P. The impact of Southern Ocean residual upwelling on atmospheric CO 2 on centennial and millennial timescales. *Climate Dynamics*, 48 (5):1611–1631, 2017. doi: 10.1007/s00382-016-3163-y.

Lüthi , D., Le Floch , M., Bereiter , B., Blunier , T., Barnola , J.-M., Siegenthaler , U., Raynaud , D., Jouzel , J., Fischer , H., Kawamura , K., and Stocker , T. F. High-resolution carbon dioxide concentration record 650,000-800,000 years before present. *Nature*, 453(7193):379–82, may 2008. doi: 10.1038/nature06949.

Mahowald , N. M., Muhs , D. R., Levis , S., Rasch , P. J., Yoshioka , M., Zender , C. S., and Luo , C. Change in atmospheric mineral aerosols in response to climate: Last glacial period, preindustrial, modern, and doubled carbon dioxide climates. *Journal of Geophysical Research*, 111(D10):D10202, 2006. doi: 10.1029/2005JD006653.

Maier , E., Méheust , M., Abelmann , A., Gersonde , R., Chapligin , B., Ren , J., Stein , R., Meyer , H., and Tiedemann , R. Deglacial subarctic Pacific surface water hydrography and nutrient dynamics and links to North Atlantic climate variability and atmospheric CO2. *Paleoceanography*, 30(7):949–968, 2015. doi: 10.1002/2014PA002763.Received.

Martínez-García , A., Sigman , D. M., Ren , H., Anderson , R. F., Straub , M., Hodell , D. a., Jaccard , S. L., Eglinton , T. I., and Haug , G. H. Iron fertilization of the Subantarctic ocean during the last ice age. *Science (New York, N.Y.)*, 343(6177):1347–50, mar 2014. doi: 10.1126/science.1246848.

Matsumoto , K., Chase , Z., and Kohfeld , K. Different mechanisms of silicic acid leakage and their biogeochemical consequences. *Paleoceanography*, 29(3):238–254, 2014. doi: 10.1002/2013PA002588.

Matsumoto , K. and Sarmiento , J. L. A corollary to the silicic acid leakage hypothesis. *Paleoceanography*, 23(2), jun 2008. doi: 10.1029/2007PA001515.

Matsumoto , K., Sarmiento , J. L., and Brzezinski , M. A. Silicic acid leakage from the Southern Ocean: A possible explanation for glacial atmospheric pCO2. *Global Biogeochemical Cycles*, 16(3), 2002.

Mayr , C., L??cke , A., Wagner , S., Wissel , H., Ohlendorf , C., Haberzettl , T., Oehlerich , M., Sch??bitz , F., Wille , M., Zhu , J., and Zolitschka , B. Intensified Southern Hemisphere Westerlies regulated atmospheric CO2 during the last deglaciation. *Geology*, 41(8):831–834, 2013. doi: 10.1130/G34335.1.

McManus , J. F., Francois , R., Gherardi , J.-M., Keigwin , L. D., and Brown-Leger , S. Collapse and rapid resumption of Atlantic meridional circulation linked to deglacial climate changes. *Nature*, 428(6985): 834–7, apr 2004. doi: 10.1038/nature02494.

Meckler , a. N., Sigman , D. M., Gibson , K. a., François , R., Martínez-García , a., Jaccard , S. L., Röhl , U., Peterson , L. C., Tiedemann , R., and Haug , G. H. Deglacial pulses of deep-ocean silicate into the subtropical North Atlantic Ocean. *Nature*, 495(7442):495–8, mar 2013. doi: 10.1038/nature12006.

Monnin , E., Indermühle , a., Dällenbach , a., Flückiger , J., Stauffer , B., Stocker , T. F., Raynaud , D., and Barnola , J. M. Atmospheric CO2 concentrations over the last glacial termination. *Science (New York, N.Y.)*, 291(5501):112–4, jan 2001. doi: 10.1126/science.291.5501.112.

Morrison , A. K. and Hogg , A. M. On the Relationship between Southern Ocean Overturning and ACC Transport. *Journal of Physical Oceanography*, 43:140–148, 2013. doi: 10.1175/JPO-D-12-057.1.

Nelson , D. M., Anderson , R. F., Barber , R. T., Brzezinski , M. A., Buesseler , K. O., Chase , Z., Collier , R. W., Dickson , M. L., François , R., Hiscock , M. R., Honjo , S., Marra , J., Martin , W. R., Sambrotto , R. N., Sayles , F. L., and Sigmon , D. E. Vertical budgets for organic carbon and biogenic silica in the Pacific sector of the Southern Ocean, 1996-1998. *Deep-Sea Research Part II: Topical Studies in Oceanography*, 49(9-10):1645–1674, 2002. doi: 10.1016/S0967-0645(02)00005-X.

Oppo , D. W. and Curry , W. B. Deep Atlantic circulation during the last glacial maximum and deglaciation. *Nature Education Knowledge*, 3(10):1–20, 2012.

Pahnke , K., Goldstein , S. L., and Hemming , S. R. Abrupt changes in Antarctic Intermediate Water circulation over the past 25,000years. *Nature Geoscience*, 1(12):870–874, nov 2008. doi: 10.1038/ngeo360.

Pena , L., Goldstein , S., Hemming , S., Jones , K., Calvo , E., Pelejero , C., and Cacho , I. Rapid changes in meridional advection of Southern Ocean intermediate waters to the tropical Pacific during the last 30kyr. *Earth and Planetary Science Letters*, 368:20–32, apr 2013. doi: 10.1016/j.epsl.2013.02.028.

Peng , T.-h., Maier-Reimer , E., and Broecker , W. Distribution of 32Si in the world ocean: model compared to observation. *Global Biogeochem. Cycles*, 7(2):463–474, 1993.

Pichevin , L. E., Reynolds , B. C., Ganeshram , R. S., Cacho , I., Pena , L., Keefe , K., and Ellam , R. M. Enhanced carbon pump inferred from relaxation of nutrient limitation in the glacial ocean. *Nature*, 459 (7250):1114–7, jun 2009. doi: 10.1038/nature08101.

Poggemann , D.-W., Hathorne , E. C., Nürnberg , D., Frank , M., Bruhn , I., Reißig , S., and Bahr , A. Rapid deglacial injection of nutrients into the tropical Atlantic via Antarctic Intermediate Water. *Earth and Planetary Science Letters*, 463:118–126, 2017. doi: 10.1016/j.epsl.2017.01.030.

Reynolds , B. C. Modeling the modern marine δ 30 Si distribution. *Global Biogeochemical Cycles*, 23(2): n/a–n/a, jun 2009. doi: 10.1029/2008GB003266.

Ridgwell , A. J. Application of sediment core modelling to interpreting the glacial-interglacial record of Southern Ocean silica cycling. *Climate of the Past*, 3(3):387–396, 2007. doi: 10.5194/cp-3-387-2007.

Roberts , J., McCave , I. N., McClymont , E. L., Kender , S., Hillenbrand , C. D., Matano , R., Hodell , D. A., and Peck , V. L. Deglacial changes in flow and frontal structure through the Drake Passage. *Earth and Planetary Science Letters*, 474:397–408, 2017. doi: 10.1016/j.epsl.2017.07.004.

Robinson , R. S., Brzezinski , M. a., Beucher , C. P., Horn , M. G. S., and Bedsole , P. The changing roles of iron and vertical mixing in regulating nitrogen and silicon cycling in the Southern Ocean over the last glacial cycle. *Paleoceanography*, pages 1179–1195, 2014. doi: 10.1002/2014PA002686.Received.

Romahn , S., Mackensen , a., Groeneveld , J., and Pätzold , J. Deglacial intermediate water reorganization: new evidence from the Indian Ocean. *Climate of the Past*, 10(1):293–303, feb 2014. doi: 10.5194/cp-10-293-2014.

Saenko , O. A., Fyfe , J. C., and England , M. H. On the response of the oceanic wind-driven circulation to atmospheric CO 2 increase. *Climate Dynamics*, 25:415–426, 2005. doi: 10.1007/s00382-005-0032-5.

Sarmiento , J. L., Gruber , N., Brzezinski , M. A., and Dunne , J. P. High-latitude controls of thermocline nutrients and low latitude biological productivity. *Nature*, 427:56–60, 2004. doi: 10.1038/nature02204.1.

Sarmiento , J. L., Simeon , J., Gnanadesikan , A., Gruber , N., Key , R. M., and Schlitzer , R. Deep ocean biogeochemistry of silicic acid and nitrate. *Global Biogeochemical Cycles*, 21(1):1–16, 2007. doi: 10.1029/2006GB002720.

Saunders , K. M., Roberts , S. J., Perren , B., Butz , C., Sime , L., Davies , S., Van Nieuwenhuyze , W., Grosjean , M., and Hodgson , D. A. Holocene dynamics of the Southern Hemisphere westerly winds and possible links to CO2outgassing. *Nature Geoscience*, 11(September), 2018. doi: 10.1038/s41561-018-0186-5.

Sigman , D. M., McCorkle , D. C., and Martin , W. R. The calcite isyocline as a constraint on glacial/interglacial low-latitude production changes. *Global Biogeochemical Cycles*, 12(3):409–427, 1998. doi: 10.1029/98GB01184.

Sigman , D. M., Hain , M. P., and Haug , G. H. The polar ocean and glacial cycles in atmospheric CO(2) concentration. *Nature*, 466(7302):47–55, jul 2010. doi: 10.1038/nature09149.

Sikes , E. L., Allen , K. A., and Lund , D. C. Enhanced δ13C and δ18O Differences Between the South Atlantic and South Pacific During the Last Glaciation: The Deep Gateway Hypothesis. *Paleoceanography*, 32(10):1000–1017, 2017. doi: 10.1002/2017PA003118.

Sikes , E. L., Cook , M. S., and Guilderson , T. P. Reduced deep ocean ventilation in the Southern Pacific Ocean during the last glaciation persisted into the deglaciation. *Earth and Planetary Science Letters*, 438: 130–138, 2016a. doi: 10.1016/j.epsl.2015.12.039.

Sikes , E. L., Elmore , A. C., Allen , K. A., Cook , M. S., and Guilderson , T. P. Glacial water mass structure and rapid δ18O and δ13C changes during the last glacial termination in the Southwest Pacific. *Earth and Planetary Science Letters*, 456:87–97, 2016b. doi: 10.1016/j.epsl.2016.09.043.

Skinner , L. C., Fallon , S., Waelbroeck , C., Michel , E., and Barker , S. Ventilation of the Deep Southern Ocean and Deglacial CO2 Rise. *Science*, 328(5982):1147–1151, may 2010. doi: 10.1126/science.1183627.

Sloyan , B. M. and Rintoul , S. R. Circulation, Renewal, and Modification of Antarctic Mode and Intermediate

Water*. *Journal of Physical Oceanography*, 31(4):1005–1030, apr 2001. doi: 10.1175/1520-0485(2001)031⟨1005:CRAMOA⟩2.0.CO;2.

Stephens , B. and Keeling , R. The influence of Antarctic sea ice on glacial–interglacial CO 2 variations. *Nature*, 404, 2000.

Stern , J. V. and Lisiecki , L. E. Termination 1 timing in radiocarbon-dated regional benthic δ18O stacks. *Paleoceanography*, 29(12):1127–1142, 2014. doi: 10.1002/2014PA002700.

Straub , D. N. On the Transport and Angular Momentum Balance of Channel Models of the Antarctic Circumpolar Current. *Journal of physical oceanography*, 23:776 – 782, 1993.

Sutton , J. N., Varela , D. E., Brzezinski , M. a., and Beucher , C. P. Species-dependent silicon isotope fractionation by marine diatoms. *Geochimica et Cosmochimica Acta*, 104:300–309, mar 2013. doi: 10.1016/j.gca.2012.10.057.

Takeda , S. Influence of iron availability on nutrient consumption ratio of diatoms in oceanic waters. *Nature*, 393(JUNE):774–777, 1998.

Toggweiler , J. Variation of atmospheric CO2 by ventilation of the ocean's deepest water. *Paleoceanography*, 14(5), 1999.

Tréguer , P. J. and De La Rocha , C. L. The world ocean silica cycle. *Annual review of marine science*, 5: 477–501, jan 2013. doi: 10.1146/annurev-marine-121211-172346.

Varela , D. E., Pride , C. J., and Brzezinski , M. a. Biological fractionation of silicon isotopes in Southern Ocean surface waters. *Global Biogeochemical Cycles*, 18:1–8, 2004. doi: 10.1029/2003GB002140.

Volk , T. and Hoffert , M. Ocean carbon pumps: Analysis of relative strengths and efficiencies in ocean-driven atmospheric CO2 changes. *The Carbon Cycle and Atmospheric CO: Natrual Variations Archean to Present*, 32:99–110, 1985.

Wetzel , F., de Souza , G., and Reynolds , B. What controls silicon isotope fractionation during dissolution of diatom opal? *Geochimica et Cosmochimica Acta*, 131:128–137, apr 2014. doi: 10.1016/j.gca.2014.01.028.

Wolff , E. W., Fischer , H., Fundel , F., Ruth , U., Twarloh , B., Littot , G. C., Mulvaney , R., Röthlisberger , R., de Angelis , M., Boutron , C. F., Hansson , M., Jonsell , U., Hutterli , M. a., Lambert , F., Kaufmann , P., Stauffer , B., Stocker , T. F., Steffensen , J. P., Bigler , M., Siggaard-Andersen , M. L., Udisti , R., Becagli , S., Castellano , E., Severi , M., Wagenbach , D., Barbante , C., Gabrielli , P., and Gaspari , V. Southern Ocean sea-ice extent, productivity and iron flux over the past eight glacial cycles. *Nature*, 440 (7083):491–6, mar 2006. doi: 10.1038/nature04614.

7

Synthesis

The aim of this thesis is to reconstruct marine nutrient cycles, their interactions with the global ocean circulation and their impacts on the marine biological carbon pump during the last deglaciation, when ocean overturning and atmospheric CO_2 changed dramatically as the world transitioned from a glacial climate state to the present interglacial. We reconstructed the biogeochemical processes that can dictate the transfer of carbon to and from the deep ocean, known as the biological pump, in the Southern Ocean, a key region for water mass production, sea air exchanges and nutrient distribution to the rest of the ocean. The focus of this work was on three sediment cores from the Indian sector of the Southern Ocean, where the ocean's deepest waters upwell today. Because of this deep upwelling, the chemistry of the surface waters provides a window into the chemical history of the deep sea. It has been suggested that during the last ice age the deep sea accumulated atmospheric CO_2, driving the global climate into its cooler state (e.g. Toggweiler, 1999; Sigman and Boyle, 2000; Sigman et al., 2010). Upon the deglaciation this CO_2 was transferred from the deep ocean to the atmosphere driving a rapid rise in global temperatures towards near-modern

conditions. This thesis both contributes to current working hypotheses and presents novel hypotheses that provide a more complete understanding of the mechanisms behind the glacial-interglacial atmospheric CO_2 variability. The following text will provide a synthesis of the major findings within this thesis. A cartoon summary of the proposed deglacial events are presented in Figure 7.1. In addition, Figure 7.2 provides an overview of some of the important data used to form the interpretations summarised in the following text.

7.1 Core selection rationale

The three piston sediment cores presented in this work were taken from Indian sector of the Southern Ocean. The core site of MD84-551 (-50.0225°N, 100.1°E) is situated on the southwest flank of the Kerguelen Plateau and south of the main branch of the polar front (PF) separating the Antarctic where deep upwelling occurs from the Subantarctic where intermediate waters form. MD88-773 (-52.9005°N, 109.869667°E) and MD88-772 (-55.01°N, 73.17°E) are located on the southwest flank of the southeast Indian ridge, north east of MD84-551. MD88-773 lies close to the PF and MD88-772 lies to the northwest between the PF and the Subantarctic front (SAF). At these positions the cores form a meridional hydrographical transect and thus provide the opportunity to reconstruct chemical gradients along the path of Ekman transport from the Antarctic to the Subantarctic.

Age models of sediment records from the Southern Ocean are a challenge to construct, largely due to the poor carbonate preservation and variable surface radiocarbon reservoir ages (Chapter 3). The chronologies of the three cores were initially constructed independent of radiocarbon due to the poor constraints on surface reservoir ages across the deglaciation. The downcore terrigenous material (%Ti, %Fe and magnetic susceptibility) records of MD88-773 and MD88-772 were aligned to nearby records (MD12-3396CQ, MD88-769, MD94-103), which all had independent age models and covariable terrigenous input records. Foraminiferal $\delta^{18}O$ records were used for MD84-551 to align to MD12-3396CQ. The paleoceanographic proxies from the three cores were fitted to their respective age models to enable the reconstruction of the environmental conditions from the last glacial maximum (LGM) to the Holocene. The relatively high sedimentation rates of the cores across the deglaciation ($>$ 3.9 cm/kyr) enables the changes in biogeochemical processes on the scale of major deglacial warming events to be resolved.

7.2 Glacial-interglacial silicon cycling

A proposed mechanism for the lowering of atmospheric CO_2 during glacials relative to interglacials is the chemical isolation of deep waters that today form within the Antarctic (Toggweiler, 1999; Sigman et al., 2010). Encumbered exchange between these deep waters and the rest of the ocean and atmosphere would promote the accumulation of respired carbon in the deep. Using diatom $\delta^{30}Si$ records (e.g. Figure 7.2v), it was demonstrated (Chapter 6) that such sluggish deep mixing would also favour the accumulation of silicic acid (DSi) and that the global DSi distribution is likely to be more sensitive to changes in deep mixing due to the efficient export of biogenic silica to depth. Sequestration of DSi in the deep sea would reduce its availability in the surface ocean thereby limiting diatom proliferation and their contribution to efficient export of carbon. Widespread Si limitation was avoided thanks to the lowering of diatom DSi demand in the presence of greater iron availability, which permitted DSi to leak from the Southern Ocean to lower latitudes. An important side-effect change in DSi demand was a partitioning of silicon isotopes between the isolated abyssal waters and the remainder of the upper ocean, with lighter isotopes within exported biogenic silica entering the abyssal waters and isotopically heavier preformed DSi remaining in the upper ocean. Consequently, it was suggested that the deep ocean exhibited stronger gradients in the isotopic composition of DSi during the LGM relative to the present. The effect of the isotope partitioning and DSi sequestration in the deep ocean was expressed in the $\delta^{30}Si$ records from the three cores upon the ventilation of the abyssal water through the Southern Ocean during the deglaciation.

This new view of the marine silicon cycle places great importance on ocean circulation and iron availability in controlling the global distribution of DSi. Further, because the global availability of DSi influences diatom abundances and thus the relative strengths of the soft tissue (biological) and carbonate pumps, this work also highlights the important role that iron plays in regulating marine CO_2 uptake.

7.3 Climatically-driven perturbations of the marine nitrogen budget

The extended isolation of the deep ocean from the atmosphere during glacial periods would have deoxygenated the deep ocean, evidence of which has been observed in redox proxy records from the Southern Ocean and Pacific Ocean (Jaccard and Galbraith, 2009; Jaccard et al., 2016). Pelagic denitrification rates increase in regions of water column suboxia and are characterised by the removal of isotopically light nitrogen from the ocean, leaving isotopically heavy $\delta^{15}NO_3$. The high-resolution Antarctic $\delta^{15}N_{DB}$ records presented in this study (e.g. Figure 7.2iv) reveal large (> 2 ‰) positive excursions in the nitrogen isotopic content of diatoms that cannot be attributed to changes in fractionation during nitrate uptake. Instead, these positive excursions were attributed to enhanced denitrification either in the deep ocean or in the upper Southern Ocean as a result of the deoxygenation of the deep sea during glacial periods.

The implication of this new finding is that deep ocean deoxygenation may play a previously unrealised role in the marine nitrogen budget. Current research on pelagic denitrification has been focused on more localised forcings such as primary production to explain observed changes in denitrification within the three major oxygen minimum zones. However, this research suggests deep ocean oxygenation may influence global denitrification rates. Looking to the future, rising sea surface temperatures in response to anthropogenic greenhouse gas emissions would decrease the solubility of oxygen and stratify the surface ocean, leading to a decline in the subsurface oxygen concentrations (Bopp et al., 2017). The evidence presented here indicates that such changes may influence pelagic denitrification rates by lowering the oxygen content of intermediate waters that feed the productive oxygen minimum zones.

Importantly, changes in pelagic denitrification act to unbalance the marine nitrogen budget, leading to changes in the inventory of nitrate in the oceans (Deutsch et al., 2004). The global inventory of nitrate has an important influence of the marine carbon cycle (Ganeshram et al.,1995; Falkowski, 1997). Decreasing the global nitrate inventory by enhanced denitrification would yield a decline in global primary productivity and carbon export from the surface oceans, thus leading to a rise in atmospheric CO_2. Hence, based on the interpretations of the work in Chapter 5 of this thesis, it is demonstrated that ocean deoxygenation and the

subsequent increase in denitrification rates may promote a rise in atmospheric CO_2 over the timescales of nitrogen cycling in the oceans (2 – 3 kyrs).

7.4 Antarctic stratification and atmospheric CO_2 change

An inhibition of deep ocean ventilation due to Antarctic stratification would also prevent the renewal of the radiocarbon content of the deep waters. Indeed, numerous benthic foraminiferal (e.g. Skinner et al., 2010; Ronge et al., 2016) and deep-sea coral (e.g. Burke and Robinson, 2012; Chen et al., 2015) records have indicated that the glacial deep ocean was indeed more ^{14}C-depleted during the LGM relative to the present. It has long been suggested that these aged deep waters were transported to the surface of the Southern Ocean during the deglaciation where the respired carbon would be allowed to degas to the atmosphere producing the rise in atmospheric CO_2 observed in ice core records. In Chapter 3 we provide the first evidence of the presence of ^{14}C-depleted surface waters in the Antarctic during the deglaciation, confirming that indeed the Southern Ocean surface was the pathway taken by the carbon-rich isolated deep waters during the deglaciation (Figure 7.2ii). Further, the absence of anomalously old radiocarbon dates prior to the Antarctic warming associated with Heinrich Stadial 1 confirms that the Southern Ocean surface waters were not readily exchanging with the deep ocean during the last glacial maximum. This contradicts mechanisms of glacial CO_2 drawdown that invoke only capping the Antarctic with sea ice to prevent outgassing rather than sluggish overturning.

7.5 Transmission of Southern Ocean chemistry through intermediate waters

Antarctic intermediate water (AAIW) and Subantarctic mode water (SAMW) are both formed from the subduction of Southern Ocean waters. Together these Southern Ocean intermediate waters represent an important limb of the meridional overturning circulation, redistributing nutrients from the upwelled deep waters to the main thermocline and the northern/Atlantic cell of the meridional overturning circulation. Hence, it has been suggested that biogeochemical processes occurring within the Southern Ocean may control the chemical

characteristics of these intermediate waters and thus the chemical composition waters feeding the low latitude surface waters (Sarmiento et al., 2004).

In this work we demonstrate that a number of biogeochemical properties were transferred from the Southern Ocean to Southern Ocean intermediate waters and beyond during the deglaciation. Firstly, the deglacial radiocarbon excursions of the Southern Ocean surface waters in MD84-551 display a remarkable similarity in both magnitude and pattern to those observed in benthic foraminifera records within low latitude intermediate waters (Chapter 3) (Marchitto et al., 2007; Bryan et al., 2010). These low latitude records of anomalously old intermediate waters during the deglaciation have previously been suggested to like to be local phenomena due to their extreme age (Hain et al., 2011). However, the good correspondence between these records and the $\Delta\Delta^{14}C$ record presented here suggests that these may indeed be demonstrating the presence highly ^{14}C-depleted Southern Ocean intermediate waters. This implies that intermediate waters and the low latitude ocean play a role in the exchange of carbon between the deep ocean and the atmosphere during deglacial transitions.

In Chapter 5 it was noted that the denitrified and ^{15}N-enriched waters detected by the Southern Ocean records presented here may have imprinted a heavy $\delta^{15}NO_3$ signal on the Southern Ocean intermediate waters that feed the low latitudes. This hypothesis is supported by coeval anomalous $\delta^{15}N$ peaks observed in sediment records derived from waters supplied by the Southern Ocean but exhibit little evidence for a local denitrification control (Martinez et al., 2006; Pichevin et al., 2005, 2010). It was also argued that the deep ocean deoxygenation that produced the denitrification signal within the Southern Ocean during the deglaciation may have been transferred into the intermediate waters. This would have supported an expansion of the low latitude oxygen minimum zones, enhancing global pelagic denitrification rates.

Finally, in Chapter 6 it was demonstrated that the deglacial pulse of DSi-rich and 30Si-depleted deep waters advected to the Southern Ocean surface were detected by sponge $\delta^{30}Si$ records situated within intermediate waters (Hendry et al., 2012), further confirming that DSi leakage from the Southern Ocean was enhanced during the deglaciation as a result of overwhelming supply. Sediment records within low latitude upwelling regions supplied by the DSi delivered within intermediate waters exhibit anomalous increases in diatom productivity during the deglaciation (Pichevin et al., 2009; Meckler et al., 2013). This demonstrates that

the increased silica leakage from the Southern Ocean directly contributed to the fertilization of diatom production at low latitudes during the deglaciation.

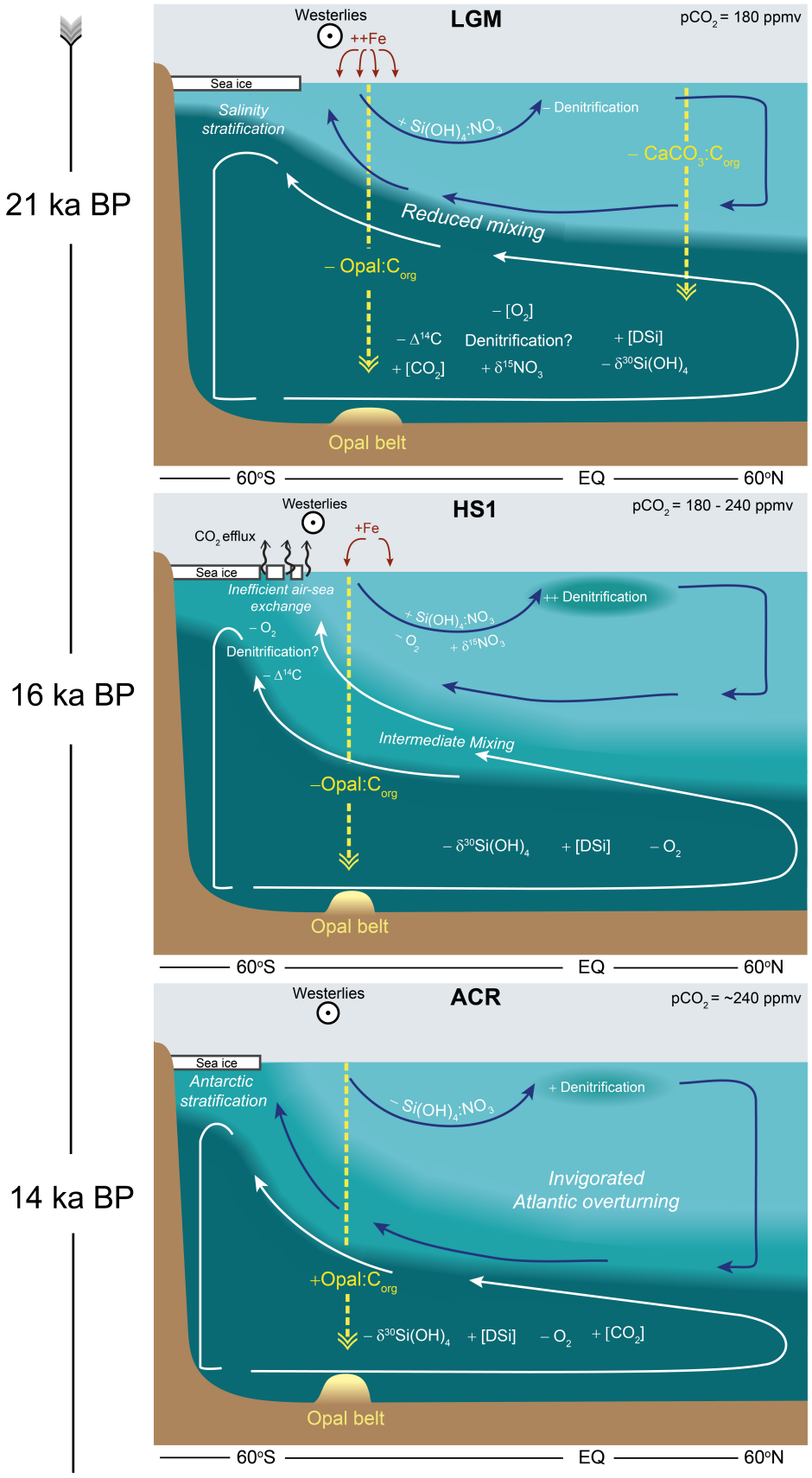
21 ka BP
LGM
Westerlies
++Fe
pCO2 = 180 ppmv
Sea ice
Salinity stratification
+ Si(OH)4:NO3
– Denitrification
– CaCO3:Corg
Reduced mixing
– Opal:Corg
– [O2]
– Δ14C
Denitrification?
+ [DSi]
+ [CO2]
+ δ15NO3
– δ30Si(OH)4
Opal belt
60°S
EQ
60°N
16 ka BP
HS1
Westerlies
+Fe
CO2 efflux
pCO2 = 180 - 240 ppmv
Sea ice
Inefficient air-sea exchange
– O2
Denitrification?
– Δ14C
+ Si(OH)4:NO3
++ Denitrification
– O2
+ δ15NO3
Intermediate Mixing
–Opal:Corg
– δ30Si(OH)4
+ [DSi]
– O2
Opal belt
60°S
EQ
60°N
14 ka BP
ACR
Westerlies
pCO2 = ~240 ppmv
Sea ice
Antarctic stratification
– Si(OH)4:NO3
+ Denitrification
Invigorated Atlantic overturning
+Opal:Corg
– δ30Si(OH)4
+ [DSi]
– O2
+ [CO2]
Opal belt
60°S
EQ
60°N

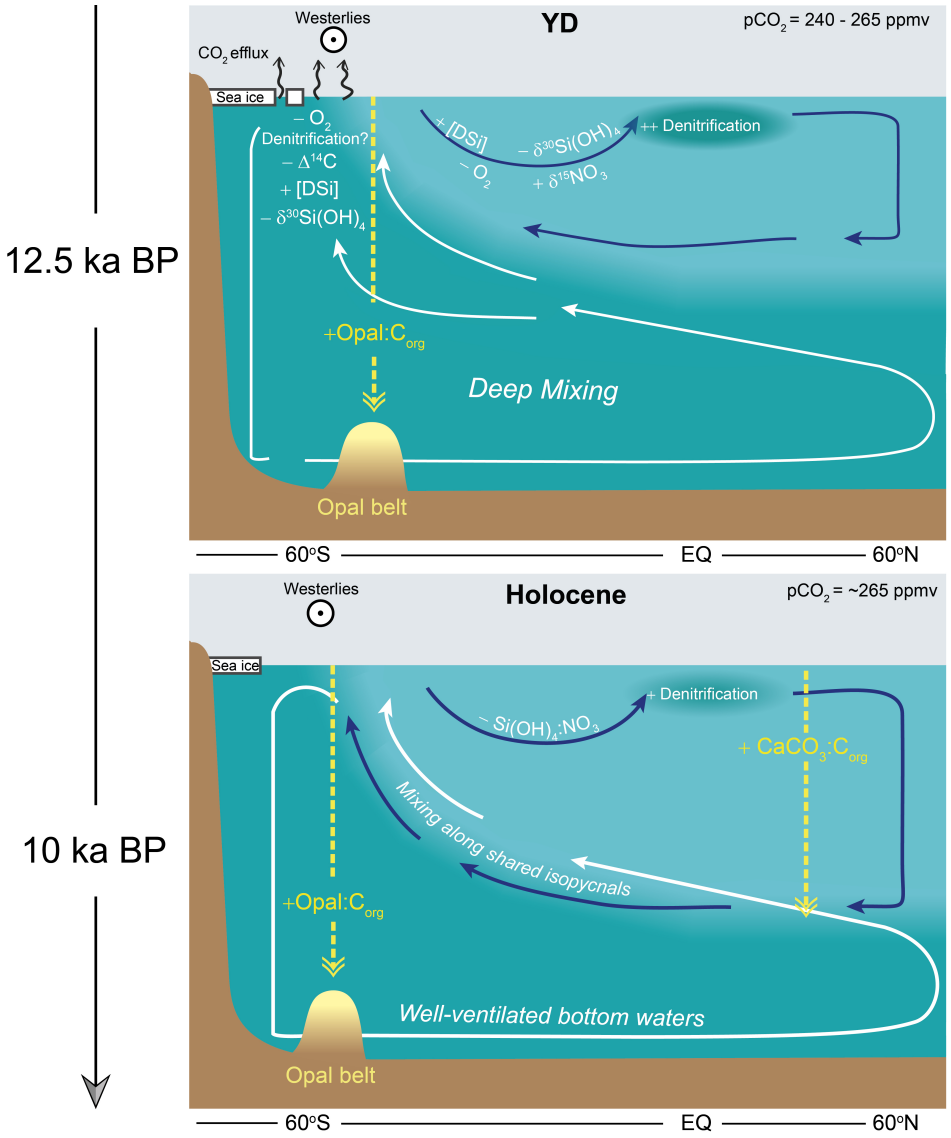

FIGURE 7.1: Includes previous page. A schematic representation of the major findings of this thesis presented in chronological order from the LGM (top) to the Holocene (bottom). + and – signs indicate the direction of change relative to the Holocene of the concentration, isotopic composition or process given in the adjacent text. **LGM**: Shoaling of the deep water mass boundary and enhanced salinity stratification of the deep ocean and Antarctic led to the isolation of the deep ocean from the upper ocean and atmosphere. The poorly ventilated and aging deep ocean accumulated DSi and respired carbon and became deoxygenated, which may have enhanced deep denitrification rates. In the Southern Ocean, sea ice driven light limitation and stratification shifted the opal belt northwards into the Subantarctic. Greater iron availability reduced the silica demand by diatoms, increasing the silicic acid to nitrate ratio in intermediate waters transported to the low latitudes. This may have enabled diatoms to maintain or even increase in dominance over other phytoplankton groups leading to a lowering of the $CaCO_3$:C_{org} ratio and more efficient carbon export to the deep ocean. **HS1**: Partial removal of sea ice from the Southern Ocean shifted the opal belt southwards and enabled a partial ventilation of the deep ocean. The ^{14}C- and O_2-depleted upwelling waters were readily transferred to the intermediate waters helped by poor air-sea gas exchange in the Antarctic under the presence of sea ice. This promoted a enhancement of denitrification in the low latitude OMZs during both HS1 and the YD, unbalancing the marine N budget and reducing the marine N inventory. **ACR**: Resumption of Atlantic overturning and a pause in Southern Hemisphere temperature rise led to a pause in the progressively deepening ocean ventilation. Dust-borne iron delivery to the Southern Ocean reached a minimum, leading to a rise in DSi demand. **YD**: Further removal of sea ice shifted the opal belt southward and enabled a deepening of ocean ventilation, releasing the DSi rich waters from the deep Pacific. The pulse of DSi was transported to low latitudes within intermediate waters, fuelling diatom production. **Holocene**: The establishment of deep water formation in the Atlantic and removal of salinity stratification in the Southern Ocean encouraged a greater homogenisation of deep ocean chemical gradients. CO_2 efflux from the Antarctic is balanced by carbon export elsewhere, maintaining stable atmospheric CO_2 concentrations.

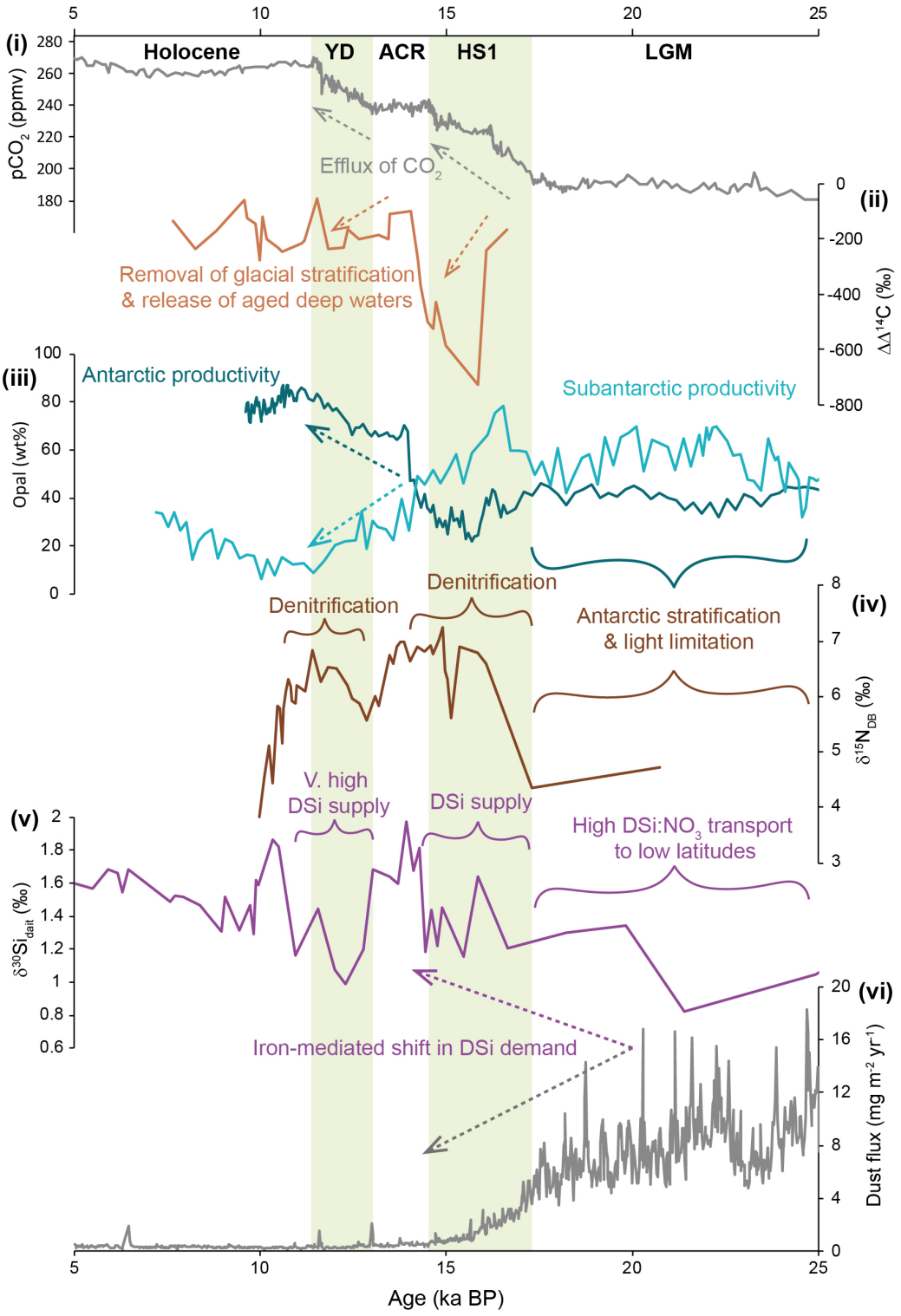

FIGURE 7.2: Plot of results summarising some of the major findings in this thesis. **(i)**: EPICA Dome C ice core record documenting the intervals of atmospheric CO_2 rise across the deglaciation (Monnin et al., 2001). **(ii)** Planktic foraminifera $\Delta\Delta^{14}C$ record from MD84-551 showing the presence of aged waters at the Antarctic surface during the deglaciation (see Chapter 3). **(iii)** %opal records from MD84-551 (dark teal) and MD88-772 (light teal) demonstrating the shift of the opal belt across the deglaciation (see Chapter 4). **(iv)** $\delta^{15}N_{DB}$ record from MD84-551 indicating the presence of denitrified waters in the Southern Ocean (see Chapter 5). **(v)** $\delta^{30}Si_{diat}$ record of MD88-773 demonstrating the deglacial shift in DSi demand by diatoms and the intervals of high DSi supply coeval with the CO_2 rise (see Chapter 6). **(vi)** Dust flux to Antarctic recorded in EPICA Dome C (Lambert et al., 2012).

References

Bopp , L., Resplandy , L., Untersee , A., Le Mezo , P., and Kageyama , M. Ocean (de)oxygenation from the Last Glacial Maximum to the twenty-first century: Insights from Earth System models. *Philosophical Transactions of the Royal Society A: Mathematical, Physical and Engineering Sciences*, 375(2102), 2017. doi: 10.1098/rsta.2016.0323.

Bryan , S. P., Marchitto , T. M., and Lehman , S. J. The release of 14C-depleted carbon from the deep ocean during the last deglaciation: Evidence from the Arabian Sea. *Earth and Planetary Science Letters*, 298(1-2):244–254, sep 2010. doi: 10.1016/j.epsl.2010.08.025.

Burke , A. and Robinson , L. F. The Southern Ocean's role in carbon exchange during the last deglaciation. *Science (New York, N.Y.)*, 335(6068):557–61, feb 2012. doi: 10.1126/science.1208163.

Chen , A. T., Robinson , L. F., Burke , A., Southon , J., Spooner , P., Morris , P. J., and Ng , H. C. Synchronous Sub-millennial Scale Abrupt Events in the Ocean and Atmosphere during the Last Deglaciation. *Science*, 1(May):1537–1542, 2015. doi: 10.1126/science.aac6159.

Deutsch , C., Sigman , D. M., Thunell , R. C., Meckler , A. N., and Haug , G. H. Isotopic constraints on glacial / interglacial changes in the oceanic nitrogen budget. *Global Biogeochemical Cycles*, 18, 2004. doi: 10.1029/2003GB002189.

Falkowski , P. Evolution of the nitrogen cycle and its influence on the biological sequestration of CO2 in the ocean. *Nature*, 387:272–275, 1997.

Ganeshram , R., Pedersen , T. F., Calvert , S. E., and Murray , J. Large changes in oceanic nutrient inventories from glacial to interglacial periods. *Nature*, 376:755–759, 1995.

Hain , M. P., Sigman , D. M., and Haug , G. H. Shortcomings of the isolated abyssal reservoir model for deglacial radiocarbon changes in the mid-depth Indo-Pacific Ocean. *Geophysical Research Letters*, 38(4), feb 2011. doi: 10.1029/2010GL046158.

Hendry , K. R., Robinson , L. F., Meredith , M. P., Mulitza , S., Chiessi , C. M., and Arz , H. Abrupt changes in high-latitude nutrient supply to the Atlantic during the last glacial cycle. *Geology*, 40(2): 123–126, 2012. doi: 10.1130/G32779.1.

Jaccard , S. L. and Galbraith , E. D. Large climate-driven changes of oceanic oxygen concentrations during the last deglaciation. *Nature Geoscience*, 5(2):151–156, 2011. doi: 10.1038/ngeo1352.

Jaccard , S. L., Galbraith , E. D., Martínez-Garcia , A., and Anderson , R. F. Covariation of abyssal Southern Ocean oxygenation and pCO2 throughout the last ice age. *Nature*, 530(7589):207–210, 2016. doi: 10.1038/nature16514.

Marchitto , T. M., Lehman , S. J., Ortiz , J. D., Flückiger , J., and van Geen , A. Marine radiocarbon evidence for the mechanism of deglacial atmospheric CO2 rise. *Science (New York, N.Y.)*, 316(5830): 1456–9, jun 2007. doi: 10.1126/science.1138679.

Martinez , P., Lamy , F., Robinson , R. R., Pichevin , L., and Billy , I. Atypical δ15N variations at the southern boundary of the East Pacific oxygen minimum zone over the last 50 ka. *Quaternary Science Reviews*, 25(21-22):3017–3028, 2006. doi: 10.1016/j.quascirev.2006.04.009.

Meckler , A. N., Sigman , D. M., Gibson , K. a., François , R., Martínez-García , A., Jaccard , S. L., Röhl , U., Peterson , L. C., Tiedemann , R., and Haug , G. H. Deglacial pulses of deep-ocean silicate into the subtropical North Atlantic Ocean. *Nature*, 495(7442):495–8, mar 2013. doi: 10.1038/nature12006.

Pichevin , L. E., Reynolds , B. C., Ganeshram , R. S., Cacho , I., Pena , L., Keefe , K., and Ellam , R. M. Enhanced carbon pump inferred from relaxation of nutrient limitation in the glacial ocean. *Nature*, 459 (7250):1114–7, jun 2009. doi: 10.1038/nature08101.

Pichevin , L. E., Ganeshram , R. S., Francavilla , S., Arellano-Torres , E., Pedersen , T. F., and Beaufort , L. Interhemispheric leakage of isotopically heavy nitrate in the eastern tropical Pacific during the last glacial period. *Paleoceanography*, 25(1):1–15, feb 2010. doi: 10.1029/2009PA001754.

Pichevin , L., Martinez , P., Bertrand , P., Schneider , R., Giraudeau , J., and Emeis , K. Nitrogen cycling on the Namibian shelf and slope over the last two climatic cycles: Local and global forcings. *Paleoceanography*, 20(2):1–13, 2005. doi: 10.1029/2004PA001001.

Ronge , T. A., Tiedemann , R., Lamy , F., Köhler , P., Alloway , B. V., De Pol-Holz , R., Pahnke , K., Southon , J., and Wacker , L. Radiocarbon constraints on the extent and evolution of the South Pacific glacial carbon pool. *Nature Communications*, 7(May):1–12, 2016. doi: 10.1038/ncomms11487.

Sarmiento , J. L., Gruber , N., Brzezinski , M. A., and Dunne , J. P. High-latitude controls of thermocline nutrients and low latitude biological productivity. *Nature*, 427:56–60, 2004. doi: 10.1038/nature02204.1.

Sigman , D. M. and Boyle , E. A. Glacial/interglacial variation in atmospheric carbon dioxide. *Nature*, 407: 859–869, 2000.

Sigman , D. M., Hain , M. P., and Haug , G. H. The polar ocean and glacial cycles in atmospheric CO(2) concentration. *Nature*, 466(7302):47–55, jul 2010. doi: 10.1038/nature09149.

Skinner , L. C., Fallon , S., Waelbroeck , C., Michel , E., and Barker , S. Ventilation of the deep Southern Ocean and deglacial CO2 rise. *Science*, 328(5982):1147–51, may 2010. doi: 10.1126/science.1183627.

Toggweiler , J. Variation of atmospheric CO2 by ventilation of the ocean's deepest water. *Paleoceanography*, 14(5), 1999.

A

Methods

A.1 Bulk sediment multi-element and Th/U analyses

Multi-element analysis was performed in two separate labs (AWI, Bremerhaven and the University of Edinburgh (UoE)) but followed the same general procedure given by Kretschmer et al (2011). Only MD84-551 was analysed at AWI, all three cores were analysed at UoE.

For both labs freeze-dried bulk sediments were weighed (50 mg) and placed in digestion vessels with ^{229}Th and ^{236}U (certified) spikes in 1 M HNO_3 at concentrations of 80 pg/g and 28.4 ng/g, respectively. The spike volume was adjusted to match the expected ^{230}Th and ^{235}U intensity peaks (in this case 25 µl spike / 50 mg sediment). Separate vessels containing standards (UREM II and NIST 2702 in AWI, MESS-3 in UoE) were also added to each digestion batch. Concentrated distilled HNO_3, HCl and HF were added to each of the digestion vessels at a volume ratio of 3:2:0.5 ml. The sediments were digested either using a CEM Mars Xpress microwave (AWI) or hotplate (UoE) until fully dissolved followed by full evaporation of the acids then redissolution in 1 M HNO_3. Each sample/standard

was diluted to 50 ml with 1M HNO_3 in pre-weighed vessels and weighed after dilution for accurate dilution correction after analysis. Each solution was subsequently split into two aliquots, with 5 ml to be used in the multi-element analysis and the remaining 45 ml to be used in the Th/U analysis.

The multi-element aliquots were spiked (^{6}Li, ^{45}Sc and ^{103}Rh at AWI, ^{89}Yt at UoE) to correct for matrix effects. Calibration standards (Merck IV multi-element ICP standard) with increasing concentrations were used to calibrate the intensities. At least two procedural blanks and three acid blanks were measured per batch ($\sim$25 samples/standards). The multi-element analysis was performed on a Thermo Scientific Element ICP-MS at AWI and a Vista Pro ICP-OES at UoE. The internal error is better than 2 %.

Th/U analysis was only performed in AWI. The Th/U aliquots were processed via ion exchange chromatography using the same procedure described in Kretschmer et al (2011). Briefly, each sample was co-precipitated with $Fe(OH)_3$ by the addition of $FeCl_2$ and NH_4OH. The samples were centrifuged, and the supernatant removed before redissolution in HNO_3. The aliquots were then added to columns of Eichrom UTEVA resin pre-conditioned with 3 M HNO_3. The thorium was eluted with 5M HCl followed by separate elution of the uranium with 0.02 M HCl. Each eluate was subsequently evaporated on a hotplate. H_2O_2 was added to dissolve any resin and the samples were left to evaporate again. Finally, the precipitate was dissolved in 1M HNO_3 followed by analysis by ICP-MS following the same procedure as Kretschmer et al (2011).

Unfortunately, digestions were not repeated which prevents a quantitative inter-laboratory comparison to be made. However, adjacent samples were analysed in part of MD84-551 allowing a qualitative comparison. A selection of the elements analysed are shown in Figure A.1. Here it can be seen that the data from the two labs compare well although there are some systematic discrepancies, particularly in the barium data. It is not clear why this offset has come about, however the use of these data are largely qualitative in this study, hence the discrepancy does not impact any of the interpretations made.

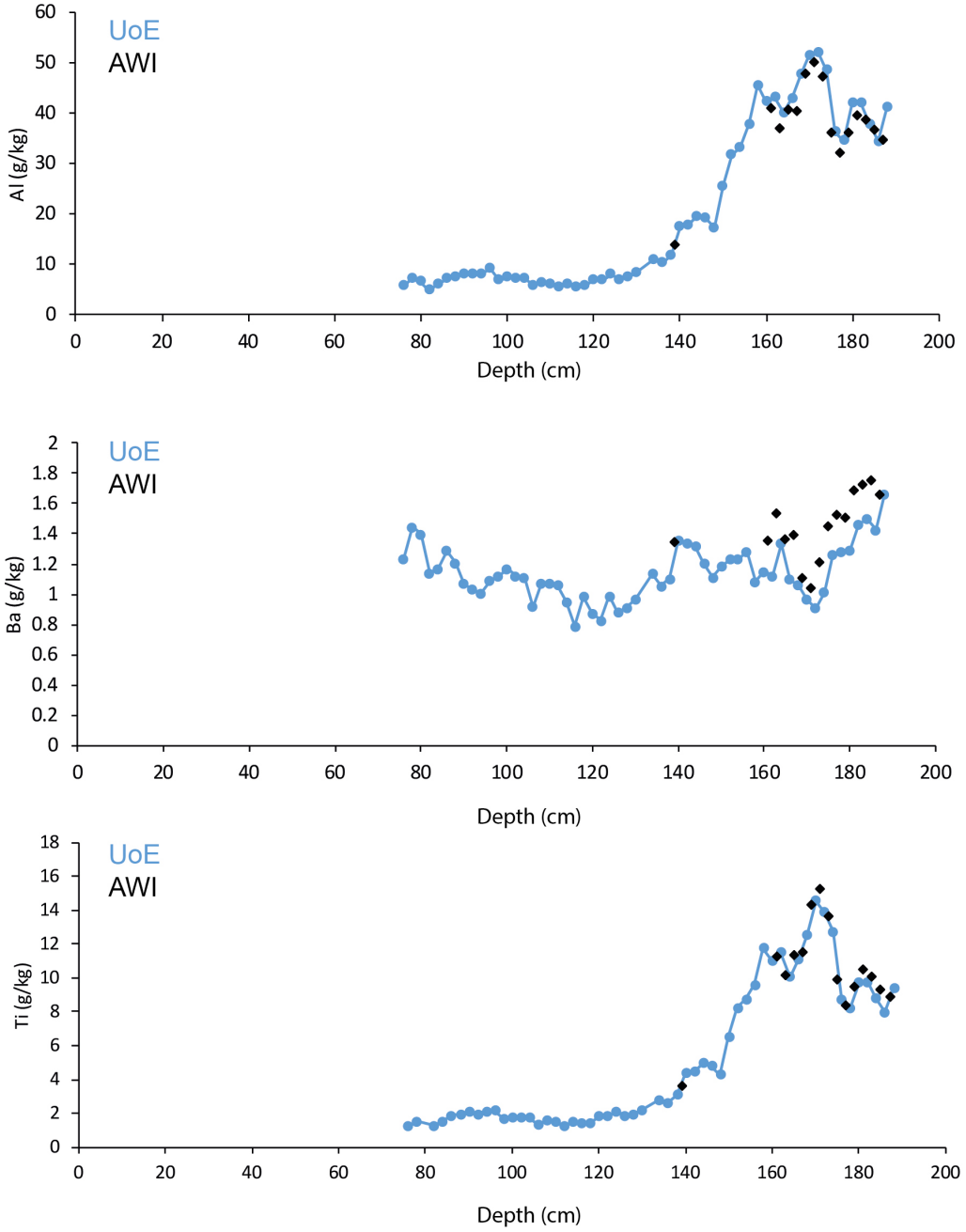

FIGURE A.1: Aluminium (top), barium (middle) and titanium (bottom) content of MD84-551 comparing measurements performed at the University of Edinburgh (blue) with those performed at the Alfred Wegener Institute (black).

The MD88-773 data produced here compares well with that previously published by Francois et al (1997) (Figure A.2), giving confidence in the data. The dataset produced in this study was used to calibrate the XRF core scanner records (see below).

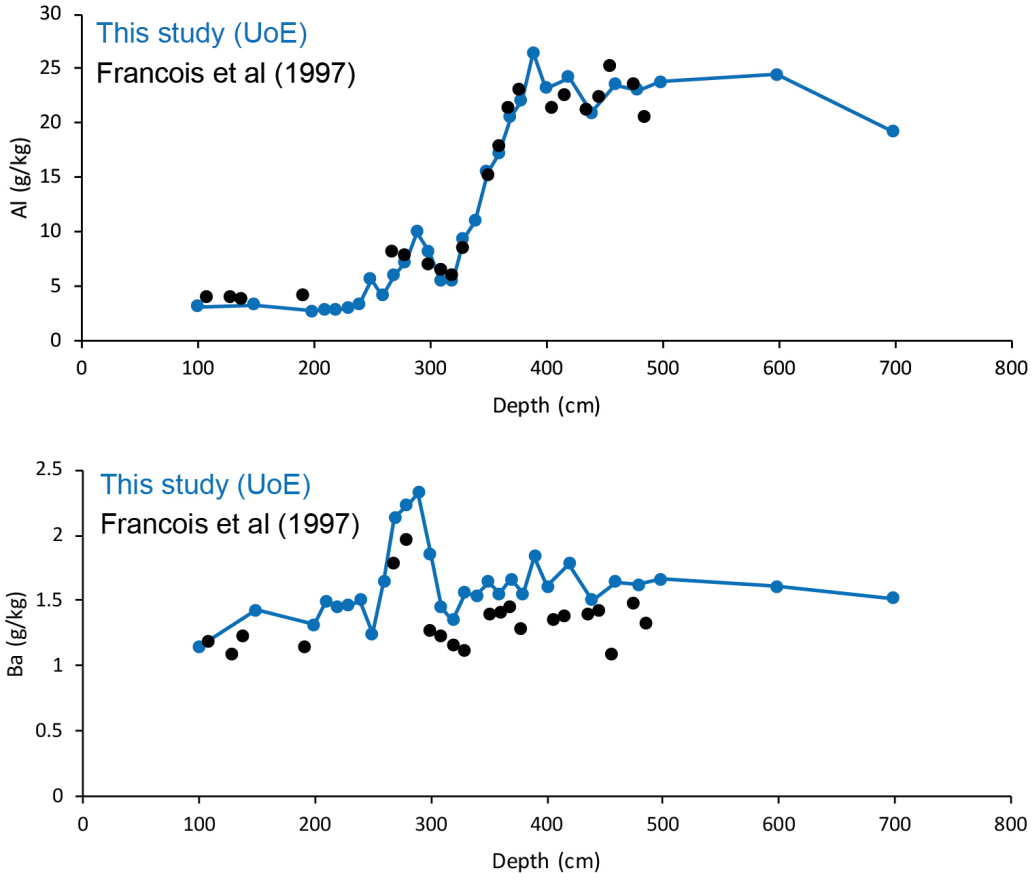

FIGURE A.2: Aluminium (top) and barium (bottom) content of MD88-773 comparing measurements performed at the University of Edinburgh (blue) with those performed as part of a previous study by Francois et al (1997) (black).

XRF core scanning

XRF core scanning was utilised to achieve a more continuous multi-element record from the sediment cores. The core scanning was performed with an Avaatech XRF core scanner (Richter et al., 2006) at EPOC, Universite de Bordeaux. Only cores MD88-773 and MD88-772 underwent this procedure. Each core section was scanned every 10 mm with ionization energy of 10, 30 and 50 kv. Visual comparison of the raw XRF data and the results from the sediment digestions (and %opal analysis) suggests that interferences strongly affected the core scanner Si and Al data, a common problem related to water content within sediments (Tjallingii et al., 2007). Consequently, the core scanner Si and Al data were not used to produce continuous down-core profiles. The remaining elements analysed (Ca, Ti, Mn, Fe, Ba, K) by the core-scanner correlated well with the digestion data and were subsequently linearly calibrated to produce continuous down-core profiles.

Barium

Detrital additions of barium are typically corrected for by subtracting the detrital barium estimated by using the average continental crust Ba/Al ratio = 0.0075 (Dymond et al., 1992). However, this may not be applicable for the Indian sector of the Southern Ocean due to high additions of basaltic material from the Kerguelen Plateau (Bareille et al., 1994). Table A.1 below lists the barium and aluminium contents of possible source material to the core sites. Ti contents are also included to provide an alternative correction due to the interferences within the XRF Al records. Based on this compilation of data the range of Ba/Al ratios is 0.0017 – 0.00863 and the Ba/Ti range is 0.0082 – 0.214.

Ba (ppm)	Al(%)	Ti (%)	Ba/Al	Ba/Ti	Ti/Al	Source (reference)
425	8.23	0.57	0.00516	0.0746	0.0693	Global average continental crust (Taylor, 1964)
250	8.76	0.9	0.00285	0.0278	0.1027	Global average basalt (Taylor, 1964)
668	7.74	0.312	0.00863	0.214	0.0403	Global average upper crust (Wedepohl, 1995)
150 – 248	5 – 9.69	1.01– 1.97	0.0017 – 0.0037	0.0082 – 0.0207	0.130 1– 0.2820	Kerguelen basalts (Gautier et al., 1990)
			0.00235 – 0.00410	0.0929 – 0.1028	0.0253 – 0.0399	Aeolian dust flux to Kerguelen island (Heimburger et al., 2013)

TABLE A.1: Barium, aluminium and titanium contents and elemental mass ratios of potential lithogenic detritus source material to the Indian sector of the Southern Ocean.

The potential terrigenous barium sources defined in Table 1 can be broadly divided into two groups, the low Ba, high Ti basalts and the high Ba, low Ti crustal sediments potentially delivered to the Southern Ocean as aeolian dust. To identify the source of Ba to the Indian sector cores the Ti/Al content of the cores will be examined and compared with the potential source material. Overall the Ti/Al contents differ between the three cores (Figure A.3). The Ti/Al content of MD84-551 is always greater than the other two cores, which is to be expected given the proximity of the Ti-rich Kerguelen basalts. Indeed, the Ti/Al content of MD84-551 corresponds well with the range of Ti/Al contents within Kerguelen basalts (yellow box in Figure A.3), further confirming that the bulk of the terrigenous material deposited at this core site is derived from the Kerguelen Plateau.

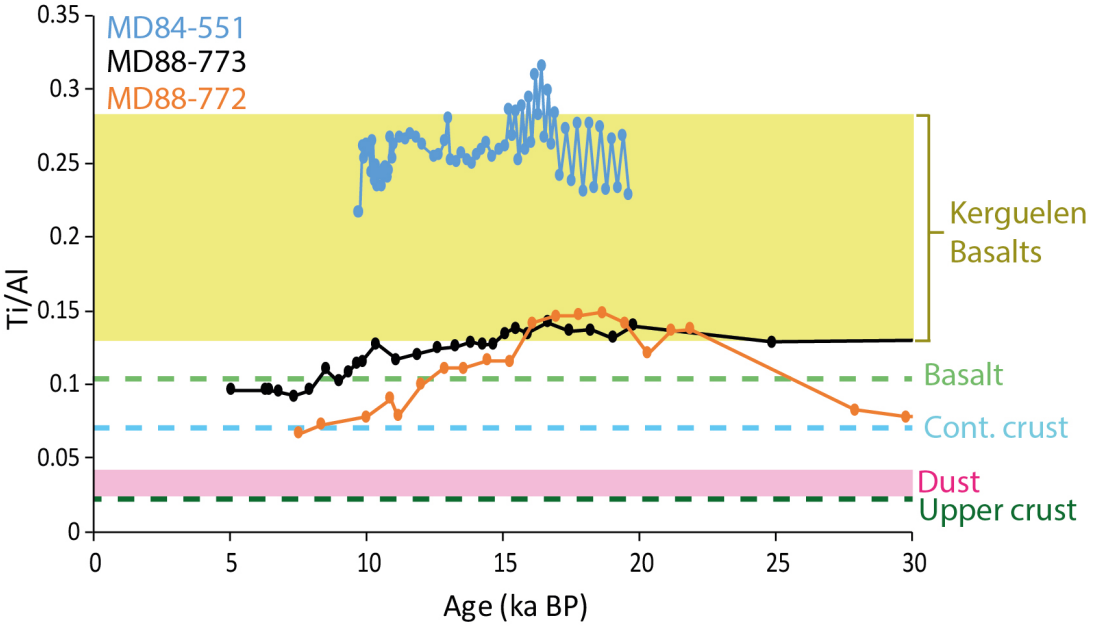

FIGURE A.3: Down-core titanium/aluminium mass ratios from the three sediment cores plotted with the Ti/Al of potential source material as given in Table A.1. Kerguelen basalts (Gautier et al., 1990), Basalt (global average; Taylor, 1964), Cont. crust (global average; Taylor, 1964), Dust (Kerguelen dust; Heimburger et al., 2013), Upper crust (global average; Wedepohl, 1995).

Both downcore Ti/Al records of MD88-773 and MD88-772 are always lower than that of MD84-551 but above the aeolian dust end member (Heimburger et al., 2013). Across the deglaciation the Ti/Al contents of both cores shift away from the basalt end member to more crustal values. Because dust fluxes are expected to decrease across this interval (e.g. Lambert et al., 2012) this shift could be interpreted as a reduction in the flux of Kerguelen material across the deglaciation (rather than a greater flux of crustal material), which agrees well with the interpretations of magnetic susceptibility records from across the Indian sector that show a decline in magnetite delivered to Indian sector cores across the deglaciation that is interpreted to be derived from the Kerguelen basalts (Mazaud et al., 2010). Based on these records, we suggest the Ba/Ti and Ba/Al ratios of terrigenous material accumulating at MD84-551 are always similar to the Kerguelen basalts, whereas the material accumulating at MD88-773 and MD88-772 is basaltic during the glacial period, becoming more crustal during the deglaciation.

Figure A.4 is a plot of the downcore Ba_{xs} data using the range of both Ba/Al and Ba/Ti ratios from Table 1. Most of the Ba_{xs} records within each core remain comparable throughout the core. Based on the interpretation of Figure A.3, cores MD88-773 and MD88-772 received less Kerguelen material within the upper (Holocene) sections. However, the convergence of

all the Ba_{xs} records (constructed using the different Ba/Ti and Ba/Al ratios) within each of these cores during the Holocene suggests a negligible impact on the change in terrigenous source material on the Ba_{xs} ratio downcore. Hence, we will use the average Ba/Ti ratio of Kerguelen basalts (Ba/Ti = 0.0128) hereon to correct for terrigenous inputs of barium across all samples, applying the equation for Ba_{xs} below, where Ba and Ti are the barium and titanium contents of the sample in g/kg, respectively.

$$Ba_{xs} = Ba - (0.0128Ti) \tag{A.1}$$

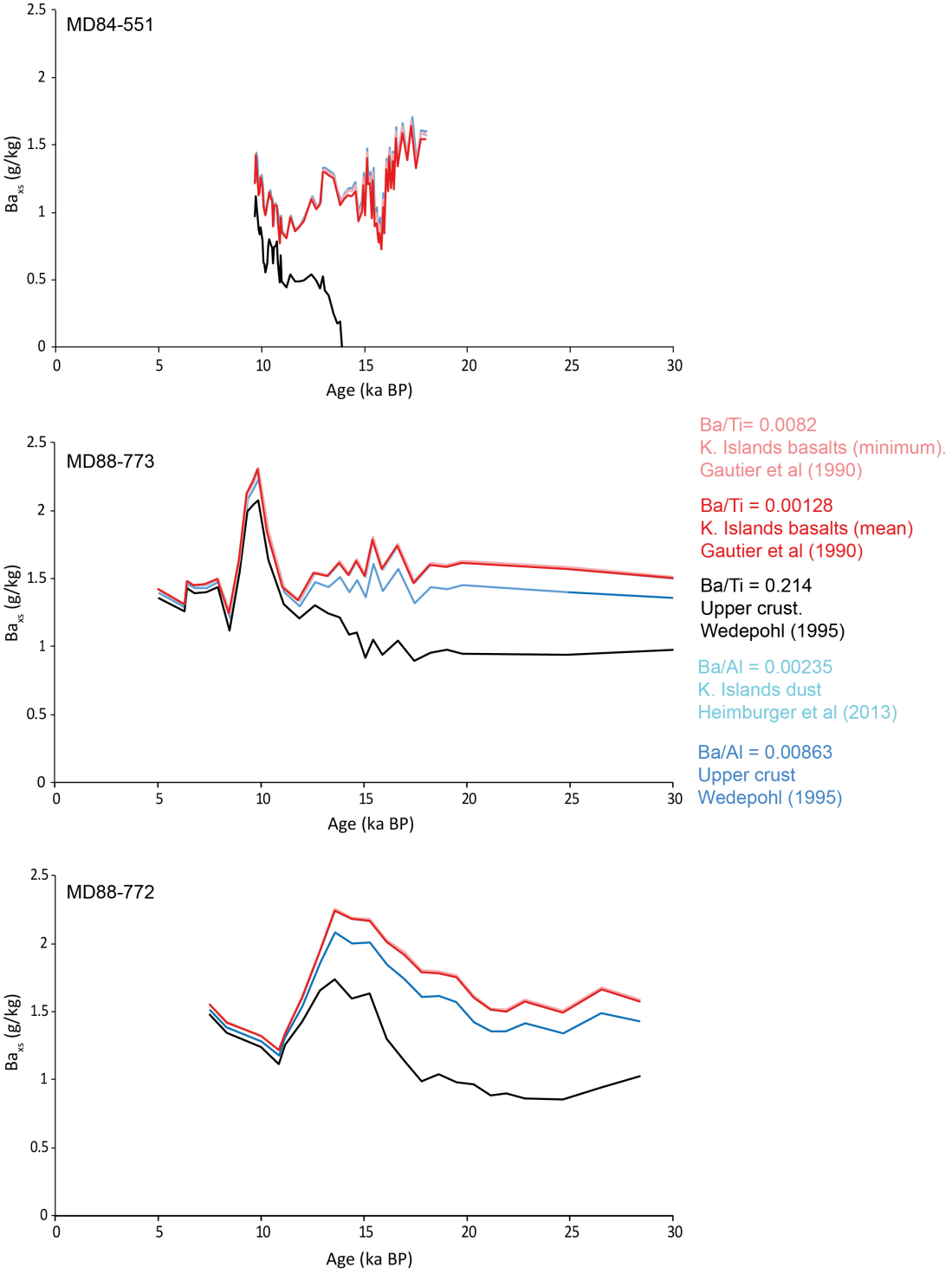

FIGURE A.4: Ba_{xs} content within the three sediment cores calculated using a range of lithogenic Ba/Ti and Ba/Al end-members. Based on the results displayed in Figure A.3 and those previous studies such as Bareille et al (1994), the Kerguelen Island basalt mean Ba/Ti was chosen as the most suitable end-member for the final Ba_{xs} calculations.

Authigenic uranium

Precipitation of uranium within sediments occurs under suboxic conditions, therefore the authigenic uranium (U_{auth}) content of sediments provides an indicator of bottom-water oxygenation (Henderson and Anderson, 2003). U_{auth} is determined by calculating the difference between the total U measured by ICP-MS and the detrital U estimated based on the average Th/U ratio in lithogenic material. Because much of the lithogenic material deposited in the Indian sector is derived from the Kerguelen Plateau (see discussion above, Bareille et al., 1994), we chose to use the average Th/U ratio found in Kerguelen basalts by Gautier et al (1990) (Th/U = 0.25).

^{230}Th-normalisation

Estimations of the fluxes of different sedimentary components (i.e. opal flux) are useful indicators of the change in surface biogeochemical process such as primary production. However, strong and variable bottom currents can horizontally transport sediments to and from the core site, biasing interpretations of vertical flux. This is particularly problematic in the Southern Ocean, where some of the strongest currents in the deep sea are observed (Dezileau et al., 2000). Correcting for this syndepositional redistribution of sediments can be achieved through the ^{230}Th-normalisation approach (Bacon, 1984; Francois et al., 1990; Francois et al., 2004). The theory behind this approach, relies on the high affinity of ^{230}Th for particle surfaces. As a result, ^{230}Th is efficiently scavenged by settling particles and has a short residence time in the water column. Over the timescales of marine sediment accumulation, the high scavenging rate of ^{230}Th results in its flux to the sediments being equal to its production rate in the overlying water column from the decay of ^{234}U ($\beta_{230} = 0.0267$ dpm m^{-3} year^{-1}). Assuming the ^{234}U content of the oceans remains unchanged and is uniformly distributed (Chen et al., 1986), the production of ^{230}Th and therefore its flux to the sediments are a function of the water column depth. Hence, the concentration of ^{230}Th within sediments (corrected for radioactive decay of ^{230}Th) associated with particle scavenging (i.e. not derived from lithogenic material or the in-growth of ^{230}Th within the sediment by radioactive decay of ^{234}U) should be inversely related to the sediment flux. In addition, the high particle affinity of ^{230}Th results in the thorium remaining in the sediments even after dissolution of any particles. Thus, the preserved vertical flux ($^{pr}F_v$) of material to the sediments can be estimated using the following equation:

$$^{pr}F_v = \frac{\beta_{230} Z}{^0A^{scav}_{Th-230}} \quad \text{(A.2)}$$

Where Z is the water column depth and $^0A^{scav}_{Th-230}$ is the decay-corrected activity of scavenged ^{230}Th within the sediment. $^0A^{scav}_{Th-230}$ is determined following the corrections given by Francois et al (2004), with the detrital ^{230}Th correction utilising the Th/U ratio found in Kerguelen basalts (Th/U = 0.25, Gautier et al., 1990) rather than the ratio of 0.4 commonly applied to Southern Ocean sediments (Henderson and Anderson, 2003).

^{230}Th-normalisation was performed on MD84-551 using the Th/U data produced in this study. A published record of Th/U data (Francois et al., 1997) was applied to MD88-773. No Th/U data are available for MD88-772, hence mass accumulation rates were applied (see Chapter 4 text).

A.2 %Opal

Diatoms, radiolaria and sponges have biomineralisation products (frustules, skeletons and spicules respectively) that once preserved in sedimentary records as amorphous hydrated silica (opal) can be used as a proxy for the conditions at which they formed. Diatomaceous matter is the major contributor to sedimentary opal in the Southern Ocean (Ragueneau et al., 2000; Geibert et al., 2005) thus its accumulation rate can be used as a diatom productivity proxy.

The percentage opal content by dry weight of samples will be determined via the heteropoly blue method (also referred to as the molybdenum-blue method), a similar methodology to that described by Mortlock and Froelich (1989). The first stage of the method involves the digestion of the sample biogenic opal. A common problem is determining the level of digestion required to only dissolved the biogenic opal and limit the dissolution of the more refractory aluminosilicates in clays (DeMaster, 1981; Conley, 1998). This can be accounted for analysing a sample at numerous intervals during a long digestion and assuming the rapid digestion of biogenic opal relative to clays. We found that digestion for 3 hours in 0.3 M NaOH at 85°C was sufficient to complete the extraction of the labile component. Silicon concentrations did not increase by four hours of digestion, suggesting negligible clay extraction.

After the digestion is completed the dissolved silica and phosphate in the sample are reacted with molybdate ions under acidic conditions to form yellow silicomolybdic acid complexes and phosphomolybdic acid complexes (Coradin et al., 2004). Addition of citric acid destroys the phosphate complexes, which would interfere with the spectrophotometric analysis. Amino Acid F Reagent is then added to reduce the yellow silicomolybdic acid to a molybdenum complex, which yields an intense blue colour. The samples are then measured by spectrophotometry with the analytical wavelength of 810 nm.

Of the 720 unique samples analysed (289 in MD84-551, 305 in MD88-773 and 126 in MD88-772) 149 were performed in triplicate with an average standard deviation of 5.4 wt% opal.

A.3 Diatom separation and cleaning

Dried sediment samples were washed through 75 µm and 10 µm sieves with deionised water. Visual inspection of these fractions revealed that the ¿75 um fraction was dominated by foraminifera and radiolaria, with very few large diatoms, sponge spicules and large clasts ($>$ 100 µm diameter) interpreted to be ice-rafted debris. The 10 – 75 µm fraction contained diatoms, foraminifera and silicoflaggelates as well as aggregated clay particles.

The 10 – 75 µm fraction was subjected to a series of chemical cleaning steps to isolate the diatoms and disaggregate adhering clays, adapted from the method originally described by Morley et al (2004). After each step the samples were centrifuged, decanted and washed with deionised water several times before moving to the next:

1. Dissolution of carbonates and disaggregation of clays in a solution of 5 % HCl and 5 % sodium hexametaphosphate at 80°C overnight. This step was repeated with fresh solution until the solution remained clear.
2. An initial organic matter oxidation step in 40 % H_2O_2 at 80°C overnight.
3. Separation of clays from opal by heavy liquid separation in sodium polytungstanate (SPT) ($\rho = 2.15$ g/ml), after which samples were washed thoroughly through a 10 µm sieve.

4. Removal of adsorbed metals (including the SPT introduced in the previous step) with sodium dithionite citrate (22 % sodium citrate, 2% sodium dithionite) (Holmgren, 1967).

5. Two final oxidations with 35 % and 75 % perchloric acid solutions at 100°C for 1 hour each (Robinson et al., 2014).

The quality of the cleaning procedure was assessed by inspection through scanning electron microscopy. The above procedure produced samples that appeared to contain >98 % diatoms, with the remaining fraction consisting of silicoflaggelates, radiolaria fragments and sponge spicule fragments. The clay fraction was reduced such that $< 0.5\%$ of the surface area of samples inspected by SEM were clay. Cleaned samples containing clay aggregates were re-cleaned as per step 1 (5% HCl and 5% hexametaphosphate) and rinsed thoroughly, which appeared to effectively reduce the clay content.

A.4 Diatom-bound nitrogen isotope ($\delta^{15}N_{DB}$) analysis

The method for determination of the nitrogen isotopic composition of diatom-bound organic matter broadly followed persulphate-denitrifier technique employed by Robinson et al. (2004). Sample preparation for IRMS is composed of two major phases, bacteria culturing and alkaline persulphate oxidation of diatoms that will be described in detail below.

The denitrifier method

The basis of the denitrifier method for $\delta^{15}N$ analysis is the utilisation of denitrifying bacteria that lack N_2O reductase activity to convert dissolved nitrate to N_2O gas for analysis by isotope ratio mass spectrometry (IRMS). This technique was first employed on dissolved inorganic nitrate within seawater and freshwater samples (Chistensen and Tiedje, 1988; Sigman et al., 2001; Casciotti et al., 2002) and was demonstrated to have several advantages over the traditional ammonia extraction method (e.g. Cline and Kaplan, 1975) including a 100-fold reduction in sample size requirement and a reduced labour/time requirement.

For particulate nitrogen, the traditional method for $\delta^{15}N$ analysis is by combustion in a CN analyser before analysis by IRMS. Typical lower working limits on these systems are on the

order of 1 µmol N. The N content within cleaned opal has been found to be approximately 10 µmol N/g opal (Robinson et al., 2004), which would necessitate the use of at least 100 mg of cleaned opal. Such large masses are not only impractical for sediments with low opal content but can also lead to erroneous results due to less intense combustion produced when overloading the combustion chamber with material (Beaumont et al., 1994; Sigman, 1997). The lower limit for the persulphate-denitrifier method is largely defined by the blank within the reagents used (discussed below), with precision better than 0.3 ‰(1σ) down to 20 nmol N (∼2 mg of cleaned opal).

Diatom-bound organic N oxidation

To prepare the diatom samples for the denitrifier method, the organic matter within the diatoms must be fully converted to nitrate so to avoid any fractionation during this process. Potassium persulphate (KPS) has been found to have the highest conversion efficiency for a range of labile and refractory compounds relative to other commonly utilised organic matter oxidation methods (D'Elia et al., 1977; Bronk et al., 2000) particularly when activated under alkaline conditions (Zhou et al., 2003).

However, one major drawback to this method is that KPS always contains a significant nitrogen blank. This blank is from ammonium persulphate, a derivative compound in the production of KPS, which is more soluble in water and methanol than KPS. Therefore, the blank can be reduced by repeated recrystallization of the KPS in water and washing with methanol. It was found that the blank within the KPS increased over time in storage. This is mitigated by washing with methanol every week and recrystallizing every two weeks. The KPS was stored in a dry crystalline state in a vacuum desiccator, and solutions for analysis were prepared daily. All containers used for handling KPS were pre-combusted to reduce contamination. The blank nitrogen content within supplied KPS was found to be inconsistent between batches. Batches with high nitrogen content, very heavy $\delta^{15}N$ values or very light $\delta^{15}N$ values were discarded completely.

The persulphate oxidation reagent is prepared following from Solorzano and Sharp (1980) and Robinson et al. (2004), consisting of 0.22 M of potassium persulphate in 1.5 M sodium hydroxide. The NaOH provides both the alkaline conditions needed for efficient oxidation of PON compounds and also enables the dissolution of diatom silica frustules. As with the KPS, the nitrogen content of the NaOH should be consistently low. We used batches of

NaOH supplied as low nitrogen solutions. The blank produced by this low nitrogen NaOH was found to be insignificantly different compared with boiled NaOH solutions (to volatise nitrogen compounds) and trace metal grade NaOH solutions. All the NaOH solutions were found to contain negligible inorganic nitrogen and any blank produced by organic nitrogen within the NaOH appeared to have negligible contribution to the overall blank after testing with varied concentrations of NaOH. All solutions used for the δ^{15}NDB method were made using UV photo-oxidized Milli-Q water.

The digestion procedure is as follows: 8 – 12 mg of cleaned opal was placed into pre-combusted 3 ml glass ampoules. 0.8 ml of the persulphate oxidation reagent was added and the ampoules immediately sealed. Glass ampoules were found to be superior to other digestion vessels as the entire vial can be combusted to eliminate organic nitrogen contaminants and caps on screw-capped vials could loosen during digestions risking contamination from atmospheric nitrogen (as also reported by Hagedorn and Schleppi, 2000).

The sealed vials were digested at 120 °C in an autoclave for 30 minutes. Several ampoules containing no opal (blanks) and others containing an L-glutamic acid δ^{15}N standard (USGS 40: $\delta^{15}N = -4.5‰$) and a glycine internal standard ($\delta^{15}N = 1.1‰$) were included within each digestion batch.

Once the digestions were completed, the ampoules were allowed to cool and the outsides rinsed with Milli-Q water so to wash away potential contaminants from the autoclave. Each ampoule was unsealed and enough 1.5 M HCl added to lower the pH to ≈6 so to prevent lysing the denitrifying bacteria in the strong basic solution. The amount of HCl required to neutralise the solution can vary with the concentration of KPS used as the KPS decomposes to sulphuric acid during the digestion process. It is therefore advisable to test the pH on a digested blank in each batch. HCl can accumulate inorganic nitrogen compounds, which raise the N blank. Therefore, we used double-distilled HCl, which was found to consistently contain negligible nitrogen. Once neutralised the solution is ready to be injected into the bacteria media for conversion of the nitrate into N_2O.

Bacterial media preparation

Aliquots of *Pseudomonas aureofaciens* were revived from a frozen stock kept in a glycerol solution at -80°C and streaked onto agar plates. Agar cultures were left in the dark at room

temperature to culture for 2 – 3 days. Individual colonies were isolated from the plates and either streaked again onto successive plates for continued culturing or placed into liquid bacterial media containing nitrate.

Liquid bacterial media cultures were stored on an orbital shaker for 6 – 10 days in the dark and at room temperature to allow for growth and depletion of nitrate within the media. Once ready the media was centrifuged and decanted. The remaining bacterial mass was resuspended within a smaller volume of prepared nitrate-free bacterial media. This concentrated the bacteria by approximately a factor of four. 3 ml of this nitrate-free bacterial media is then pipetted into crimp-sealed serum vials, which are fitted to an N_2 purge apparatus for three hours to deoxygenate the media and purge any inferring gases (residual N_2O and CO_2). Once purged, samples/standards are injected into the media and then left overnight to allow the full conversion of nitrate to N_2O. Before analysis, the media is injected with 10M NaOH to lyse the bacteria and sequester CO_2.

For analysis via isotope ratio mass spectrometry (IRMS), each of the headspace vials were loaded into a Combi PAL auto-sampler. The autosampler was linked through a Thermo Fisher Scientific GasBench II to a Thermo Fisher Scientific Delta+ Advantage stable isotope ratio mass spectrometer. Detection limits using this system are better than 0.5 ppm.

$\delta^{15}N_{DB}$ data handling

The persulphate-denitrifier technique has a number of data quality checks and corrections that must be performed for there to be sufficient confidence in the data. For data quality, each batch of $\delta^{15}N$ measurements included the following:

- Bug blank: A blank, known as the 'bug blank' containing no introduced sample or standard to check for unaccounted for N_2O. No N_2O was ever found within the bug blank.
- Sample repeats: $>$ 70% of the samples analysed were repeated at least three times from the bacterial denitrification stage onwards, ¿ 40% had repeated digestions.
- IRMS calibration standards: Three each of IAEA-NO-3 ($+4.7 \pm 0.2‰$) and USGS-32 ($+180 \pm 1‰$) dissolved in Milli-Q at concentrations similar to the samples (20 µM). These were used to normalise any variability in the bacterial and instrumental stages.

- Blank correction standards: The blank introduced by the persulphate reagent is significant and must be accounted for. However, due to its very low intensity, direct measurements of the blank often produced highly variable and unrealistic values for its isotopic composition. Instead, an indirect method (Gelwicks and Hayes, 1990; Ohlsson, 2013) of calculating the isotopic composition and intensity of the blank was performed. For this method, three each of IAEA-NO_{-3} and USGS-32 dissolved in the persulphate oxidation reagent at a range of concentrations (10 µM, 20 µM and 30 µM) were included in each batch. For each standard, the reciprocals of the intensities (peak areas) were regressed against the isotopic compositions. The slopes (m_1 and m_2) and intercepts ($delta_1$ and $delta_2$) of the regression lines for each standard were then used in the following equations to calculate the intensity (n_b) and isotopic composition (δ_b) of the blank.

$$n_b = \frac{m_1 - m_2}{\delta_1 - \delta_2} \tag{A.3}$$

$$\delta_b = \frac{m_2\delta_1 - m_1\delta_2}{m_2 - m_1} \tag{A.4}$$

  These data were then used to subtract the blank from each of the samples and standards using the following:

$$\delta_s = \frac{\delta_T n_T - \delta_b n_b}{n_T - n_b} \tag{A.5}$$

  Where n_T is the intensity of the uncorrected sample and δ_s and δ_T are the corrected and uncorrected isotopic compositions of the sample, respectively.

- Organic standards: One each of USGS-40 (-4.5 $\pm$ 0.1 ‰) and internal standard Gly-1 (1.1 ‰). These standards underwent the same correction protocol as the samples and were used as a final data quality check. Significantly large deviations outside of the typical analytical error (1σ= 0.3 ‰) would result in a discarding of the batch.

124 unique samples were analysed, 91 of which were triplicated from the denitrifier stage onwards and 50 were measured in duplicate or triplicate from the persulphate digestion stage onwards. Average errors calculated were ±0.33 ‰(1σ), an improvement on previously published errors (e.g. Robinson et al., 2014). All δ^{15}NDB data are quoted with reference to air N_2.

A.5 Silicon isotope ($\delta^{30}Si$) analysis

The method for $\delta^{30}Si$ analysis of diatom material largely follows the methods described by Georg et al. (2006). This method uses cation exchange chromatography to reduce cation interferences that occur during ICP-MS analysis whilst omitting the use of hydrofluoric acid, which is hazardous and may volatise some silicon as SiF_6^{-2}. The technique is conducted as follows:

Silica digestion

Cleaned diatom material (see diatom cleaning method above) was suspended in Milli-Q water and 10 µl of the suspension was pipetted into PTFE vessels. 1 ml of 0.1 M suprapure NaOH was added, and each vessel was sonicated for 5 minutes then placed on a hot plate at 80 °C overnight to allow for the full dissolution of the biogenic opal. Previous studies have used shorter digestion times so to minimize digestion of non-biogenic opal silica. However, due to the cleanliness of the cleaned diatom samples, the contribution from clays is likely to be negligible. Furthermore, longer digestion times ensure full digestion of the diatom material, which reduces the possibility of fractionation under partial digestion.

Once fully dissolved the solution was neutralised to pH 7 with 1 M double-distilled HCl. At neutral pH, room temperature and concentrations under 100 ppm, the silica should remain in solution as monosilicic acid (Iler, 1979). The concentration of silicic acid within the solutions was determined by the molybdate-blue method (Mortlock and Froelich, 1989) and the solutions were diluted to 20 ppm with Milli-Q water.

Cation exchange chromatography

Cations within the solution being introduced into an ICP-MS can produce non-spectroscopic interferences (matrix effects) whereby the analyte signal is biased relative to a matrix-free solution. This problem can be mitigated against by suppressing the matrix signal and removing the interfering species. Removal of major cations and trace metals (mostly Na but also Ca, K, Mg, Al, Fe and Ni) from the solution can be achieved by cation exchange chromatography. During this process cations within the solution exchange with those held within the exchange sites of the cation exchange resin. In this case the sulphonic acid resin

(BioRad AG 50W-X8) in the H^+ form will preferentially retain cations with greater ionic size and charge (Na^+, K^+, Mg^{2+} etc). Between pH 2 and 8 silicon is in the non-ionic $Si(OH)_4$ and anionic H_3SiO_4 forms, therefore the cation exchange resin will not retain the silicon, thereby separating silicon from the cations.

The method for the cation exchange chromatography is as follows:

1. 1 ml 3 M HCl (**column clean**)
2. 1 ml 6 M HCl (**column clean**)
3. 1 ml 3 M HCl (**column clean**)
4. 2 ml MQ H_2O (**column clean**)
5. 1 ml MQ H_2O (**neutral pH**)
6. 0.5 ml 20 ppm sample (**load column**)
7. 0.5 ml MQ H_2O (**elute**)
8. 0.5 ml MQ H_2O (**elute**)
9. 1 ml MQ H_2O (**elute**)
10. 1 ml MQ H_2O (**elute**)
11. 2 ml 3 M HCl (**column clean**)
12. 2 ml 6 M HCl (**column clean**)
13. 2 ml 6 M HCl (**column clean**)
14. 2 ml 3 M HCl (**column clean**)

1.8 ml of resin is loaded into each column and 0.5 ml of solution containing 20 ppm of Si. The capacity of BioRad AG 50W-X8 is 1.7 meq/ml. The maximum concentration of Na+ (the major cation) in the solutions would be 0.1 M, or 0.05 meq loaded onto the columns. Hence the capacity of the resin would be more than sufficient to remove all the cations from the solutions.

The elution with Milli-Q water dilutes the solution to 2.5 – 3 ppm. Eluting with a further 5 ml of Milli-Q water was found to produced effluent that that contained negligible Si and major cations. The samples and standards were then further diluted to 0.6 - 0.8 ppm before analysed by ICP-MS. The final solutions contained major cation concentrations similar to or

below that of Milli-Q water and were kept at neutral pH. Some studies suggest reducing the pH to 2 – 3 to ensure the silicon remains as monosilicic acid (Georg et al., 2006; Zambardi and Poitrasson, 2011). However, adding either HCl or HNO_3 could produce undesirable matrix effects or Si fractionation (Fitoussi et al., 2009). Nevertheless, we found no difference between solutions reduced to pH 2 and those at neutral pH.

A drawback of the cation exchange chromatography method is that anionic- and organic-based interferences are not removed. In particular, sulphate has been found to produced significant biases in $\delta^{30}Si$ measurements of sulphur-rich materials and water samples (Hughes et al., 2011). However, there is little evidence to suggest major anionic interferences involved in measuring cleaned diatom material.

Dissolved organic matter interferences are mitigated by the perchloric acid oxidation steps described in the diatom cleaning method above. Diatom-bound organic matter does not appear to produce a significant matrix effect after comparing with diatom material that is digested in NaOH and H_2O_2.

MC-ICP-MS

Inductively-coupled mass spectrometry (ICP-MS) involves the ionization of a solution within an argon plasma and subsequent separation of the ions according to their mass to charge ratio (m/z) within an ion beam. Multi-collector (MC) -ICP-MS instruments allow for simultaneous measurements of several different m/z signals (isotopes) within the ion beam focal plane. This significantly increases the precision of isotope ratio measurements relative to traditional (quadrupole) ICP-MS instruments by mitigating against inherent instabilities in the ion beam.

One important part of ICP-MS instrumentation is the minimization of the signals produced by elements and molecules that have the same m/z as the isotope of interest. Most commonly, these interferences are produced by either monovalent species of the same mass residing in the analyte solution or atmosphere (isobaric), and divalent/polyvalent species that have the double or more the molecular weight but retain the same m/z ratio.

For the latter in silicon isotope work Table A.2 lists common divalent species that could exhibit interferences. Fortunately, both iron and nickel are effectively extracted from the

solutions during cation exchange chromatography and so represent a minor or negligible interference.

Si isotope	Divalent interferences	Polyatomic interferences
^{28}Si	$^{56}Fe_{2+}$	$^{12}C^{16}O^{+}$, $^{14}N_2{}^{+}$
^{29}Si	$^{58}Fe^{2+}$, $^{58}N_2{}^{+}$	$^{12}CH^{16}O^{+}$, $^{14}N_2H^{+}$
		$^{14}N^{15}N^{+}$, $^{28}SiH^{+}$, $^{13}C^{16}O^{+}$
^{30}Si	$^{60}Ni^{2+}$	$^{29}SiH^{+}$, $^{14}N^{16}O^{+}$

TABLE A.2: A list of the more common divalent and polyatomic interferences in the ICP-MS analysis of stable silicon isotopes.

Monovalent interferences, particularly from polyatomic isobaric species are a major source of interference in silicon isotope work. Most notably the species $^{14}N^{16}O^{+}$ produces an interfering signal so great that accurate measurements of the isotope 30Si remained prohibited until recently. The use of a desolvating device (Cetac Aridus) significantly reduces the input of H_2O, CO_2, O2 and N_2 into the plasma, which upon ionization would produce the interfering polyatomic species. This 'dry' plasma has the added benefit of reduced matrix effects. However, the important polyatomic interferences of $^{12}CH^{16}O^{+}$ on ^{28}Si and $^{14}N^{16}O^{+}$ on ^{30}Si must still be resolved. The Nu Plasma II MC-ICP-MS instrument has the capability of resolving these interferences under the pseudo-high-resolution mode. This is achieved by reducing the width of the source defining slit and alpha slit. Under this setup the ^{28}Si and ^{30}Si signals can be accurately determined by analysing the flat left shoulder of the peak, because the interferences on both isotopes are expressed on the heavy side of the peak. Sample-standard bracketing was performed with silicon isotope reference material, NBS-28 to minimize variable mass bias effects. Long-term reproducibility was monitored by analysis of Big Batch standard (- 10.48 $\pm$0.29 ‰, Reynolds et al., 2007).

Overall, average internal reproducibility at 1σ. was 0.06 ‰(n $\geq$ 3 per sample, total 124 samples including repeats). Average external reproducibility at 1s.d was 0.09 ‰(n $\geq$ 3 per sample, total 14 samples). All $\delta^{30}Si$ values are quoted relative to the NBS28 standard.

A.6 Foraminifera-based analyses

The $>$ 75 µm fraction of the sediment samples not used for the diatom $\delta^{15}N$ and $\delta^{30}Si$ analyses was kept in order to isolate foraminifera. The samples were thoroughly washed with Milli-Q water to remove adhering clay particles. The remaining material mostly consisted of foraminifera, radiolaria, sponge spicules and clastic grains interpreted to be ice-rafted debris.

Planktic foraminiferal $\delta^{18}O$ data (various monospecific records) were already available for MD84-551 and MD88-773 (Michel, E and Francois, R pers comms). *Globigerina bulloides* were hand-picked from MD88-772 for $\delta^{18}O$ analysis.

Radiocarbon

Planktic foraminiferal ^{14}C data (*Neogloboquadrina pachyderma*) were available for MD84-551 only (Labracherie et al., 1989; Pichon et al., 1992; Michel, E., pers comms). Planktic foraminifera were present throughout MD84-551 in high enough abundance for more ^{14}C dates to be added, however, the presence of planktic foraminifera declines to zero at approximately 60 cm in MD88-772 and 360 cm in MD88-773. This is confirmed by XRF core scanning data that shows minimal calcium beyond these depths. Foraminifera were picked for $\delta^{18}O$ and ^{14}C analysis where preservation permitted. Picked foraminifera samples for ^{14}C analysis were sent to the NERC Radiocarbon Facility, East Kilbride for graphitization and analysis by accelerator mass spectrometry.

Oxygen isotopes

$\delta^{18}O$ analysis was performed at the University of Edinburgh, Wolfson Laboratory. The foraminiferal carbonate samples were reacted with 100 % orthophosphoric acid at 75°C in a Kiel Carbonate III preparation device and the resulting CO_2 was then analysed on a Thermo Electron Delta+ Advantage stable isotope ratio mass spectrometer. The standard deviation (n=29) of a powdered coral laboratory standard (COR1D, $\delta^{18}O$ = -4.927) run as a sample on the same six days as the study samples, was $\pm$0.063 ‰. All $\delta^{18}O$ values quoted relative to VPDB.

References

Bacon , M. P. Glacial to interglacial changes in carbonate and clay sedimentation in the Atlantic Ocean estimated from 230Th measurements. *Chemical Geology*, 46(2):97–111, 1984. doi: 10.1016/0009-2541(84)90183-9.

Bareille , G., Grousset , F. E., Labracherie , M., Labeyrie , L. D., and Petit , J. Origin of detrital fluxes in the southeast Indian Ocean during the last climatic cycles. *Paleoceanography*, 9(6):799–819, 1994.

Beaumont , V., Agrlnier , P., Robert , F., De , L., Paris , U., Cedex , P., Mineralogie , L. D., and Naturelle , H. Determination of the CO Contribution to the 15N / 14N Ratio Measured by Mass Spectrometry. *Analytical Chemistry*, 66(13):2187–2189, 1994. doi: 10.1021/ac00085a039.

Bronk , D. A., Lomas , M. W., Glibert , P. M., Schukert , K. J., and Sanderson , M. P. Total dissolved nitrogen analysis: Comparisons between the persulfate, UV and high temperature oxidation methods. *Marine Chemistry*, 69(1-2):163–178, 2000. doi: 10.1016/S0304-4203(99)00103-6.

Casciotti , K. L., Sigman , D. M., Hastings , M. G., Böhlke , J. K., and Hilkert , a. Measurement of the oxygen isotopic composition of nitrate in seawater and freshwater using the denitrifier method. *Analytical Chemistry*, 74(19):4905–4912, 2002. doi: 10.1021/ac020113w.

Chen , J., Edwards , R. L., and Wasserburg , G. J. 238U, 234U and 232Th in seawater. *Earth and Planetary Science Letters*, 80(3-4):241–251, 1986.

Christensen , S. and Tiedje , J. M. Sub-parts-per-billion nitrate method: use of an N_2O producing denitrifier to convert NO_3^- or ^{15}NO_3^- to N_2O. *Applied and Environmental Microbiology*, 54(6):1409–1413, 1988.

Conley , D. J. An interlaboratory comparison for the measurement of biogenic silica in sediments. *Marine Chemistry*, 63(1-2):39–48, 1998. doi: 10.1016/S0304-4203(98)00049-8.

Coradin , T., Eglin , D., and Livage , J. The silicomolybdic acid spectrophotometric method and its application to silicate/biopolymer interaction studies. *Spectroscopy*, 18(4):567–576, 2004. doi: 10.1155/2004/356207.

D'Elia , C. F., Steudler , P. A., and Corwin , N. Determination of total nitrogen in aqueous samples using persulfate digestion. *Limnology and Oceanography*, 22(4):760–764, 1977. doi: 10.4319/lo.1977.22.4.0760.

Demaster , D. The supply and accumulation of silican in the marine environment. *Geochemica et Cosmochimica*, Acta 45 (1:1715–1732, 1981.

Dezileau , L., Bareille , G., Reyss , J. L., and Lemoine , F. Evidence for strong sediment redistribution by bottom currents along the southeast Indian ridge. *Deep-Sea Research Part I: Oceanographic Research Papers*, 47(10):1899–1936, 2000. doi: 10.1016/S0967-0637(00)00008-X.

Dymond , J., Suess , E., and Lyle , M. Barium in deep-sea sediment: A geochemical proxy for paleoproductivity. *Paleoceanography*, 7(2):163–181, 1992.

Fitoussi , C., Bourdon , B., Kleine , T., Oberli , F., and Reynolds , B. C. Si isotope systematics of meteorites and terrestrial peridotites: implications for Mg/Si fractionation in the solar nebula and for Si in the Earth's core. *Earth and Planetary Science Letters*, 287(1-2):77–85, 2009. doi: 10.1016/j.epsl.2009.07.038.

Francois , R., Altabet , M. A., Yu , E.-f., Sigman , D. M., Bacon , M. P., Frank , M., Bohrmann , G., Bareille , G., and Labeyrie , L. D. Contribution of Southern Ocean surface-water stratification to low atmospheric CO 2 concentrations during the last glacial period. *Nature*, 389:929–935, 1997.

Francois , R., Bacon , M., and Suman , D. Thorium 230 profiling in deep-sea sediments: High-resolution records of flux and dissolution of carbonate in the equatorial Atlantic during the last 24,000 years. *Paleoceanography*, 5(5):761–787, 1990.

Francois , R., Frank , M., Rutgers van der Loeff , M. M., and Bacon , M. P. 230 Th normalization: An essential tool for interpreting sedimentary fluxes during the late Quaternary. *Paleoceanography*, 19(1): n/a–n/a, mar 2004. doi: 10.1029/2003PA000939.

Gautier , I., Weis , D., Mennessier , J. P., Vidal , P., Giret , A., and Loubet , M. Petrology and geochemistry of the Kerguelen Archipelago basalts (South Indian Ocean): evolution of the mantle sources

from ridge to intraplate position. *Earth and Planetary Science Letters*, 100(1-3):59–76, 1990. doi: 10.1016/0012-821X(90)90176-X.

Geibert , W., Rutgers van der Loeff , M. M., Usbeck , R., Gersonde , R., Kuhn , G., and Seeberg-Elverfeldt , J. Quantifying the opal belt in the Atlantic and southeast Pacific sector of the Southern Ocean by means of 230 Th normalization. *Global Biogeochemical Cycles*, 19(4):n/a–n/a, dec 2005. doi: 10.1029/2005GB002465.

Gelwicks , J. T. and Hayes , J. M. Carbon-Isotopic Analysis of Dissolved Acetate. *Analytical Chemistry*, 62: 535–539, 1990.

Georg , R. B., Reynolds , B. C., Frank , M., and Halliday , A. N. New sample preparation techniques for the determination of Si isotopic compositions using MC-ICPMS. *Chemical Geology*, 235:95–104, 2006. doi: 10.1016/j.chemgeo.2006.06.006.

Heimburger , A., Losno , R., Triquet , S., and Nguyen , E. B. Atmospheric deposition fluxes of 26 elements over the Southern Indian Ocean: Time series on Kerguelen and Crozet Islands. *Global Biogeochemical Cycles*, 27(2):440–449, 2013. doi: 10.1002/gbc.20043.

Henderson , G. and Anderson , R. The U-series toolbox for paleoceanography. *Reviews in mineralogy and . . .*, 52(1):493–531, 2003.

Hughes , H. J., Delvigne , C., Korntheuer , M., de Jong , J., André , L., and Cardinal , D. Controlling the mass bias introduced by anionic and organic matrices in silicon isotopic measurements by MC-ICP-MS. *Journal of Analytical Atomic Spectrometry*, 26(9):1892, 2011. doi: 10.1039/c1ja10110b.

Iler , R. *The Chemistry of Silica: Solubility, Polymerization, Colloid and Surface Properties and Biochemistry of Silica*. Wiley, 1979.

Kretschmer , S., Geibert , W., Rutgers van der Loeff , M. M., Schnabel , C., Xu , S., and Mollenhauer , G. Fractionation of 230Th, 231Pa, and 10Be induced by particle size and composition within an opal-rich sediment of the Atlantic Southern Ocean. *Geochimica et Cosmochimica Acta*, 75(22):6971–6987, 2011. doi: 10.1016/j.gca.2011.09.012.

Mazaud , A., Michel , E., Dewilde , F., and Turon , J. L. Variations of the Antarctic Circumpolar Current intensity during the past 500 ka. *Geochemistry Geophysics Geosystems*, 11(8):1–10, 2010. doi: 10.1029/2010GC003033.

Mortlock , R. and Froelich , P. A simple method for the rapid determination of biogenic opal in pelagic marine sediments. *Deep Sea Research Part A. Oceanographic Research Papers*, 36(9):1415–1426, 1989.

Ohlsson , K. E. A. Uncertainty of blank correction in isotope ratio measurement. *Analytical Chemistry*, 85 (11):5326–5329, 2013. doi: 10.1021/ac4003968.

Ragueneau , O., Treguer , P., Leynaert , A., Anderson , R. F., Brzezinski , M. A., Demaster , D. J., Dugdale , R. C., Dymond , J., Fischer , G., Franc , R., Heinze , C., Nelson , D. M., and Queguiner , B. A review of the Si cycle in the modern ocean : recent progress and missing gaps in the application of biogenic opal as a paleoproductivity proxy. *Global and Planetary Change*, 26:317–365, 2000.

Reynolds , B. C., Aggarwal , J., Andre , L., Georg , R. B., Beucher , C., Brzezinski , M. A., Engstro , E., Land , M., Leng , M. J., Opfergelt , S., Rodushkin , I., Sloane , H. J., Boorn , S. H. J. M. V. D., and Vroon , Z. An inter-laboratory comparison of Si isotope reference materials. *Journal of Analytical Atomic Spectrometry*, 22:561–568, 2007. doi: 10.1039/b616755a.

Richter , T. O., Van Der Gaast , S., Koster , B., Vaars , A., Gieles , R., De Stigter , H. C., De Haas , H.,

and Van Weering , T. C. The Avaatech XRF Core Scanner : technical description and applications to NE Atlantic sediments. In *New Techniques in Sediment Core Analysis*, volume 267, pages 39–50. Geological Society, London, 2006.

Robinson , R. S., Brunelle , B. G., and Sigman , D. M. Revisiting nutrient utilization in the glacial Antarctic: Evidence from a new method for diatom-bound N isotopic analysis. *Paleoceanography*, 19(3), sep 2004. doi: 10.1029/2003PA000996.

Robinson , R. S., Brzezinski , M. a., Beucher , C. P., Horn , M. G. S., and Bedsole , P. The changing roles of iron and vertical mixing in regulating nitrogen and silicon cycling in the Southern Ocean over the last glacial cycle. *Paleoceanography*, pages 1179–1195, 2014. doi: 10.1002/2014PA002686.Received.

Shemesh , A., Mortlock , R., Smith , R., and Froelich , P. Determination of Ge/Si in marine siliceous microfossils: Separation, cleaning and dissolution of diatoms and radiolaria. *Marine Chemistry*, 25:305–323, 1988.

Sigman , D. M. *The role of biological production in pleistocene atmospheric carbon dioxide variations and the nitrogen isotope dynamics of the southern ocean*. Massachusetts Institute of Technology and Woods Hole Oceanographic Institution, Woods Hole, MA, 1997. doi: 10.1575/1912/5691.

Sigman , D., Casciotti , K., Andreani , M., Barford , C., Galanter , M., and Bohlke , J. K. A bacterial method for the nitrogen isotopic analysis of nitrate in seawater and freshwater. *Analytical Chemistry*, 73 (17):4145–4153, 2001.

Taylor , S. Abundance of chemical elements in the continental crust: a new table. *Geochimica et Cosmochimica Acta*, 28(8):1273–1285, 1964. doi: 10.1016/0016-7037(64)90129-2.

Tjallingii , R., Röhl , U., Kölling , M., and Bickert , T. Influence of the water content on X-ray fluorescence corescanning measurements in soft marine sediments. *Geochemistry, Geophysics, Geosystems*, 8(2):1–12, 2007. doi: 10.1029/2006GC001393.

Zambardi , T. and Poitrasson , F. Precise Determination of Silicon Isotopes in Silicate Rock Reference Materials by MC-ICP-MS. *Geostandards and Geoanalytical Research*, 35:89–99, 2011. doi: 10.1111/j.1751-908X.2010.00067.x.

B

Data appendix

B.1 MD84-551

Depth (cm)	Opal (%)	$\pm 1\sigma$	Ba (g/kg)	Ca (%)	Mn (mg/kg)	Fe (g/kg)	Ti (g/kg)	Al (g/kg)	K (g/kg)
74	76.0								
75	79.4								
76	79.9		1.23	6.30	542	5.47	1.21	5.58	3.16
77	71.8								
78	71.1		1.45	5.87	976	7.00	1.53	7.09	3.78
79	78.9								
80	77.5		1.40	4.78	1314	6.98		6.42	3.43
81	75.3								
82	80.0	6.6	1.14	4.11	1272	5.63	1.26	4.82	2.86
83	81.8								
84	78.3	1.9	1.17	3.72	1526	7.00	1.53	6.05	3.38
85	80.0								
86	75.1		1.29	3.95	1716	8.13	1.86	7.10	3.59
87	71.5								
88	73.9		1.21	4.11	1387	8.75	1.95	7.47	3.70
89	75.3								
90	80.9		1.07	3.69	1467	9.50	2.06	7.99	3.89
91	78.7								
92	74.7		1.03	3.61	1567	9.50	1.95	8.01	3.76
93	75.5								
94	77.2	5.7	1.01	3.39	1069	9.47	2.11	7.98	3.77
95	75.8								

Depth (cm)	Opal (%)	$\pm 1\sigma$	Ba (g/kg)	Ca (%)	Mn (mg/kg)	Fe (g/kg)	Ti (g/kg)	Al (g/kg)	K (g/kg)
96	78.1		1.09	3.86	1477	10.54	2.16	9.10	4.17
97	81.5								
98	78.9		1.12	3.43	1189	7.94	1.69	6.81	3.46
99	75.5								
100	79.2		1.17	3.53	1212	8.22	1.72	7.32	3.59
101	78.2								
102	79.2		1.12	2.58	2438	8.00	1.72	7.12	3.62
103	82.3	3.7							
104	82.4		1.11	2.53	6633	8.13	1.72	7.09	3.70
105	79.8								
106	86.0		0.91	2.21	7571	6.86	1.35	5.78	3.52
107	87.1								
108	78.0		1.07	2.43	5251	7.39	1.57	6.38	3.40
109	82.0								
110	86.7		1.07	2.27	2358	7.04	1.48	6.01	3.22
111	86.8								
112	85.3	8.2	1.06	2.32	1988	5.85	1.27	5.30	3.17
113	82.3	6.8							
114	84.9	5.1	0.95	2.46	2529	6.96	1.49	6.09	3.58
115	84.4	4.0							
116	82.7	5.6	0.79	1.77	467	6.56	1.44	5.40	3.06
117	80.2	4.9							
118	81.2	8.4	0.98	2.74	367	6.68	1.42	5.63	3.09
119	80.2	4.6							
120	84.1		0.87	2.15	345	8.58	1.81	6.90	3.58
121	85.7								
122	84.7		0.83	2.48	182	8.24	1.80	6.74	3.41
123	81.5								
124	80.3		0.99	2.32	178	9.89	2.10	7.91	3.77
125	83.4								
126	81.2		0.88	2.22	130	8.17	1.84	6.84	3.50
127	77.1								
128	79.6		0.91	2.69	153	9.12	1.96	7.31	3.49
129	76.4								
130	77.5	3.0	0.96	2.51	156	10.17	2.19	8.37	3.66
133	70.6	6.0							
134	66.2	6.7	1.13	2.85	190	13.68	2.79	10.95	4.51
135	69.0	5.3							
136	69.5	7.2	1.06	3.05	300	12.46	2.62	10.23	4.30
137	70.7	7.0							
138	67.4	5.5	1.10	3.00	419	14.13	3.10	11.68	4.72
139	65.5	8.4	1.35	3.36		15.85	3.84	13.72	
140	67.6	4.4	1.35	3.22	415	20.72	4.37	17.32	6.44
141	65.9	5.4							
142	66.5	4.4	1.34	3.19	446	22.39	4.45	17.75	6.63
143	67.1	2.8							
144	66.0	3.2	1.32	3.21	410	23.80	4.97	19.40	6.94
145	65.7	1.7							
146	64.1	4.4	1.20	2.72	1142	23.07	4.79	19.05	6.97
147	65.7	7.2							
148	70.0	5.8	1.11	2.90	334	20.77	4.29	17.18	6.43
149	67.6	5.7							
150	47.3	4.9	1.18	3.89	404	30.74	6.52	25.50	8.99
151	47.7	6.4							
152	41.2	4.0	1.23	4.64	492	37.50	8.21	31.63	10.64
153	36.2	5.7							
154	41.6	4.6	1.23	4.66	525	39.99	8.73	33.15	11.04
155	36.1	2.4							
156	34.0	1.9	1.28	5.11	528	44.93	9.59	37.78	12.51
157	37.0	1.9							
158	27.7	2.6	1.08	5.18	602	51.02	11.77	45.37	14.71
159	31.3	2.3							
160	27.8		1.15	5.30	848	49.77	11.04	42.18	13.31

Depth (cm)	Opal (%)	$\pm 1\sigma$	Ba (g/kg)	Ca (%)	Mn (mg/kg)	Fe (g/kg)	Ti (g/kg)	Al (g/kg)	K (g/kg)
161	30.7		1.35	5.31		46.09	11.69	40.79	
162	24.9		1.12	5.28	603	51.93	11.55	43.00	13.81
163	35.9		1.53	4.75		42.32	10.51	36.86	
164	30.7		1.34	5.35	514	47.02	10.06	40.00	12.80
165	31.4		1.37	4.90		45.39	11.69	40.55	
166	28.0		1.10	4.83	580	50.36	11.10	42.91	14.19
167	34.3		1.39	5.26		46.20	11.87	40.27	
168	22.7		1.06	5.23	727	55.21	12.54	47.60	15.24
169	25.2		1.11	5.21		53.58	14.73	47.54	
170	21.8		0.97	5.60	732	59.34	14.54	51.40	16.21
171	23.9		1.04	5.17		57.56	15.72	49.82	
172	24.7		0.91	5.23	739	59.57	13.86	51.96	16.23
173	29.6		1.22	5.09		52.19	14.03	46.97	
174	33.2		1.01	5.16	638	54.67	12.72	48.44	15.36
175	40.1		1.45	5.10		42.80	10.22	35.97	
176	37.2		1.27	6.80	458	40.75	8.71	36.12	11.79
177	43.7		1.53	4.89		36.37	8.70	31.91	
178	42.6	7.7	1.28	4.77	468	39.66	8.21	34.49	11.38
179	38.6		1.51	5.03		40.57	9.94	35.99	
180	32.2		1.29	5.64	507	45.52	9.71	42.06	12.76
181	36.9		1.69	5.33		44.56	10.91	39.49	
182	33.6		1.47	5.37	510	46.62	9.74	41.84	13.12
183	35.8		1.72	5.50		42.28	10.57	38.60	
184	42.3		1.50	4.82	434	40.80	8.76	37.73	12.26
185	41.0		1.76	4.76		39.30	9.71	36.44	
186	46.1		1.43	4.31	412	37.48	7.99	34.28	11.08
187	44.7		1.66	4.85		38.44	9.28	34.49	
188	41.4		1.66	5.80	471	43.96	9.35	41.04	13.12
189	36.8								
190	42.0								
191	43.5								
192	45.4								
193	40.0								
194	41.8								
195	40.5								
196	43.5								
197	45.2								
198	43.0								
199	39.3								
200	42.1								
201	40.3	4.7							
202	38.9								
203	35.2								
204	38.0								
205	33.4								
206	38.2								
207	32.2								
208	39.3								
209	35.1								
210	41.4								
211	39.9								
212	36.7								
213	41.1								
214	42.0								
215	44.5								
216	44.3								
217	44.8								
218	44.1								
219	43.2								
220	49.2								
221	42.0								
222	52.0								
223	44.7								

Depth (cm)	Opal (%)	$\pm 1\sigma$	Ba (g/kg)	Ca (%)	Mn (mg/kg)	Fe (g/kg)	Ti (g/kg)	Al (g/kg)	K (g/kg)
224	50.0								
225	47.0								
226	44.2								
227	51.8								
228	50.9								
229	53.1								
230	55.8								
231	54.7								
232	54.0								
233	52.6								
234	57.8								
235	58.9								
236	52.7								
237	57.0								
238	57.3								
239	56.9								
240	55.5								
241	58.4								
242	61.2								
243	61.2								
244	51.2								
245	52.3								
246	54.8								
247	54.5								
248	52.8								
249	47.6								
250	48.3								

Depth (cm)	^{232}Th (dpm/g)	$\pm 1\sigma$	^{234}U (dpm/g)	$\pm 1\sigma$	^{238}U	$\pm 1\sigma$	^{235}U (dpm/g)	$\pm 1\sigma$	^{230}Th (dpm/g)	$\pm 1\sigma$
74										
75										
76	0.1461	0.0007	0.3224	0.0022	0.2810	0.0052	0.01294	0.00024	2.242	0.019
77										
78	0.1724	0.0016	0.4233	0.0025	0.3718	0.0044	0.01712	0.00020	2.295	0.023
79										
80	0.1707	0.0026	0.4493	0.0040	0.3917	0.0031	0.01803	0.00014	2.135	0.042
81										
82	0.1512	0.0032	0.3738	0.0030	0.3269	0.0012	0.01505	0.00005	1.819	0.064
83										
84	0.1706	0.0027	0.4066	0.0020	0.3569	0.0024	0.01643	0.00011	1.909	0.038
85										
86	0.1959	0.0025	0.4283	0.0031	0.3771	0.0024	0.01737	0.00011	2.170	0.042
87										
88	0.2092	0.0016	0.4224	0.0031	0.3755	0.0018	0.01729	0.00008	2.165	0.022
89										
90	0.2134	0.0027	0.4286	0.0029	0.3786	0.0014	0.01743	0.00006	2.084	0.022
91										
92	0.2195	0.0017	0.4263	0.0024	0.3720	0.0013	0.01713	0.00006	2.102	0.021
93										
94	0.2476	0.0027	0.4402	0.0029	0.3934	0.0033	0.01811	0.00015	2.288	0.045
95										
96	0.2296	0.0032	0.4333	0.0042	0.3875	0.0020	0.01784	0.00009	2.128	0.041
97										
98	0.1933	0.0018	0.3853	0.0015	0.3420	0.0021	0.01575	0.00010	2.042	0.030
99										
100	0.2026	0.0030	0.3869	0.0018	0.3435	0.0013	0.01582	0.00006	2.167	0.035
101										
102	0.2020	0.0020	0.3959	0.0038	0.3515	0.0014	0.01618	0.00007	2.072	0.023
103										
104	0.2008	0.0034	0.4238	0.0057	0.3728	0.0038	0.01717	0.00017	2.062	0.039
105										

Depth (cm)	^{232}Th (dpm/g)	$\pm1\sigma$	^{234}U (dpm/g)	$\pm1\sigma$	^{238}U	$\pm1\sigma$	^{235}U (dpm/g)	$\pm1\sigma$	^{230}Th (dpm/g)	$\pm1\sigma$
106	0.1737	0.0021	0.3977	0.0026	0.3493	0.0025	0.01608	0.00011	1.710	0.027
107										
108	0.1873	0.0030	0.3882	0.0033	0.3444	0.0026	0.01586	0.00012	1.910	0.044
109										
110	0.1685	0.0014	0.3515	0.0030	0.3118	0.0007	0.01435	0.00003	1.820	0.030
111										
112	0.1499	0.0023	0.3923	0.0036	0.3461	0.0035	0.01594	0.00016	1.680	0.015
113										
114	0.1700	0.0019	0.3349	0.0028	0.2930	0.0014	0.01349	0.00006	1.775	0.036
115										
116	0.1552	0.0018	0.3191	0.0045	0.2825	0.0025	0.01301	0.00011	1.509	0.024
117										
118	0.1592	0.0030	0.3212	0.0021	0.2840	0.0029	0.01308	0.00013	1.765	0.037
119										
120	0.1871	0.0012	0.3456	0.0031	0.3081	0.0046	0.01419	0.00021	1.698	0.021
121										
122										
123										
124	0.2254	0.0019	0.3808	0.0028	0.3311	0.0040	0.01525	0.00018	2.134	0.023
125										
126	0.2026	0.0011	0.3627	0.0032	0.3209	0.0058	0.01477	0.00026	1.888	0.019
127										
128	0.2135	0.0016	0.3780	0.0039	0.3218	0.0040	0.01482	0.00018	2.083	0.024
129										
130	0.2468	0.0020	0.3783	0.0063	0.3388	0.0049	0.01560	0.00022	2.257	0.030
133										
134	0.2966	0.0095	0.4272	0.0055	0.3850	0.0027	0.01773	0.00013	2.698	0.036
135										
136	0.2954	0.0027	0.4211	0.0042	0.3820	0.0057	0.01759	0.00026	2.576	0.043
137										
138	0.3261	0.0033	0.4413	0.0068	0.4001	0.0062	0.01842	0.00028	2.684	0.028
139										
140	0.4838	0.0033	0.5561	0.0070	0.5172	0.0095	0.02382	0.00044	3.491	0.021
141										
142	0.5004	0.0045	0.5724	0.0038	0.5264	0.0061	0.02424	0.00028	3.504	0.034
143										
144	0.5507	0.0042	0.6084	0.0033	0.5665	0.0079	0.02608	0.00036	3.550	0.044
145										
146	0.5422	0.0077	0.6154	0.0094	0.5674	0.0047	0.02613	0.00022	3.364	0.023
147										
148	0.4707	0.0041	0.5498	0.0088	0.5154	0.0067	0.02373	0.00031	2.875	0.019
149										
150	0.7060	0.0089	0.6629	0.0079	0.6242	0.0094	0.02874	0.00043	3.648	0.049
151										
152	0.8681	0.0087	0.7298	0.0091	0.690	0.012	0.03176	0.00057	4.162	0.023
153										
154	0.9094	0.0098	0.7544	0.0058	0.7110	0.0062	0.03274	0.00028	4.147	0.053
155										
156	1.049	0.011	0.776	0.013	0.7505	0.0166	0.03456	0.00076	3.414	0.035
157										
158	1.067	0.014	0.951	0.039	0.861	0.017	0.03966	0.00078	4.822	0.056
159										
160	1.084	0.012	0.8053	0.0092	0.783	0.014	0.03607	0.00063	3.886	0.038
161										
162	1.073	0.018	0.7988	0.013	0.779	0.012	0.03589	0.00054	3.781	0.071
163										
164	1.0197	0.0034	0.7528	0.0045	0.7363	0.0090	0.03390	0.00042	4.494	0.040
165										
166	1.0671	0.0098	0.922	0.022	0.845	0.015	0.03892	0.00069	3.682	0.032
167										
168	1.1676	0.0060	0.843	0.011	0.819	0.011	0.03771	0.00050	3.373	0.048
169										
170	1.2406	0.0098	0.9022	0.0083	0.879	0.013	0.04049	0.00061	3.109	0.030

Depth (cm)	^{232}Th (dpm/g)	$\pm 1\sigma$	^{234}U (dpm/g)	$\pm 1\sigma$	^{238}U	$\pm 1\sigma$	^{235}U (dpm/g)	$\pm 1\sigma$	^{230}Th (dpm/g)	$\pm 1\sigma$
171										
172	1.2455	0.0090	0.923	0.017	0.8968	0.0137	0.04129	0.00063	3.046	0.030
173										
174	1.1825	0.0095	0.860	0.011	0.850	0.010	0.03916	0.00046	3.486	0.034
175										
176	0.9349	0.0099	0.7577	0.0073	0.7246	0.0076	0.03337	0.00035	4.421	0.029
177										
178	0.8840	0.0037	0.7356	0.0054	0.7104	0.0043	0.03271	0.00020	4.153	0.054
179										
180	0.9922	0.0032	0.7480	0.0040	0.7298	0.0073	0.03360	0.00034	4.379	0.019
181										
182	1.0313	0.0094	0.770	0.011	0.749	0.011	0.03448	0.00051	4.811	0.042
183										
184	0.980	0.014	0.7578	0.0099	0.735	0.017	0.03384	0.00078	5.032	0.019
185										
186	0.8890	0.0060	0.7298	0.0091	0.7021	0.0041	0.03233	0.00019	4.564	0.028
187										
188	1.0288	0.0058	0.8005	0.0022	0.7783	0.0069	0.03584	0.00032	5.325	0.018

Depth (cm)	$\delta^{15}N_{DB}$ (‰)	$\pm 1\sigma$	$\delta^{30}Si_{diat}$ (‰)	StdE (‰)	$\delta^{30}Si_{diat}$	StdE (‰)	$\delta^{30}Si_{diat}$	StdE
86	3.83	0.26	1.64	0.08				
87								
88								
89			1.46	0.10				
90	4.52	0.33						
91								
92								
93								
94	5.11	0.22						
95								
96								
97								
98	4.44	0.45						
99								
100	5.14		1.84	0.04	2.01	0.02	1.60	0.11
101								
102	5.84	0.16						
103								
104	5.79	0.22						
105								
106	5.16	0.18						
107								
108	5.78							
109								
110	6.09	0.33						
111								
112	6.30	0.27						
113								
114	6.18	0.25	1.70	0.03				
115	5.91	0.23	1.89	0.15				
116								
117								
118	5.87	0.17						
119								
120	6.21							
121								
122	6.10	0.49	1.53	0.23	1.46	0.04		
123								
124	6.83	0.25	1.19	0.05				
125								
126	6.27	0.30	1.68	0.01	1.32	0.05		

Depth (cm)	$\delta^{15}N_{DB}$ (‰)	$\pm 1\sigma$	$\delta^{30}Si_{diat}$ (‰)	StdE (‰)	$\delta^{30}Si_{diat}$	StdE (‰)	$\delta^{30}Si_{diat}$	StdE
127								
128	6.52	0.25	0.86	0.16				
129								
130	6.49	0.05						
133	6.20	0.34						
134	5.96	0.32						
135								
136	5.87	0.29	1.17	0.17	1.07	0.12	1.14	0.12
137								
138	5.57	0.40	2.07	0.04	2.01	0.05		
139								
140	6.01	0.34	1.57	0.08	1.56	0.12		
141	5.83	0.26	1.80	0.04				
142	6.12	0.12	1.69	0.06				
143								
144	6.74	0.26	1.68	0.05				
145	6.58							
146	6.90	0.20						
147	6.97							
148	6.97		1.67	0.16	1.73	0.09		
149								
150	6.63	0.23						
151								
152	6.89	0.23	1.69	0.13				
153								
154	6.80	0.19						
155								
156	6.90	0.34	1.64	0.17	1.75	0.14	1.69	0.13
157	6.76							
158	6.92	0.24						
159	7.01							
160	7.24		1.12	0.08				
161	6.47	0.32						
162	6.30							
163	5.62							
166	6.90							
172	6.79							
175	6.59	0.44	0.99	0.05				
185	4.35	0.48	0.83	0.06				
200	4.71	0.19						

B.2 MD88-773

Depth (cm)	Opal (%)	$\pm 1\sigma$	Al (g/kg)	Ba (g/kg)	Ca (%)	Fe (g/kg)	Ti (g/kg)	Mn (g/kg)	K (g/kg)
100									
101			3.17	1.15	3.91	2.63	0.32	0.88	2.33
102	76.0	5.1							
103									
104	86.6								
105									
106	88.5								
107									
108	77.5	1.8							
109									
110	92.5								
111									
112	86.5								
113									

Depth (cm)	Opal (%)	$\pm 1\sigma$	Al (g/kg)	Ba (g/kg)	Ca (%)	Fe (g/kg)	Ti (g/kg)	Mn (g/kg)	K (g/kg)
114									
115									
116	88.6								
117									
118									
119									
120									
121									
122	79.2								
123									
124	90.4								
125									
126	88.1								
134	90.4								
144	86.9								
150			3.30	1.42	4.07	2.58	0.32	0.33	2.36
160	88.6								
161									
162	91.1								
163									
164	88.7								
165									
166	90.4								
174	91.7								
180	93.0								
194	86.5								
200	92.2		2.73	1.31	3.39	2.18	0.26	0.10	2.42
204	89.5								
208	78.3								
210	93.5		2.93	1.49	5.31	2.24	0.28	0.12	2.47
216	89.5								
218	80.3								
220	84.2		2.84	1.45	6.04	2.22	0.27	0.15	2.34
222	88.1								
224	84.0								
226	81.5								
230	77.5		3.02	1.46	7.12	2.45	0.28	0.19	2.39
234	77.9								
236	74.5								
238	69.2								
240	63.2		3.30	1.50	7.65	2.80	0.32	0.18	2.43
242	74.7								
244	70.4								
246	71.1								
248	68.0								
250	66.1		5.64	1.25	4.89	5.18	0.62	0.31	3.54
252	58.1								
253	54.0								
254	62.9								
255	60.8								
256	62.1								
257	57.8								
258	65.6								
259	63.9								
260	56.4		4.18	1.64	11.09	3.40	0.43	0.25	2.90
261	59.3								
262	50.9								
263	53.1								
264	52.4								
265	55.5								
266	54.4								
267	59.6								
268	54.8								

Depth (cm)	Opal (%)	$\pm 1\sigma$	Al (g/kg)	Ba (g/kg)	Ca (%)	Fe (g/kg)	Ti (g/kg)	Mn (g/kg)	K (g/kg)
269	55.0								
270	52.1		6.04	2.14	11.64	4.91	0.65	0.36	3.37
271	59.3	1.2							
272	55.0								
273	54.2								
274	56.9								
275	56.4								
276	52.7								
277	51.1								
278	51.4								
279	58.7								
280	61.6		7.24	2.23	12.81	6.02	0.83	0.29	3.61
281	58.7	4.7							
282	58.2	1.7							
283	58.4	6.5							
284	62.1								
285	55.7								
286	52.6								
287	54.7								
288	58.1								
289	58.0								
290	52.8		9.98	2.32	12.49	8.90	1.15	0.33	4.63
291	55.9	2.1							
292	56.6								
293	58.0								
294	54.1	5.7							
295	65.0	8.1							
296	64.0	4.3							
297	71.2								
298	81.7								
299	83.1								
300	77.0		8.17	1.86	4.89	7.02	1.04	0.19	4.82
301	80.9								
302	86.2								
303	88.0								
304	82.5								
305	91.5								
306	84.8								
307	92.2								
308	88.9								
309	88.8								
310	92.3		5.47	1.44	2.86	4.70	0.64	0.11	3.51
311	88.5								
312	82.7	11.1							
313	88.7	8.4							
314	83.8	7.7							
315	90.4								
316	92.4								
317	89.6								
318	90.0								
319	88.3								
320	90.9		5.52	1.35	2.81	4.89	0.66	0.11	3.36
321	90.1								
322	92.0								
323	89.2								
324	85.1								
325	86.5								
326	90.0								
327	83.9								
328	83.6								
329	79.9								
330	79.5		9.36	1.56	5.47	8.82	1.17	0.41	4.54
331	79.6								

Depth (cm)	Opal (%)	$\pm 1\sigma$	Al (g/kg)	Ba (g/kg)	Ca (%)	Fe (g/kg)	Ti (g/kg)	Mn (g/kg)	K (g/kg)
332	78.2								
333	76.5	2.7							
334	79.8								
335	79.2	1.9							
336	77.0								
337	73.5	6.1							
338	63.4	6.8							
339	68.8	5.7							
340	67.1	5.6	10.97	1.54	5.47	10.85	1.38	0.25	5.28
341	68.0	7.6							
342	72.1	7.3							
343	72.3	6.5							
344	68.0	3.3							
345	79.5	2.7							
346	76.2	0.5							
347	78.1	4.9							
348	72.8	5.0							
349	70.1	7.1							
350	72.9	9.9	15.47	1.64	2.12	14.53	1.99	0.28	6.26
351	72.0	6.9							
352	80.3	4.9							
353	73.1	5.9							
354	69.8								
355	72.0								
356	80.3	5.0							
357	76.0								
358	79.7								
359	77.1								
360	78.6		17.19	1.55	1.27	14.77	2.18	0.35	6.45
361	73.5	9.1							
362	74.2	5.3							
363	81.2								
364	78.9	7.5							
365	80.5								
366	78.5								
367	79.1								
368	82.1								
369	72.9	4.6							
370	74.5		20.59	1.66	0.75	22.24	2.62	0.38	7.26
371	71.5								
372	72.6								
373	78.0								
374	77.1								
375	73.5	2.2							
376	73.8	2.0							
377	73.4	3.9							
378	71.7	5.7							
379	74.8	1.0							
380	78.3		22.07	1.55	0.81	19.29	2.96	0.32	7.62
381	76.1	4.8							
382	69.0	8.1							
383	64.5	4.7							
384	69.7	8.6							
385	68.5	8.4							
386	75.9								
387	68.8	3.6							
388	70.5	2.9							
389	71.1	2.0							
390	70.7	7.3	26.44	1.83	0.92	25.43	3.65	0.41	8.73
391	71.6								
392	69.1	3.3							
393	66.7	8.4							
394	70.6	6.7							

Depth (cm)	Opal (%)	$\pm 1\sigma$	Al (g/kg)	Ba (g/kg)	Ca (%)	Fe (g/kg)	Ti (g/kg)	Mn (g/kg)	K (g/kg)
395	71.9	2.0							
396	71.2	5.7							
397	69.8	4.9							
398	75.8	3.5							
399	77.8	4.6							
400	70.5	6.9							
401	73.3		23.18	1.61	0.84	21.89	3.12	0.28	7.56
402	74.4	5.7							
403	79.4								
404	77.0	3.8							
405	81.8								
406	80.0	5.6							
408	82.7	5.1							
410	73.8	4.4							
412	71.7								
414	67.5								
416	67.4	7.2							
418	67.4								
420	75.8	3.0	24.21	1.78	0.88	21.90	3.44	0.31	7.73
422	75.5								
424	70.4								
426	73.5								
428	75.1								
430	77.8	5.0							
432	74.4								
434	77.4								
436	73.1								
438	68.7	7.1							
440	73.5	1.9	20.91	1.50	0.78	24.48	2.85	0.35	7.64
442	78.9								
444	72.6	2.6							
446	82.7								
448	75.5	3.8							
450	69.3								
452	77.1								
454	76.4								
456	66.9								
458	77.4								
460	65.6		23.49	1.64	0.88	23.20	3.21	0.42	7.92
462	77.9								
464	73.5								
466	75.0								
468	77.5								
470	78.6								
472	82.2								
474	79.4								
476	74.0								
478	80.6								
480	81.9		22.98	1.62	0.86	20.54	3.03	0.37	7.59
482	81.5								
484	80.3								
486	79.5								
488	76.2								
490	79.4								
492	79.5								
494	62.1	7.2							
496	73.2								
498	81.5								
499			23.79	1.66	0.92	21.10	3.32	0.36	7.56
500	77.2								
502	76.1								
504	75.8								
506	77.6								

Depth (cm)	Opal (%)	$\pm 1\sigma$	Al (g/kg)	Ba (g/kg)	Ca (%)	Fe (g/kg)	Ti (g/kg)	Mn (g/kg)	K (g/kg)
508	81.7								
510	73.7								
512	80.4								
514	83.1								
516	78.2								
518	65.3								
520	77.1								
522	85.0								
524	81.4								
526	80.4								
528	79.5								
530	70.9	1.4							
532	77.5								
534	70.2								
536	72.2								
538	69.3								
540	72.4								
542	74.1								
544	70.5								
546	78.2	10.2							
548	70.1								
550	77.9								
554	70.4								
558	64.9								
560	76.1								
562	74.0								
566	66.7								
570	70.4								
574	73.9								
578	74.5								
582	75.1								
586	71.9								
590	69.8								
594	75.0								
598	73.1								
599			24.44	1.61	0.89	25.39	3.14	0.65	8.53
602	77.7								
606	76.9								
610	71.5								
614	72.0								
618	77.9								
622	72.6								
626	66.9								
630	76.2								
634	77.9								
638	71.9								
642	74.3								
646	77.7								
650	75.3								
654	75.9								
658	70.4								
662	76.7								
666	74.0								
670	80.5								
674	75.3								
678	73.0								
682	71.9								
686	81.0								
690	80.4								
694	81.5								
698	79.1								
700			19.14	1.52	0.72	16.36	2.48	0.22	6.76

Depth (cm)	Al (xrf counts)	Ca (xrf counts)	Ti (xrf counts)	Mn (xrf counts)	Fe (xrf counts)	Ba (xrf counts)	K (xrf counts)
100	229	50743	335	2766	6259	4216	1863
101	205	52061	488	3451	6595	4951	1821
102	246	55329	613	4007	9390	5337	1780
103	279	57852	547	4153	6483	5041	1768
104	205	44851	531	3267	6100	4302	1490
105	260	52148	719	3646	6446	4895	1707
106	278	52354	793	4829	7695	4954	1754
107	500	54735	513	5273	7197	5358	1681
108	196	56822	233	4647	7174	5937	1856
109	126	35270	376	2242	4713	5113	1206
111	316	26750	178	828	3852	4738	662
112	251	33078	138	811	4629	4359	1362
113	231	40946	271	1026	6229	5245	1604
114	214	35658	505	825	6007	5527	1534
115	279	42016	642	821	5318	5483	1653
116	147	40903	504	977	5264	5575	2031
117	143	42929	512	1021	5378	5780	1747
118	270	42364	767	1374	5201	5281	1630
119	293	41670	762	1728	5256	5626	1589
120	314	50379	770	2423	6112	5894	1784
121	303	51200	646	2337	6352	6588	1743
122	292	51675	732	2711	6826	6033	1748
123	255	48604	621	2281	6385	6182	1625
124	208	55788	708	2214	6825	5972	2192
125	235	58802	1065	2639	6617	6129	1713
126	334	50409	451	2385	6404	6622	1733
127	248	41368	508	2957	5951	6150	1738
128	282	49786	561	3845	6463	6779	1639
129	214	50459	468	3131	7009	6515	1529
130	204	52360	536	3153	5976	6133	1721
131	232	51080	541	3435	5884	5830	1688
132	331	56398	782	2567	6143	5916	1669
133	257	58374	655	1824	6040	5824	1926
134	256	50412	385	1418	6451	5696	1951
135	167	46479	460	1936	7368	5553	1659
136	232	46628	764	1566	7035	5867	1653
137	292	51271	723	1732	6979	6255	1638
138	214	46886	253	1490	6382	6039	1775
139	295	48484	513	1690	7180	6598	1929
140	238	49955	577	2952	7031	6411	1748
141	332	42931	516	2566	6401	6279	1729
142	286	50090	842	1390	6321	6430	1631
143	371	50827	729	1392	6442	6707	1737
144	235	42956	641	1613	6650	6831	1595
145	347	45295	314	1518	6733	6359	1771
146	170	47288	679	1914	6644	6360	1644
147	382	46415	570	1683	6534	6552	1723
148	244	46395	577	1313	6852	6771	1646
149	219	46226	374	1238	6241	5948	1757
150	284	49784	466	997	6297	5624	1700
151	531	50866	632	1220	6220	6037	1952
152	243	49759	598	1477	6161	6704	1507
153	319	48306	595	1883	6421	6324	1564
154	318	45270	1002	2296	7831	6219	1855
155	269	46552	518	2354	6817	6083	1649
156	286	43756	367	2757	6313	5550	1767
157	299	43998	780	3565	6172	4998	1668
158	258	41445	891	2723	9851	5432	1537
159	245	42575	510	2230	5837	5293	1888
160	306	36717	461	1247	5091	5980	1737
161	165	38972	625	1260	5309	5429	1825
162	325	39873	326	5020	5709	5388	1808
163	157	37398	646	6526	6052	5497	1592

Depth (cm)	Al (xrf counts)	Ca (xrf counts)	Ti (xrf counts)	Mn (xrf counts)	Fe (xrf counts)	Ba (xrf counts)	K (xrf counts)
164	307	41831	638	9990	6280	6195	1613
165	312	43297	398	5878	6585	6169	1467
166	294	41218	655	4991	6301	6481	1632
167	436	46546	427	2987	5813	6851	1430
168	346	43243	514	708	6466	6267	1698
169	187	44846	352	614	5941	5877	1336
170	203	44299	427	581	5710	5750	1570
171	269	48291	241	654	6647	6439	1371
172	181	57035	627	694	6553	7220	1537
173	327	55206	783	1435	7732	6883	1774
174	220	53198	654	1811	8240	6390	1339
175	314	46171	661	762	6413	6181	1459
176	325	51619	723	667	6162	5904	1522
177	284	44586	262	852	6556	5888	1530
178	332	46594	867	1752	7180	5747	1732
179	232	41909	749	1156	6167	5589	1537
180	242	46166	489	812	5513	5935	1588
181	219	46163	409	852	5992	5847	1693
182	301	40384	693	849	5663	5944	1331
183	209	34377	494	611	5568	5427	1447
184	202	38684	594	873	5790	5749	1453
185	327	41023	500	963	5201	5583	1654
186	279	41415	842	1037	6039	5604	1729
187	320	38201	568	669	6489	5700	1840
188	281	39519	438	616	6190	5568	1772
189	306	37897	648	869	5562	5410	1785
190	260	41071	641	536	5959	5408	1644
191	228	40435	500	869	4437	5577	1614
192	246	39389	435	614	5311	5263	1537
193	250	31060	283	672	4407	3982	1414
194	270	36606	326	878	5155	4896	1370
195	213	42392	577	741	5649	5587	1528
196	282	52096	526	878	7055	5237	1798
197	294	48769	469	754	5356	5144	1790
198	320	50380	533	1153	6075	5394	1703
199	239	47996	619	1041	6606	5466	1608
200	349	44344	118	911	5408	5255	1765
201	195	47859	296	701	5617	6290	1573
202	325	42496	425	808	5611	5829	1478
203	200	41949	212	980	5366	5240	1568
204	181	40369	548	899	7247	5705	1450
205	471	49370	105	1107	7917	6413	1550
206	233	56706	184	946	7649	6164	1583
207	208	64264	399	675	6726	6148	1594
208	341	61230	447	884	5551	6114	1470
209	245	69732	518	807	5113	5954	1449
210	250	72385	835	945	5362	5390	1380
211	250	58227	382	863	5037	4496	1722
212	321	53376	175	599	4347	5015	1545
213	314	51117	393	689	4908	5360	1354
214	137	47483	187	1013	4092	5287	1616
215	340	47887	356	917	4565	5935	1488
216	246	66616	425	915	5407	6034	1443
217	382	73074	773	873	5606	5467	1546
218	335	54453	659	777	3744	5544	1690
219	395	77982	545	969	4568	6298	1353
220	262	73223	589	843	5138	6071	1421
221	225	84382	652	712	5470	6119	1628
222	234	85734	606	1006	6085	6182	1614
223	338	96948	794	873	6184	6161	1513
224	304	87436	596	1375	5970	6384	1278
225	300	88172	856	1204	6527	6665	1578
226	272	98017	1034	934	7054	6454	1394

Depth (cm)	Al (xrf counts)	Ca (xrf counts)	Ti (xrf counts)	Mn (xrf counts)	Fe (xrf counts)	Ba (xrf counts)	K (xrf counts)
227	150	94317	533	799	6045	6351	1739
228	296	97060	759	783	5760	6268	1530
229	249	90139	822	728	5371	6216	1544
230	290	100045	800	883	5547	5964	1466
231	280	93297	621	917	6328	5611	1356
232	226	73082	337	856	5912	5446	1342
233	347	85517	780	868	6292	5475	1665
234	222	82327	669	991	5344	5864	1589
235	201	77674	559	1061	5373	5516	1563
236	253	80705	645	960	6010	5743	1460
237	392	95854	707	749	6038	6146	1319
238	274	110005	664	1090	6397	5718	1639
239	415	119374	1218	1222	6753	5184	1452
240	207	90485	721	1029	5892	5224	1561
241	246	89253	588	1181	5596	5262	1558
242	414	92578	699	889	6399	4437	1515
243	274	76385	550	602	4141	4849	1484
244	276	67065	394	739	5156	5831	1678
245	271	99564	1000	941	6215	6860	1591
250	363	91081	1049	726	7024	4849	2145
251	311	92630	955	1060	6115	5479	1933
252	246	100613	919	917	7553	6249	2348
253	325	90503	637	1766	7601	6485	1954
254	281	97819	838	1198	7226	6660	2329
255	330	107729	929	1217	8244	6612	1977
256	360	118099	1288	1440	7797	6746	2264
257	412	124284	1079	1261	9418	6599	2036
258	183	114951	1232	925	7564	6198	1943
259	209	114365	1208	870	7262	6570	2216
260	409	116276	1408	1095	7166	7665	1940
261	252	116745	1407	950	9095	7259	2166
262	256	97082	639	797	6365	7660	2190
263	225	115693	1518	901	9872	9162	2080
264	379	133476	1869	1045	10961	9357	2514
265	341	131376	1438	953	10468	8633	1879
266	287	120318	1527	1014	9895	8321	2291
267	185	121398	1704	707	8794	8609	1935
268	361	133987	2066	834	11693	9503	2460
269	245	135093	1820	967	10878	8769	2306
270	346	128801	2051	1141	12512	9582	2253
271	288	140532	1907	1016	11804	9663	2207
272	222	181250	2316	856	11326	8803	2320
273	233	144952	2287	663	12948	9316	2796
274	273	165040	2798	1165	14291	10368	2734
275	351	140743	2128	1252	13710	10147	2781
276	174	125599	1917	965	10642	8154	2459
277	557	102948	2190	896	14216	9605	2789
278	290	139685	2854	936	16669	10048	3140
279	355	112092	2325	924	15083	9260	2822
280	335	126189	2463	1011	16678	11363	3029
281	284	186323	2256	1113	12043	9345	2488
282	317	83929	1277	939	9480	8757	2206
283	539	114400	2426	849	16562	9584	2941
284	322	89458	1835	894	12842	9038	2526
285	367	82116	1530	747	10691	8204	2262
286	342	98076	2255	794	16154	9167	2991
287	271	107744	2222	942	17918	8889	2978
288	333	125824	2888	717	20311	10180	3584
289	332	108171	3127	1456	21932	9934	3692
290	529	110943	2899	898	21884	9682	3801
291	355	111086	2908	989	21730	9641	3632
292	461	106125	2407	989	18457	9070	3201
293	403	90821	2104	834	15167	9706	2592

Depth (cm)	Al (xrf counts)	Ca (xrf counts)	Ti (xrf counts)	Mn (xrf counts)	Fe (xrf counts)	Ba (xrf counts)	K (xrf counts)
294	346	50855	1749	804	17470	7646	3058
295	325	75247	2153	744	15166	6725	2862
296	344	45484	1207	635	12122	6707	2444
297	304	40514	1281	685	12966	6512	2355
298	231	46385	1576	690	16349	6865	3223
299	157	30202	1759	904	14433	6675	2530
300	224	26247	1202	702	11762	5937	2353
301	215	28281	1361	814	13074	6517	2591
302	277	27915	1604	808	13463	6478	2533
303	365	34581	1492	760	15445	6867	2779
304	235	30472	943	847	13156	6911	2512
305	301	30919	1392	597	13046	6097	2638
306	376	26429	1239	903	11412	5341	2254
307	283	26654	779	770	7802	4623	2437
308	261	19125	924	514	7756	4280	2083
309	192	21800	954	683	8924	5600	2309
310	220	27161	1176	752	11296	5009	2366
311	218	31649	1338	512	10651	5723	2417
312	288	38842	1271	876	12395	5956	2553
313	390	26361	1069	876	10697	5695	2213
314	195	20960	947	792	9240	5297	2273
315	307	38314	1272	801	10418	5523	2509
316	234	28124	1044	786	11478	5631	2316
317	174	22776	1072	776	11377	5472	2416
318	361	24954	1125	554	12431	6003	2600
319	184	24333	971	542	11775	4788	2399
320	299	25856	1124	937	12275	5482	2453
321	321	28809	1245	723	13049	5270	2494
322	436	31094	1079	539	11280	5166	2324
323	363	27215	1296	696	12468	5824	2405
324	326	36517	1519	717	15903	5707	2853
325	341	49999	1242	739	16668	6290	2920
326	386	46407	1455	360	17002	6085	2999
327	286	34230	1421	470	13829	6071	2758
328	401	76087	2614	694	22952	6566	3247
329	347	46128	2575	676	21911	5991	3740
330	243	35299	1969	848	19921	6971	3044
331	484	65888	2744	813	27089	7007	4130
332	471	44968	3511	1107	33228	6948	4143
333	284	37908	3401	934	31702	6700	4200
334	459	38365	3183	1126	29551	6656	4176
335	323	46739	2872	620	28407	7303	4108
336	537	46915	2666	1052	26875	6653	3764
337	290	31446	1871	925	18005	5449	3142
338	400	31572	2575	1013	30763	6611	4141
339	359	30905	3069	768	29522	6438	3788
340	270	30728	2467	969	27938	6356	3898
341	420	31461	3067	690	29288	6501	3967
342	283	33631	2448	1117	25956	6025	3691
343	363	27219	2450	776	27712	5741	4013
344	465	30695	3648	1250	35571	5985	4768
345	413	28207	3092	824	31266	6186	4119
346	501	25671	3083	790	33308	6078	4189
347	542	25250	3395	857	40980	6338	4390
348	375	30725	3546	1132	38793	6429	4637
349	571	30725	3724	988	35119	6608	4862
350	560	34165	3563	1159	34524	6470	4719
351	598	40955	3884	963	41947	6217	4904
352	601	31849	3951	1215	49664	6576	5130
353	436	25427	4037	1464	53535	6312	5171
354	637	19920	4592	1330	58636	6017	5859
355	334	19447	4345	1139	49065	6232	4984
356	460	25900	4153	1656	61350	5876	5228

Depth (cm)	Al (xrf counts)	Ca (xrf counts)	Ti (xrf counts)	Mn (xrf counts)	Fe (xrf counts)	Ba (xrf counts)	K (xrf counts)
357	647	15767	4879	899	45492	7121	5450
358	628	13795	4954	1142	44970	6824	5806
359	480	18461	4348	884	39359	5869	5262
360	384	16779	3456	1046	30278	5529	4433
361	545	17798	4869	1096	43949	6876	5534
362	473	9283	3845	842	37487	6512	4656
363	657	13607	5196	1050	46308	6583	5978
364	629	11086	5781	1285	54998	6421	6794
365	672	12175	5545	1167	54982	6716	6280
366	716	10750	5764	1673	58348	6005	6340
367	766	9655	5265	1703	62019	5853	6308
368	460	9200	4636	1169	57276	6548	5262
369	681	9823	5264	923	59963	6945	6353
370	620	10525	5917	1104	58233	6895	6838
371	711	10813	6507	1337	60721	7593	7296
372	617	10442	6031	854	57845	7682	6449
373	717	11922	6923	1229	62038	7364	7464
374	894	11717	7306	1629	69073	7548	7770
375	548	10716	6058	1282	63369	7936	6731
376	639	11627	6772	1402	67223	7943	7295
377	710	11528	7027	1653	66875	7843	7631
378	717	10617	6755	1123	64207	7338	7166
379	717	11313	6856	1278	63111	6425	7519
380	850	12367	7894	1845	66152	7738	7977
381	858	11823	7550	1357	67374	7779	8027
382	678	11592	6832	1320	65673	7543	7143
383	721	11228	6978	1859	77868	6812	7533
384	616	10249	6574	1210	63375	7192	6640
385	539	9047	6202	1255	60548	7476	5418
386	442	10881	6650	1440	62834	7270	6641
387	693	11398	7208	1579	65960	7701	7205
388	502	11454	7159	853	68758	7703	7106
389	386	10590	6681	1506	63687	7236	6081
390	194	9668	6343	1478	61175	6659	5537
391	207	8930	5370	1282	57680	7207	4481
392	319	10037	6316	848	60990	6906	5687
393	412	10340	6239	1014	59847	6449	5792
394	499	12915	5060	1116	59480	5916	5523
395	457	9965	5981	864	66290	5445	5904
396	707	10717	6748	1518	67021	6205	6641
397	585	9000	5301	820	50287	5841	5839
398							
399							
400	686	12056	7092	981	56754	7477	7837
401	750	11869	7371	1346	58838	7067	7756
402	663	11394	7044	722	56073	6937	7311
403	817	11770	7358	1204	64289	6719	7596
404	827	11109	7137	862	65517	6877	7225
405	738	11913	7578	1030	61663	6750	7646
406	699	11670	6956	1189	58422	7225	7509
407	626	11620	7167	1279	60503	6914	7542
408	687	11593	7264	1198	59233	6601	7400
409	812	11519	7255	1197	61870	6690	7445
410	759	12124	7537	1137	62579	7195	7517
411	825	12242	7632	963	63311	7091	7734
412	748	12080	7192	822	60200	7416	7576
413	903	12274	8019	1268	64463	7635	7983
414	770	11134	7296	976	58626	6669	7192
415	820	11358	7033	1053	59717	7941	7431
416	752	10562	6540	990	54672	7368	6608
417	827	12086	7702	1229	59444	7128	7290
418	690	10874	7444	1074	64760	7781	6867
419	850	12257	7744	701	61443	7438	7722

Depth (cm)	Al (xrf counts)	Ca (xrf counts)	Ti (xrf counts)	Mn (xrf counts)	Fe (xrf counts)	Ba (xrf counts)	K (xrf counts)
420	772	11435	7489	1135	59485	7477	7239
421	652	11693	7490	1361	61272	7768	7357
422	857	12137	7465	1072	66537	7604	7514
423	686	11308	7361	1305	60864	8017	7117
424	672	11654	7429	1241	63630	7871	6948
425	638	11570	7714	1131	62660	7648	6830
426	688	11982	7478	973	63943	7718	7238
427	747	12888	7369	806	62841	7501	6989
428	733	11959	7098	929	61180	6779	7179
429	689	10683	6683	724	53008	5896	6606
430	680	10694	6875	1228	51621	6240	6575
431	685	11041	6560	1221	52598	6367	6414
432	689	11080	6858	923	55593	6903	6855
433	870	11093	6595	1305	55322	6779	6779
434	861	10995	6977	922	63016	7147	6768
435	674	11120	7033	1055	68541	7129	7059
436	741	10744	6869	841	60653	6927	7074
437	643	11113	7273	1127	59458	7076	6711
438	602	10888	6523	775	59926	7351	6639
439	622	10838	6955	1120	61721	6817	7191
440	760	10879	7177	807	67288	7392	6880
441	808	10788	6679	1243	65688	7013	6918
442	624	10443	6230	826	54868	6955	6566
443	646	11318	7056	1019	66854	7170	7047
444	656	11677	7461	584	64998	7955	7288
445	728	11715	7222	1064	58034	6966	7223
446	618	10547	5654	953	48635	6683	6488
447	712	11277	7003	992	57454	7066	7044
448	721	11560	7737	1178	63021	7651	7458
449	768	11498	7293	961	60582	7406	7214
450	684	11275	7230	881	60524	7615	7013
451	737	10554	6797	1054	57048	7220	6476
452	660	11213	7129	1136	66697	7057	7137
453	757	11180	7029	1207	65691	6704	7445
454	876	11501	7705	1090	66977	7387	7643
455	732	11451	7256	1250	66884	6843	7381
456	952	11755	7534	1008	70699	7129	7636
457	873	12009	8059	787	65934	7390	7522
458	916	12183	7687	1323	63575	8194	7510
459	821	12303	7731	1123	68248	7631	7990
460	681	11887	7658	1412	66357	7570	7748
461	673	11669	7417	1065	74413	6877	7276
462	789	11824	7289	625	67551	7504	7377
463	852	11664	7373	1753	68370	8230	7615
464	717	10790	6844	914	62809	7341	6988
465	784	11453	6926	1130	63055	7275	7373
466	859	11869	7182	1536	65752	6901	7681
467	747	11530	7291	1186	64552	7641	7462
468	841	11133	6924	1241	75398	6865	7431
469	635	10784	7069	852	73033	7552	7566
470	720	11871	7749	2029	75750	7845	8026
471	837	11486	7782	1438	62928	7674	7628
472	761	10705	6790	1012	66448	6716	7047
473	628	11041	6833	1039	75215	7655	7143
474	580	10472	6260	1015	61646	7284	6588
475	658	10512	6152	991	55292	6638	7148
476	675	10568	6277	1171	51360	6862	6692
477	746	11977	7653	1356	64584	7500	7945
478	861	11605	7412	1141	60448	7978	7718
479	717	11458	7116	1029	59310	7196	7449
480	582	10414	5825	941	51719	6916	6515
481	535	10768	6629	685	57946	7231	7364
482	753	10631	6427	1098	58142	7343	7119

Depth (cm)	Al (xrf counts)	Ca (xrf counts)	Ti (xrf counts)	Mn (xrf counts)	Fe (xrf counts)	Ba (xrf counts)	K (xrf counts)
483	556	10685	6440	1173	63047	7057	6764
484	564	10649	6495	1327	65428	7493	6785
485	667	11072	7070	1553	61982	7412	7064
486	814	11236	7092	1062	62479	7498	7326
487	595	11652	7524	1245	64554	7739	7609
488	690	11250	7310	915	66831	6712	7369
489	596	11021	7246	643	72226	7059	7190
490	796	10681	6933	1086	75322	7049	7281
491	678	10651	6717	1013	66755	6685	7016
492	620	10193	5840	1595	51292	6660	6498
493	636	10080	5859	842	53505	7124	6226
494	782	10603	6579	1083	67797	5481	8607
495	1174	11091	6862	2551	88540	4506	20823
496	1224	12095	6976	2284	86184	6316	19834
497	703	11858	7707	1154	66702	7328	10124
498	655	11925	7336	1190	61747	6427	8140
499	548	10761	6499	1039	59736	7037	6683
500	693	11832	7378	1166	64727	7046	7479
501	746	11256	7041	1241	60101	6828	7101
502	666	11082	6711	1264	63016	6818	7475
503	688	11019	7507	971	65556	7178	7038
504	760	11574	7000	1073	63946	7424	7582
505	648	11499	6901	1161	59051	7496	7466
506	736	11418	7379	926	61230	7587	7338
507	761	12257	7860	1397	64803	7834	7763
508	728	12381	7868	1265	66197	7466	8144
509	706	11604	7721	1386	67514	8059	7328
510	686	11728	6999	1152	66019	7539	7388
511	684	11596	7180	1316	66282	7792	7184
512	717	11409	7068	1324	82209	6991	7323
513	745	11315	7037	1338	78112	7068	7600
514	672	12028	7335	1642	79326	7308	7677
515	496	11043	6803	1054	65084	7847	6698
516	717	11570	7341	927	62161	7235	7465
517	638	11068	6969	724	55148	6183	6868
518	681	10946	6196	1043	53746	6562	6550
519	651	11942	7118	1180	60467	7150	7699
520	668	12147	7805	978	66315	7293	8027
521	647	12216	7453	1228	70398	6927	7958
522	629	11825	7239	1167	64651	7007	7563
523	710	11627	7214	1227	62885	7639	7829
524	777	11816	7203	1437	62143	6915	7698
525	528	11577	6854	1307	62096	6101	7513
526	741	11489	6729	957	59556	6841	7447
527	658	10862	6269	1282	66027	5701	7472
528	711	11370	6753	1361	93998	6159	7734
529	771	10526	6101	1823	67726	6139	7101
530	559	10430	6142	1032	66709	6277	6826
531	709	10274	5878	1139	75687	6364	7000
532	825	11062	6790	787	67359	6048	7404
533	725	11297	7233	1027	62406	6271	7405
534	702	11023	7465	1690	61257	6567	7253
535	829	11354	7331	1628	60789	6306	7440
536	791	11041	6931	1202	56737	5404	7064
537	814	11376	6698	865	58794	6255	6996
538	814	10623	6315	1264	53739	5965	6776
539	594	9821	5402	878	46244	5599	6271
540	752	11575	7186	1016	56436	6197	7352
541	790	11549	7085	1113	58784	6223	7362
542	657	11950	6926	1064	58485	5967	7290
543	658	11311	6404	890	53781	5682	6520
544	595	11064	6720	1277	53423	5685	6550
545	628	11576	6497	1308	57103	5954	6966

Depth (cm)	Al (xrf counts)	Ca (xrf counts)	Ti (xrf counts)	Mn (xrf counts)	Fe (xrf counts)	Ba (xrf counts)	K (xrf counts)
546	460	11033	6572	1259	57146	6767	7125
547	429	10661	6500	1145	62718	7095	7000
548	688	11156	6787	1164	65771	6967	6843
549							
550							
551							
552	823	12748	7043	1038	57921	6479	7753
553	832	12200	6417	1165	52210	7772	7398
554	1312	14915	9825	1056	73320	8561	9620
555	1130	14296	9176	1460	77049	7735	9469
556	1143	13531	8211	1427	72544	7182	8945
557	1055	12229	7161	1132	60560	6954	8242
558	1100	14298	9296	1871	77690	7377	9467
559	965	12768	7937	1634	76709	6664	8688
560	1028	12940	7808	1239	68400	6984	8659
561	1293	13559	8450	1681	75866	6512	9223
562	850	12621	7840	1062	70515	6604	8722
563	1039	12865	7702	1145	67121	6660	8947
564	1000	12987	7454	1311	77892	6762	9129
565	1142	12779	8066	1704	70574	7262	8635
566	996	13427	8682	1496	72951	7270	9083
567	1171	13734	8914	1016	72974	7500	9413
568	1154	13866	8824	1556	74332	7774	9855
569	1334	13880	9165	1216	73118	7475	9664
570	1126	13419	8630	1486	67266	7140	9150
571	1074	13044	8111	1196	71009	6828	9179
572	991	12525	7717	1191	76386	6671	8796
573	875	12227	7474	1261	68700	6839	8465
574	868	11799	6606	1122	61371	6681	8017
575	944	12326	7531	1396	67875	6439	8937
576	1057	12709	7695	1032	74012	7136	9104
577	1039	12334	7355	878	60821	6950	8642
578	1117	13219	8143	1110	64397	7748	8939
579	1040	13202	8120	1476	65934	7161	9229
580	956	12581	7940	1541	66562	6845	8905
581	1091	12381	7777	1126	63846	6631	8468
582	943	13055	8159	1671	63939	6838	9068
583	924	12278	7538	1802	62421	6930	8759
584	1203	13328	8306	1492	79824	6898	9536
585	1102	12471	7879	1572	72238	6753	9125
586	1038	12761	7784	1606	67588	6679	8947
587	1102	12657	7774	925	68161	7350	9179
588	1176	13055	8123	1509	67019	7373	8936
589	1063	12899	8045	1183	65929	6911	8966
590	1134	13205	8213	1071	66557	7457	9165
591	1181	13004	8760	1515	73719	7284	9597
592	1048	13031	7993	832	66201	7117	8780
593	1134	13577	8235	1641	66629	7613	9467
594	1068	12513	7824	1969	63835	7215	8948
595	1105	11591	6546	1136	57187	5877	7991
596	834	10839	5736	1348	48040	5690	7094
597	1020	13022	7768	1573	65267	7208	9293
598	1230	12621	8489	1535	68572	7860	9390
599	1183	12424	7980	1294	70232	7255	9085
600	980	11786	7188	1772	76907	6728	8450
601	1137	11692	7365	1842	73417	7090	8636
602	1119	11915	7023	1328	84253	6864	8889
603	1022	11926	6913	1364	73067	7185	8558
604	885	11372	6799	939	60349	7186	8335
605	864	12119	7319	1006	70439	6998	8985
606	660	9854	5575	974	53433	6951	6380
607	986	11062	6602	1202	59949	6463	7610
608	839	11001	6421	1004	55424	6851	7818

Depth (cm)	Al (xrf counts)	Ca (xrf counts)	Ti (xrf counts)	Mn (xrf counts)	Fe (xrf counts)	Ba (xrf counts)	K (xrf counts)
609	597	10662	5986	986	52067	7463	6967
610	805	10763	6513	1201	55917	7830	7320
611	674	10931	6576	1066	62862	7478	7336
612	852	11496	7440	1515	61859	7416	8113
613	907	11598	6942	1438	59570	8233	8217
614	1033	12247	7725	1750	73376	7006	9005
615	925	12201	7405	1014	68909	7897	8926
616	890	12476	7837	1523	65756	8401	9413
617	1160	12942	8528	1498	67197	8398	9279
618	865	12242	7455	1368	62573	8383	8529
619	1140	13005	8151	1267	66281	7889	9289
620	1132	11775	7613	1445	66097	7474	8623
621	937	11796	7361	1377	64728	7673	8879
622	891	11133	6617	1051	58702	7389	8226
623	942	11776	7169	1271	61018	7341	8479
624	1015	11366	7296	1209	58824	7224	8221
625	725	11454	6864	1252	56964	7218	7764
626	832	11115	6471	1373	59626	7178	7942
627	935	10799	6461	1392	61337	7040	8437
628	910	11304	6344	1411	63217	7248	8255
629	846	11088	6695	1861	62802	7735	8458
630	1015	11220	6910	1380	59097	7486	8098
631	869	11180	7042	1896	62774	7926	8274
632	702	11480	6883	2426	64375	7777	8449
633	823	9866	5941	975	51961	6839	6922
634	908	10311	6174	1032	54836	7774	7511
635	873	10995	6651	1097	56862	7890	8239
636	917	12409	7577	1189	66007	8207	9430
637	1017	11631	7438	1012	63052	8333	8502
638	963	10685	6489	1362	59478	7795	8223
639	875	11034	6722	1395	60478	7667	8189
640	824	11102	6657	1398	62177	7085	8038
641	1014	10128	6770	1906	67668	7619	8248
642	850	10862	6436	1132	62305	7175	7728
643	704	10601	6857	1073	62002	8140	7792
644	803	10831	6619	1370	62916	7394	8129
645	702	9949	6261	1342	58605	7527	7266
646	807	10285	6270	1508	66663	6876	7697
647	820	10378	6117	1136	61573	6873	8002
648	1071	10736	6487	1644	59599	7356	7858
649	1016	10844	6743	1679	60622	7278	8208
650	813	10364	6309	944	57685	7584	7603
651	728	9588	5955	975	54645	6663	7136
652	554	9521	5440	1525	60283	7087	6751
653	755	10439	6121	1210	59330	7341	8088
654	956	11554	6883	1456	61601	7484	8809
655	894	11255	6903	1786	63063	7404	8548
656	1164	12266	7545	1601	65441	7151	9438
657	968	11425	7032	1288	62934	7279	8759
658	853	11556	7098	1280	62301	6942	8635
659	1045	11495	6848	1581	61622	6402	8706
660	975	11432	6577	1350	61115	7151	8686
661	1166	11928	7323	1056	62181	7322	9012
662	1228	11346	7174	1369	62190	6731	8918
663	895	11032	6278	1479	61680	6651	8598
664	777	10685	6011	1694	72727	5999	8382
665	810	10925	5874	1730	77572	6176	8368
666	1048	11087	6620	1526	76718	6390	8493
667	1065	10821	6976	1673	68392	7051	8833
668	917	11046	6498	1019	64239	6487	8467
669	848	11069	6502	1366	57991	6279	8178
670	948	10788	6903	1150	55968	7028	8360
671	1190	11822	7274	1156	60197	7122	8704

Depth (cm)	Al (xrf counts)	Ca (xrf counts)	Ti (xrf counts)	Mn (xrf counts)	Fe (xrf counts)	Ba (xrf counts)	K (xrf counts)
672	1070	11687	7638	1405	61014	7192	8880
673	891	11511	7122	921	58632	6852	8381
674	997	10944	7282	1189	61581	6407	8370
675	890	11388	6814	996	58017	6525	8419
676	1102	10966	6768	1319	60134	7073	8433
677	978	10456	6359	1525	63882	6794	7872
678	886	11399	7275	1327	63784	6747	8566
679	911	10619	6347	862	56061	6219	7855
680	961	11034	6892	964	57275	6183	8469
681	1047	10970	6897	812	59405	6583	8193
682	956	11451	6832	1265	59835	6535	8719
683	902	10812	6530	1785	63194	5989	8162
684	792	10160	5623	1945	76814	5371	7823
685	816	10265	6149	1945	64348	5811	7828
686	918	10659	6462	1167	52874	6201	7764
687	777	10479	5977	1145	50580	6317	7768
688	912	10944	6256	974	53102	6539	7929
689	1035	10678	6654	1024	54346	6516	7742
690	934	10202	5985	1152	52473	5649	7258
691	953	10440	6092	1151	55578	6023	7348
692	806	10116	6188	1008	53649	5873	7297
693	926	9686	5902	734	50163	5569	7051
694	795	10248	5835	773	50216	5942	6899
695	812	9594	5069	981	47058	5556	6632
696	711	9150	5215	1083	46345	5514	6695
697	851	10078	6266	1367	53657	6275	7140
698	760	9846	5580	1130	52862	6041	6643
699	535	9179	4732	1020	45363	6130	5810
700	930	12179	5735	1136	50099	7158	7533
701	666	10123	5143	1168	48781	6864	6452
702	618	9685	5428	899	43858	6792	6453
703	779	9454	4996	858	43607	6869	5943
704	852	10017	6154	1043	48905	6743	6504
705	946	10140	5857	835	45561	6506	6176
706	799	9302	4742	1481	42664	6585	6095
707	917	9754	5508	978	44299	6089	6182
708	802	9783	5243	1474	49867	6160	6444
709	704	9324	5141	1025	47462	6491	6116
710	687	9614	4976	1039	45138	6073	6122
711	736	9460	5447	1551	51726	5919	6399
712	609	9298	4810	1308	47040	5972	6024
713	702	9325	4802	1731	59970	5825	6245
714	675	9185	5128	928	45154	6566	5780
715	657	8615	4332	917	38705	6476	5179
716	634	9479	4964	727	42380	6671	5802
717	765	9764	5652	843	46731	6480	6224
718	814	9386	5207	890	40767	5760	5805
719	641	8948	5021	957	40579	6546	5736
720	845	9581	5634	1189	44039	6542	6572
721	641	9966	5362	1027	46936	5869	6630
722	737	9109	4465	670	41246	5472	5862
723	669	8969	4504	864	41467	5584	5431
724	776	9802	5337	1193	45779	6366	6278
725	696	9514	5122	850	44660	6659	6065
726	780	9294	5194	975	47943	6433	6154
727	664	9700	5333	1194	44265	6330	6181
728	659	9765	5467	1043	50635	6075	6435
729	483	8735	4651	910	46395	5863	5746
730	571	8176	4435	1517	59589	5393	5604
731	641	8968	4514	936	41504	6498	5744
732	738	9039	4971	668	39377	6336	6206
733	748	9609	5162	872	41227	6275	6382
734	668	9258	5052	984	42165	6086	5910

Depth (cm)	Al (xrf counts)	Ca (xrf counts)	Ti (xrf counts)	Mn (xrf counts)	Fe (xrf counts)	Ba (xrf counts)	K (xrf counts)
735	624	14689	4741	1086	41230	6335	5913
736	663	9419	5044	979	41725	7003	5837
737	693	8966	4996	1909	41208	6706	5879
738	665	9470	5175	6065	41600	6936	5898
739	552	9020	4254	2951	40754	5364	5798
740	813	9539	5891	1085	50099	6914	6473
741	729	8953	5145	999	42347	6812	5889
742	697	8486	4754	771	41154	7041	5861
743	713	9197	5196	874	43034	6821	6313
744	714	9373	5105	853	41839	6563	6121
745	723	8717	4873	713	39818	6249	5788
746	533	9119	4465	1127	43891	6621	5911
747	585	9122	4874	1214	45602	6677	5810
748	737	8391	4189	625	38205	6634	5392
749	735	8139	4453	886	34654	6809	5398
750	659	8832	4378	572	36426	6536	5442
751	636	8039	4455	627	36987	6799	5436
752	754	8998	5178	846	42570	6614	6113
753	730	10051	4943	800	41029	7140	6370
754	743	9124	4999	902	41368	6440	5883
755	829	8684	4908	665	38096	6772	5652
756	763	8445	4272	927	35230	6354	5479
757	825	8175	4425	908	35677	6721	5427
758	788	8098	4080	788	32864	6100	5859
759	500	7758	3912	768	33618	6167	5216
760	579	8136	4197	1006	35009	6205	5200
761	573	7759	3966	1152	36350	6516	5642
762	550	7960	4375	1212	41927	6810	5553
763	646	8013	4239	1401	45918	6122	5600
764	494	8749	4590	1541	44296	6463	6183
765	642	8066	4218	1266	41443	6644	5832
766	877	8938	4939	1286	46396	6310	6263
767	707	8671	4394	812	38837	6372	5986
768	591	7781	3605	1063	33167	5789	4954
769	613	8460	4452	963	38397	5900	5753
770	650	8590	4616	746	38783	6056	5852
771	487	8254	3680	914	32334	5706	5553
772	681	8596	4179	993	36511	6900	5242
773	615	8207	4136	745	37178	6408	5418
774	582	8555	3978	797	36872	6429	5463
775	579	8307	4609	972	40509	6349	5792
776	638	8746	4276	1048	48740	5816	6075
777	612	8599	4484	905	47417	6212	6371
778	563	8468	3980	824	37439	5972	5562
779	427	7943	3812	879	34086	5711	5020
780	588	8676	4102	984	39888	6038	5110
781	612	7997	4042	673	34259	6469	5250
782	515	8366	3982	551	35147	6559	5460
783	648	8269	4663	570	37287	6411	5693
784	580	8272	4180	971	34683	5512	5562
785	560	7861	3720	965	32520	5816	5340
786	605	7601	4156	842	34438	6458	5042
787	552	7343	3652	1111	32001	6301	4714
788	541	7533	3608	624	34061	6298	4929
789	541	7389	3675	1111	32864	6196	5161
790	611	7185	3200	784	28939	6014	4762
791	513	7095	3589	937	30049	5939	4743
792	467	6825	3211	1145	29339	5702	4302
793	519	6373	2906	802	29621	5412	4176
794	446	6618	3182	802	30350	4496	4409
795	512	6380	2267	1130	26992	4578	4126
796	453	6188	2517	1196	31616	5165	4213
797	381	5922	2782	1145	29350	4761	4203

Depth (cm)	Al (xrf counts)	Ca (xrf counts)	Ti (xrf counts)	Mn (xrf counts)	Fe (xrf counts)	Ba (xrf counts)	K (xrf counts)
798	586	6433	3257	543	28558	5581	4507
799	524	6650	2885	2225	26805	5538	4260
800	489	6295	3084	881	27585	4744	4299
801	495	6465	2762	910	25994	5317	4137
802	481	6161	2544	933	23467	5375	4175
803	383	6180	2843	830	23504	5831	3798
804	522	5857	2157	1295	23334	5379	3817
805	461	5613	2080	906	23181	5421	3810
806	513	5972	2363	947	23893	5278	4125
807	430	5934	2545	1385	26004	5531	4349
808	346	6755	2855	776	24241	5689	4271
809	445	6944	2658	594	23031	5719	4554
810	493	6668	2869	894	23274	5909	4254
811	220	6882	2512	1253	23998	6017	4175
812	415	6985	2905	674	27940	6315	4206
813	405	6641	2570	917	26689	6094	4178
814	387	7882	3639	1159	33582	6416	5207
815	404	8113	3947	1187	35535	6189	5411
816	438	7510	3412	1402	32611	6077	4768
817	612	7732	4216	1057	37116	6326	5752
818	554	7605	2845	767	25969	4924	4603
819	500	7811	2914	981	28269	5977	4760
820	407	7101	2809	1724	38566	5301	5233
821	544	6972	3313	745	30482	6391	4896
822	515	9192	3855	1022	37071	6420	5449
823	520	14321	3453	1031	32867	6614	5057
824	670	11961	3768	817	33288	5979	5590
825	595	8350	3870	961	34550	6201	5348
826	753	8246	4314	775	40956	6858	6095
827	575	11007	4034	1285	35338	5603	5535
828	571	15525	3188	885	28552	6063	4883
829	529	16018	3553	1097	30031	5687	5084
830	523	14268	3537	859	33253	6362	5494
831	587	9988	4627	1076	41158	6568	6381
832	656	9197	4684	904	36142	5778	5904
833	688	9237	4011	964	34824	5662	5641
834	561	7917	3814	780	32397	5477	5217
835	678	9672	4061	844	38079	6389	5834
836	573	9359	4524	963	38673	6134	5573
837	799	8917	4845	825	42322	6324	6248
838	549	9747	4903	974	42218	6754	6456
839	720	10973	5012	1239	43171	6217	6271
840	706	10348	4679	1041	39397	6166	5612
841	745	8792	5116	1784	46324	5885	6005
842	840	8617	4959	2249	50810	5709	6148
843	568	8444	4413	3030	45506	5226	5577
844	446	8152	4120	1079	39434	5612	5092
845	330	7062	2886	997	30422	5370	4005
846	543	11941	3832	706	36224	5688	5165
847	626	15111	4690	753	40171	6240	5742
848	496	10314	3986	1011	39774	6167	5795
849	517	8258	3954	1093	36516	5559	4729
850	797	10095	4617	1168	44738	5383	6279
851	650	10362	5437	1296	47012	6246	6302
852	786	9675	5145	1404	47319	6665	6693
853	725	9794	5573	2143	51929	6554	6504
854	810	10175	5430	1696	52416	6153	6890
855	841	10092	4808	1303	45359	5678	6202
856	796	12174	5153	918	43557	5724	5933
857	650	13603	5008	1336	46917	6734	6617
858	873	10301	5605	1504	58341	5838	6821
859	902	10240	5368	1059	51473	5850	7038
860	740	9298	4823	918	41837	6066	6207

Depth (cm)	Al (xrf counts)	Ca (xrf counts)	Ti (xrf counts)	Mn (xrf counts)	Fe (xrf counts)	Ba (xrf counts)	K (xrf counts)
861	846	9759	5273	1135	44967	6315	6474
862	756	9539	5567	1440	45574	6857	6489
863	798	9042	4633	1380	49233	6231	6242
864	829	9231	5046	1202	47317	5655	6661
865	751	9633	4768	1090	40462	5881	6188
866	709	9284	5140	932	43253	6356	5879
867	834	9446	5465	1013	43420	5957	6318
868	818	8823	4934	1164	40549	5847	6421
869	654	9525	4774	1236	42217	6286	6262
870	700	9620	5430	1488	44832	6620	6589
871	689	9204	4995	1176	41378	5743	6351
872	933	9037	5117	1583	47569	6364	6459
873	773	9589	5312	1734	49762	6671	6830
874	751	9448	5522	1708	48047	6551	6852
875	837	9662	5351	1536	45915	6431	6783
876	844	9241	5231	1149	48713	6296	7015
877	851	9958	5825	1998	57347	5885	7623
878	702	9139	4873	1629	54115	5031	6748
879	769	8393	4398	941	40251	5253	6138
880	749	8442	4377	1070	40207	5320	5794
881	844	9193	5352	1315	47844	6076	6806
882	855	9031	4878	823	45435	6080	6442
883	751	8801	4400	1221	40088	5867	6161
884	763	9521	5132	1248	47409	6096	6978
885	712	8897	5127	1104	51251	5796	6818
886	999	9102	5445	1586	51261	6292	6849
887	851	9037	5215	806	45821	6313	6939
888	848	9303	5057	1091	41939	6413	6657
889	1005	9391	5693	1189	46170	6507	7474
890	914	9452	5781	1036	43967	6851	7137
891	914	9734	5319	780	44459	6008	7392
892	832	8647	4957	1076	42939	6298	6822
893	779	8551	4767	1236	42535	6309	6531
894	915	9193	5128	726	44059	6897	7143
895	1035	9795	5900	839	48486	6464	7304
896	878	9142	5145	1508	43197	6619	6714
897	859	9046	5010	1618	45573	6529	7219
898	780	9073	5631	1814	54170	5580	7477
899	761	8634	4979	2360	54535	5908	6865
900	874	9184	5040	1407	47661	5981	6674
901	699	9085	5085	1272	45616	5752	7273
902	730	8834	4593	1496	45609	6562	6884
903	819	9287	5324	1268	45845	6916	7068
904	969	8990	5045	1342	44388	6053	6786
905	821	8687	5089	1324	43803	6622	6851
906	909	9107	5358	1021	48082	6709	7521
907	986	8874	5351	1056	47580	6354	7099
908	744	8405	4926	1077	43881	6146	6776
909	733	8321	4418	1192	40231	5854	6469
910	809	9830	4292	936	37209	5211	6081
911	827	10074	4364	912	38594	6165	6662
912	792	9065	4161	1168	35354	6016	5895
913	679	8164	4393	958	36573	6222	5833
914	739	8193	4505	808	37592	6003	6064
915	630	8160	4381	1073	37442	5691	6424
916	765	8039	4372	1039	39256	6185	6375
917	835	7962	4605	743	45832	5792	6510
918	667	8098	4127	1016	36814	6814	5801
919	662	8023	4105	787	39629	6144	6042
920	751	7805	4572	992	39907	6183	6254
921	873	8822	4740	798	38903	5837	6527
922	856	8386	4645	733	36723	6267	6640
923	594	8250	4528	1012	36250	6175	6548

Depth (cm)	Al (xrf counts)	Ca (xrf counts)	Ti (xrf counts)	Mn (xrf counts)	Fe (xrf counts)	Ba (xrf counts)	K (xrf counts)
924	768	8387	4700	1131	37995	6535	6582
925	740	8109	4685	1372	35886	5965	6448
926	905	7882	4343	1698	37255	6164	6602
927	910	7943	4508	1057	37460	5926	6517
928	918	7591	4197	728	37040	6219	6580
929	847	7682	4257	1184	39043	6195	6633
930	767	7283	4034	1356	38537	6160	6417
931	899	8129	4639	1190	44137	6019	7224
932	840	7927	4319	1192	46126	5638	6939
933	916	7838	4482	1121	40967	5920	6748
934	904	8132	4376	835	38887	6142	6827
935	751	8240	4154	1159	39497	6202	6505
936	849	7896	4327	1252	38032	6276	6815
937	701	7968	4298	1256	40064	6514	6540
938	823	8098	4712	1888	49798	6938	7034
939	917	8380	4914	1370	46895	7181	6934
940	744	8154	4432	1108	41706	6355	7023
941	735	7899	4362	1008	37735	6336	6547
942	769	7430	4219	1877	43393	6092	6484
943	695	8116	4192	1991	47039	6150	6614
944	814	8161	4663	938	41787	6437	7362
945	791	7719	4364	788	39115	6868	6714
946	720	7845	4056	735	36855	6071	6361
947	669	7067	3624	750	32624	4727	5561
948	757	7476	4197	1098	44031	6313	6179
949	739	7780	3996	1013	56775	6043	6832
950	699	7850	4658	915	42555	5825	6507
951	804	7884	4337	1144	50705	5838	6284
952	733	7688	4293	1338	43588	5916	6812
953	768	7602	3846	798	35470	6577	6295
954	755	7741	4419	918	36432	6751	6639
955	750	8031	4551	1136	37674	6612	6568
956	897	8208	4604	939	39137	6403	6986
957	795	8236	4784	961	39520	7201	7032
958	854	8077	4715	947	39985	6358	6567
959	731	7991	4242	896	37467	6315	6911
960	718	7805	4236	539	36519	6344	6539
961	753	7651	4104	1065	34510	5843	6301
962	965	7215	4150	826	33558	5662	5802
963	760	7617	4367	1061	34838	5609	6130
964	781	7179	4037	841	34614	5533	6182
965	780	7524	4089	1132	34875	5710	6400
966	622	6775	3526	855	33465	5720	5756
967	751	7205	3950	796	31755	5977	5442
968	546	6473	3216	949	27553	5624	5262
969	754	6312	3143	1018	28325	5625	5288
970	690	6635	3141	1099	27020	5454	5156
971	739	6443	3293	761	29524	5347	5408
972	614	6321	3620	679	30141	5519	5660
973	821	6293	3273	793	29382	5403	5311
974	653	6339	2698	1040	30953	4621	5458
975	552	5683	2067	600	21926	3948	4621
976	559	5855	2154	734	22604	4582	4530
977	550	6453	3078	961	26316	4922	5146
978	641	5947	2848	920	25162	5323	4673
979	558	6013	2913	985	25123	5783	4829
980	521	6110	2866	903	26620	5054	5188
981	651	5974	2699	820	24682	5367	4920
982	611	6158	2655	689	24050	5036	5003
983	552	5941	2613	834	24659	5160	4958
984	535	5722	2346	900	24355	4912	4698
985	524	5888	2599	776	22586	4949	4534
986	609	5521	2273	732	20068	4297	4064

Depth (cm)	Al (xrf counts)	Ca (xrf counts)	Ti (xrf counts)	Mn (xrf counts)	Fe (xrf counts)	Ba (xrf counts)	K (xrf counts)
987	498	5518	2398	694	20671	4740	4599
988	538	5677	2401	670	20897	4799	4268
989	529	5591	2387	1138	21137	5151	4179
990	609	5810	2259	1067	21513	4510	4628
991	439	5177	2321	760	18749	4231	3810
992	459	5751	2605	733	20976	4697	4348
993	560	6088	2805	848	23561	5826	4484
994	616	6476	2515	960	25027	5411	4956
995	423	6911	2925	858	27700	5874	4954
996	505	6572	2401	528	21008	4879	4376
997	399	6865	2491	1068	23769	5195	4712
998	570	7657	2781	1045	26973	5686	5552
999							
1000	796	8237	3530	895	33636	6975	5973
1001	700	7224	3787	1162	34225	6703	5296
1002	567	7195	3519	1403	37820	6368	5224
1003	552	6943	3410	2256	40372	6202	5291
1004	540	8167	3634	834	33441	6399	5237
1005	787	8611	4593	1344	44187	6595	6192
1006	612	7566	4060	1083	42088	6358	6075
1007	697	8269	4454	1228	42031	6648	6504
1008	635	10252	4473	1080	39254	6720	5961
1009	651	8372	4088	1256	40484	6268	5683
1010	655	8262	4109	1386	41228	6591	5887
1011	710	8264	3824	1002	38954	6661	6126
1012	612	7829	3874	1100	36206	6584	5838
1013	684	7905	4365	1342	41570	6637	5999
1014	710	8485	4595	1089	39765	6873	6358
1015	629	11401	4082	1490	42451	6812	6185
1016	772	8796	4782	1664	50891	6928	6636
1017	723	8663	4968	2013	52696	6780	6814
1018	832	8247	4514	1223	41136	6543	6596
1019	815	8298	4526	958	38956	6478	6317
1020	809	8177	4929	1128	39981	6186	6456
1021	670	8577	4591	908	39133	6282	6360
1022	745	8823	4696	1244	46328	6499	6910
1023	708	8734	5115	1066	41981	6969	6644
1024	692	8410	4531	1066	41575	6586	6671
1025	701	8806	4869	985	41386	6602	6616
1026	657	8835	5590	1350	47482	6942	7142
1027	888	8652	5247	1118	45249	6934	7119
1028	679	8286	5045	1066	43002	7054	6567
1029	850	8693	5023	1051	44872	6960	6747
1030	770	8562	4578	1250	44081	7109	6961
1031	714	8673	4843	897	43902	7150	7120
1032	653	8043	4970	1053	42028	6858	6718
1033	563	8168	4579	1106	38207	6468	6397
1034	688	8078	4669	926	37714	6570	6492
1035	634	7681	4260	1022	38194	6336	5931
1036	761	7990	4297	1437	38656	6319	6428
1037	677	7753	4613	1191	39538	7166	6468
1038	602	7484	4318	2049	51120	5918	6482
1039	687	7633	4062	1226	36669	6341	5832
1040	708	7222	4134	1814	46589	6652	6153
1041	811	7859	4460	1176	41718	6701	6107
1042	717	8499	4907	861	40500	7288	6978
1043	823	8010	4988	853	41753	6683	6852
1044	740	7896	4416	1193	39384	6369	6473
1045	713	7486	3900	925	42930	6579	6157
1046	695	7860	4231	998	37095	7019	6272
1047	650	7087	4207	1057	34934	6876	5909
1048	808	7804	4651	1074	38182	7015	6106
1049	690	7479	4076	1144	34994	6730	6155

Depth (cm)	Al (xrf counts)	Ca (xrf counts)	Ti (xrf counts)	Mn (xrf counts)	Fe (xrf counts)	Ba (xrf counts)	K (xrf counts)
1050	728	7038	4144	846	34695	6728	5822
1051	631	7440	3756	496	31876	6326	5784
1052	647	6808	3672	939	31364	6758	5514
1053	704	7036	3401	1071	30385	6668	5360
1054	669	6769	3650	894	30159	6765	5339
1055	672	6998	3588	834	30899	6618	5968
1056	637	6883	3332	1010	32479	6629	5343
1057	497	6531	3170	1218	41089	6315	5067
1058	606	5738	2608	1420	30703	6338	4628
1059	707	5963	2737	1010	27418	6453	4552
1060	704	5497	2947	970	27153	6251	4357
1061	589	6087	2871	730	25638	6104	4379
1062	545	6623	3523	1065	27798	6246	4894
1063	627	5909	2540	2094	23368	5561	4496
1064	532	5472	2464	1131	25580	5671	4322
1065	475	5541	2479	1006	22030	6124	4359
1066	563	5698	2005	752	20327	5400	4250
1067	508	5416	2442	832	19896	5619	3953
1068	491	5271	2380	688	19529	5979	3966
1069	508	5383	2286	495	19714	6123	3872
1070	512	5254	2056	789	18953	5771	4068
1071	470	5641	1910	951	20993	5278	4250
1072	407	5544	1954	1200	22561	5612	4136
1073	421	5802	2350	781	21982	5776	4414
1074	443	5922	2380	854	20091	6042	4137
1075	523	5364	2165	786	18520	5652	3735
1076	515	4788	1976	922	17685	5391	3588
1077	371	5394	1962	1059	18092	5582	3761
1078	517	5944	1847	1055	19634	5783	3922
1079	468	6052	1778	731	17750	5579	3809
1080	439	5693	2092	947	17001	5233	3418
1081	447	7236	1738	967	17017	5015	3513
1082	464	6945	1785	615	17139	4989	3409
1083	407	5784	1881	793	17389	5839	3145
1084	294	5584	2038	718	17469	5723	3584
1085	492	6032	2272	1076	19935	5635	3792
1086	486	7567	1788	764	18682	5463	3895
1087	408	7462	1765	792	15963	5404	3667
1088	534	7915	1920	754	18703	5987	3548
1089	515	9191	2108	1105	18982	5766	3807
1090	482	10731	1867	820	18567	6231	3859
1091	494	9710	1930	880	19745	5686	3543
1092	471	9802	1802	951	18976	4942	3695
1093	400	12446	1610	719	15794	5855	3453
1094	366	15171	2194	901	19528	5975	3862
1095	432	16187	2159	780	17996	5576	3424
1096	358	16884	2148	903	17868	5791	3598
1097	473	13620	2120	1058	17954	5702	3883
1098	479	15696	2178	1086	18202	5264	3625
1099	360	12750	1667	913	16897	5703	3270
1100	503	13250	2111	1250	19136	6184	3545
1101	527	11153	1864	1169	19864	5566	3457
1102	315	10897	1803	1467	21386	4917	3328
1103	477	12309	1972	1735	25440	5624	4090
1104	427	12114	1509	1021	21512	4246	3553
1105	269	20379	1658	1452	21821	5608	3430
1106	467	14824	2407	1367	29573	5602	4130
1107	505	12789	2744	1253	28475	5903	4425
1108	595	11629	2935	891	27831	6061	4544
1109	597	11066	2428	1064	24413	6154	4512
1110	510	12050	2716	842	23094	5180	4341
1111	499	10974	2698	720	24257	6182	4328
1112	525	9139	3372	1340	27878	5667	4646

Depth (cm)	Al (xrf counts)	Ca (xrf counts)	Ti (xrf counts)	Mn (xrf counts)	Fe (xrf counts)	Ba (xrf counts)	K (xrf counts)
1113	649	8939	2858	769	25829	5715	4672
1114	680	9122	3179	882	28396	6333	4815
1115	463	9043	2786	1149	25889	6232	4708
1116	466	10493	2724	926	28999	6174	4781
1117	603	9324	3080	1011	30127	6530	5191
1118	550	8870	3149	1595	28876	6615	5082
1119	790	9789	3872	1234	34905	6426	5547
1120	715	10075	3270	1505	32403	6377	5050
1121	651	8382	3431	1244	33475	6559	5219
1122	474	8828	3415	868	33722	6228	5597
1123	663	7764	3652	1323	36561	7125	5564
1124	586	7890	3942	1508	37789	6414	5750
1125	624	10413	3493	842	32582	6831	5391
1126	639	10980	3881	1158	34669	6870	5766
1127	549	10932	3859	1181	33395	6914	5730
1128	698	9921	4179	1163	35213	6275	5777
1129	608	9199	3967	1195	33621	7003	5936
1130	734	8586	3789	1012	37013	7343	6102
1131	805	8487	4210	943	39238	7489	6251
1132	637	8439	4001	1143	39834	6557	6336
1133	630	9297	4100	1202	37093	6292	6380
1134	774	10663	4109	1073	36644	6831	6276
1135	754	10578	4112	1101	36153	6887	6234
1136	670	9302	3970	1182	36297	7062	5965
1137	828	9902	3928	1255	34348	6318	5798
1138	575	9857	3640	1766	31248	6748	5466
1139	575	9824	3304	1263	31781	6086	5300
1140	565	10490	3291	804	31652	7082	5306
1141	473	10349	3355	1208	29662	6532	4798
1142	640	11647	3013	875	28877	6911	4903
1143	667	13277	3127	926	29475	6801	4944
1144	413	14169	2924	1483	27148	6803	4786
1145	539	14222	3044	635	27615	6265	5010
1146	537	15466	3020	843	26017	6165	4838
1147	567	15086	2722	1016	23438	6183	4701
1148	455	12393	2216	1003	21067	5462	3874

Depth (cm)	$\delta^{15}N_{DB}$ (‰)	$\pm 1\sigma$	$\delta^{30}Si_{diat}$ (‰)	StdE	$\delta^{30}Si_{diat}$ (‰)	StdE	$\delta^{30}Si_{diat}$ (‰)	StdE	$\delta^{30}Si_{diat}$ (‰)	StdE
150	3.11	0.31	1.50	0.08	1.66	0.10	1.63	0.03		
160			1.57	0.03						
170					1.68	0.02				
188	3.62									
190	3.18	0.08	1.66	0.04						
200	4.07	0.23	1.54	0.05	1.55	0.05				
212	5.23	0.71	1.77	0.05	1.59	0.08				
224	5.01	0.50								
234	4.43	0.63	1.40	0.04	1.58	0.03				
236			1.52	0.12						
240	4.65		1.39	0.07	1.59	0.04	1.56	0.07		
248	5.21	0.17	1.37	0.05	1.56	0.09				
260			1.31	0.03						
262	4.42	0.24	1.52	0.02						
264	5.53	0.21								
268	5.76									
272	5.45	0.11	1.31	0.09						
278	5.33	0.42								
280	5.93	0.31								
284	5.07	0.23	1.47	0.06						
288	6.50	0.15	1.27	0.06	1.31	0.06				
292	7.51	0.27	1.62	0.04						
294	5.66	0.71	1.59	0.06						

Depth (cm)	$\delta^{15}N_{DB}$ (‰)	$\pm 1\sigma$	$\delta^{30}Si_{diat}$ (‰)	StdE	$\delta^{30}Si_{diat}$ (‰)	StdE	$\delta^{30}Si_{diat}$ (‰)	StdE	$\delta^{30}Si_{diat}$ (‰)	StdE
296	6.34	0.23								
300	6.65	0.73	1.86	0.07						
302	5.42	0.40	1.82	0.05						
304	6.35	0.62								
308	6.73	0.59	1.10	0.06	1.20	0.04	1.20	0.01		
312	6.01	0.42								
316	5.43	0.21	1.53	0.02	1.36	0.03				
322	5.75	0.04	1.14	0.06	1.01	0.04				
324	6.61	0.40								
326	5.49	0.52	0.99	0.09						
328	5.04	0.36								
332	5.41	0.38	1.21	0.03	1.14	0.02	1.18	0.10	1.26	0.04
336	5.01	0.22	1.68	0.05						
340	5.81									
344	6.00	0.33	1.64	0.10						
348			1.60	0.04						
352	6.28	0.45	1.97	0.04						
356	6.64	0.41	1.68	0.06						
360	6.92	0.40	1.83	0.07	1.66	0.01	1.94	0.09		
364	7.56		1.18	0.07						
368			1.43	0.07						
372	7.96	0.42	1.14	0.06	1.29	0.07				
376	6.91	0.15	1.45	0.04						
380	7.25	0.40								
390	6.42	0.11	1.00	0.05	1.31	0.03	1.16	0.10		
400			1.64	0.06						
420	5.53	0.19	1.22	0.02	1.20	0.10	1.19	0.08		
460	5.51	0.15	1.30	0.04						
500	5.25	0.20	1.44	0.05	1.24	0.05				
540	5.88	0.13	0.82	0.04						
600	6.19	0.36	1.05	0.04						
650	6.13	0.44	1.45	0.05						
700	5.42	0.58								

B.3 MD88-772

Depth (cm) (cm)	Opal (%)	$\pm 1\sigma$	Al (g/kg)	Ba (g/kg)	Ca (%)	Fe (g/kg)	Ti (g/kg)	Mn (g/kg)	K (g/kg)
4	35.0								
5	22.1		4.48	1.41	24.26	3.36	0.32	0.21	1.91
6	25.7								
7	34.8								
8	38.8								
9	21.3								
10	29.7		4.65	1.40	25.34	3.35	0.31	0.20	1.99
11	33.0								
12	27.7								
13	32.6								
14	17.5								
15	26.6		4.97	1.49	26.06	3.78	0.36	0.19	2.06
16	16.7								
17	31.5								
18	33.8								
19	33.7								
20	27.8		5.19	1.55	26.87	3.76	0.35	0.25	1.77
21	34.2								
22	26.4								
23	30.1								
24	14.3								

Depth (cm) (cm)	Opal (%)	$\pm 1\sigma$	Al (g/kg)	Ba (g/kg)	Ca (%)	Fe (g/kg)	Ti (g/kg)	Mn (g/kg)	K (g/kg)
25	21.8		5.10	1.43	28.73	3.87	0.37	0.28	1.65
26	24.9								
27	27.1								
28	14.7								
29	23.1								
30	21.2								
31	15.1								
32	16.6								
33	15.7								
34	6.4		5.51	1.33	32.11	4.43	0.43	0.25	2.04
35	14.2								
36	7.7								
37	15.5								
38	12.2		5.57	1.22	32.65	4.74	0.50	0.23	2.02
39	13.0		5.23	1.35	30.90	3.95	0.41	0.22	1.96
40	8.9								
41	13.8								
42	20.3		8.96	1.62	29.85	7.79	0.89	0.35	3.11
43	21.9								
44	22.4								
45	34.5								
46	18.8		12.86	1.97	22.17	11.69	1.43	0.56	4.23
47	30.7								
48	28.1								
49	26.9								
50	22.4		22.55	2.27	10.50	21.10	2.50	0.75	6.65
51	39.6								
52	26.7								
53	49.1								
54	45.7		24.94	2.22	4.71	24.23	2.89	1.44	7.55
55	51.6								
56	46.0								
57	52.0								
58	58.2		23.12	2.20	4.23	22.46	2.68	1.64	5.65
59	46.1								
60	58.6								
61	62.2								
62	66.0		25.15	2.06	1.42	26.81	3.56	0.73	7.88
63	75.2								
64	78.1								
65	59.5								
66	59.5		26.50	1.97	1.04	31.29	3.88	0.46	8.08
67	59.1								
68	49.4								
69	55.3								
70	45.1		27.21	1.84	1.09	31.23	4.00	0.37	8.32
71	60.9								
72	42.0								
73	49.1								
74	56.9		24.85	1.83	1.81	26.02	3.69	0.37	7.59
75	58.1								
76	45.4								
77	65.0								
78	53.5		27.00	1.80	1.09	23.98	3.82	0.38	7.46
79	65.1								
80	67.3								
81	69.5								
82	51.3		26.27	1.65	0.91	19.33	3.18	0.26	8.22
83	64.1								
84									
85	61.1								
86	51.7		22.71	1.55	0.84	19.62	3.10	0.21	6.90
87	64.7								

Depth (cm) (cm)	Opal (%)	$\pm 1\sigma$	Al (g/kg)	Ba (g/kg)	Ca (%)	Fe (g/kg)	Ti (g/kg)	Mn (g/kg)	K (g/kg)
88	52.9								
89	66.3								
90	57.7		21.95	1.54	0.80	18.04	3.02	0.20	6.87
91	69.1								
92	64.5								
93	69.2								
94	70.0								
95	68.0								
96									
97	63.6								
98									
99	57.9								
100			24.23	1.62	0.90	20.83	3.55	0.22	7.59
101	58.3								
102									
103	47.6								
104									
105	47.1								
106									
107	42.9								
108									
109	64.8	14.8							
110	59.0	6.9							
111	55.6	9.4							
112	57.0	10.8							
113	48.8	1.7							
114	42.6	2.8							
115	54.4	5.4							
116	52.4	6.4							
117	49.8	10.6							
118	47.6	15.5							
119	31.9	3.0							
120	36.3	8.3	22.69	1.53	1.11	20.32	3.15	0.20	7.25
121	48.6	8.2							
122	48.2	2.6							
123	47.4	4.9							
124	47.9	10.1							
125	43.7	4.4							
126	42.1	9.2							
127	48.7	3.1							
128	46.0	1.4							
129	55.1	10.8							
130	54.6	2.5							
131	48.8	5.5							
132	60.7	12.9							
133	54.4	6.6							
134	52.1	1.2							
135	47.6	2.4							
136	51.6	3.4							
140			25.71	1.71	0.95	22.65	3.58	0.23	8.01
160			20.89	1.61	0.78	17.13	2.74	0.18	7.08

Depth773 (cm)	Al (xrf counts)	Ca (xrf counts)	Ti (xrf counts)	Mn (xrf counts)	Fe (xrf counts)	Ba (xrf counts)	K (xrf counts)
4	470	410122	2455	872	10095	7623	1856
5	484	370766	2282	924	10732	7685	1980
6	297	372667	2336	894	10188	7829	2023
7	301	301872	1886	994	8123	7083	1749
8	238	366510	2391	1175	10727	8536	2042
9	350	345120	2421	976	11185	8743	2306
10	350	368199	2560	866	10869	8219	2166
11	437	393365	2142	1123	9770	7809	1980

Depth773 (cm)	Al (xrf counts)	Ca (xrf counts)	Ti (xrf counts)	Mn (xrf counts)	Fe (xrf counts)	Ba (xrf counts)	K (xrf counts)
12	454	404816	2254	696	9953	8163	2097
13	386	386070	2564	973	10962	8128	2182
14	507	366077	2350	1069	10906	8291	2018
15	434	370698	2389	1161	10390	7603	1859
16	387	361579	2135	1059	9644	8243	1618
17	304	369167	2232	1292	9989	8350	1943
18	188	385894	1938	866	8540	7555	1634
19	426	371191	2266	1076	8811	7669	1672
20	389	340263	2072	1199	9609	7550	1514
21	360	412847	2287	967	11337	8229	2246
22	377	388919	2406	1325	11006	8531	1947
23	318	405915	2746	1570	11365	8338	2214
24	382	398117	2331	1244	10809	7839	1703
25	321	386842	2407	1176	10213	7422	2045
26	494	439763	2574	1349	11727	7827	1908
27	269	457928	2472	1064	11590	7584	2113
28							
29	545	463744	2641	1371	13447	7728	2303
30	484	453250	2598	872	12464	7603	2105
31	452	484300	2588	1524	12244	7961	1801
32	658	454494	3253	1309	16742	8553	2672
33	559	462180	3496	1412	17232	8327	2809
34	460	390650	2690	1109	16367	8165	2536
35	722	389052	3963	1459	21633	8863	3396
36	590	485656	3314	1146	15940	8578	2395
37	492	486753	3119	1004	16378	9000	2922
38	572	404126	3259	1274	19216	9485	2978
39	792	349649	5077	1419	30980	10885	4696
40	703	313031	4770	1740	32520	10838	4521
41	765	327826	4799	1413	31081	9692	4357
42	747	355140	4195	1690	27137	10272	3975
43	880	348515	5257	2067	33855	10267	5304
44	1316	225371	7013	2592	51069	11097	6609
45	845	303642	6046	1863	40383	11101	6113
46	1276	165743	7727	1459	59483	11049	7565
47	1416	173893	8208	1772	60939	10785	7764
48	1029	138312	6828	1847	50955	10275	6049
49	1419	77627	8499	4997	70452	10350	8537
50	1190	60020	8333	5563	70524	9950	8143
51	1144	151326	7110	3043	53721	10873	7004
52	1291	194214	7636	2485	49332	10698	6970
53	1426	144710	8493	4001	62487	9639	7983
54	1206	24397	8827	6592	72250	8983	8067
55	775	77318	5348	3027	45516	8829	5578
56	974	103909	6288	2614	47982	9545	6011
57	1273	47767	9160	4734	76282	9795	9151
58	1021	113969	7173	2794	56859	9407	6410
59	1035	29923	9026	2545	76486	8892	7819
60	1115	16649	8778	1524	78469	8713	7839
61	1193	20428	10090	1240	85913	8761	8495
62	1176	16826	9565	1250	88522	8973	8240
63	1221	23310	9259	1908	78066	9124	8174
64	1058	42323	8666	1630	76456	9527	8245
65	1180	22612	10424	1426	112705	8993	9143
66	1327	23205	11092	1010	114592	8731	9860
67	1609	19552	12864	1230	109774	9721	11081
68	1491	23498	10764	2130	86728	9269	9517
69	1314	39490	8095	1789	65584	8488	7455
70	1277	44804	8377	1251	67219	8226	7545
71	1487	16423	10565	1419	96596	8371	9174
72	1580	17099	11239	1468	88457	8473	9363
73	1515	16935	11182	1061	85606	8465	9577
74	1485	16272	10614	679	75531	8519	8998

Depth773 (cm)	Al (xrf counts)	Ca (xrf counts)	Ti (xrf counts)	Mn (xrf counts)	Fe (xrf counts)	Ba (xrf counts)	K (xrf counts)
75	1623	17194	11539	1158	80451	8306	9454
76	1358	15443	10586	1545	70802	8483	8360
77	1470	16029	9934	1042	68587	8121	8718
78	1396	15061	9295	962	63004	8156	8130
79	1092	14146	8964	941	61748	8036	7960
80	1113	12835	7794	864	55034	7933	7040
81	1096	12242	7778	1012	55611	7073	6787
82	700	9292	5523	1087	43998	5880	4687
83							
84	903	10367	6689	883	47726	6603	5591
85	948	11942	6469	857	46471	6443	5640
86	1040	11330	6862	786	47763	6596	5901
87	948	10723	6445	690	44478	6357	5514
88	682	10007	5714	1003	40392	5988	5168
89	581	10795	4765	411	36685	5356	4894
90	792	9465	4938	786	37524	5912	4708
91	918	11036	6523	1165	45094	7040	5655
92	874	12655	7513	944	52891	7008	6526
93	1112	14503	7898	987	58675	6977	7088
94	1079	14192	8957	1099	65560	7084	7989
95	967	10523	5639	753	48001	6040	5956
152	1340	14490	9636	491	67202	7064	9026
153	1108	13870	7533	979	57808	6701	7686
154	1084	13722	7703	727	58482	6355	7506
155	1074	13027	8019	785	59481	6901	7842
156	938	15521	6948	958	54551	7465	7544
157	922	12190	6572	1193	54204	6431	7230
158	907	10777	6619	687	51155	5846	6664
159	863	13647	6852	1090	53913	6849	7102
160	1061	11562	6540	915	54014	7217	6792
161	867	11502	6710	901	53773	6794	6842
162	967	11129	6935	1081	54214	7406	6988
163	1002	10686	6948	1114	56459	6599	6956
164	960	10595	6341	873	53023	6240	6586
165	889	11344	6668	1059	54394	6132	7045
166	1091	10718	6622	1001	54111	5982	6744
167	922	10443	6610	1012	53389	6342	6800
168	891	9947	6093	918	50308	6574	6197
169	850	10199	6082	662	54891	6379	6517
170	920	10366	6360	401	52419	6998	6735
171	761	9775	5974	850	50200	6527	6271
172	777	10361	6057	1023	52291	6395	6356
173	980	13438	7938	843	62080	6766	7792
174	961	12501	7240	803	59352	6637	7494
175	737	9724	5315	653	42811	5828	5970
176	796	10401	6083	1052	50200	6957	6496
177	824	10523	6358	1238	53320	6990	6645
178	954	10600	6738	729	53322	6928	6721
179	989	10935	7214	898	56707	7162	7232
180	874	10898	6482	517	58007	6341	6697
181	945	11011	6791	899	56077	5845	6918
182	952	9629	6007	744	50449	5923	6650
183	779	11308	6001	1056	47828	5469	6328
184	740	9832	5550	918	52231	5349	5956
185	678	8758	4948	456	49871	5645	5580
186	573	8700	4946	633	49272	4782	5581
187	754	8157	4189	755	47236	5067	5317
188	878	9409	5323	891	47196	5299	6003
189	598	8952	4626	1127	47892	4897	5526
190	843	8542	4767	758	49284	5261	5210
191	581	8658	4241	478	45066	4543	4635
192	632	8712	4566	956	44347	5418	5066
193	737	8873	4898	749	46391	5480	5131

Depth773 (cm)	Al (xrf counts)	Ca (xrf counts)	Ti (xrf counts)	Mn (xrf counts)	Fe (xrf counts)	Ba (xrf counts)	K (xrf counts)
194	566	8300	4105	717	42309	5283	5126
195	694	8128	4304	617	38197	4901	4718
196	475	8685	3798	655	33256	4687	4291
197	578	8547	4443	508	41034	5341	5152
198	637	10072	4181	786	37875	5424	4935
199	517	8978	4000	515	33756	5026	4600
200	607	13953	4002	885	35418	5539	4674
201	661	8916	3741	750	37498	5558	4451
202	655	8608	4223	813	35514	5203	4574
203	566	8466	4452	948	34433	5418	4578
204	580	8243	4063	611	33238	5920	4490
205	601	8299	4398	796	35173	6169	4590
206	554	7927	4054	660	39769	5998	4473
207	519	7700	3862	677	34815	5197	4063
208	440	7599	3362	764	29897	4740	4351
209	389	8199	3274	844	30868	5703	3339
210	554	7774	3604	665	36390	5626	4245
211	504	7885	3933	585	38761	6250	4592
212	640	7988	4386	1055	38459	6217	4801
213	515	8099	4355	1065	38203	5991	4681
214	682	8176	4421	781	39722	5884	4704
215	598	8457	3939	671	36239	5926	4791
216	707	7949	4323	885	34299	6464	4683
217	689	7555	4025	704	32364	5968	4633
218	632	7234	3569	824	30249	5742	4711
219	663	7428	3474	787	30648	5674	4502
220	682	7347	3440	683	30603	5823	4286
221	564	7176	3504	732	30912	5740	4149
222	501	6754	3313	693	26745	5429	4200
223	474	6822	3355	551	26768	5284	4215
224	506	6719	3133	767	28593	5752	3902
225	509	7171	3691	776	29557	5234	4372
226	484	6940	2789	663	24839	5622	3947
227	502	7162	3371	894	27437	5446	4159
228	550	6997	3388	622	27375	5119	4210
229	552	7788	3757	564	32027	4942	4296
230	514	7375	3108	806	27794	5011	4129
231	541	6206	2710	519	22879	5202	3336
232	512	6663	2722	464	24964	4903	3497
233	499	7099	3417	862	26782	5277	3504
234	517	7858	3827	517	32608	5797	4063
235	610	7644	3910	546	30035	5561	3889
236	605	7765	3681	655	30831	5603	4507
237	503	7464	3348	711	30356	5883	4441
238	630	7705	3793	944	38330	5336	4349
239	630	7492	3140	572	36844	4991	4755
240	624	7275	3054	907	32240	5212	4342
241	567	6531	3041	916	31553	4980	3745
242	630	6441	2851	822	30398	5094	3760
243	506	6709	2953	484	32357	5740	3842
244	503	6612	3172	867	30228	5038	4028
245	682	6622	3299	561	29144	5491	3541
246	547	7153	3984	856	29954	5971	3778
247	509	6597	2480	538	24606	5256	3734
248	471	6107	2617	700	26594	5242	3656
249	497	6378	3027	932	24007	4788	3770
250	437	6196	2604	704	24467	4564	3409
251	432	6710	2748	838	24315	4370	3566
252	511	6571	2436	827	23393	4445	3627
253	396	6826	2825	702	22597	4744	3528
254	551	6034	2393	552	22465	5306	3127
255	316	6441	2489	1156	25471	4539	2948
256	377	6078	2073	779	20892	4434	3451

Depth773 (cm)	Al (xrf counts)	Ca (xrf counts)	Ti (xrf counts)	Mn (xrf counts)	Fe (xrf counts)	Ba (xrf counts)	K (xrf counts)
257	464	6081	1918	568	20330	4179	3393
258	472	6343	2378	580	23931	4606	3248
259	459	6393	2457	753	25889	5097	3112
260	474	7766	2541	539	22628	4601	3441
261	480	9403	2751	896	22352	4849	3547
262	570	8768	2626	770	22046	4658	3314
263	578	7962	2449	503	21832	4875	3304
264	648	10298	2839	578	23872	5125	3374
265	703	13576	3431	533	29325	6139	3927
266	656	16001	4111	665	33302	6218	4335
267	817	17189	4556	838	36964	7027	4628
268	615	20042	4857	436	37206	6881	4957
269	698	24772	3871	504	30382	6528	4275
270	618	22960	3027	541	24620	4913	3526
271	729	23371	4335	817	36478	6419	4930
272	696	22400	4924	927	41541	6779	5244
273	784	25781	4637	920	40703	7239	5290
274	889	30237	5110	665	41415	6468	5010
275	490	24835	2449	808	23367	5018	3530
276	549	22970	3521	804	28084	5922	3837
277	834	21030	5224	782	42936	6462	5166
278	683	20396	4687	656	38851	5689	5104
279	868	26835	4560	706	38517	6056	5085
280	726	40100	4728	762	42233	6342	5085
281	719	15648	5242	991	52940	6239	5728
282	731	18076	5751	840	60572	6340	6041
283	900	24103	5715	807	50952	6040	5517
284	776	10068	5831	831	56535	5958	6096
285	848	10166	5226	843	49639	6411	6169
286	741	9514	4763	900	44216	5260	5255
287	661	9732	4528	571	38162	5411	4911
288	821	9874	4723	471	40156	4921	5604
289	573	10215	4146	670	36463	5227	5030
290	797	11708	5437	685	43807	6102	5522
291	896	9388	4944	720	44158	5849	5870
292	695	8994	4343	656	39582	5285	5632
293	682	11384	4917	688	40623	5184	5351
294	667	9385	4477	780	37693	5493	5262
295	632	10317	4764	610	36833	5539	5434
296	713	10775	4996	1080	41710	6166	5411
297	477	9245	3515	595	30062	5138	4683
302	785	11376	4412	838	36142	5355	5319
303	649	9023	4080	970	33989	5529	5284
304	744	9229	3615	437	35714	4828	5188
305	747	8860	3788	649	32712	5117	4997
306	618	7939	3327	869	31747	4754	4585
307	692	8154	3354	850	29561	4722	4636
308	637	9058	3468	850	29911	4868	4870
309	699	8226	3535	994	30972	4914	4520
310	703	10328	3629	692	31281	5223	4648
311	577	9291	3244	732	32026	5065	4568
312	700	9592	3712	773	32722	5126	4899
313	529	8875	3147	838	27648	4900	4436
314	578	9283	3387	648	29879	5064	4443
315	526	9311	3354	713	29742	4948	4729
316	662	10876	3863	644	32265	4964	4848
317	551	11461	3877	712	29724	5100	4619
318	660	14444	3560	868	30019	5342	4652
319	587	11753	3901	798	29938	5091	4769
320	656	10091	3154	617	28239	5037	4332
321	619	9367	3322	726	27866	4922	4834
322	685	9796	3275	716	28847	4682	4373
323	717	9800	3326	1010	29818	5207	4421

Depth773 (cm)	Al (xrf counts)	Ca (xrf counts)	Ti (xrf counts)	Mn (xrf counts)	Fe (xrf counts)	Ba (xrf counts)	K (xrf counts)
324	873	10728	3576	507	31706	5524	5315
325	838	9908	3454	530	30622	5629	4984
326	546	8423	3240	655	26682	5361	4412
327	614	8730	3688	923	33168	5777	5036
328	844	12030	5003	1049	41729	6436	6120
329	762	12153	4897	554	42988	6680	5773
330	859	13312	4548	870	41695	7087	6042
331	772	10873	4434	526	37731	5787	5422
332	732	10912	3780	800	32335	5076	4662
333	705	9544	3718	717	35090	5108	4837
334	598	7163	3536	911	31868	4727	4569
335	852	8065	3969	732	33395	5193	5123
336	773	7542	3675	820	30160	5078	4633
337	544	7385	3684	692	34807	5731	4596
338	594	7112	3673	704	32825	4951	4889
339	614	7239	3258	549	28447	4951	4758
340	737	7400	3835	938	31259	4952	4973
341	659	7399	3457	655	29059	5547	4433
342	810	7477	4075	1081	31780	5242	4894
343	600	6511	3152	761	25915	4723	4390
344	669	6766	2733	825	26390	4420	4622
345	597	6453	3202	616	26517	4980	4238
346	657	6486	2680	984	27577	4934	4121
347	550	6472	2763	765	26270	4652	3975
348	507	6050	2524	414	26858	4659	3650
349	605	6351	2755	964	29431	4571	4083
350	527	6363	2202	694	21672	4590	3774
351	576	5898	1895	961	18965	4275	3370
352	556	5983	2210	539	20304	4807	3150
353	597	6369	2591	675	21399	4169	3638
354	514	5662	2259	913	22112	4120	3399
355	431	6530	2157	498	19764	4667	3266
356	456	6217	1691	936	19782	4464	3094
357	361	7099	1896	712	19092	4430	3182
358	569	8439	1782	653	19781	3272	3092
359	407	12504	1688	1016	17811	3856	2912
360	357	8646	1486	579	13921	3899	3033
361	365	10125	1553	925	14426	3672	2953
362	378	9952	1783	693	15306	4432	3224
363	413	10559	1525	880	14789	4398	3094
364	523	12600	1724	798	17445	4432	3479
365	531	11029	2982	729	24075	5206	4055
366	539	13490	2163	949	19204	4937	3195
367	411	13000	1772	627	17310	5003	2899
368	419	14437	1859	751	15900	4222	2839
369	394	15327	1318	654	15023	5227	2742
370	484	19086	1668	667	16472	4795	2922
371	468	22869	2067	869	17796	5779	3109
372	488	27677	2376	821	20958	5769	3217
373	500	28624	2115	546	19827	5550	3262
374	410	30699	2030	559	19733	5878	3306
375	525	31748	2196	667	22029	5868	2981
376	526	28744	1577	819	16687	4623	2954
377	427	28182	1445	389	15534	5867	2704
378	601	38169	2883	657	28212	7192	3994
379	499	40698	3484	983	32869	6371	4626
380	390	21150	1942	678	18449	4538	3079
381	565	19192	1741	669	18411	5791	2970
382	663	38379	3547	695	30937	6397	4273
383	683	34134	3561	1005	32701	6150	4623
384	713	33857	4368	777	38888	6587	5465
385	768	33241	3988	737	37780	6432	5266
386	751	31501	4148	936	39114	6630	5231

Depth773 (cm)	Al (xrf counts)	Ca (xrf counts)	Ti (xrf counts)	Mn (xrf counts)	Fe (xrf counts)	Ba (xrf counts)	K (xrf counts)
387	765	32166	4402	907	38394	6747	5243
388	817	32219	4545	605	39457	7050	5559
389	790	28312	4705	687	38154	7049	5594
390	674	26605	3560	409	30626	6323	4347
391	558	36860	3361	796	28397	6628	4725
392	652	37201	3573	499	32479	5927	4607
393	656	18358	3647	858	35348	5247	5010
394	475	16714	3231	1007	33483	6077	4355
395	592	25707	3672	519	33153	5778	4486
396	422	20387	2794	802	30089	5040	4224
397	594	23327	3512	665	31063	4914	4315
398	723	26746	3064	683	28356	5221	4137
399	638	39848	3257	1052	30520	6088	4428
400	520	41231	3269	598	29458	5350	4755
401	528	22971	3730	735	31171	5129	4217
402	691	14891	4420	981	38623	5412	5101
403	706	11618	4407	1144	39288	5619	5140
404	600	11706	3638	834	35032	5148	4478
405	563	11830	4455	867	40418	5319	5334
406	598	16886	3600	822	35061	5570	4853
407	605	14677	3843	819	43962	5240	5089
408	550	8731	3853	808	45450	5502	5221
409	684	7730	4076	836	45436	5438	5332
410	602	7659	3847	811	40501	5561	5047
411	630	7244	3985	943	36591	5406	4991
412	616	7481	4117	832	41756	5184	4913
413	615	6724	3789	829	47669	5377	4811
414	526	7274	3808	779	39846	5638	4715
415	694	7632	3880	877	37008	5665	4938
416	771	8743	3873	594	31949	5422	4957
417	681	7568	3727	715	31392	5630	4766
418	543	7129	3793	836	30295	5372	4619
419	583	6368	3390	714	28640	5212	4339
420	696	7390	3742	821	35310	5244	4524
421	676	7739	3253	883	34188	4727	4660
422	550	7430	3131	776	29289	5148	4392
423	562	6982	3226	689	30019	4771	4236
424	478	6578	2623	894	29718	4825	4452
425	537	7925	3772	778	36968	5040	5157
426	641	7642	3537	722	34364	5803	4446
427	667	7140	3814	660	33702	5335	4520
428	610	7036	3083	700	31929	5603	3922
429	530	6974	3154	636	30364	4210	4324
430	505	7495	3176	684	26623	4798	4379
431	643	8055	3882	1022	30718	5270	5143
432	550	7875	3473	525	27104	5727	4467
433	616	6751	2652	782	24022	4976	3577
434	566	6184	2814	637	24186	4908	3863
435	536	6393	2444	717	25973	4415	4105
436	550	7940	2523	733	21582	4145	3634
437	562	7440	2486	524	23228	4076	3738
438	583	8079	3091	662	24770	4661	3847
439	594	7361	2684	774	25159	4727	4078
440	621	7724	2652	699	25940	4627	3923
441	511	8503	2913	743	24007	4785	3642
442	450	11697	2533	821	21888	4947	3271
443	386	8278	2081	640	23911	4467	3660
444	340	6222	2049	600	20498	3852	3240
445	373	6917	1893	817	20448	4302	3221
446	464	8354	2284	810	20926	4340	3358
447	523	7610	1872	553	19250	4063	3128
448	371	7437	1734	606	17186	3734	3141
452	530	10381	1822	999	19414	3688	2801

Depth773 (cm)	Al (xrf counts)	Ca (xrf counts)	Ti (xrf counts)	Mn (xrf counts)	Fe (xrf counts)	Ba (xrf counts)	K (xrf counts)
453	530	8507	1523	969	17465	3876	2656
454	414	7619	1445	546	16769	4006	2468
455	387	7603	1995	1013	18436	3996	2716
456	467	7810	1876	582	17402	4482	2891
457	440	6852	1854	691	19244	4449	2718
458	470	8089	1910	545	19475	4610	2955
459	362	9120	1903	715	18716	4851	2855
460	488	8952	1977	657	19998	4444	2945
461	439	8486	1861	918	17821	4458	2979
462	406	8897	1809	833	17914	4449	2755
463	468	9910	1774	732	18955	4028	3341
464	465	11099	1642	644	21601	4213	2946
465	374	15494	1753	576	19986	3674	2435
466	577	16367	1784	671	20723	4251	2661
467	446	11892	1580	598	20165	4038	2604
468	382	13059	1656	815	16711	4334	2502
469	343	13466	1398	762	15601	4255	2601
470	409	12824	1421	509	13982	4305	2639
471	436	11565	1425	428	12932	4293	2128
472	382	12677	1300	569	13306	3830	2318
473	411	11483	1566	817	13998	3895	2404
474	348	12376	1341	649	16503	4206	2475
475	425	15770	1601	641	16663	3917	2196
476	455	16439	1252	493	11457	3872	1961
477	481	14967	926	698	10832	4224	2117
478	341	13252	1185	800	12153	3951	2201
479	371	18000	1384	1034	12944	4035	1998
480	356	18453	1274	647	14373	4254	2179
481	393	21569	1174	565	12555	3896	2160
482	433	25382	1314	565	13113	4457	2191
483	495	25983	1201	530	14140	3976	2329
484	352	23886	1111	620	12199	3692	2168
485	331	22735	955	704	11697	3857	1932
486	363	21641	1208	766	12158	3869	2034
487	483	26248	1330	790	12060	3791	2188
488	313	27003	986	703	11104	3871	2153
489	286	27922	923	637	11395	4054	2360
490	283	27113	1150	413	11924	3979	2390
491	419	30550	1056	791	12034	3934	2392
492	344	35775	1093	652	13553	3774	2374
493	269	30786	796	618	11946	3639	2288
494	372	36716	1164	605	11525	4514	2313
495	372	39436	1293	613	12249	3947	2162
496	446	37136	843	825	11310	3929	2215
497	423	35359	629	714	7777	3353	1737
498	430	41583	953	901	12096	4241	2395
499	262	52218	1039	822	12819	4714	2373
500	293	51608	930	949	12033	3987	1945
501	345	33416	1166	1119	11380	4124	2371
502	363	27097	817	848	11138	4533	2464
503	410	26699	1423	520	12978	4865	2160
504	408	47601	1151	727	12929	4818	2225
505	454	59648	1440	806	13777	4886	2600
506	537	68575	1322	666	14707	4864	2652
507	370	83249	1462	650	14070	5087	2583
508	333	63681	1163	609	14258	4640	2419
509	407	63785	1451	668	14576	4684	2303
510	393	65147	1453	676	15265	4955	2520
511	440	66670	1247	849	14586	5222	2481
512	370	72847	1583	607	15235	5082	2438
513	410	78065	1447	412	14637	5982	2177
514	555	75774	1589	905	16193	4860	2535
515	626	71870	1768	720	17036	4847	2468

Depth773 (cm)	Al (xrf counts)	Ca (xrf counts)	Ti (xrf counts)	Mn (xrf counts)	Fe (xrf counts)	Ba (xrf counts)	K (xrf counts)
516	497	80603	1955	686	17310	5648	2438
517	599	93576	2130	875	24159	5420	2906
518	375	74477	1716	703	21075	4911	2985
519	448	63502	1862	774	17705	4942	2699
520	505	49570	1566	835	16355	5213	2526
521	617	59161	2063	576	21753	4996	3165
522	572	50436	2146	653	21599	5043	2917
523	473	43765	1787	674	20062	5456	2512
524	519	53211	2184	707	20163	4521	3022
525	485	46718	1967	749	20884	5326	2932
526	588	27182	2173	805	22539	5132	3080
527	682	30967	2527	524	23551	5744	3626
528	491	39769	1878	716	19764	5513	2801
529	583	36778	2468	845	26360	5292	3536
530	580	26543	2445	466	22778	5021	3321
531	518	23689	2246	998	21326	5171	3215
532	607	21590	2397	922	23387	5594	3452
533	557	25321	2490	898	21989	5544	3222
534	473	30788	2076	534	21267	5131	3374
535	467	21190	2544	617	24390	5195	3519
536	683	23388	3093	1111	25429	6047	3645
537	457	22157	2301	564	21918	5406	3349
538	639	23252	2193	808	21319	5026	3022
539	495	25448	2707	654	25403	5425	3883
540	556	25147	2807	723	23545	5243	3268
541	506	27783	2978	1352	27373	5481	4360
542	502	37432	2342	486	22088	5772	3554
543	506	26235	2420	651	22673	5272	3337
544	563	27712	2667	768	24858	5024	3806
545	491	22594	2223	769	24105	5526	3470
546	415	18959	2575	962	24606	5168	3197
547	578	14920	2658	733	26400	5432	3775
548	487	15273	2790	761	28707	5113	3917
549	585	15753	2841	910	26604	4650	3689
550	521	17733	2290	816	24076	3845	3260
551	437	17746	2415	806	25695	5266	3729
552	532	12638	2564	874	24635	4995	3312
553	456	14259	2431	776	22634	5076	3323
554	542	20524	3015	699	24884	5729	3563
555	475	19436	2211	883	22424	4680	3447
556	422	15996	1449	681	14173	3596	2842
557	471	19815	1544	896	15095	3474	2663
558	337	36401	1413	653	16392	4872	2349
559	518	34727	1484	807	24677	5328	2691
560	293	35498	1814	620	24906	5292	2585
561	351	34416	1943	770	23266	5413	2759
562	486	30138	1561	1018	21958	5232	2525
563	372	29026	1597	511	21873	5617	2889
564	432	29353	2107	891	26662	4749	2946
565	355	25711	1483	643	18995	4926	2548
566	483	23277	2043	970	24091	5170	2901
567	488	20238	2250	673	25048	5246	2962
568	449	20983	1978	697	27890	4988	3476
569	505	20813	2359	1005	25625	5712	3241
570	486	28948	2097	827	24108	5105	3023
571	505	43582	1659	716	20964	5306	2971
572	478	64203	1404	542	14175	5349	2515
573	527	58951	1190	483	13517	5494	2163
574	450	60455	1431	827	14296	5465	2107
575	461	58096	1108	821	12870	5107	2579
576	439	41752	1105	957	13767	5152	2270
577	434	53728	1536	931	15123	5346	2478
578	493	63734	1188	984	16056	5107	2569

Depth773 (cm)	Al (xrf counts)	Ca (xrf counts)	Ti (xrf counts)	Mn (xrf counts)	Fe (xrf counts)	Ba (xrf counts)	K (xrf counts)
579	460	67375	1452	602	14558	5233	2539
580	438	52658	1278	803	13095	4712	1987
581	453	44905	1781	995	16540	4840	2576
582	496	38197	1577	852	14851	4613	2486
583	558	42315	1803	764	15875	4983	2884
584	513	27595	2493	556	21046	5534	3287
585	423	49613	1633	651	16795	4855	2873
586	501	59545	1580	624	14359	4776	2574
587	368	69587	1091	690	13281	4816	2411
588	384	76913	1648	874	14685	4558	2622
589	344	57785	1050	874	11008	4290	2056
590	413	67543	1644	508	14176	4484	2539
591	288	69192	1358	561	12865	4628	2456
592	473	64879	1153	371	13277	4961	2389
593	391	58196	1297	473	13174	4075	2264
594	419	59159	895	659	9232	5364	1946
595	555	104216	2916	755	23817	6475	3747
596	564	101356	2629	634	22876	6823	3441
597	464	85442	2711	947	22203	5869	3550
602	752	78608	3487	743	30781	5012	5135
603	599	105937	2954	655	23977	6166	4260
604	644	115433	3374	1077	30054	6354	4727
605	493	114646	3617	977	27651	6381	4786
606	576	111631	3364	742	26072	5671	4454
607	471	77590	2186	462	19123	5474	3632
608	423	76179	2364	664	23053	6743	3593
609	508	67826	3103	710	27422	7707	4247
610	428	57832	3396	744	31481	7276	4478
611	490	60869	2859	706	29816	6846	4281
612	436	61896	3086	461	27582	6445	4094
613	632	64506	3958	676	36925	6911	4980
614	450	51256	2804	921	27832	6044	4234
615	405	61666	3153	566	31080	7338	4392
616	603	64052	3236	874	36143	7702	4477
617	633	62378	3981	1077	36510	7627	4842
618	558	66231	3898	725	32959	6741	4833
619	602	63243	3661	790	32312	6803	4705
620	564	57476	3145	818	30295	6265	4552
621	503	47026	2762	737	27639	6658	4042
622	706	48191	3842	584	33885	6523	4799
623	687	50550	4184	1026	37113	7074	5470
624	589	57626	4178	884	37878	7964	5230
625	639	64836	4337	849	38901	6682	5651
626	608	51832	5003	942	44876	7286	5954
627	656	47939	4980	811	47684	8293	5872
628	652	32246	5552	971	50689	7830	6238
629	786	40482	5588	1074	48767	7484	6424
630	641	33540	5771	952	50617	7031	5974
631	719	33052	5685	968	49899	6574	6190
632	735	30134	4901	1079	46903	7465	5400
633	765	34322	6084	811	54409	7405	6476
634	528	22307	5122	1056	46318	7120	5279
635	675	25063	5730	626	50070	6708	6367
636	626	31240	4706	723	40975	6925	5442
637	862	28889	6235	932	52081	7589	6684
638	756	24841	6741	1084	54228	7601	6713
639	839	22784	5881	1099	50859	7259	6376
640	627	21677	6204	852	51155	7959	6388
641	569	21972	5967	602	51254	6933	6552
642	756	37803	5127	769	43420	6407	5726
643	762	35930	5221	689	41354	6876	5817
644	647	28971	5445	1265	46602	7257	5691
645	831	24986	7034	1030	59408	7327	7110

Depth773 (cm)	Al (xrf counts)	Ca (xrf counts)	Ti (xrf counts)	Mn (xrf counts)	Fe (xrf counts)	Ba (xrf counts)	K (xrf counts)
646	760	25878	5908	734	53145	7082	6233
647	693	18152	6293	1144	54505	7105	6499
648	884	19026	7158	750	64629	7616	6618
649	773	19088	6384	1109	64928	6976	6539
650	687	19706	5750	1231	56543	6695	6238
651	624	19281	6117	970	63847	7073	6558
652	665	18855	6046	1233	65490	7212	6793
653	726	24056	6830	890	61887	7493	6926
654	662	18284	7274	1149	68637	6949	7001
655	841	26112	7238	684	73681	7142	7455
656	888	21497	8001	1272	76315	7614	7542
657	796	18114	7945	849	71159	7477	7743
658	821	15108	7777	745	71839	7399	7663
659	923	14599	7594	900	71466	7571	7693
660	877	13632	7963	819	67858	7929	7186
661	801	14909	7840	862	65880	7814	7554
662	742	19261	8478	817	68287	7957	7783
663	949	18616	8287	628	66190	8203	8098
664	924	13826	7733	972	66040	7896	7392
665	695	11921	6480	800	62048	8051	6730
666	719	13295	7053	807	57923	7632	6872
667	573	12332	6670	800	54136	7361	6505
668	791	13816	7384	984	61955	8278	7133
669	760	14898	7489	879	64406	8669	7016
670	703	15912	7049	795	58316	7703	7011
671	704	16899	7290	1023	61516	8113	6727
672	975	16152	7935	1022	67054	7954	7617
673	968	15811	8502	666	66995	7744	8013
674	688	15018	7030	1206	58400	7878	6914
675	763	15251	6791	727	56455	7548	6979
676	1004	17609	8905	1081	66974	8308	7886
677	763	16446	7372	1109	58026	7942	7495
678	718	16202	7443	769	59547	7829	6812
679	876	20421	8158	1500	65199	8446	7727
680	810	18787	7977	880	59321	7180	6969
681	635	17874	6246	760	54830	7589	6205
682	731	19551	7518	936	61585	8482	6727
683	638	19180	7009	727	55032	7850	6740
684	778	20222	8324	701	62050	8188	7265
685	693	20991	8664	1268	64635	8722	7757
686	823	23091	8939	985	66406	8198	7931
687	873	21391	7785	969	65869	8079	7930
688	790	22327	7968	1017	61577	8575	7767
689	865	25329	8399	864	64857	8808	7199
690	994	28607	9744	940	72063	9200	8657
691	970	28977	9931	1155	72124	9320	8622
692	971	18395	7942	1220	65506	7736	7072
693	724	15386	6910	1143	69313	7573	6832
694	559	12803	5937	925	55418	7925	5758
695	879	15794	7336	999	62075	8468	6858
696	827	15282	7519	901	60345	8192	6730
697	640	14455	6641	751	59939	7858	6391
698	714	13823	6921	788	56804	7477	6807
699	873	16793	7631	1149	59819	7779	7091
700	812	17441	7381	1225	59223	8251	6578
701	613	15460	7420	666	58484	8123	7090
702	672	15669	7514	800	56851	8044	6737
703	786	21563	9106	1221	65550	8287	8004
704	808	15315	7282	1004	57275	8004	6806
705	679	12010	6196	966	52867	7098	6059
706	537	12069	5692	585	47429	7334	5775
707	693	12193	6178	1105	49856	7002	5694
708	854	23664	5991	733	49146	7811	6013

Depth773 (cm)	Al (xrf counts)	Ca (xrf counts)	Ti (xrf counts)	Mn (xrf counts)	Fe (xrf counts)	Ba (xrf counts)	K (xrf counts)
709	607	12239	5465	763	44393	7370	5422
710	646	10469	4682	814	40529	7076	5154
711	537	10131	4331	855	37136	7276	4705
712	475	9312	4495	625	32183	6813	5267
713	520	10169	4843	648	35305	6846	4608
714	544	9626	4295	676	33975	6684	4225
715	557	10906	4657	755	37048	6612	4686
716	546	10235	3892	830	33683	6579	4401
717	635	9883	4285	634	33083	5925	4366
718	434	9510	3547	562	32164	5645	4094
719	553	9837	4073	712	32112	5970	4262
720	544	8079	3784	471	31400	6065	3866
721	422	7286	2935	518	27437	5488	3482
722	416	7235	2913	354	26761	5076	3814
723	588	8708	3935	926	34101	6070	4278
724	548	8262	3361	633	29863	5188	4298
725	521	6572	2497	903	22914	4661	3495
726	586	7358	3037	524	24724	4930	3798
727	597	7752	3119	770	27206	5079	3794
728	514	7505	3128	709	25755	5567	3516
729	474	7463	3195	578	26762	4860	3676
730	447	6895	2641	578	22855	4351	3572
731	515	8014	3456	762	27707	5592	3827
732	456	7313	3062	642	25357	6234	3556
733	435	6208	1937	598	19092	4829	3208
734	244	5609	2061	962	15867	4156	3126
735	278	5490	1484	639	14835	3816	2808
736	330	5204	1441	904	13910	3758	2439
737	340	5289	1381	522	13545	3779	2481
738	356	4918	933	636	11834	3574	2330
739	283	4747	1227	382	10630	3485	2232
740	240	4412	1069	722	9958	3249	2120
741	482	4636	1341	516	10534	3847	2172
742	309	4940	1364	580	11368	3838	2439
743	466	5353	1224	369	11560	4006	2518
744	360	5308	1479	572	11668	3844	2653
745	342	5391	1271	572	12337	3771	2736
746	308	5454	883	950	10596	3676	1970
747	362	5766	1251	877	12383	3773	2360
748	262	6770	1228	384	11870	3994	2418
752	787	16291	2143	693	20185	3853	3954
753	512	15186	2038	536	19683	3586	3538
754	562	12952	2079	775	18530	4101	3620
755	570	13327	1792	756	16557	4364	3109
756	532	10280	1603	795	13242	4699	3075
757	527	11897	1642	744	15897	4835	3055
758	409	13080	1895	724	16042	5136	3079
759	594	11719	1619	547	16437	5093	2888
760	533	11853	2075	676	16545	5358	3083
761	542	12722	1855	933	18849	5600	3336
762	552	12124	2484	606	22643	6805	3570
763	525	13102	2787	709	22462	7293	3723
764	556	14174	2978	672	24416	6783	3571
765	578	15031	3121	657	24466	6570	3780
766	524	13264	3240	481	27791	6227	3544
767	546	11769	2152	580	18895	6839	3168
768	514	12607	2697	615	27025	6636	3520
769	579	13448	2388	863	23446	5637	3463
770	576	16465	2042	881	19144	5685	3417
771	525	16656	2309	340	17385	6272	3125
772	433	16171	2461	524	19947	6277	3487
773	611	16165	2439	848	21183	7018	3228
774	593	14210	2987	817	24677	6529	3647

Depth773 (cm)	Al (xrf counts)	Ca (xrf counts)	Ti (xrf counts)	Mn (xrf counts)	Fe (xrf counts)	Ba (xrf counts)	K (xrf counts)
775	512	13179	3266	931	25809	6178	3862
776	575	13973	2962	859	25145	6434	3785
777	467	17672	2845	636	22489	6877	3500
778	595	14912	3170	641	26993	6841	3754
779	528	11569	3153	570	27112	5782	3909
780	749	12311	3242	650	25596	5850	3692
781	541	13005	2627	867	24363	6143	3373
782	450	17028	2728	802	25296	6481	3716
783	549	20183	2957	629	25885	5997	3638
784	390	17363	1923	887	18091	4637	3044
785	489	15044	1869	703	16991	4249	2892
786	388	11394	1761	643	16789	4099	2986
787	431	11403	1999	682	17629	4453	2872
788	495	10154	1908	602	19051	4694	2679
789	414	10224	1682	647	18640	5233	2850
790	444	14328	2180	566	17237	5598	2610
791	518	18671	2087	517	17551	4691	3047
792	390	13212	1395	606	12115	3745	2601
793	405	9110	1481	473	13178	3764	2791
794	477	9224	1692	844	14965	3939	2978
795	497	11781	1643	761	14677	4330	2737
796	397	9301	1500	736	14260	4428	2748
797	456	6503	1684	587	14177	4306	2509
798	335	6444	1330	392	13577	4191	2740
799	449	6232	1566	321	13707	3899	2834
800	420	5617	1243	663	12291	4009	2719
801	387	5757	1575	841	13029	4294	2525
802	336	5632	1235	743	11738	3656	2499
803	408	5569	1277	577	11008	3577	2458
804	255	5264	1077	706	10449	4255	2190
805	377	6152	1219	559	11085	3977	2479
806	354	5594	1210	390	10233	3685	2160
807	319	6941	941	785	10031	3806	2227
808	357	5794	1114	387	9371	3323	2095
809	331	6471	1022	710	10603	3262	2419
810	365	6739	1034	552	10696	3589	2288
811	262	6875	787	907	9603	3467	1962
812	425	7291	849	646	9408	3706	1858
813	400	5764	1000	917	10817	4016	2082
814	424	5325	1106	739	10981	4245	2382
815	315	6322	820	529	10850	4278	2593
816	414	7169	846	380	10407	3705	2267
817	429	8926	1100	719	10402	3391	2166
818	425	8270	597	766	8793	3402	1879
819	251	8512	566	744	8266	3873	1806
820	281	8486	637	615	9228	3600	1929
821	347	9455	985	629	10615	3937	2078
822	372	10360	845	882	9959	4131	2044
823	344	12297	748	684	9680	3900	2073
824	477	12852	1101	468	10111	4104	2239
825	321	13313	877	984	11009	3788	2727
826	364	11087	717	901	10174	4066	2156
827	396	10059	569	540	8361	3414	1930
828	408	9554	619	590	8045	3381	1903
829	299	11012	681	616	8212	3487	2153
830	364	12981	658	598	8221	4190	2272
831	402	13626	813	561	9336	3966	1936
832	407	15845	784	535	8709	3623	1877
833	228	19290	554	552	8666	4284	2133
834	284	20943	579	955	9797	4053	2119
835	264	19057	951	447	9867	3921	1920
836	299	19641	550	449	9324	4286	1907
837	265	21819	470	527	8330	4399	2255

Depth773 (cm)	Al (xrf counts)	Ca (xrf counts)	Ti (xrf counts)	Mn (xrf counts)	Fe (xrf counts)	Ba (xrf counts)	K (xrf counts)
838	376	23228	868	651	9504	4182	1856
839	295	25533	879	729	8507	4051	1923
840	332	27293	708	766	8434	3855	1890
841	325	34599	628	745	8338	4066	2125
842	233	36899	782	679	8138	3888	1864
843	344	41728	694	743	9640	4392	2080
844	373	50583	638	658	8260	4734	1980
845	379	49757	840	640	9291	4886	2095
846	348	49808	1172	580	11681	4799	2062
847	385	46831	892	831	10312	5250	2356
848	475	57613	1122	617	12718	5750	2427

Depth (cm)	$\delta^{15}N_{DB}$ (‰)	$\pm 1\sigma$	$\delta^{30}Si_{diat}$ (‰)	StdE	$\delta^{30}Si_{diat}$ (‰)	StdE	$\delta^{30}Si_{diat}$ (‰)	StdE
8	2.28							
9								
10			1.63	0.03	1.61	0.05		
11								
12								
13								
14	2.30							
15								
16	2.72	0.18	1.91	0.10				
17								
18								
19								
20	2.47	0.37	1.71	0.08				
21								
22	2.65							
23								
24	2.87	0.08	1.88	0.08				
25								
26	3.06		1.56	0.03				
27								
28	2.79							
29								
30	3.14	0.96			1.23	0.10		
31								
32	3.24	0.52						
33								
34	3.02		1.14	0.01	1.16	0.05	1.06	0.05
35								
36	3.55	0.75			1.24	0.05		
37	5.26							
38								
39	5.66							
40	4.47	0.09	1.06	0.04				
41								
42	4.48							
43								
44	5.80		0.89	0.02				
45								
46	5.16							
47								
48	6.30	0.13	0.98	0.06	1.15	0.02	1.07	0.04
49								
50	7.11							
51								
52	7.01	0.10						
53								
54	6.64				1.22	0.07		
55								

Depth (cm)	$\delta^{15}N_{DB}$ (‰)	$\pm 1\sigma$	$\delta^{30}Si_{diat}$ (‰)	StdE	$\delta^{30}Si_{diat}$ (‰)	StdE	$\delta^{30}Si_{diat}$ (‰)	StdE
56	7.35							
57								
58	6.92	0.29						
59								
60			1.63	0.04	1.36	0.04	1.59	0.09
61								
62								
63								
64								
65			1.70	0.09				
66								
67								
68								
69								
70	7.69	0.77			1.46	0.05		
71								
72								
73								
74					1.68	0.02		
75			1.26	0.01				
100	6.41	0.64	1.19	0.05				
104		0.23			1.55	0.05		
116		0.71			1.59	0.08		
128		0.50						
130	6.96		1.11	0.06				